STUDIES OF ALLOSTERY IN THE POTASSIUM CHANNEL KcsA BY SOLID-STATE NMR

Yunyao Xu

Submitted in partial fulfillment of the requirements for the degree of Doctor of Philosophy

in the Graduate School of Arts and Sciences

COLUMBIA UNIVERSITY

2018

ABSTRACT

Studies of Allostery in the Potassium Channel KcsA by Solid-State NMR

Yunyao Xu

In this thesis, I focus on studies of the mechanism of inactivation in KcsA. Allosteric coupling between the pH gate and the selectivity filter in the protein is hypothesized to be the cause of inactivation. Allosteric coupling refers to changes at one site of a protein due to perturbations at a remote site. In chapter 3, I measured the potassium affinities at the selectivity filter at neutral and low pH, which corresponds to the closed and open conformation at the pH gate. The results show a three order of magnitude shift in the potassium affinity. This is direct evidence that the pH gate and the selectivity filter are coupled, in support of the activation-coupled inactivation hypothesis. The allosteric coupling factor, defined as the ratio of the affinities, can be used as a benchmark to study other factors in the allosteric process, such as the membrane and specific residues. Because of the potential deleterious effect of the acidic pH on the protein and membrane, we studied a mutant E118A&H25R, in which the pH gate is mutated to be open. Thus we were able to measure the K^+ affinity change in the open and closed conformation at the pH gate at neutral pH. The results confirmed that the opening of the pH gate results in an energetic stabilization of the collapsed (K^+-unbound) state, and shifts the K^+ affinity towards looser binding. In chapter 4, I tested the important role of residue F103 in mediating allosteric coupling, as suggested by electrophysiology and crystallography studies. I mutated this residue and measured the allosteric coupling factor on the mutant. The affinity at low pH is much tighter than wild-type and the coupling factor is significantly reduced. From the spectra, I observe local structural changes on I100 and T74 as a result of F103A mutation, implying the interaction among F103, I100 and T74 to mediate the allosteric coupling. F103 is distant from the pH gate and the selectivity filter; its effect on the coupling and inactivation behaviors confirms that inactivation involves coupling between the pH gate and the selectivity filter. In chapter 5, I developed a method to probe those allosteric participants, such as F103 in KcsA by NMR measurements. I tested this method on KcsA, dissecting KcsA into various functional compartments. Various allosteric participants T75Cg T74Cg I100 were identified. The importance of residue T74 for the coupling was confirmed by

electrophysiology and NMR thermodynamics characterization. In chapter 6, we applied SSNMR to probe the structural and magnetic properties of superatom clusters.

TABLE OF CONTENTS

INDEX OF FIGURES

Acknowledgements

In this long journey, I am really grateful for a lot of individuals, who supported, inspired me in so many different ways and made my life here at Columbia University one of the best memories in my life.

First of all, I would like to express my sincere gratitude to my advisor-Professor Ann McDermott. It is truly an honor to be her student; simply by listening to her and talking to her, I was benefited so much, not only in science but also in life. Her profound and diverse knowledge, unique scientific vision, enthusiasm to science kept me motivated to be a better scientist. I am really grateful for her guidance on my research, the tremendous support whenever I needed it, the trust and the freedom allowing me to explore so many projects, the encouragement to me to overcome my scientific weakness. It is truly my fortune to be in this McDermott family.

I would like to thank Professor Ruben Gonzalez for your instructive discussion and comments in the past five years; Professor Arthur Palmer III for the knowledge you passed in the NMR class and many insightful conversions on the way back to Columbia University from New York Structural biology center; Professor Xavier Roy for your great support in the our cooperative project and Professor Crina Nimigean at Weill Cornell Medical College for your generosity to allow me to do experiments in your lab and your tremendous support and instruction in my project. I want to thank you all again for taking your time to read my thesis and examining me.

I want to express my thanks to all the current and former members of the McDermott group: Wenbo Li, who took me under his wing when I started and taught me how to do SSNMR; Ivan Sergeyev, who provided me with tremendous help on the instruments, computer and patiently passed his knowledge; Manasi Bhate, who laid the foundation of my projects and taught me how to do protein preparation; Benjamin Wylie and Segolene Laage who helped a lot on experimental setup and spectra analysis; Caitlin Quinn and Claribel Nunez, who kindly helped me blend in the new culture; Rivkah Rogawshi, who is a great friend, coworker, listener and helped me so much on my thesis writing; Dongyu Zhang, who is an critical thinker and great collaborator and brought so many insightful discussions in our projects; Gary Howard, who brought me a close look at America with his diverse knowledge and colorful experience; Keith Fritzsching, with whom I enjoyed so many interesting discussions on various scientific topics; Eric Keeler, who helped me on the simulations in the material project ; Zhiyu Sun, who is a great friend and coworker; Kelsey, who helped proofread part of this thesis and Xu Yi, who kept the group meeting organized; Noah, Sonya and Lia, who were wonderful undergraduates and brought new energy to the lab. I really enjoyed our lab atmosphere and thank you all for being wonderful labmates.

A special thank you to my collaborators: Bonnie Choi on the superatom project, for being an ideal collaborator and providing samples whatever you asked for; Jia Chen on the superatom project, for his contribution to the DFT calculation; Dorothy Kim, David Posson and Philipp Schmidpeter in Crina lab for their help on the single channel recording experiments and many enlightening discussion on KcsA.

I collected almost all of the KcsA data at the New York Structural Biology Center. I want to thank scientific staff there - Mike Goger, Boris Itin, Shibani Bhattacharya for their helps with the instrumentation.

I would like to thank friends I made here: Qizhi, Fanghao, Yihui, Boyuan, Hengrui, just to name a few. You made my life colorful; you fueled me with the energy and courage to get over the various bumpers in this journey.

Last but no least, I would like to thank my family: my parents, who unfortunately did not have the chance to receive much education, but firmly believe in education and knowledge, provided whatever they could provide to win me an opportunity to receive better education; my sister and her family, for their love, support and encouragement; my grandparents, for their thoughtfulness and unconditional loves.

Chapter I: Overview of NMR

1.1 What is NMR?

NMR is a technique developed based on nuclear spin science. The nuclear spin of an atom, which can be simply viewed as a small quantum magnet, precesses about a magnetic field with a certain frequency. The characteristic Larmor frequency of the different elements is influenced by the local magnetic environment of the atom. This environment consists of the local electronic field, inter-nuclear spin interactions, molecule orientation, and molecular motion. Hence, the frequency can provide rich information on the atoms, such as the electronic environment, interatomic distance etc.[1–3] The rates of nuclear spin relaxation also provide a large amount of useful information on molecular dynamics.[4,5] NMR is a great and quite unique tool to quantitate molecular conformational dynamics across a large spectrum of time scales and at multiple sites. Modern pulse NMR has been extensively developed to decouple and recouple certain spin interactions so that specific structural or dynamic information can be extracted from the complicated system.[6]

NMR has been applied to a wide variety of systems, including DNA,[7,8] RNA,[9,10] lipid membrane[11] and numerous proteins systems, including globular and membrane proteins, ordered and intrinsically disordered protein, and soluble and insoluble proteins.[1,2,12–14] It is routinely used for various biological questions, such as illustrating structure or dynamics relations to functions, studying protein interactions with other biological compartments such as DNA and RNA, searching for ligands docking sites, monitoring conformational changes under perturbations, revealing enzymatic mechanism etc.[5,15–21] It also has a powerful applications in the field of material science, including analyzing structural and dynamic properties (such as translocation, rotation) of polymer building blocks and relating them to their functions,[22] studying the structure and absorption properties of Metal-Organic Framework (MOF),[23,24] characterizing the surface features of many nanomaterials,[25,26] identifying and quantifying chemical species and their atomic connectivity in electrodes of lithium battery,[27,28] measuring magnetic susceptibility in materials with special magnetic properties,[29,30] and charactering local electronic environment and atomic distances for quadrupolar nuclei.[31,32] Many of these applications have been well-reviewed and excellent reviews on biological and material systems are recommended for more

details.[1,16,22,33,34] In this thesis, we also add another two examples of NMR application: one on a membrane protein and the other on a metallic cluster system.

Clearly, a variety of NMR techniques are required to make these applications feasible. Since the discovery of magnetic resonance phenomena here at Columbia University in 1939 and the first NMR spectrum was taken in 1945,[35] there have been continuing developments in NMR techniques in general, as well as in special techniques associated with the three major subfields: solution NMR, solid state NMR (SSNMR), and magnetic resonance imaging (MRI). Along the path, five Nobel Prizes have been awarded, including the Nobel Prize in Physics (1943) to Isidor I. Rabi, "for his contribution to the development of molecular ray method and his discovery of the magnetic moment of the proton", the Nobel Prize in Physics (1952) to Felix Bloch and Edward M. Purcell "for their discovery of new methods for nuclear magnetic precision measurements and discoveries in connection therewith", the Nobel Prize in Chemistry (1991) to Richard R. Ernst "for his contributions to the development of the methodology of high resolution nuclear magnetic resonance (NMR) spectroscopy", the Nobel Prize in Chemistry (2002) to Kurt Wüthrich "for his development of nuclear magnetic resonance spectroscopy for determining the three-dimensional structure of biological macromolecules in solution", and the Nobel Prize in Physiology or Medicine (2003) to Paul C. Lauterbur and Peter Mansfield, "for their discoveries concerning magnetic resonance imaging".[36] Many excellent reviews and book chapters have been focused on these exciting developments.[2,13,37–43]

1.2 Uniqueness of solid state NMR

SSNMR is the major technique applied in this thesis. In contrast to solution NMR, SSNMR specializes in the study of non-liquid samples, such as solid or gel-phase samples, which do not have a fast tumbling motion. This is of significant importance to the study of membrane proteins[1] and pathological proteins like amyloids[34,44], which are generally insoluble in a physiological environment.

From a spectroscopic perspective, a solid sample can be both advantageous and troublesome. In solution, due to the fast tumbling of molecules, the anisotropies in nuclear spin interactions, such as the chemical shift, the dipolar coupling, and the quadrupolar coupling are averaged out. Therefore, factors

to that contribute to the spectral lineshape are limited and the spectra are highly resolved, which is a great advantage for spectra assignment and analysis. In contract, solid samples have very restricted global motions. Therefore, angular features underlying the chemical shift anisotropy (CSA), the dipolar coupling and the quadrupolar coupling, causing orientation dependent shifts, persist in the solid state. One the other hand, the solid lineshapes therefore contain useful information such as interatomic distance and local torsion restraints, which can be used for structure calculation as well as dynamics study. However, due to these anisotropic interactions, the linewidth of SSNMR spectra are generally worse than those in solution spectra due to Hamiltonians that are insufficiently decoupled or not fully averaged by magic angle spinning (discussed below), making spectral assignment challenging. Many new developments such as fast magic angle spinning (over 100 kHz sample spinning) are intended to solve this problem.[45]

In solution NMR, the linewidth of NMR peaks is inherently limited by the size of macromolecules since the slower tumbling of larger macromolecules in solution leads to faster relaxation of transverse magnetization (shorter T2s) due to enhanced spin-spin interactions. Thus, the size of macromolecule that can be studied by solution NMR without special strategies such as perdeuteration or TROSY is limited.[46] However, the linewidth in SSNMR is not intrinsically limited by molecular sizes since it is generally dominated by other factors, instead of relaxation. Therefore, SSNMR can be applied to large macromolecules, such as GPCRs or EGFR.[47,48]

Unlike macromolecular crystallography, SSNMR does not need a crystal. It greatly expands the systems that SSNMR can be applied to and reduces the amount of work to prepare samples, since good crystals are essential to obtain high quality diffraction patterns for solving crystal structures, which is a formidable task for crystallographers. In most cases, protein modifications such as mutagenesis or truncation are needed in crystallography studies. In contrast, SSNMR can study the protein in the intact form. Due to the low requirements for sample preparation, the protein can be studied in native environments, such as lipid bilayers for membrane proteins. This is important for reducing artifacts like crystal stacking. Also, SSNMR, allows the study of protein response to various external perturbations such as pH change or ligand binding more directly. These advantages are also applied to materials

studies. For example, in many cases, it is necessary or beneficial to study the materials in a complicated environment, which are hard to study by X-ray diffraction.

Moreover, for dynamics, NMR provides many advantages over X-ray crystallography and Cryo-EM, which are generally limited to extrapolating from static snapshots of a protein's conformations. The dynamics information in atomic resolution provided by NMR is critical for studying mechanisms of function in large systems. Many theoretical works, such as Redfield theory, and experimental methods, such as T1ρ relaxation dispersion, have been developed and are still undergoing development to expand the ability of NMR to study more systems. The ease of applying a wide range of temperatures in NMR gives it the ability to study both kinetics and thermodynamics of the systems.

While SSNMR is a unique tool that has many advantages, it has its drawbacks as well. For example, NMR is generally an insensitive method, and lengthy signal averaging is often required. The interpretation of a multidimensional NMR spectrum is not a trivial task, even for an NMR expert. As the number of observable signals scales with the size of the system, it cannot compete efficiently with Cryo-EM or X-ray crystallography for solving the structures of very large systems. However, it is highly complimentary to these methods; for example, accurate distance constraints acquired in NMR can be combined in Cryo-EM or X-ray structure calculation to improve resolution.

Importantly, solid state NMR is still developing technically. Hardware developments, including probes capable of spinning at faster rates, as well as dynamic nuclear polarization (DNP) are being developed to cope with issues of insensitivity.[8] Strategic isotope-labeling schemes can be used to reduce the spectra congestion.[49] Computational methods are developed to assist spectra assignment and theoretical calculations are used to interpret the origin of chemical shifts.[50] With the field continually evolving, I believe NMR, especially SSNMR, will become an even more powerful tool.

1.3 NMR Hamiltonian

Since almost all the information extracted from NMR is associated with certain types of Hamiltonians of nuclear spin interaction, here we give a brief introduction to the general Hamiltonian in NMR research and associated molecular information.

The NMR Hamiltonian can be written in the following equations in general:

$$\hat{H} = \hat{H}_0 + \hat{H}_{RF} + \hat{H}_{inter} \quad (1.1)$$

where $\hat{H}_0$ represents the dominant Zeeman interaction, which is the interaction between the spin and the external magnetic field, $\hat{H}_{RF}$ represents the interaction between the spins and the radio frequency (RF) pulse, and $\hat{H}_{inter}$ represents the overall internal spin interactions, including chemical shift, dipolar interaction, J-coupling, and quadrupolar coupling interaction.[42]

The isotropic part of the Zeeman interaction H_0 can be written as:

$$\hat{H}_0 = -\gamma B_0 \hat{I}_Z, \quad (1.2)$$

where γ is gyromagnetic ratio, B_0 is the external magnetic field, and $\hat{I}_Z$ is the spin Hamiltonian operator. Because of the dominant effect of the Zeeman interaction, its eigenstates are normally used as the basis set for NMR calculations.

A general form of $\hat{H}_{RF}$ term can be written into:

$$\hat{H}_{RF} = \omega_1(\cos\phi \hat{I}_X + \sin\phi \hat{I}_y) + \omega_{off} \hat{I}_Z. \quad (1.3)$$

where ω_1 is the applied RF pulse field strength, ϕ is the phase of the applied pulse, and ω_{off} is the offset between the carrier frequency and the frequency of the observed nuclear spin. All these parameters can be purposely set in the spectrometer.

The internal Humiliation $\hat{H}_{inter}$ contains atomic-specific information including local electronic environment, through-bond and through space interactions with other nuclei, and it is the major goal of modern NMR to elucidate the $\hat{H}_{inter}$. Here we provide a brief introduction to the major components of $\hat{H}_{inter}$.

1.3.1 Chemical Shift

The chemical shift originates from the shielding effect of nearby electrons on a nucleus. The motions of the electrons in the shell induce a magnetic field in addition to the external magnetic field based on Lenz's law, changing the overall magnetic field and thus affecting the NMR frequency of the nuclei. The detailed quantum mechanical explanation of it can be seen in the Ramsey formula[49] for the chemical shift caused by an electron:

This is a first order approximation of the induced chemical shift along the z-axis by the magnetic field. It contains a diamagnetic term and a time-independent paramagnetic term. The diamagnetic part accounts

$$\sigma_{zz} = \frac{\mu_0 e^2}{2m}\langle\psi_0\left|\frac{x^2+y^2}{r^3}\right|\psi_0\rangle - \frac{\mu_0 e\hbar}{2m}\sum_n\left(\frac{\langle\psi_0|l_z|\psi_n\rangle\langle\psi_n|2l_z/r^3|\psi_0\rangle}{E_n-E_0} + \frac{\langle\psi_0|2l_z/r^3|\psi_n\rangle\langle\psi_n|l_z|\psi_0\rangle}{E_n-E_0}\right) \quad (1.4)$$

for shielding of electrons in the ground state and the paramagnetic parts accounts for shielding of electrons in the excited orbitals.[49,50]

Due to the angular features of the electronic wave functions and chemical bonding, the chemical shift interaction is angular and anisotropic. This means that the induced magnetic field and according NMR frequency shifts are orientation-dependent. An example is shown below for a carbonyl group. (Fig. 1.1)

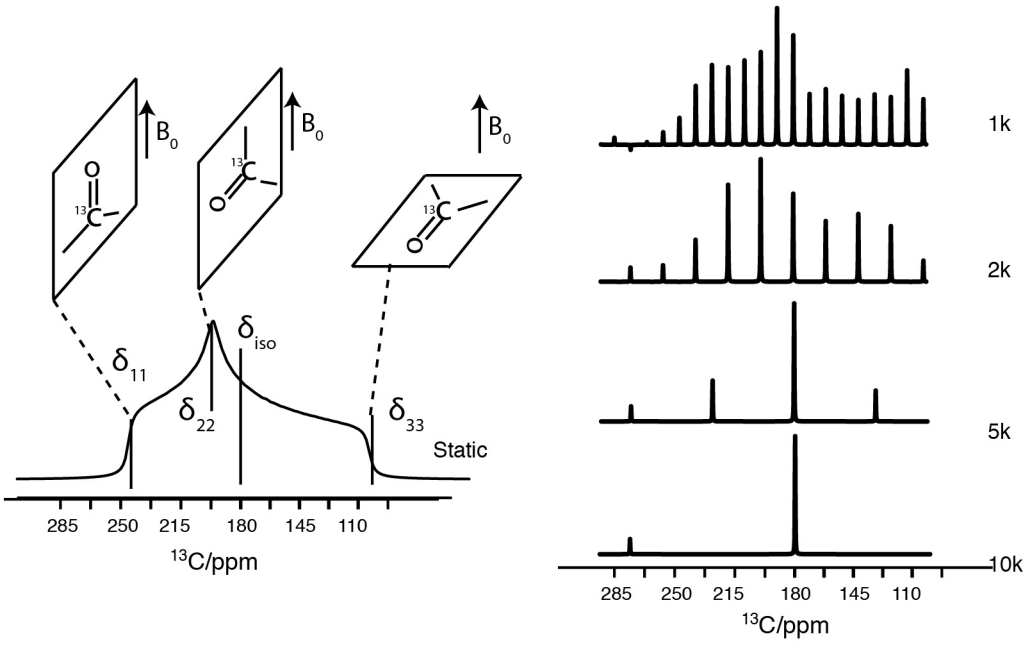

Figure 1.1. Simulated orientation dependent chemical shifts of a carbonyl group. On the left, a static ^{13}C spectrum of a carbonyl group is simulated with the software SIMPSON.[51] The orientations at which the chemical shifts equals the principle values are indicated. In the right panel, magic angle spinning (MAS) spectra with various spinning speeds are simulated. The position of isotropic chemical shift does not change in various MAS spectra, which is identical to the isotropic chemical shift in the static spectrum; the sidebands are separated by the spinning frequency. With increasing spinning speed, the intensities of the sidebands get weaker, indicating the anisotropy of the chemical shift tensor is significantly averaged by MAS spinning. The simulation file can be found in the appendix 1.

The chemical shift tensor can be written as a second order tensor:

$$\delta_{CS} = \begin{pmatrix} \delta_{xx} & \delta_{yx} & \delta_{zx} \\ \delta_{xy} & \delta_{yy} & \delta_{zy} \\ \delta_{xz} & \delta_{yz} & \delta_{zz} \end{pmatrix} = \delta_{iso} + \delta_{sym} + \delta_{antisym} \tag{1.5}$$

in which the three terms $\delta_{iso}, \delta_{sym}, \delta_{antisym}$ can be written as:

$$\sigma_{iso} = 1/3\left(\delta_{xx} + \delta_{yy} + \delta_{zz}\right) \tag{1.6}$$

$$\delta_{sym} = \begin{pmatrix} \delta_{xx} - \frac{\delta_{iso}}{3} & \frac{\delta_{yx}+\delta_{xy}}{2} & \frac{\delta_{zx}+\delta_{xz}}{2} \\ \frac{\delta_{yx}+\delta_{xy}}{2} & \delta_{yy} - \frac{\delta_{iso}}{3} & \frac{\delta_{zy}+\delta_{yz}}{2} \\ \frac{\delta_{zx}+\delta_{xz}}{2} & \frac{\delta_{zy}+\delta_{yz}}{2} & \delta_{zz} - \frac{\delta_{iso}}{3} \end{pmatrix} \tag{1.7}$$

$$\delta_{antisym} = \begin{pmatrix} 0 & \frac{\delta_{yx}-\delta_{xy}}{2} & \frac{\delta_{zx}-\delta_{xz}}{2} \\ \frac{-\delta_{yx}+\delta_{xy}}{2} & 0 & \frac{\delta_{zy}-\delta_{yz}}{2} \\ \frac{-\delta_{zx}+\delta_{xz}}{2} & \frac{-\delta_{zy}+\delta_{yz}}{2}\sigma_{yz} & 0 \end{pmatrix} \tag{1.8}$$

As shown above, the tensor can be decomposed into an isotropic part, a zero-trace symmetric tensor, and an antisymmetric tensor. The former two parts will manifest as the chemical shifts in the spectra; the antisymmetric part does not cause chemical shift change, but affects nuclear relaxation behaviors.[40] The first two parts can be diagonalized in the principle molecular frame through certain Euler angle rotation. The $\delta_{XX}\ \delta_{YY}\ \delta_{ZZ}$ parameters in this frame are used to define the magnitude of the anisotropy δ and the asymmetric parameter η in Haeberlen Convention[52]:

$$\delta = \delta_{ZZ} - \delta_{iso} \tag{1.9}$$

$$\eta = (\delta_{YY} - \delta_{XX})/\delta \tag{1.10}$$

where δxx δyy δzz are defined as : $|\delta zz - \delta iso| \geq |\delta xx - \delta iso| \geq |\delta yy - \delta iso|$.

The isotropic chemical shift is a powerful reporter of chemical environment that forms the basis of modern high-resolution NMR. In protein NMR, the isotropic chemical shift is a powerful reporter of secondary structural elements.[53–55] The isotropic chemical shift values of Cα, CO, and Cβ sites show

significant differences between atoms in an α-helix, β-sheet, or random coil. In general, isotropic chemical shifts in α-helices tend to be downfield relative to β-sheets for Cα and CO by an average of 4-5 ppm, while the opposite trend is observed for Cβ, with random coil shifts manifesting as an average of the two other secondary structural elements. The isotropic chemical shift is therefore a very sensitive reporter for protein conformational changes, and has also been used as a reporter for ligand binding and protein interaction.[14,56,57]

The chemical shift anisotropy (CSA) is mostly averaged out by magic angle spinning (a SSNMR technique; discuss more in the following) in SSNMR to improve spectral resolution, generating a single narrow peak at the isotropic chemical shift with sidebands mapping out the full CSA powder pattern. However, the CSA can be strategically recoupled and thus provided another source of information on chemical bonding and molecular conformation. For example, the CSA is a good reporter for protonation state as well as hydrogen bonding. Gu et al found the δ_{11} value of a carboxyl group is closely related to its protonation state and the δ_{22} value is dependent on the strength of CO…HN hydrogen bonding.[58] By taking advantage of these phenomena, Bhate et al determined the protonation state of a key residue E71 in ion channel protein KcsA.[59] Systematic measurements of carbon and nitrogen CSA tensors of GB1 by Wylie et al and incorporation of them as constraints in structural calculation greatly improve backbone rmsd to 0.16 Å. [60,61]

As a side note, the CSA is also used in transverse relaxation-optimized spectroscopy (TROSY) experiments in solution NMR to improve spectra resolution by making use of mutual cancellation of HN dipole-dipole coupling and CSA to attenuate T2 relaxation.[62] This technique has greatly increased the protein size that can be studied by solution NMR to an order of 100kDa.[62,63]

1.3.2 Dipolar Interaction

The dipolar interaction is the through-space interaction between two nuclear spins. An analogy of the interaction is two small magnets interacting with each other (Fig. 1.2). The full expression of the dipolar interaction Hamiltonian between two nuclear spin j and k is[66]:

$$\hat{H}_{jk}^{dd} = d_{jk}\cdot(3(\hat{I}_j \cdot e_{jk})(\hat{I}_k \cdot e_{jk}) - \hat{I}_j \cdot \hat{I}_k\ ), \tag{1.11}$$

$$d_{jk} = -\frac{\mu_0}{4\pi r^3}\hbar^2\gamma_j\gamma_k \tag{1.12}$$

The magnitude of this interaction is characterized by the dipolar coupling constant d_{jk}, given in Hz. It depends on the inverse cube of the distance between the interacting nuclei. Under the secular approximation,[43] which simplifies the Hamiltonian by only retaining components commuting with the dominant Zeeman terms, the simplified Hamiltonian for the homonuclear dipolar coupling is

$$\hat{H}_{homo}^{0} = -\frac{\mu_0}{4\pi r^3}\hbar^2\gamma_j\gamma_k\frac{1}{2}(3\hat{I}_{jz}\hat{I}_{kz} - \hat{I}_j\cdot\hat{I}_k)(3cos^2\theta - 1) \tag{1.13}$$

The Hamiltonian for the heteronuclear dipolar coupling is

$$\hat{H}_{homo}^{0} = -\frac{\mu_0}{4\pi r^3}\hbar^2\gamma_j\gamma_k 2\hat{I}_{jz}\hat{I}_{kz}(3cos^2\theta - 1) \tag{1.14}$$

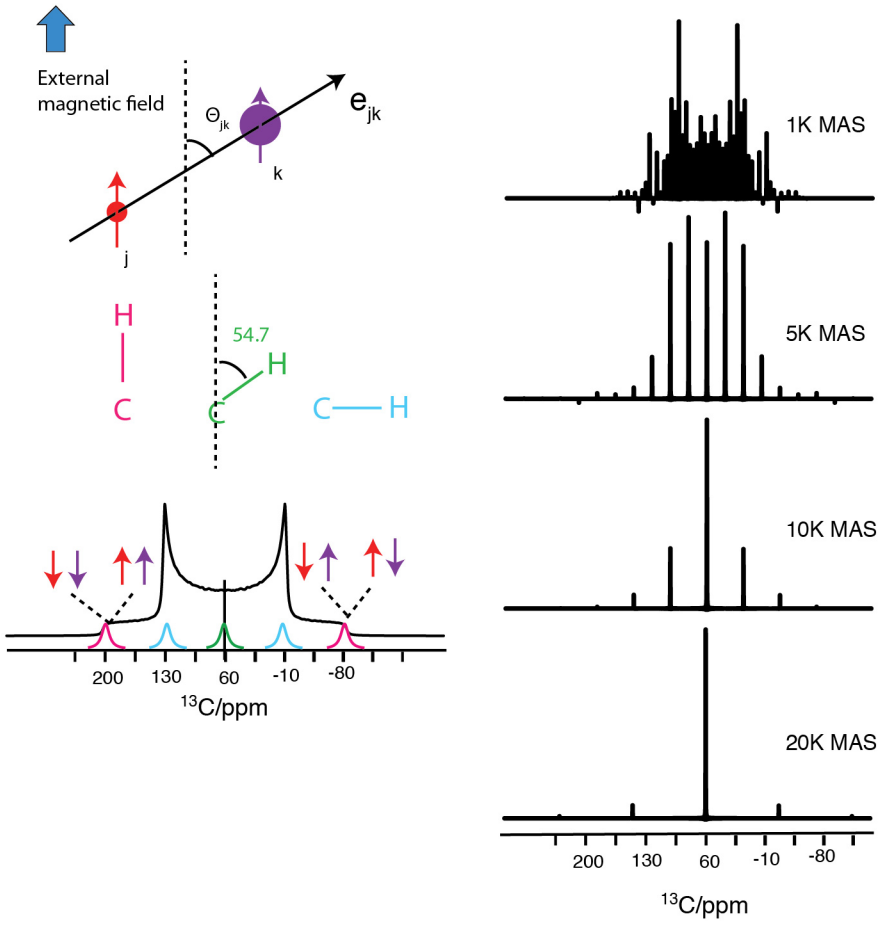

Figure 1.2. Orientation dependent dipolar interaction between ^{1}H and ^{13}C in a C-H bond is simulated. In the left panel, a scheme of dipolar interaction of two spins (red and purple) is shown. The static dipolar interaction Pake pattern of a ^{13}C spin coupled with ^{1}H in a C-H bond is simulated with SIMPSON and three angels (i.e. 0°, 54.7°, 90°) are colored and their according chemical shifts were labeled in the static spectrum. The directions of the spins (i.e. up and down) are indicated by the pointers. In the angle 54.7°, the dipolar interaction equals zero, therefore only isotropic chemical shift is displayed (the green peak). In the right panel, magic angle spinning (MAS) spectra with various spinning speeds are simulated for the same system. With the increasing spinning speed, the sideband peaks get weaker, indicating that the dipolar interaction is significantly averaged. The simulation file can be found in the appendix 1.

The dipolar interaction is averaged out in the normal solution NMR due to the fast tumbling of molecules. In SSNMR, it is also averaged by magic angle spinning (MAS, details are discussed later), which improves spectra resolution. However, the dipolar interaction contains rich useful information such as distance constraints, which are important to study ligand docking, structure calculation, etc. Therefore, specific techniques are developed to reintroduce this interaction. In solution NMR, special solvents are used to partially align the samples so that the dipolar interaction is not completely averaged out. The residual dipolar coupling then are measured to provide distance constraints.[67] In SSNMR, specific pulse sequences, such as REDOR, can be applied to recouple this interaction for measuring the coupling constant.[68] For example, Fanghao et al measured the Cα-Nδ1 distance in an imidazole ring by measuring dipolar interaction using REDOR, which was further used to determine the Cα-Cb-Cg-Nδ1 torsion angle.[69] Thus, the packing pattern of a key residue H37 in the M2 influenza channel was determined. (Figure 1.3) Many homonuclear recoupling pulse sequences such as DRAW, SPC5, POST-C7 and PAR were developed to recouple the dipolar interactions for polarization transfer or multi-quantum coherence experiments.[70–75]

The dipolar interaction can also be widely applied to investigate protein dynamics. The dipolar interaction can be partially averaged out by local motions, rendering a scaled coupling strength. In the above example, Fanghao et al measured the dipolar interaction information at both low and physiological temperature for samples at neutral and low pH.[69] They observed the dipolar interaction strength is scaled at the physiological temperature and low pH, indicating a ring flipping motion. Through the scaling factor,

they were able to measure an approximately 45 degree change of the χ2 angle during the flipping, which helped them illustrate the proton conducting mechanism in M2 at low pH. (Figure 1.4)

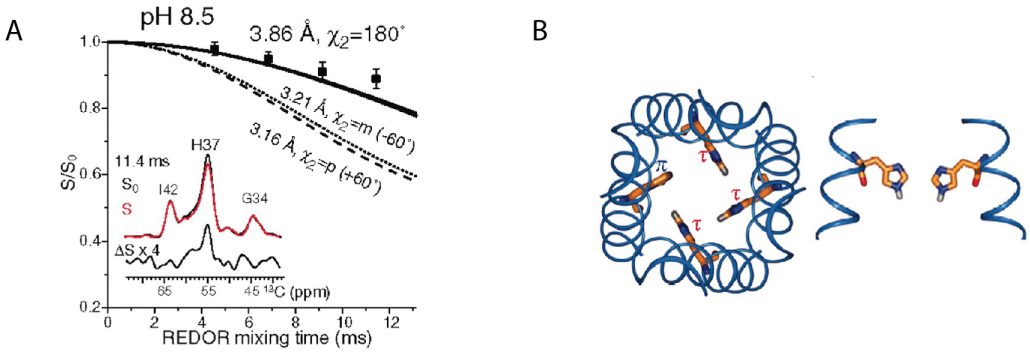

Figure 1.3 An example of using dipolar interaction to determine the distance and torsion angle in M2 channel. In panel A, a REDOR diphase experiments data were fitted to acquire the distance between Cα and Nδ1 distance in the H37 residue in M2 proton channel. In panel B, with the distance information, the conformation arrangement of the H37 is determined. Figures are taken from the reference 67.[69]

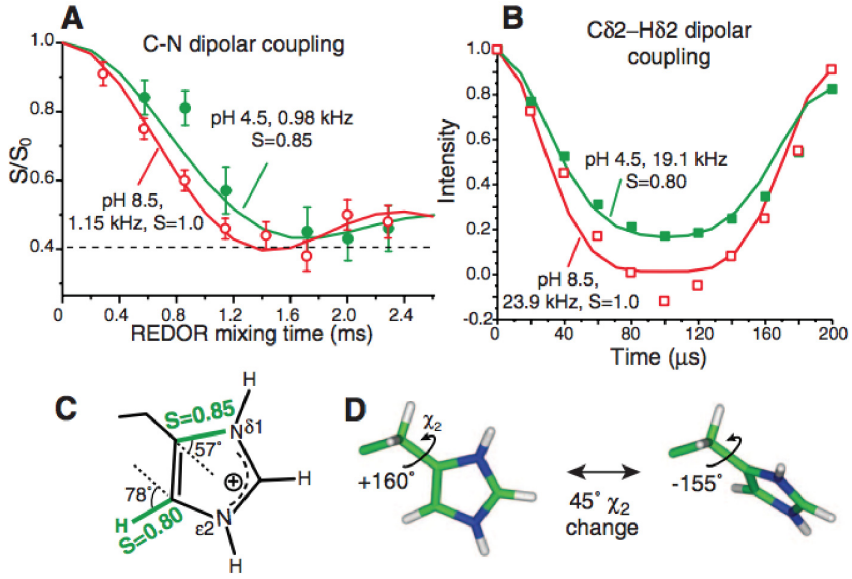

Figure 1.4 An example of applying dipolar interaction to study the molecular motion in M2 channel. (A, B) Order parameters of C-N and N-H bonds are calculated in the REDOR and DIPSHIFT experiments at pH 4.5 and pH 8.5. It shows that at pH 4.5, the order parameter is around 0.85 for C-N and 0.8 for N-H, in contrast to S=1 at pH 8.5, indicating that the imidazole ring is flipping at pH 4.5. (C,D) Figures are taken from the reference 67.

1.3.3 J- Coupling

The J coupling (also called *indirect dipole–dipole coupling)* is the through-bond interaction between two nuclear spins. The full form of the *J*-coupling interaction between spins I_j and I_k is[42]:

$$\hat{H}_{j\text{-}coupling} = 2\pi\, \hat{I}_j \cdot J_{jk} \cdot \hat{I}_k \qquad (1.15)$$

where J_{jk} is the *J*-coupling tensor, a real 3 × 3 matrix. It depends on molecular orientation, but in an isotropic liquid it reduces to a number, the so-called scalar coupling, which is retained despite isotropic tumbling.

In solution NMR, since molecular tumbling averages out many Hamiltonians, such as the dipolar interaction and the CSA, the J-coupling is used to mediate polarization transfer between nuclei, as seen in the many INEPT building blocks in solution pulse sequence. Their values have been found to be conformation dependent and can be applied for structural calculation.[76]

In solid state NMR, since its strength (ex J_{CH} ~140 Hz) is much weaker than other components of the Hamiltonian, such as dipolar interaction (ex C-H dipolar interaction at 1 Å is about 30kHz), the effect of J-coupling is normally not visible in biological solid state NMR studies without special decoupling techniques. However, with the development of fast magic angle spinning techniques (i.e. MAS rate >100kHz), the dominant proton-proton dipolar interaction can be significantly averaged out by spinning and partial deuteration, thus J-coupling becomes substantial. In this scenario, many J-coupling based pulse program are adapted from solution NMR for SSNMR studies.[45,77]

1.3.4 Quadrupolar Interaction

A quadrupole arises from an uneven distribution of charge inside a nucleus. The nuclear electric quadrupole moment is a parameter to describe the effective shape of the ellipsoid of nuclear charge distribution. The quadrupolar interaction is an interaction between a nuclear spin (I>1/2) and its surrounding electronic field gradient. The general interaction between electron and nucleus can be written as[50]:

$$E=\int \rho(\vec{r})V(\vec{r})d\tau \qquad (1.16)$$

in which $V(\vec{r})$ can be expanded into a Taylor series:

$$V(\vec{r}) = V(\vec{0}) + \sum_{\alpha} x_{\alpha}(\frac{\partial V}{\partial x_{\alpha}})_{r=0} + \frac{1}{2!}\sum_{\alpha,\beta} x_{\alpha}x_{\beta}(\frac{\partial^2 V}{\partial x_{\alpha}\partial x_{\beta}})_{r=0} \quad (1.17)$$

Then

$$\text{E= } V(\vec{0}) \int \rho(\vec{r})d\tau + \sum_{\alpha} V_{\alpha} \int x_{\alpha}\rho(\vec{r})d\tau + \frac{1}{2!}\sum_{\alpha,\beta} V_{\alpha,\beta} \int x_{\alpha}x_{\beta}\rho(\vec{r})d\tau \quad (1.18)$$

The first and second terms are corresponding to the coulomb and the dipole interaction. The third term is the quadrupole term, which can be rewritten into

$$E_Q = \frac{1}{6}\sum_{\alpha,\beta} V_{\alpha,\beta}Q_{\alpha,\beta} \quad (1.19)$$

where

$$Q_{\alpha,\beta} = \int (3x_{\alpha}x_{\beta} - \delta_{\alpha\beta}r^2)\rho(\vec{r})d\tau \quad (1.20)$$

The Hamiltonian then can be written into:

$$\widehat{H}_q = \frac{1}{6}\sum_{\alpha,\beta} V_{\alpha,\beta}\hat{Q}_{\alpha,\beta} = \frac{1}{6}\hat{Q}\otimes V \quad (1.21)$$

$$\hat{Q}_{\alpha\beta} = \left[\frac{3(\hat{I}_{\alpha}\hat{I}_{\beta} + \hat{I}_{\beta}\hat{I}_{\alpha})}{2} - \delta_{\alpha\beta}\hat{I}^2\right].\frac{eQ}{I(2I-1)} \quad (1.22)$$

where eQ is the nuclear electric quadrupole moment, *I* is the nuclear spin quantum number, and V is the electronic field gradient (EFG) tensor, which can be written as:

$$\text{V=}\begin{pmatrix} V_{xx} & V_{yx} & V_{zx} \\ V_{xy} & V_{yy} & V_{zy} \\ V_{xz} & V_{yz} & V_{zz} \end{pmatrix}, V_{\alpha\beta} = \frac{\partial^2 V}{x_{\alpha}x_{\beta}} \quad (1.23)$$

This matrix, as with the CSA matrix, can be diagonalized in the principle axis frame with V_{XX}, V_{YY}, V_{ZZ}, where $|V_{ZZ}| \geq |V_{XX}| \geq |V_{YY}|$, and $V_{ZZ} + V_{XX} + V_{YY} = 0$. The asymmetry parameter is defined as $\eta_Q =$

$\frac{V_{XX}-V_{YY}}{V_{ZZ}}$. The value V_{ZZ} is defined as the principle component of the EFG tensor and is usually denoted as *eq*, where e is the electron charge. In the principle axis frame, the Hamiltonian can be written as:

$$\widehat{H}_q = \frac{eQ.eq}{4I(2I-1)}[3\hat{I}_z^2 - \hat{I}(\hat{I}+1) + \eta(\hat{I}_x^2 - \hat{I}_y^2)] \quad (1.24)$$

Under the secular approximation, in the laboratory reframe, only the terms with Hamiltonian commuting with the Zeeman interaction along the Z-axis are preserved. By transferring from the principle axis frame to lab frame, we have the

$$V_{zz}^{lab} = \sqrt{\frac{2}{3}} V_{ZZ}\left(\frac{3cos^2\beta - 1}{2} + \frac{\eta}{2} sin^2\beta cos2\alpha\right) \quad (1.25)$$

Then the zero order approximation of the Hamiltonian is

$$\widehat{H}_q^0 = \sqrt{\frac{2}{3}} \frac{eQ.eq}{4I(2I-1)}[3\hat{I}_z^2 - \hat{I}(\hat{I}+1)]\left(\frac{3cos^2\beta-1}{2} + \frac{\eta}{2} sin^2\beta cos2\alpha\right) \quad (1.26)$$

As we can see, the quadrupole transition is also orientation dependent. By fitting the spectra, parameters such as quadrupole coupling constant (QCC) C_q (defined as $\frac{eQ.eq}{\hbar}$) and the asymmetry parameter η_Q can be acquired, which contains rich information on the electronic configuration.

Due to the large strength of the quadrupolar interaction, even the second order term of the Hamiltonian is large enough that it must be considered.[42] As the interaction could couple with other Hamiltonians like dipolar interaction or CSA, the spectra become difficult to interpret directly.[32] The development of various software, such as SIMPSON, Spinevolution, and Wsolids, provide great help on simulating the spectra and extracting important parameters.[51,76]

1.4 Theoretical Tools for Understanding NMR

Theoretical frames of NMR are well developed, and they are important to understand the results of modern NMR experiments as well as develop new NMR methodologies. In the section, we will introduce the basic quantum mechanical theory for NMR and some useful tools for NMR Hamiltonian calculation.

There are many different frameworks to describe NMR theory, such as the Block equations, spin operators, and the density matrix.[43] Here, we first introduce the NMR frame using the density matrix.

1.4.1 Equation of Motion in Density Operators

A density operator can be used to represent a spin system,

$$\hat{\rho}(t) = |\psi(t)\rangle\langle\psi(t)| = \sum_{i,j}^{n} C_i C_j^* |\psi i\rangle\langle\psi j| \tag{1.27}$$

where $|\psi(t)\rangle$ is the wave function of the system and $|\psi i\rangle$, $|\psi j\rangle$ are the basis set.[42] As a great advantage of using density matrix in calculation, the expectation value for any operator $\hat{A}$ (for example, $\hat{I}^+$ in NMR) can be calculated as,

$$\langle \hat{A} \rangle = Tr\left[\hat{\rho}(t) \cdot \hat{A}\right] \tag{1.28}$$

where Tr is the trace operator.

The time-dependent Schrödinger equation for a spin systems can be represented by the Liouvilee-Von Neumann equation in the density matrix representation[41]:

$$\frac{d\hat{\rho}(t)}{dt} = -\frac{i}{\hbar}\left[\hat{H}, \hat{\rho}\right] \tag{1.29}$$

where $\hat{H}$ is the total Hamiltonian operator and $\left[\hat{H}, \hat{\rho}\right] = \hat{H} \cdot \hat{\rho} - \hat{\rho} \cdot \hat{H}$, when the relaxation effects are neglected.

When the $\hat{H}$ is time independent, a solution can easily achieved:

$$\hat{\rho}(t) = \hat{U}(t, t_0)\hat{\rho}(t_0)\hat{U}(t, t_0)^{-1},\ \hat{U}(t, t_0) = \exp\left(-i\hat{H}(t - t_0)\right) \tag{1.30}$$

In a more general solution, the propagator $\hat{U}(t, t_0)$ becomes $\mathcal{T}\exp\left\{-i\int_{t_0}^{T} \hat{H}\, dt\right\}$, where $\mathcal{T}$ is the Dyson time-ordering operator, indicating that the infinitesimal propagators $\hat{U}(t' + dt, t') = \exp\left\{-i\int_{t'}^{t'+dt} \hat{H}\, dt\right\}$ need be multiplied in order from right to left with t' increasing.[79] This is generally difficult to achieve an analytical solution unless special properties of the Hamiltonian are met. However, with the improvement in the computation ability, the solution can be calculated in numerical fashion, which is the basis for much NMR simulation software, such as SIMPSON, Spin Evolution, Spinach.

1.4.2 Rotating Frame

In the many case, an analytical solution is needed for the Liouvilee-Von Neumann equation for analyzing or developing a NMR pulse program. Transferring from the laboratory frame to the rotating frame as reference, in such cases, provides great mathematic convenience to analyze the solution.

In the laboratory frame, due to the spinning of nuclear spins under the dominant Zeeman effect and oscillating feature of RF pulse, the whole system is rotating. By transferring to a rotating frame, some dominant Hamiltonian can be separated from the rest, allowing certain approximation, such as using Average Hamiltonian Theory (AHT), to be converged when the rest Hamiltonians are analyzed.[79]

Mathematically, transferring to a rotating frame equals to transferring to a new representation by an arbitrary unitary operator $\hat{R}$ for the wave functions and operators:

$$\widetilde{|\psi(t)\rangle} = \hat{R}|\psi(t)\rangle,\ \tilde{\hat{Q}} = \hat{R}\hat{Q}\hat{R}^{-1} \tag{1.31}$$

where $\hat{Q}, |\psi(t)\rangle$ are the operator and wave function for the laboratory frame; $\tilde{\hat{Q}}, \widetilde{|\psi(t)\rangle}$ are the operator and wave function for the new frame.

The effective Hamiltonian in the rotating frame can be transformed by following operator[43]:

$$\hat{H}_{eff} = \hat{R}\hat{H}\hat{R}^{-1} - i\hat{R}\frac{d\hat{R}^{-1}}{dt}, \tag{1.32}$$

For example, in a typical Hamiltonian in NMR experiment,[79]

$$\hat{H} = 2\omega_1 \cos\omega t\ \hat{I}_X + \omega_0\,\hat{I}_Z + \hat{H}_{\text{inter}}. \tag{1.33}$$

To separate the dominate Zeeman effect, $\hat{R} = \exp(i\omega\hat{I}_z t)$ is applied so that $\hat{H}_{eff}$ in the rotating frame is:

$$\hat{H}_{eff} = (\omega_0 - \omega)\hat{I}_z + \omega_1\{(1+\cos 2\omega t)\hat{I}_x - \sin 2\omega t\ \hat{I}_y\} + \hat{R}\hat{H}_{inter}\hat{R}^{-1}. \tag{1.34}$$

The lowest order approximation is:

$$H^0_{eff} = (\omega_0 - \omega)\hat{I}_z + \omega_1\hat{I}_x + \widetilde{\hat{H}^0_{eff}} \tag{1.35}$$

where $\widetilde{\hat{H}^0_{eff}}$ is the average Hamiltonian of $\hat{R}\hat{H}_{inter}\hat{R}^{-1}$.

In some cases, a second transfer is needed and the new reframe is called double rotating frame. In the above case, $\hat{R} = \exp\left(i\left((\omega_0 - \omega)\hat{I}_z + \omega_1\hat{I}_x\right)t\right)$ can be applied for further simplifying the $\widetilde{\hat{H}^0_{eff}}$ term.

1.4.3 Average Hamiltonian Theory

As we have seen in the above section that after the system is transferred to a suitable rotating frame, certain approximation can be made to simplify the Hamiltonian. The theoretical basis for such a simplification is the average Hamiltonian theory.[79]

In the average Hamiltonian theory, when the perturbation is the periodic, the time-dependent Hamiltonian over periods can be approximated by a series of time-independent Hamiltonian:

$$H(\tau_p) = \bar{H}^0 + \bar{H}^1 + \bar{H}^2 + \cdots \quad (1.36)$$

Where

$$\bar{H}^0 = \frac{1}{\tau_p}\int_0^{\tau_p} \hat{H}\,(t)dt \quad (1.37)$$

$$\bar{H}^1 = \frac{-i}{2\tau_p}\int_0^{\tau_p} dt_1 \int_0^{t_1} [H(t_1), H(t_2)]\, dt_2 \quad (1.38)$$

$$\bar{H}^2 = \frac{1}{6\tau_p}\int_0^{\tau_p} dt_1 \int_0^{t_1} dt_2 \int_0^{t_2} [[H(t_1), H(t_2)], H(t_3)] + [H(t_3), [H(t_1), H(t_2)]]\, dt_3 \quad (1.39)$$

In most case in NMR study, the first and second terms are sufficient and higher orders are not necessary. However, caution need be taken to make sure that the approximation is converged.

1.5 Techniques to Improve Resolutions in SSNMR

1.5.1 Magic Angle Spinning

In SSNMR, due to the anisotropy feature of many interactions, which cannot be averaged out like in solution NMR, the resolution of the spectra is poor, making it impossible to assign spectra in a complicated macromolecule like protein. In 1958, Andew and coworkers introduced a solution to this problem by mechanically spinning the sample around an axis inclined at the magic angle (54.7) with respect to the external magnetic field (Figure 1.5).[80] Importantly, in this angle, $3cos^2\theta - 1 = 0$.

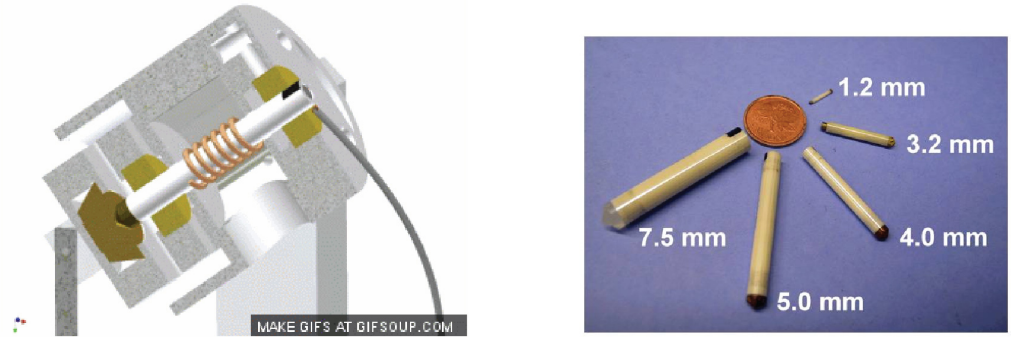

Figure 1.5 The scheme picture of the magic angle spinning module is shown. The right panel shows the Varian rotors with various diameters. The figures are taken from https://www.youtube.com/watch?v=13NLti-1ErA.

As shown in above, in the lowest order approximation of many terms, such as dipolar interaction, chemical shift anisotropy, quadrupole interaction, are modulated by an angular term ($3cos^2\theta - 1$). At the

magic angle, the dipolar term and chemical shift anisotropy etc can be effectively averaged. (Figs.1.1 and 1.2) However, a complete averaging of dipolar interaction and CSA demands that the spinning speed (in Hz) is stronger than the strength of dipolar interaction and CSA. Because the proton has a large gyromagnetic ratio, dipolar coupling to protons, both heteronuclear and homonuclear are generally difficult to average out; therefore, other techniques such as decoupling are introduced to improve spectra resolution.

The hardware development for fast magic angle spinning, at speeds above ca 40kHz has achieved great success in recent years. MAS spinning rate at 110kHz has been developed.[81] It can successfully decrease the effect of ^{1}H-^{1}H homonuclear coupling in fully protonated sample, which enables proton detection methods for SSNMR.

However, both CSA and dipolar interaction contains rich structural and dynamical information. These interactions can be recoupled through special designs of pulse sequence.[6] In some experiments, the isotropic information and anisotropy information are correlated: the isotropic information provides assignments to the atoms and anisotropy information provides the atoms' angular or distance information.[63] We will introduce some of these recoupling pulse programs in the later sections.

1.5.2 Homonuclear and Heteronuclear Decoupling

Decoupling techniques are another invention to improve spectra resolution. It is applied to remove effects of certain Hamiltonians. In solution NMR, decoupling is used to decouple the scalar J-Coupling. In SSNMR, decoupling is used to remove the effect of dipolar interaction. Decoupling is accomplished by irradiating at the frequency of the decoupled nucleus. The principle of decoupling could be simply understood as fast flipping between $|\alpha\rangle$(i.e. spin down) and $|\beta\rangle$ (i.e. spin up) state of the decoupled nucleus. When the flipping rate is fast enough, the two split peaks by dipolar or J-coupling are emerged into one peak. An analogy to this is that fast exchange in chemical exchange: when the chemical exchange rate is significantly large than the chemical shift different, only an averaged peak appears in the spectra.[82] In order to fully decouple, the decoupling strength needs be larger than the strength of decoupled Hamiltonian.

There are various decoupling schemes. The simplest scheme is continue-wave (CW) decoupling.[83] In SSNMR, the most commonly used decoupling schemes are Two-Pulse Phase-Modulated

(TPPM),[84] X-inverse-X decoupling scheme (XiX),[85] SPINAL[86] for heteronuclear coupling. They are discovered to be favorable at certain MAS spinning rates.[87] For homonuclear decoupling, the Phase Modulated Lee Goldburg (PMLG) experiment,[88] Frequency Switched Lee Goldburg (FSLG)[89] and Decoupling Using Mind Boggling Optimization (DUMBO)[90] have good performance and are wildly applied for 2D HX heteronuclear experiment at 10-25 kHz MAS spinning.

1.5.3 Cross Polarization

Cross polarization is an important technique used in almost every SSNMR pulse sequence to improve the experimental sensitivity.[91] The major principle of cross polarization is to transfer polarization from nucleus with high gyromagnetic ratio to nucleus with low gyromagnetic ratio. In SSNMR, ^{13}C and ^{15}N or other nuclei like ^{31}P are detected instead of ^{1}H due to the low resolution of proton spectra caused by strong ^{1}H-^{1}H homonuclear coupling. The use of these low-gyromagnetic ratio nuclei (γ_H is about 10 times larger than γ_N, and 4 times larger than γ_C) makes NMR less sensitive. Detection on the low-gyromagnetic ratio nuclei also causes a longer T_1 relaxation time, which is essentially the time needed for the spin to equilibrium before next acquisition. Therefore a long pulse delay between each scan during signal averaging is needed, which significantly increases the experimental times for the same signal-to-noise ratio in spectra.

The basic pulse sequence scheme can be see figure 1.6. Firstly invented by Hartmann and Hahn in 1962 in static NMR,[92] cross polarization between two nuclei (I and S) involve continuous irradiating RF on the resonance frequencies of both the I and S spins, such that the nutation frequencies ω_{1I}, ω_{1S} are equal, noted as Hartmann-Hahn condition. After MAS technique was invented, the cross polarization mechanism is found still efficient for transferring polarization at moderate-to-high spinning rates; similar matching conditions are modified to be:

$$|\omega_{1I} - \omega_{1S}| = n\omega_r \qquad (1.40)$$

where n is a integer number and ω_r is the MAS rate.[93]

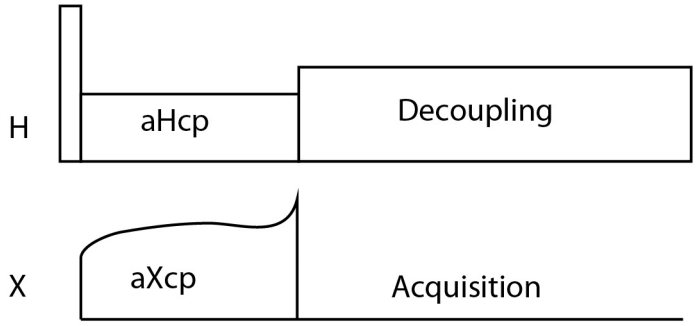

Figure 1.6. A general scheme of ^{1}H-X(X is the detection nucleus) cross polarization pulse sequence is shown. aHcp and aXcp is the spinning lock power during the cross polarization process. The power of aXcp is modulated by certain functions to improve the polarization transfer performance, as indicated by the shaped curve.

Here we provide a brief validation for the conditions using the theoretical tool we have introduced. For the internal Hamiltonian, only the dipolar interaction is considered as it is driving force for the polarization transfer. The Hamiltonian for the system can be written into:

$$H = 2\omega_{1I}\hat{\mathrm{I}}_y \cos\omega_I t + 2\omega_{1S}\hat{S}_y \cos\omega_S t + \beta_{IS}\hat{\mathrm{I}}_z\hat{S}_z \tag{1.41}$$

where β_{IS} is the dipolar coupling strength, ω_I, ω_S are carrier frequencies for nuclei I and S, respectively.[79] By first transferring to the rotating frame using $\hat{R} = \exp(i\omega_I\hat{I}_z t + i\omega_S\hat{S}_z t)$, by AHT, the lowest order approximation is

$$H^0_{eff,1} = \omega_{1I}\hat{\mathrm{I}}_y + \omega_{1S}\hat{S}_y + \beta_{IS}\hat{\mathrm{I}}_z\hat{S}_z. \tag{1.42}$$

Then by transferring to the second rotating frame using $\hat{R} = \exp(i\omega_{1I}\hat{I}_y t + i\omega_{1S}\hat{S}_y t)$,

$$H_{eff,2} = \beta_{IS}(\hat{\mathrm{I}}_z \cos\omega_{1I}t + \hat{\mathrm{I}}_x \sin\omega_{1I}t)(\hat{S}_z \cos\omega_{1S}t + \hat{S}_x \sin\omega_{1S}t) \tag{1.43}$$

$$H_{eff,2} = \beta_{IS}(\hat{\mathrm{I}}_z\hat{S}_z \cos\omega_{1I}t\cos\omega_S t + \hat{\mathrm{I}}_x\hat{S}_z \sin\omega_{1I}t\cos\omega_{1S}t + \hat{S}_x\hat{\mathrm{I}}_z \cos\omega_{1I}t\sin\omega_{1S}t + \hat{S}_x\hat{\mathrm{I}}_x \sin\omega_{1I}t\sin\omega_S t) \tag{1.44}$$

By using the equation $\sin\omega_{1I}t\sin\omega_{1S}t = (\cos(\omega_{1I} + \omega_{1S})\,t + (\cos(\omega_{1I} - \omega_{1S})\,t)/2$, only when the $|\omega_{1I} - \omega_{1S}| = n\omega_r$ is met, $\cos(\omega_{1I} - \omega_{1S})\,t$ term will not vanish over a rotor period in the zero order approximation in AHT. $\hat{S}_x\hat{\mathrm{I}}_x$ can be rewritten into $\hat{S}^+\hat{I}^+ + \hat{S}^-\hat{I}^+ + \hat{S}^+\hat{I}^- + \hat{S}^-\hat{I}^-$, indicating that the polarization can be transferred through the double or zero quantum.

1.6 Techniques to retrieve information by recoupling pulse sequence

In MAS SSNMR, the mechanically averaged Hamiltonian like Dipolar interaction can be strategically reintroduced by recoupling pulse sequence. These recoupled Hamiltonian are useful to provide a measurement of dipolar interaction or CSA to provide distance or orientation information.[68] They can also be applied to mediate polarization transfer between nuclei.[94] Many recoupling pulse sequences have been developed over the past two decades and Levitt et. al summarized these pulse sequences through their symmetry properties and further introduced a new library of recoupling pulses named as RN and CN sequences.[95] The applications of these sequences to extract structural and biological information can be found in numerous cases.[13,69,96–98] Here we introduce a few recoupling pulse sequences, which were applied in the thesis.

1.6.1 Dipolar Assistant Rational Recoupling (DARR)

Dipolar assistant rational recoupling pulse sequence is the extensively used in this thesis for ^{13}C-^{13}C correlation experiment. The technique was introduced by Takegoshi et al in 2001 and the pulse scheme is shown in Figure 1.7.[99] After the CP build block, the coherence on carbon channel is flipped to Z-axis by 90º pulse, the polarization can be transferred between homonuclear pairs through RF radiation on proton channel at the field strength matches the MAS frequency, $\omega_{1H} = \omega_r$. The theoretic validation is complicated and can be found in the reference without further introduction.[100] The length of the DARR block can be varied to control the transfer path length. For example, for carbon-carbon transferring, with a 15ms DARR period, it is around one or two bonds transfer; with 100ms, it is around two or three bonds transfer.

1.6.2 Double Cross Polarization (DCP)

Double cross polarization, also called specific-CP is widely applied for directional transfer polarization, such as nitrogen to CA or nitrogen to CO. Due to the directional feature, the spectra is easy to interpret; thus it is widely applied as a functional unit in pulse programs used for protein assignment, such as NCACX, NCOCX.[101] It is firstly introduced by Baldus and Griffin.[102] The basic pulse scheme can be seen in the Figure 1.8. The DCP is a combination of two cross polarization between different nuclei. In a typical NCA or NCO experiment, the polarization is first transferred from proton to nitrogen, and then

transferred from nitrogen to carbon (CA or CO based on the carrier frequency and cross polarization conditions) and detected on carbon channel.

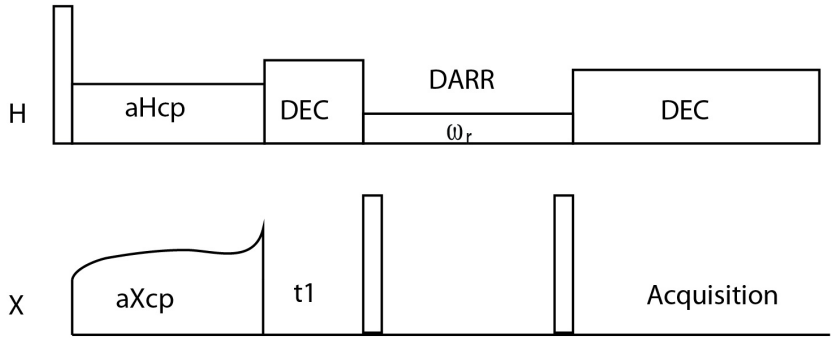

Figure 1.7 A general scheme of DARR pulse sequence is shown. After the CP block, the coherence at X is coded before flipped by the first 90° pulse to Z-axis for experiencing the DARR condition to mix polarization between X nuclei. In the DARR condition, spinning lock pulse is put on proton channel with its power equal to the spinning frequency. The polarization is then flipped by the second 90° pulse to coherence plane for acquisition.

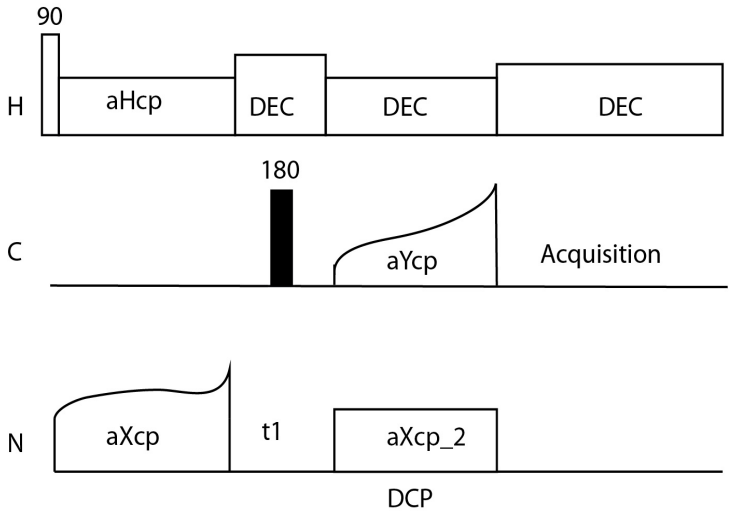

Figure 1.8. A general scheme of ^{15}N-^{13}C double Cross Polarization pulse sequence is shown. After the first ^{1}H-^{15}N CP, the coherence is encoded in the nitrogen dimension and then further transferred by a second ^{15}N-^{13}C CP to ^{13}C nuclei, and then the coherence on ^{13}C is acquired.

1.6.3 Rotational Echo Double Resonance (REDOR).

Rotational Echo Double Resonance (REDOR) is a common technique to recover the hetronuclear dipolar interaction that is normally averaged by the magical angle spinning. Since dipolar coupling strength is distance-dependent, the recoupled dipolar interaction can be used to measure interatomic distance. The pulse was developed by Gullion and Schaefer in 1989 and the general scheme is shown in Figure 1.9.[68,103] In the REDOR building block, 180° pulses are applied on one of the two channels to flip the nuclei polarizations at the every half-rotor period. Under the MAS spinning condition, the dipolar coupling is modulated to have a period of $\frac{2\pi}{\omega_r}$. By arranging 180 pulse in a such way, the dipolar interaction can be recoupled. (see Figure 1.10). The recoupled dipolar interaction will dephase the coherence, and the signal intensity is dependent on how many rotor periods are used (i.e. the dephase time). By comparing to the reference spectrum, where the dipolar coupling is not recoupled, the difference in intensity can be fitted to extract the dipolar coupling strength and by extension the interatomic distance.

In the real application, the situation is more complicated since networks of NMR spins are interconnected, and the REDOR dephasing time reflects the effects all of the available nearby coupling partners. This problem is more sever for long distance calculation (i.e. weak dipolar coupling) due to the dipolar truncation caused the nearby strong dipolar interaction. Various improved methods, such as frequency-selective REDOR have been developed to cope with this problem.[104,105] On the other hand, special sample preparation, such as introducing labeling pairs can be applied to simplify the data interpretation.[105–107]

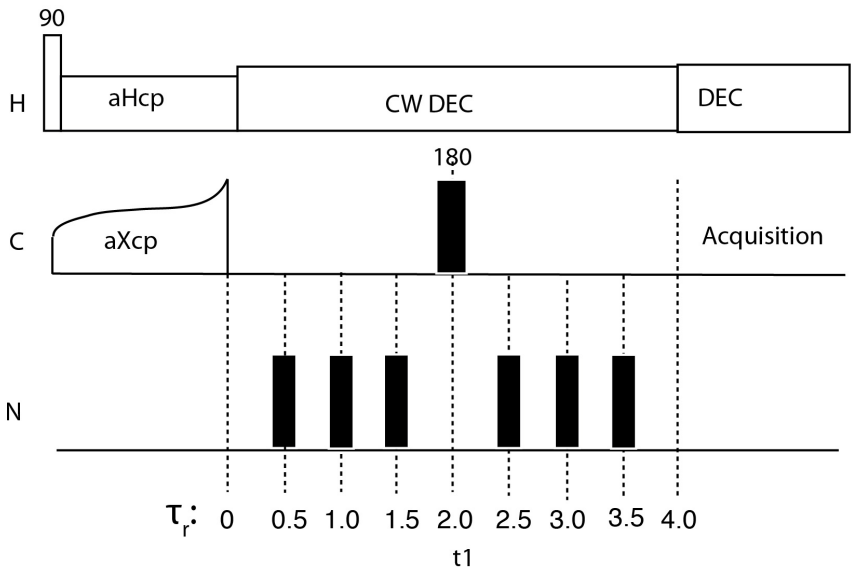

Figure 1.9. A general scheme of ^{15}N-^{13}C double REDOR pulse sequence is shown. After the first ^{1}H-^{13}C CP, the coherence on ^{13}C is dephased by the recoupled the ^{13}C-^{15}N dipolar interaction, before acquisition. In the recoupling block, a 180° pulse (black rectangle) is placed at the half rotor cycle. The central 180° pulse is placed on carbon channel in order to refocus the effect of unwanted ^{1}H-^{13}C J- interaction.

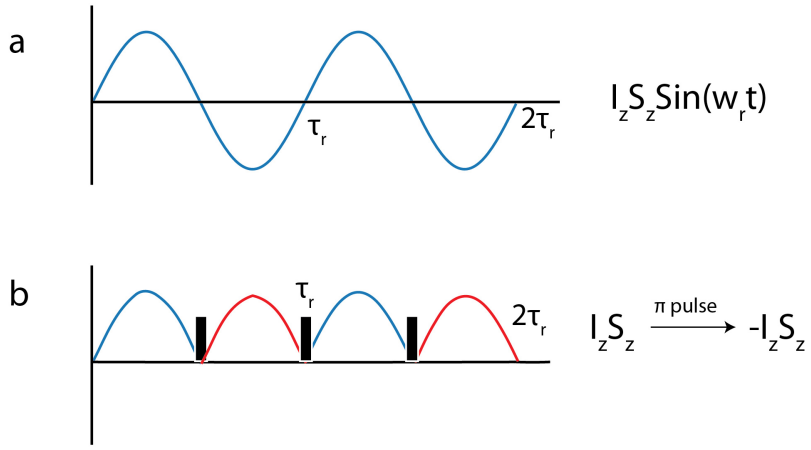

Figure 1.10. The mechanism of dipolar interaction recoupling in REDOR. In the MAS experiment, the dipolar interaction terms are modulated at a frequency of the spinning frequency. Without the 180° pulses (black rectangle) placed at the half rotor cycle, the averaged interaction over a rotor period equals zero for the zero-order approximation in average Hamiltonian theory (a). By introducing the 180° pulse placed at the half rotor cycle, the sign of the spin operator for the dipolar interaction changes so that the averaged dipolar interaction no longer averages out (b).

1.6.4 Transferred Echo Double Resonance (TEDOR).

Transferred Echo Double Resonance (TEDOR) shared the theoretical basis with REDOR pulse, and was developed by Hing et al.[108] The scheme can be seen in Figure 1.11. It can be viewed as HSQC experiment with the INEPT section replaced by REDOR building block. The coherence is generated on carbon through ^{1}H-^{13}C CP, and then transferred to nitrogen and the nitrogen frequency is encoded in the t1 period, and then the coherence is transferred back to carbon by another REDOR building block and then is acquired as free induction decay. The dwell time in t_1 period is required to be integer number of the rotor period, which limits the spectrum width.

A series of TEDOR experiments can be acquired with various rotor periods in the REDOR building blocks, which determines transferring time. A rough estimate of the dipolar interaction for a peak can be achieved by measuring the signal building up in the various spectra.[108,109] When the transferring time is short, the spectra can also be used for protein assignment. But unlike DCP, the polarization transfer is without specific direction.

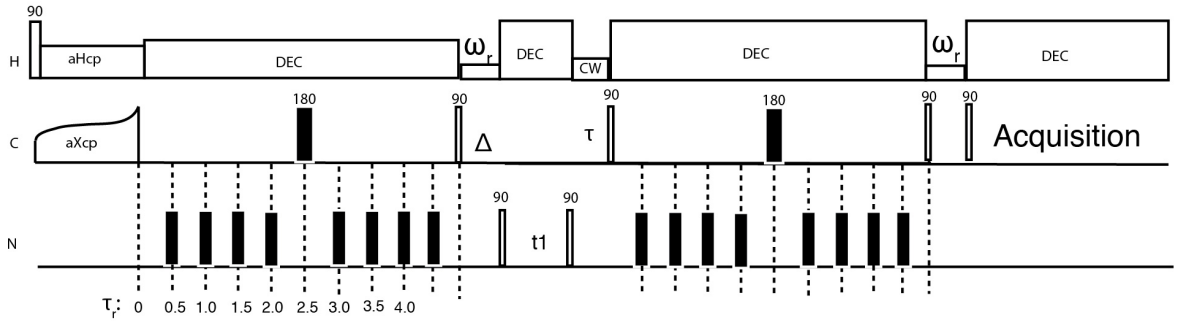

Figure 1.11. A general scheme of ^{15}N-^{13}C double TEDOR pulse sequence is shown. After the first ^{1}H-^{13}C CP, the coherence on ^{13}C is transferred to ^{15}N by the recoupled the ^{13}C-^{15}N dipolar interaction and the coherence at 15N is encoded before it is transferred back to 13C by another coupled dipolar interaction. In the recoupling block, a 180° pulse (black rectangle) is placed at the half rotor cycle. The two proton pulses with power equal to Wr are used for destroyed the unwanted coherence after the Z-flip. The delay time is used to allow for an integer number of rotor periods between the two REDOR blocks.

1.7 References

1. McDermott, A. Structure and dynamics of membrane proteins by magic angle spinning solid-state NMR. *Annu. Rev. Biophys.* **38,** 385–403 (2009).
2. Drobny, G. P. Multiple Quantum NMR: Studies of Molecules in Ordered Phases. *Annu. Rev. Phys. Chem.* **36,** 451–489 (1985).
3. Sapienza, P. J. & Lee, A. L. Using NMR to study fast dynamics in proteins: methods and applications. *Curr. Opin. Pharmacol.* **10,** 723–30 (2010).
4. Palmer, A. G. Enzyme Dynamics from NMR Spectroscopy. *Acc. Chem. Res.* **48,** 457 (2015).
5. Arthur G. Palmer III, ‡, John Williams, †,§ and & Ann McDermott*, †. Nuclear Magnetic Resonance Studies of Biopolymer Dynamics. (1996). doi:10.1021/JP9606117
6. Edén, M. & Levitt, M. H. Pulse sequence symmetries in the nuclear magnetic resonance of spinning solids: Application to heteronuclear decoupling. *J. Chem. Phys.* **111,** 1511 (1999).
7. Aboul-ela, F. & Varani, G. Novel techniques in nuclear magnetic resonance for nucleic acids. *Curr. Opin. Biotechnol.* **6,** 89–95 (1995).
8. Sergeyev, I. V, Itin, B., Rogawski, R., Day, L. A. & McDermott, A. E. Efficient assignment and NMR analysis of an intact virus using sequential side-chain correlations and DNP sensitization. *Proc. Natl. Acad. Sci. U. S. A.* **114,** 5171–5176 (2017).
9. Rinnenthal, J. *et al.* Mapping the Landscape of RNA Dynamics with NMR Spectroscopy. *Acc. Chem. Res.* **44,** 1292–1301 (2011).
10. Getz, M., Sun, X., Casiano-Negroni, A., Zhang, Q. & Al-Hashimi, H. M. NMR studies of RNA dynamics and structural plasticity using NMR residual dipolar couplings. *Biopolymers* **86,** 384 (2007).
11. Molugu, T. R., Lee, S. & Brown, M. F. Concepts and Methods of Solid-State NMR Spectroscopy Applied to Biomembranes. *Chem. Rev.* **117,** 12087–12132 (2017).
12. Sugase, K., Dyson, H. J. & Wright, P. E. Mechanism of coupled folding and binding of an intrinsically disordered protein. *Nature* **447,** 1021–1025 (2007).

13. Hong, M. & Schmidt-Rohr, K. Magic-Angle-Spinning NMR Techniques for Measuring Long-Range Distances in Biological Macromolecules. *Acc. Chem. Res.* **46,** 2154 (2013).

14. Jameson, C. J. Understanding Nmr Chemical Shifts. *Annu. Rev. Phys. Chem.* **47,** 135–169 (1996).

15. Su, Y., Andreas, L. & Griffin, R. G. Magic Angle Spinning NMR of Proteins: High-Frequency Dynamic Nuclear Polarization and ^{1}H Detection. *Annu. Rev. Biochem.* **84,** 465–497 (2015).

16. Hong, M., Zhang, Y. & Hu, F. Membrane Protein Structure and Dynamics from NMR Spectroscopy. *Annu. Rev. Phys. Chem.* **63,** 1–24 (2012).

17. Schnell, J. R., Dyson, H. J. & Wright, P. E. Structure, dynamics, and catalytic function of dihydrofolate reductase. *Annu. Rev. Biophys. Biomol. Struct.* **33,** 119–40 (2004).

18. Tjandra, N. & Bax, A. Direct Measurement of Distances and Angles in Biomolecules by NMR in a Dilute Liquid Crystalline Medium. *Science (80-.).* **278,** 1111 (1997).

19. Mittermaier, A. & Kay, L. E. New Tools Provide New Insights in NMR Studies of Protein Dynamics. *Science (80-.).* **312,** 224 (2006).

20. Clore, G. M. & Iwahara, J. Theory, Practice, and Applications of Paramagnetic Relaxation Enhancement for the Characterization of Transient Low-population States of Biological Macromolecules and Their Complexes. *Chem. Rev.* **109,** 4108 (2009).

21. Gajan, D. *et al.* Hybrid polarizing solids for pure hyperpolarized liquids through dissolution dynamic nuclear polarization. *Proc. Natl. Acad. Sci. U. S. A.* **111,** 14693–14697 (2014).

22. Spiess, H. W. 50th Anniversary Perspective: The Importance of NMR Spectroscopy to Macromolecular Science. *Macromolecules* **50,** 1761–1777 (2017).

23. Hoffmann, H. *et al.* Solid-State NMR Spectroscopy of Metal–Organic Framework Compounds (MOFs). *Materials (Basel).* **5,** 2537–2572 (2012).

24. Deng, H. *et al.* Multiple functional groups of varying ratios in metal-organic frameworks. *Science* **327,** 846–50 (2010).

25. Kurihara, T., Noda, Y. & Takegoshi, K. Quantitative Solid-State NMR Study on Ligand–Surface Interaction in Cysteine-Capped CdSe Magic-Sized Clusters. *J. Phys. Chem. Lett.* **8,** 2555–2559 (2017).

26. Anderson, N. C., Hendricks, M. P., Choi, J. J. & Owen, J. S. Ligand Exchange and the Stoichiometry of Metal Chalcogenide Nanocrystals: Spectroscopic Observation of Facile Metal-Carboxylate Displacement and Binding. *J. Am. Chem. Soc.* **135,** 18536–18548 (2013).

27. Sideris, P. J., Nielsen, U. G., Gan, Z. & Grey, C. P. Mg/Al ordering in layered double hydroxides revealed by multinuclear NMR spectroscopy. *Science* **321,** 113–7 (2008).

28. and, C. P. G. & Dupré, N. NMR Studies of Cathode Materials for Lithium-Ion Rechargeable Batteries. (2004). doi:10.1021/CR020734P

29. Belesi, M., Zong, X., Borsa, F., Milios, C. J. & Perlepes, S. P. Proton NMR study in hexanuclear manganese single-molecule magnets. *Phys. Rev. B* **75,** 64414 (2007).

30. Borsa, F., Lascialfari, A. & Furukawa, Y. in *Novel NMR and EPR techniques* 297–349 (Springer Berlin Heidelberg, 2006). doi:10.1007/3-540-32627-8_10

31. Nimerovsky, E. & Goldbourt, A. Efficient rotational echo double resonance recoupling of a spin-1/2 and a quadrupolar spin at high spinning rates and weak irradiation fields. *J. Magn. Reson.* **206,** 52–58 (2010).

32. Nielsen, U. G., Jakobsen, H. J. & Skibsted, J. 59Co Chemical Shift Anisotropy and Quadrupole Coupling for K3Co(CN)6 from MQMAS and MAS NMR Spectroscopy. *Solid State Nucl. Magn. Reson.* **20,** 23–34 (2001).

33. Igumenova, T. I., Frederick, K. K. & Wand, A. J. Characterization of the fast dynamics of protein amino acid side chains using NMR relaxation in solution. *Chem. Rev.* **106,** 1672–99 (2006).

34. Tycko, R. Solid-state NMR studies of amyloid fibril structure. *Annu. Rev. Phys. Chem.* **62,** 279–99 (2011).

35. Kellogg, J. M. B., Rabi, I. I., Ramsey, N. F. & Zacharias, J. R. The Magnetic Moments of the Proton and the Deuteron. The Radiofrequency Spectrum of H 2 in Various Magnetic Fields. *Phys. Rev.* **56,** 728–743 (1939).

36. https://www.nobelprize.org/.

37. Ni, Q. Z. *et al.* High Frequency Dynamic Nuclear Polarization. *Acc. Chem. Res.* **46,** 1933–1941 (2013).

38. Otting, G. Protein NMR Using Paramagnetic Ions. *Annu. Rev. Biophys.* **39,** 387 (2010).

39. Boulton, S. & Melacini, G. Advances in NMR Methods To Map Allosteric Sites: From Models to Translation. *Chem. Rev.* **116,** 6267–6304 (2016).

40. Ann E. McDermott, T. P. *Solid State NMR Studies of Biopolymers*.

41. Richard R. Ernst , Geoffrey Bodenhausen, A. W. *Principles of Nuclear Magnetic Resonance in One and Two Dimensions*.

42. Malcolm H. Levitt. *Spin Dynamics: Basics of Nuclear Magnetic Resonance 2nd Edition*.

43. Arthur G. Palmer III , Wayne J. Fairbrother , John Cavanagh , Nicholas J. Skelton, M. R. *Protein NMR Spectroscopy, Second Edition: Principles and Practice*.

44. Qiang, W., Yau, W.-M., Lu, J.-X., Collinge, J. & Tycko, R. Structural variation in amyloid-β fibrils from Alzheimer's disease clinical subtypes. *Nature* **541,** 217–221 (2017).

45. Andreas, L. B., Le Marchand, T., Jaudzems, K. & Pintacuda, G. High-resolution proton-detected NMR of proteins at very fast MAS. *J. Magn. Reson.* **253,** 36–49 (2015).

46. Guerry, P. & Herrmann, T. Advances in Automated NMR Protein Structure Determination. *Q. Rev. Biophys.* **44,** 257 (2011).

47. Kaplan, M. *et al.* EGFR Dynamics Change during Activation in Native Membranes as Revealed by NMR. *Cell* **167,** 1241–1251.e11 (2016).

48. Park, S. H. *et al.* Structure of the chemokine receptor CXCR1 in phospholipid bilayers. *Nature* **491,** 779–83 (2012).

49. Tugarinov, V., Kanelis, V. & Kay, L. E. Isotope Labeling Strategies for the Study of High-Molecular-Weight Proteins by Solution NMR Spectroscopy. *Nat. Protoc.* **1,** 749 (2006).

50. Marion, D. An introduction to biological NMR spectroscopy. *Mol. Cell. Proteomics* **12,** 3006–25 (2013).

51. Ramsey, N. F. Magnetic Shielding of Nuclei in Molecules. *Phys. Rev.* **78,** 699–703 (1950).

52. Chernyshev, Vladimir I. Chizhik, Y. S., Frolov, Alexey V. Donets, V. V. & Shelyapina, A. V. K. • M. G. *Magnetic Resonance and Its Applications*.

53. Bak, M., Rasmussen, J. T. & Nielsen, N. C. SIMPSON: A General Simulation Program for Solid-State NMR Spectroscopy. *J. Magn. Reson.* **147,** 296–330 (2000).

54. NMR Ramblings Klaus Eichele. Available at: http://anorganik.uni-

tuebingen.de/klaus/nmr/index.php?p=conventions/csa/csa. (Accessed: 22nd April 2018)

55. Spera, S. & Bax, A. Empirical correlation between protein backbone conformation and C.alpha. and C.beta. 13C nuclear magnetic resonance chemical shifts. *J. Am. Chem. Soc.* **113,** 5490–5492 (1991).

56. Ando, I., Saito, H., Tabeta, R., Shoji, A. & Ozaki, T. Conformation-dependent carbon-13 NMR chemical shifts of poly(L-alanine) in the solid state: FPT INDO calculation of N-acetyl-N'-methyl-L-alanine amide as a model compound of poly(L-alanine). *Macromolecules* **17,** 457–461 (1984).

57. Wishart, D. & Sykes, B. The 13C Chemical-Shift Index: A simple method for the identification of protein secondary structure using 13C chemical-shift data. *J. Biomol. NMR* **4,** 171–180 (1994).

58. Oldfield, E. Chemical shifts in amino acids, peptides, and proteins: from quantum chemistry to drug design. *Annu. Rev. Phys. Chem.* **53,** 349–78 (2002).

59. Dalvit, C. Ligand- and Substrate-based 19F NMR Screening: Principles and Applications to Drug Discovery. *Prog. Nucl. Magn. Reson. Spectrosc.* **51,** 243 (2007).

60. Gu, Z., Zambrano, R. & McDermott, A. Hydrogen Bonding of Carboxyl Groups in Solid-State Amino Acids and Peptides: Comparison of Carbon Chemical Shielding, Infrared Frequencies, and Structures. *J. Am. Chem. Soc.* **116,** 6368–6372 (1994).

61. Bhate, M. P. & McDermott, A. E. Protonation state of E71 in KcsA and its role for channel collapse and inactivation. *Proc. Natl. Acad. Sci. U. S. A.* **109,** 15265–70 (2012).

62. Wylie, B. J., Schwieters, C. D., Oldfield, E. & Rienstra, C. M. Protein Structure Refinement Using ^{13} Cα Chemical Shift Tensors. *J. Am. Chem. Soc.* **131,** 985–992 (2009).

63. Wylie, B. J. *et al.* Ultrahigh resolution protein structures using NMR chemical shift tensors. *Proc. Natl. Acad. Sci. U. S. A.* **108,** 16974–9 (2011).

64. Loria, J. P., Rance, M. & Palmer, A. G. A TROSY CPMG sequence for characterizing chemical exchange in large proteins. *J. Biomol. NMR* **15,** 151 (1999).

65. Schwieters, C. D. *et al.* Solution structure of the 128 kDa enzyme I dimer from Escherichia coli and its 146 kDa complex with HPr using residual dipolar couplings and small- and wide-angle X-ray scattering. *J. Am. Chem. Soc.* **132,** 13026 (2010).

66. Levitt, M. H. The Signs of Frequencies and Phases in NMR. *J. Magn. Reson.* **126,** 164–182

(1997).

67. Clore, G. M., Starich, M. R. & Gronenborn, A. M. Measurement of Residual Dipolar Couplings of Macromolecules Aligned in the Nematic Phase of a Colloidal Suspension of Rod-Shaped Viruses. *J. Am. Chem. Soc.* **120,** 10571 (1998).

68. Schaefer, J. 'Development of REDOR rotational-echo double-resonance NMR' by Terry Gullion and Jacob Schaefer [J. Magn. Reson. 81 (1989) 196–200]. *J. Magn. Reson.* **213,** 421–422 (2011).

69. Hu, F., Luo, W. & Hong, M. Mechanisms of proton conduction and gating in influenza M2 proton channels from solid-state NMR. *Science* **330,** 505–8 (2010).

70. Raleigh, D. P., Levitt, M. H. & Griffin, R. G. Rotational resonance in solid state NMR. *Chem. Phys. Lett.* **146,** 71–76 (1988).

71. Nielsen, N. C., Bildso/e, H., Jakobsen, H. J. & Levitt, M. H. Double - quantum homonuclear rotary resonance: Efficient dipolar recovery in magic - angle spinning nuclear magnetic resonance. *J. Chem. Phys.* **101,** 1805–1812 (1994).

72. Bennett, A. E. *et al.* Homonuclear radio frequency-driven recoupling in rotating solids. *J. Chem. Phys.* **108,** 9463 (1998).

73. Bennett, A. E., Griffin, R. G., Ok, J. H. & Vega, S. Chemical shift correlation spectroscopy in rotating solids: Radio frequency - driven dipolar recoupling and longitudinal exchange. *J. Chem. Phys.* **96,** 8624–8627 (1992).

74. Brinkmann, A., Edén, M. & Levitt, M. H. Synchronous helical pulse sequences in magic-angle spinning nuclear magnetic resonance: Double quantum recoupling of multiple-spin systems. *J. Chem. Phys.* **112,** 8539 (2000).

75. De Paëpe, G., Lewandowski, J. R., Loquet, A., Böckmann, A. & Griffin, R. G. Proton assisted recoupling and protein structure determination. *J. Chem. Phys.* **129,** 245101 (2008).

76. Gabriel Cornilescu, †, Ad Bax, *,† and & David A. Case*, ‡. Large Variations in One-Bond 13Cα−13Cβ J Couplings in Polypeptides Correlate with Backbone Conformation. (2000). doi:10.1021/JA993609C

77. Agarwal, V. *et al.* De Novo 3D Structure Determination from Sub-milligram Protein Samples by Solid-State 100 kHz MAS NMR Spectroscopy. *Angew. Chemie Int. Ed.* **53,** 12253–12256 (2014).

78. Veshtort, M. & Griffin, R. G. SPINEVOLUTION : A powerful tool for the simulation of solid and liquid state NMR experiments. **178,** 248–282 (2006).

79. Waugh, J. S. in *Encyclopedia of Magnetic Resonance* (John Wiley & Sons, Ltd, 2007). doi:10.1002/9780470034590.emrstm0020

80. ANDREW, E. R., Bradbury, A. & Eades, R. G. Nuclear Magnetic Resonance Spectra from a Crystal Rotated at High Speed. *Nature* **182,** 1659 (1958).

81. Lakomek, N.-A. *et al.* Microsecond Dynamics in Ubiquitin Probed by Solid-State ^{15}N NMR Spectroscopy $R_{1\rho}$ Relaxation Experiments under Fast MAS (60-110 kHz). *Chem. - A Eur. J.* **23,** 9425–9433 (2017).

82. Jen, J. Chemical Exchange and NMR T2 Relaxation – The Multisite Case. *J. Magn. Reson.* **30,** 111 (1978).

83. Haeberlen, U. & Waugh, J. S. Coherent Averaging Effects in Magnetic Resonance. *Phys. Rev.* **175,** 453–467 (1968).

84. Bennett, A. E., Rienstra, C. M., Auger, M., Lakshmi, K. V. & Griffin, R. G. Heteronuclear decoupling in rotating solids. *J. Chem. Phys.* **103,** 6951–6958 (1995).

85. Ernst, M. Heteronuclear spin decoupling in solid-state NMR under magic-angle sample spinning. *J. Magn. Reson.* **162,** 1–34 (2003).

86. Fung, B. M., Khitrin, A. K. & Ermolaev, K. An Improved Broadband Decoupling Sequence for Liquid Crystals and Solids. *J. Magn. Reson.* **142,** 97–101 (2000).

87. Schilling, F. *et al.* Next-generation heteronuclear decoupling for high-field biomolecular NMR spectroscopy. *Angew. Chem. Int. Ed. Engl.* **53,** 4475–9 (2014).

88. Vinogradov, E., Madhu, P. K. & Vega, S. High-resolution proton solid-state NMR spectroscopy by phase-modulated Lee–Goldburg experiment. *Chem. Phys. Lett.* **314,** 443–450 (1999).

89. Bielecki, A., Kolbert, A. C. & Levitt, M. H. Frequency-switched pulse sequences: Homonuclear decoupling and dilute spin NMR in solids. *Chem. Phys. Lett.* **155,** 341–346 (1989).

90. Paul, S. *et al.* Supercycled Homonuclear Dipolar Decoupling Sequences in Solid-State NMR. (2008).

91. Kolodziejski, W. & Klinowski, J. Kinetics of cross-polarization in solid-state NMR: a guide for

chemists. *Chem. Rev.* **102,** 613–28 (2002).

92. Hartmann, S. R. & Hahn, E. L. Nuclear Double Resonance in the Rotating Frame. *Phys. Rev.* **128,** 2042–2053 (1962).

93. Hediger, S., Meier, B. H. & Ernst, R. R. Cross polarization under fast magic angle sample spinning using amplitude-modulated spin-lock sequences. *Chem. Phys. Lett.* **213,** 627–635 (1993).

94. Verel, R. & Meier, B. H. Polarization-transfer methods in solid-state magic-angle-spinning NMR: adiabatic CN pulse sequences. *Chemphyschem* **5,** 851–62 (2004).

95. Carravetta, M., Edén, M., Zhao, X., Brinkmann, A. & Levitt, M. H. Symmetry principles for the design of radiofrequency pulse sequences in the nuclear magnetic resonance of rotating solids. *Chem. Phys. Lett.* **321,** 205–215 (2000).

96. Lu, M. *et al.* Dynamic allostery governs cyclophilin A-HIV capsid interplay. *Proc. Natl. Acad. Sci. U. S. A.* **112,** 14617–22 (2015).

97. Xu, Y., Bhate, M. P. & McDermott, A. E. Transmembrane allosteric energetics characterization for strong coupling between proton and potassium ion binding in the KcsA channel. *Proc. Natl. Acad. Sci. U. S. A.* **114,** 8788–8793 (2017).

98. Franks, W. T. *et al.* Magic-angle spinning solid-state NMR spectroscopy of the beta1 immunoglobulin binding domain of protein G (GB1): 15N and 13C chemical shift assignments and conformational analysis. *J. Am. Chem. Soc.* **127,** 12291–305 (2005).

99. Takegoshi, K., Nakamura, S. & Terao, T. 13C–1H dipolar-assisted rotational resonance in magic-angle spinning NMR. *Chem. Phys. Lett.* **344,** 631–637 (2001).

100. Veshtort, M. & Griffin, R. G. Proton-driven spin diffusion in rotating solids via reversible and irreversible quantum dynamics. *J. Chem. Phys.* **135,** 134509 (2011).

101. Wylie, B. J., Bhate, M. P. & McDermott, A. E. Transmembrane allosteric coupling of the gates in a potassium channel. *Proc. Natl. Acad. Sci. U. S. A.* **111,** 185–90 (2014).

102. BALDUS, M., PETKOVA, A. T., HERZFELD, J. & GRIFFIN, R. G. Cross polarization in the tilted frame: assignment and spectral simplification in heteronuclear spin systems. *Mol. Phys.* **95,** 1197 (1998).

103. Gullion, T. Measurement of dipolar interactions between spin- and quadrupolar nuclei by

rotational-echo, adiabatic-passage, double-resonance NMR. *Chem. Phys. Lett.* **246,** 325–330 (1995).

104. Nimerovsky, E. *et al.* Phase-modulated LA-REDOR: A robust, accurate and efficient solid-state NMR technique for distance measurements between a spin-1/2 and a quadrupole spin. *J. Magn. Reson.* **244,** 107–113 (2014).

105. Jaroniec, C. P., Tounge, B. A., Herzfeld, J. & Griffin, R. G. Frequency Selective Heteronuclear Dipolar Recoupling in Rotating Solids: Accurate 13 C− 15 N Distance Measurements in Uniformly 13 C, 15 N-labeled Peptides. *J. Am. Chem. Soc.* **123,** 3507–3519 (2001).

106. Ohki, S. & Kainosho, M. Stable isotope labeling methods for protein NMR spectroscopy. *Prog. Nucl. Magn. Reson. Spectrosc.* **53,** 208–226 (2008).

107. Lichtenecker, R. J., Coudevylle, N., Konrat, R. & Schmid, W. Selective isotope labelling of leucine residues by using α-ketoacid precursor compounds. *Chembiochem* **14,** 818–21 (2013).

108. Hing, A. W., Vega, S. & Schaefer, J. Measurement of Heteronuclear Dipolar Coupling by Transferred-Echo Double-Resonance NMR. *J. Magn. Reson. Ser. A* **103,** 151–162 (1993).

109. Jaroniec, C. P., Filip, C. & Griffin, R. G. 3D TEDOR NMR Experiments for the Simultaneous Measurement of Multiple Carbon−Nitrogen Distances in Uniformly 13 C, 15 N-Labeled Solids. *J. Am. Chem. Soc.* **124,** 10728–10742 (2002).

Chapter II: Introduction to Membrane Proteins and Inactivation in potassium channel

2.1. Biological Significance of Membrane Proteins

Cellular membranes isolate the cell from the environment and enable the creation of intracellular compartments, allowing numerous biological processes to occur simultaneously without interference.[1,2] Membrane proteins, which are embedded in cell membrane, are therefore vital for exchanging chemical and information between different compartments and between intracellular and extracellular environment.[3,4] Based on gene sequencing estimation, membrane proteins constitute between 20 and 30% of proteins in most organisms.[5] They are generally classified into categories based on their functionalities, such as ion channels, transporters, growth factor receptors and G-protein coupled receptors (GPCR).[6,7] Many diseases have been identified as related to the malfunction of a membrane protein, around two-thirds of known druggable targets are membrane proteins and around half of current small molecule drugs work through binding to membrane proteins.[8,9]

Due to the importance of membrane proteins in both understanding basic biological function mechanism and solving health related problems, much attention has been given to their structure and dynamics, and the relationship of these properties to function.[3,10–13] In spite of the tremendous amount of efforts, the field is still in its developing stage, as only small portion of membrane proteins have been revealed their structures. By January 2013, less than 1% of proteins with solved structures are membrane protein, while, as we mentioned above, membrane protein consist of 20-30% of the proteome.[14]

Membrane proteins are more challenging to study comparing to soluble proteins for various reasons.[12] The first obstacle is the preparation of membrane protein. Membrane proteins are normally difficult to express in high yield due to their low natural abundance and toxicity to the host cell. Extraction of membrane proteins from cell membrane usually requires violent methods such as sonication and French press to break the cell wall, which could potentially affect integrity of the protein. The trans-membrane part of membrane proteins is very hydrophobic and insoluble in normal biological buffers; therefore detergents are needed to solubilize the protein from the membrane. In many cases, the choice of detergent is critical: the chain length and head group of the detergent can easily affect the extraction efficiency as well as the stability of the protein.[15,16] In cases where protein precipitates from solution, fusion of a soluble domain to the target membrane protein is often necessary.[17] Some membrane proteins are overexpressed in inclusion bodies. For purification, protein is denatured in a high concentration of

guanidine chloride buffer and need be refolded. However, it is a great challenge to fold membrane protein into its native conformation and only a few successful examples are reported.[18,19]

The second obstacle for studying membrane protein is that conventional biophysical and biochemical techniques to study soluble protein are difficult to apply to membrane proteins. For example, crystallography has been the most powerful tool to solve structures for soluble protein; however, for membrane proteins, it is generally hard to form high quality crystals. Various tricks, such as mutations, truncation, co-crystallization with antibody or usage of extreme crystal conditions are required.[20] However, the choice of the technique is heavily experience-based and implementation is time-consuming. Also, there is the caveat that structures acquired from X-Ray could be biased by the crystallization conditions and mutations and do not represent its original structures in the physiological conditions.[12]

This is related to the third difficulty. The presence of a lipid membrane is often key for the membrane protein to maintain its structure, function and energetics. This requires studying membrane proteins in a lipid complex.[21,22] This requirement further limits the number of applicable techniques due to the large size of lipoprotein and its low solubility property.

The surging development of Cryo-EM technique together with the advancement of computation biology has greatly helped accelerate the progress of membrane protein study.[23–25] Cryo-EM has no requirement for crystal sample and has the ability to study proteins with a large size with multiple domains, which is difficult to study by other methods. The technique is still in development and much effort is still needed in sample preparation, software development for image collection and classification and further structural calculations, but we see it will play an more crucial role in structural biology.[23]

Solid state NMR is another important tool to study membrane protein.[3,13] It allows the preparation of membrane protein in an authentic lipid bilayer environment and does not require a crystal sample for study. Importantly, SSNMR can provide information both on structures while also providing rich information on protein dynamics, which is an integral part of protein function.[26,27]

One outstanding feature for membrane proteins is transmembrane allostery, which means perturbations from one side of membrane are transferred to the other side.[28,29] Transmembraen allosterly allows membrane proteins to transmit information between two sides of the membrane. In the thesis, we focus on this transmembrane allostery in the study of a potassium channel.

2.2 Potassium channels: Open Functional Questions

Potassium channels are the second largest family of membrane proteins, play a critical role in communicating between different membrane bound environments through the passage of ions[30,31] and facilitate the passive diffusion of potassium ions through the low dielectric membrane.[30] Potassium channels have a wide distribution: they are in all excitable cells, such as neurons and muscle cells[30], and are also found in plant cells, bacterial, and other organisms.[32] The simple function of conducting potassium ions through the membrane is coupled to other environmental factors and cascading partners to form various complicated physiological functions.[33] One famous example discovered by Andrew Huxley and Alan Hodgkin is in membrane potential generation.[34] In the neuron cells, the intracellular potassium ion concentration is higher than the extracellular concentration, and sodium ions have the opposite distribution. At hypo-potential voltages, sodium channels are activated and sodium ions flow into the intracellular site. This enhances the hypo-potential and forms a positive loop to drive more sodium ions into intracellular side until the sodium channels inactivate. In order to achieve re-excitability, potassium channels are activated at the repolarization potential, and potassium ions flow toward the extracellular side and recover the membrane potential.[30,35]

Many diseases have been found related to potassium channels.[36] They are shown to regulate firing patterns critical for movement control and have been suggested as drug targets for treatment of behavior disorder, such as bipolar disorder.[37] Deletion of one of the background potassium channels TREK-1 results in a depression-resistant phenotype.[38] One recent finding shows that potassium channel expression level in cancer cells is notably higher than normal cells, causing a 2-3 fold lower intracellular potassium concentration. This destabilizes the K^+ stabilized G-quadruplex structure, which is an important transcription factor for cancer inhibiton.[39]

Because of potassium channels' ubiquitous distribution and significance in physiological functions, they have been the subjects of numerous studies.[40–49] Potassium channels have been discovered to have various forms in their structures: most potassium channels are tetrameric, but some are dimeric; for each monomer, some have six transmembrane helices, but some have two.[30] In spite of the diversity, they all share a structural motif and are conserved in key portions of their sequences (Figure 2.1).[50,51]

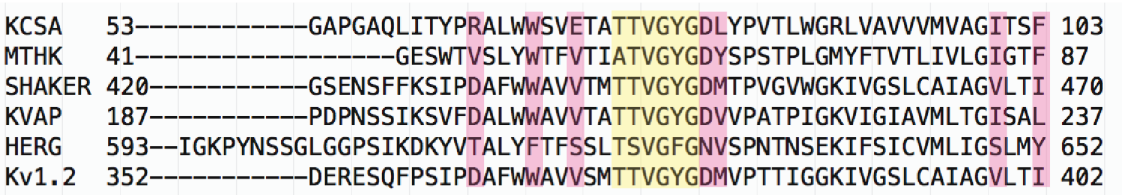

Figure 2.1 Sequence alignment of KcsA with other potassium channels. The residues highlighted yellow is the most conserved sequence named the selectivity filter. Residues highlighted magenta are those shown to be critical for the inactivation in KcsA and their according positions at other potassium channels.

KcsA is a prokaryotic tetrameric channel with two transmembrene helices.[32] Due to the easiness to prepare KcsA and that its structure is quite simple, it has been the model system for potassium channel research.[32] Even though each potassium channel has its own 'personality', the research to understand potassium channel can be generally divided into three aspects that pertain to essentially all channels: permeation, gating, and inactivation.[52,53]

2.2.1 Energetics of Potassium Permeation

The key question about permeation is to understand how potassium channels can simultaneously achieve high selectivity and a high permeation rate. Potassium channels are selective for K^+ over other ions such as Na^+ by more than three orders of magnitude.[54] This is crucial considering the complicated intracellular environments. On the other hand, potassium channels can conduct K^+ at a rate around 10^7-10^8 ions/second, close to the diffusion limit.[30,55] These two properties seem contradictory from an energetic point of view as it suggests both high k_{on} and high k_{off} rate. The explanation was not clear until the high-resolution crystal structure of KcsA was revealed; the pore helix loops form a selectivity filter at the N-terminus of the channel.[51,54](Figure 2.2). The backbone carbonyls of the residues in the selectivity filter arrange themselves to coordinate K^+ with their oxygen atoms in a 4-site tube form. The hopping between sites is at minimal energy cost, therefore fast.[51] Meanwhile, the energy gain of the interactions between K^+ and the selectivity filter compensates the dehydration energy of potassium ions; therefore, potassium ions can enter the selectivity filter with minimal energy barriers. However, for ions like sodium ion, such conditions cannot be met due to the smaller radius, causing higher dehydration energy and

lower binding energy with the selectivity filter. Other factors such as induced electronic repulsion between pore loops when sodium ions are coordinated could also contribute to the channel selectivity.[56–58] For summaries of mechanisms of channel selectivity and high conductivity, recent reviews are recommended.[31,59]

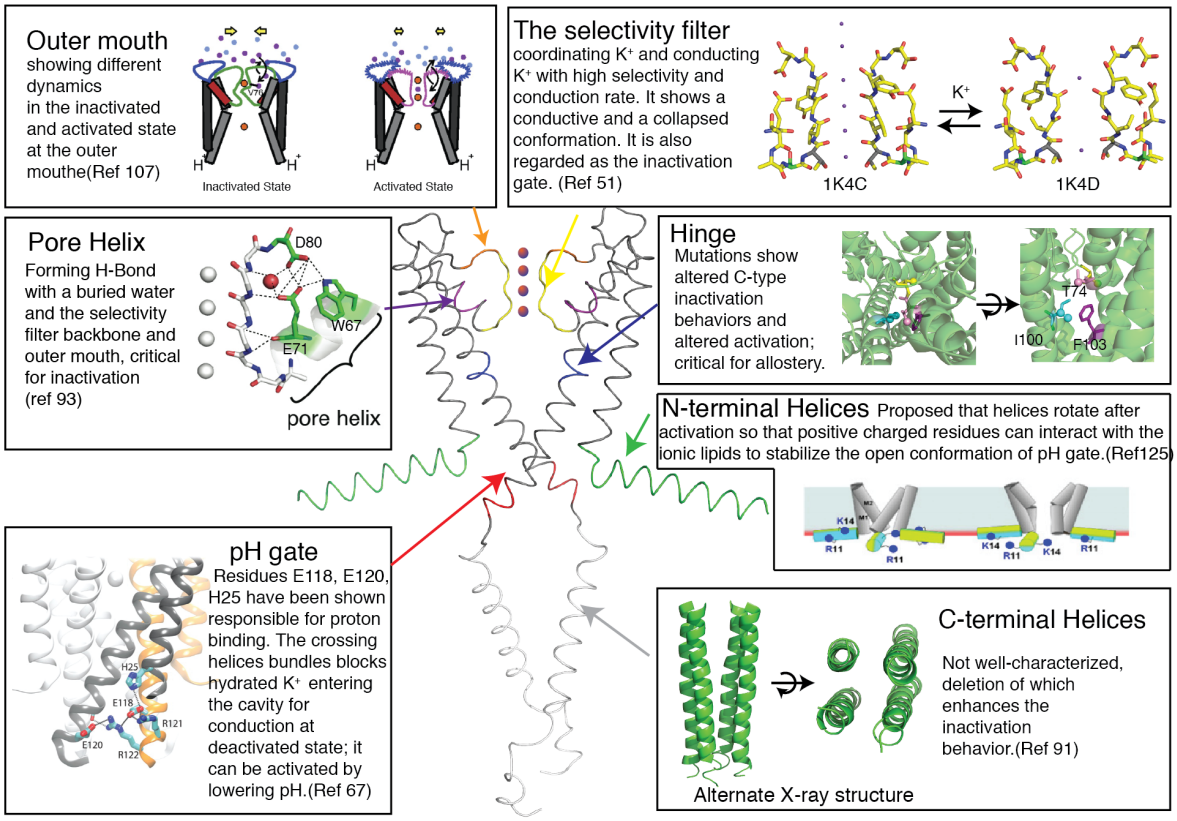

Figure 2.2. Overview of the various parts in the structure of KcsA and their according functions. The protein has been dissected into the outer month, the selectivity filter, the pore helix, the hinge, the N-terminal helices, the pH gate and the C-terminal helices.

2.2.2 Gating and Activation

The selectivity filter structure is highly conserved over almost all potassium channels, but different channels are activated by various stimuli, such as ligands (proton, calcium ion and nucleotide), or voltage.[60–62] The key question regarding gating is how the channels respond to external stimuli and therefore open their gate for conducting. In the C-terminus, transmembrane helices are bundled together to prevent hydrated ions (~8 Å) from entering the channels, which is called the activation gate.[60,63,64] There are residues sensitive to voltages or ligand binding and after activation they induce movement of

helices to open the channel.[65,66] KcsA is a proton-activated channel and residues such as H25 E118, E120, are protonated during activation to disrupt the original hydrogen-bonding network, which holds the helices bundle, thus opens the pH gate.[67,68] (Figure 2.2) The membrane has been reported to stabilize the open conformation by interacting with positively charged side chains of the N-terminal helices. Activation happens on a fast dynamic timescale in the majority of potassium channels compared to the inactivation process, which we will talk about in the following; in KcsA, the activation rate is in the range of 10^1-10^2 s^{-1}.[69]

2.2.3 Inactivation question

Activation is a process via which the channel is opened; inactivation is a process to close the channel. Inactivation is different from the reverse process of activation: the stimuli that activate the channel are still present, but the channels not longer conduct ions efficiently.[70,71] In almost all potassium channels and many other ion channels, inactivation starts right after activation and happens spontaneously, manifested as a decrease in current until it reaches a plateau with minimal conductance.[69,72] (Figure 2.3) Two major types of inactivation were identified in the Shaker channel, a voltage-gated bacterial potassium channel.[40] One is called N-type inactivation. It has a fast timescale and is caused by the positive N-terminus entering the channel cavity and blocking potassium ion conducting pathway.[73] After deleting N-terminal residues, a slow inactivation process, normally on a seconds timescale, was discovered and named C-type inactivation.[40,74] KcsA does not exhibit N-type inactivation, but it inactivates in a similar way to the C-type inactivation in Shaker and other voltage-gated potassium channels.[70] C-type inactivation is crucial for regulating the physiological potassium ion concentration with high time accuracy and to control the firing frequency and duration of excitable cells.[35,75] Malfunction of the process is related many arrhythmias, including a death-causing disease called long QT syndrome.[33,76] Below where I refer to “inactivation”, it is understood to be C-type inactivation unless otherwise specified.

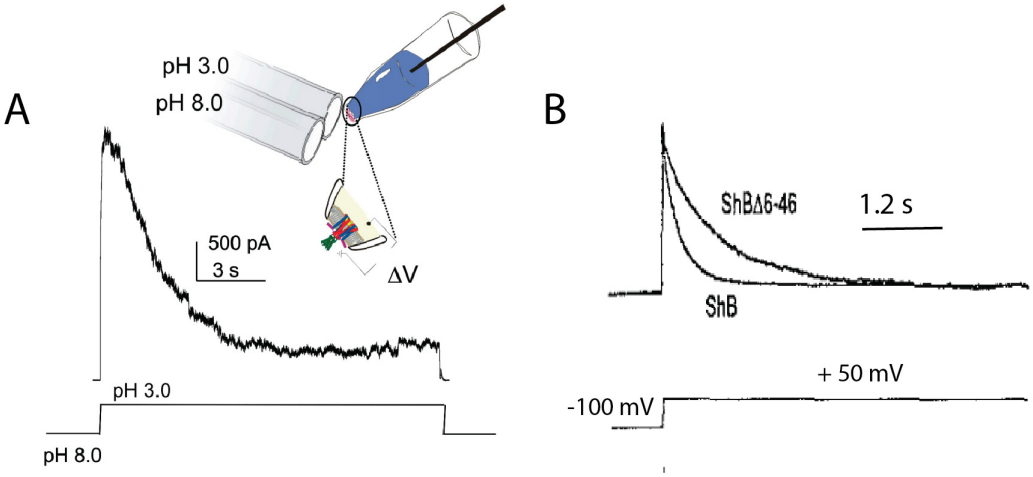

Figure 2.3 Inactivation of potassium channels. (A) The macroscopic current of KcsA in the patch-clamp measurement. KcsA is a pH gated potassium channel. After the channel is activated by dropping pH from pH 8.0 to pH 3.0, the channel inactivates and the current decreases gradually. (B) The macroscopic current of Shaker in patch-clamp. Shaker is a voltage-gated potassium channel. The channel is activated by switching the voltage from -100mV to 50mV. The Shaker has two inactivation processes, as shown the fast-decay current for the N-type inactivation and the slow-decay current for the C-type inactivation after the residues 6-46 are deleted. The figures are adapted from reference 67 and 72.[69,72]

Numerous studies using molecular biology, electrophysiology, crystallography, EPR, NMR, molecular simulation, ITC etc. have focused on studying the mechanism of C-type inactivation.[48,68,77–87] A consensus appears that the inactivation process is mainly related to the selectivity filter. This conclusion was based on several facts: firstly, many mutations around the selectivity filter modulate C-type inactivation process;[88,89] secondly, the concentration of permeating ion and type of permeating ion, such as as Rb^+ also strongly affect the inactivation process;[90] thirdly, many channels, after inactivation, show different ion selectivity.[71] Thus, the selectivity filter is also referred as the inactivation gate. However, much debate still exists surrounding the molecular details of the conformational changes at the selectivity filter to lead to inactivation, and various hypotheses have been proposed based on different experimental results.

Here we review three main hypotheses surrounding the mechanism of C-type inactivation. The first two hypotheses are mainly discussed in the context of KcsA, even though some effects are shared with voltage-gated channels. The last hypothesis is mainly discussed in the context of voltage-gated channels. In the following chapters, we will provide detailed descriptions of our experimental efforts towards elucidation of the inactivation mechanism.

2.2.3.1 Activation-coupled Inactivation Hypothesis

In the activation-coupled inactivation hypothesis, the inactivation process involves both the selectivity filter and the activation gate.[70] The opening of the activation gate is dual-functional: it not only allows the ions to enter the channel for conducting, but also leads to a deformation at the selectivity filter via an allosteric coupling. In KcsA, activation and channel opening via protonation occurs on a millisecond timescale, but the inactivation process has a dynamics on the timescale of seconds; therefore, ions can be permeated through the membrane in a controlled fashion. [69]

This hypothesis can explain the macroscopic electrophysiological study in great detail. When the channel is in the deactivated or resting state, i.e. when the activation gate is closed and the selectivity filter is in the conducting form, there is no current. After the channel is activated by stimuli, such as a pH change for KcsA, the activation gate is opened on the millisecond-scale and the selectivity filter is still in the conductive conformation, thus there is current going through the membrane. However, the opening of the activation gate allosterically induces the collapsed state of the selectivity filter. Therefore, the selectivity filter enters the collapsed conformation on a seconds timescale. The current drops accordingly until it reaches a low-conducting plateau. (Fig. 2.4)

The first question regarding this hypothesis is: what is the non-conducting form of the selectivity filter? MacKinnon and coworkers published two crystal structures of KcsA that show two conformations of the selectivity filter: the conductive form and the collapsed form. They were crystalized in a high (200mM) and low (3 mM) potassium concentration buffer, respectively, at neutral pH.[51] (Fig. 2.2). Even though the collapsed conformation was not crystalized in inactivating conditions, it is hypothesized to be the non-conducting conformation in the inactivation process.

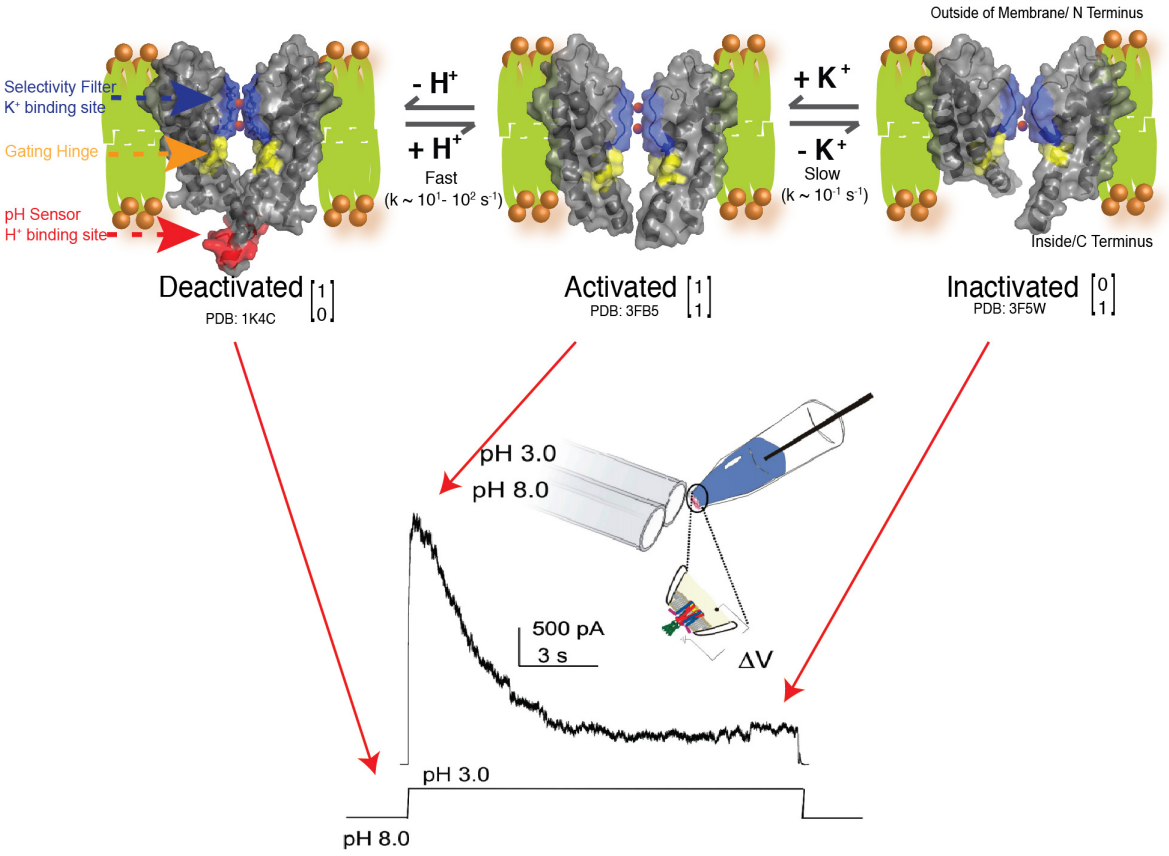

Figure 2.4. The activation-coupled inactivation mechanism of the C-type inactivation shown in KcsA. At pH 8.0, the channel is in the deactivated state and the activation gate is closed and the selectivity filter is the conductive conformation. After pH is dropped to pH 3.0, the channel is in the activated state and both the activation gate and the selectivity filter are in the open conformation, hence potassium ions flow through the channel. The opening of the pH gate is coupled to the selectivity filter and biases the collapsed conformation. Therefore, the current decreases gradually until it reaches a plateau with minimal conducting.

Many experimental studies support this assumption, showing that perturbations causing less inactivation stabilize the conductive structure. Electrophysiology studies show that the kinetics of inactivation is dependent on permeant ions; a high K^+ concentration slows the inactivation rate.[91] Much evidence shows that a high K^+ concentration stabilizes the conductive conformation.[51,92] Other permeant ions, like Rb^+ also decelerate the inactivation; they are hypothesized to prevent the selectivity filter from collapsing by a longer residence time in the selectivity filter due to their slightly larger radius, which is

known as ‘a foot at the door’ mechanism.[71] Cordero-Morales et al showed that disruption of the hydrogen-bonding network between residues in the selectivity filter and its adjacent pore helix by mutating the E71 residue to alanine abolished the inactivation.[89] (Fig. 2.2) Crystallographic studies showed that the collapsed structure of the E71A mutant was not observed. NMR potassium affinity measurement by Bhate et al revealed that E71A stays in a conductive conformation at low pH condition with low potassium concentration, further confirming that the collapsed conformation observed in the WT channel is significantly destabilized in E71A.[93]

In this thesis, we prepare WT-KcsA samples in various limiting conditions, i.e. at pH 3.5 and 7.5 with low and saturated [K^+].[92] Experimental results showed that two sets of chemical shifts existed for the selectivity filter, in accordance with the two conformations seen in the crystal structures. Interestingly, we discovered that the spectra of the selectivity filter displayed in the sample prepared in an inactivation condition (pH 3.5 and low [K^+]) superpose well with the spectra of the sample prepared at neutral pH and low [K^+], implying that the collapsed and K^+-depleted structure may be a good model for the inactivated state.

The second question regarding this hypothesis is how we can know that the two gates are connected. The selectivity filter is located at the extracellular side of the membrane, while the activation gate locates at the intracellular side. The distance between these two gates are about 30Å. Such long distance communication is quite ubiquitous in biology and referred as ‘allosteric coupling’. [94]

Several strategies have been used in order to answer the proposed question. In the first strategy, one of the gates can be specifically perturbed, and the response in the other gate is monitored. Several studies have measured the potassium affinity at the selectivity filter as a function of pH to test the allostery. Shimada et al measured potassium affinity for KcsA embedded in detergent micelle at pH 3.2 and pH 6.6, showing a 10-fold decrease in affinity at pH 3.2.[68] In this thesis, we conduct a similar measurement for KcsA prepared in lipid bilayer at pH 3.5 and pH 7.5, discovering that proton binding at the pH sensors caused more than three orders of magnitude change in potassium affinity.[92] The reduced potassium affinity after the pH gate activation can well explain the decreasing current during inactivation since potassium binding at the selectivity filter is required for ion conducting. The discrepancy in the coupling strength between solution NMR and Solid State NMR (SSNMR) could be due to the

experimental conditions: in solution NMR detergent micelles were used and the measurement was done on a C-terminus truncated KcsA at relatively high temperature (i.e. 45°C), but in solid state NMR liposomes were used and the experimental temperature was done on a full-length KcsA at around 0°C.[68,92] It was also suggested that in the detergent micelles the pH gate of C-terminus truncated KcsA tends to be in an open conformation at pH 7, rendering a smaller coupling energy between the pH gate and the selectivity filter.[95]

In a similar vein, SSNMR studies have indicated that the pKa of the proton binding residue at the activation gate is dependent on the conformation of the selectivity filter. Ader et al showed that the relative protonation of E118/120 was influenced by both pH and ambient [K^+].[83] Wylie et al discovered that the collapsed selectivity filter induced by low ambient [K^+] biased an open activated gate and shifted the pKa of E118/E120 higher than 7.5. [96] Tilegenova et al monitored the pH gate opening at various conditions by EPR studies and showed a 1 pH unit pKa shift between the transition from deactivated to inactivated state and the reverse transition, indicating that different intermediate states are involved in these two processes and the proton binding and associated pH gate opening is coupled with the potassium binding.[86] When perturbations that inhibit the C-type inactivation were introduced, such as mutating E71 to alanine, substituting Cs^+ or Rb^+ for K^+, the observed pKa shift was diminished, confirming that such a coupling is closely related to inactivation.

The discovery of a series of KcsA crystal structures with open activation gates provides further direct support to the coupling mechanism.[53,70] In these crystals, the pH gate is mutated to be open in order to mimic the activated and inactivated state. Various extents of opening at the activation gate were observed and they are correlated to conformation and ion binding at the selectivity filter: large opening at the activation gate leads to a more collapsed conformation and less ion binding at the selectivity filter. (Fig. 2.5).

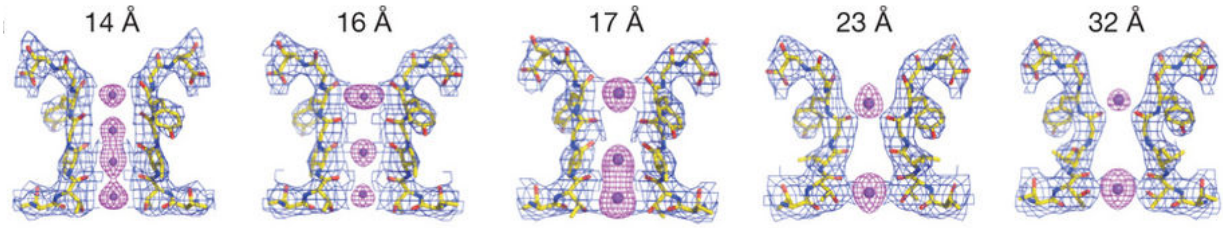

Figure 2.5. Crystal structures show that the extent of opening at the pH gate is coupled to the conformation and ion binding at the selectivity filter.

In the second strategy, residues between these two gates are perturbed to see if the coupling is attenuated or abolished. Several residues are revealed to be vital for the coupling between these two gates, many of which are located between the selectivity filter and the activation gate. For example, F103's bulky aromatic side chain displays two torsion angles, correlating to the conductive and collapsed conformation. Mutation to a smaller sidechain residue such as alanine greatly reduces the C-type inactivation; in mutations to other residues with bulky sidechain such as Tyr, C-type inactivation is not affected.[53] It is hypothesized that the bulky sidechain in F103 interacts with I100 and T74 to mediate the coupling from activation gate to the selectivity filter. In this thesis, we explore this hypothesis and find that protonation at the pH gate for an F103A mutant has a much weaker effect on potassium affinity at the selectivity filter than in the WT-KcsA (2uM to 150uM for F103A comparing to 4uM to 14mM for WT-KcsA), suggesting that the coupling strength was perturbed by the mutant. Functional tests on I100 by electrophysiology also show that mutating I100 to alanine weakens the inactivation.[84] In this thesis, we further tease apart this coupling network by NMR thermodynamic measurements and single channel recordings showing that removal of T74 Cg side chain by mutating to serine greatly abolishes the pH effect on the potassium affinity and by extrapolation the inactivation of this mutant. These mutations are distant from the pH gate and the selectivity filter; their effects on the coupling strength and inactivation behaviors confirm that inactivation involves coupling between the pH gate and the selectivity filter and clarify the participants in this coupling.

However, this hypothesis was challenged by Valiyaveetil and coworkers based on experimental results on semi-synthesized KcsA channels.[48] They introduced an unnatural amino acid D-alanine at the selectivity filter to replace a glycine at Gly77. This substitution restricts the rotation of Gly77-Val76 peptide

bond and prevents the selectivity filter entering the collapsed state. Its crystal structure was collected at 1mM [K^+] and the selectivity filter stays in the conductive form, in contract to a collapsed structure for WT at a similar condition (i.e. 3mM [K^+]). However, this structural modification did not cause changes the inactivation behavior of KcsA, challenging the hypothesis that the collapsed conformation represents the selectivity filter in the C-type inactivation. These studies were also performed on the voltage-gated KvAP channel and similar results were achieved.

A recent computational study by Li et al raised questions about this study, reporting that KcsAD-Ala77 channel could adopt an asymmetrical constricted-like nonconductive conformation in a molecular dynamics simulation. [97] We reason that the chemical substitution or difference in crystallization conditions might account for the fact that the collapsed structure was not seen at 1mM [K^+] for KcsAD-Ala77 as they shifted K^+ K_d to a tighter binding relative to WT. Our NMR measurement has indicated that the potassium affinity is very tight, around 4-10 uM in lipid bilayers at neutral pH, much lower than the 1 mM concentration. Importantly, these crystal structures were acquired with a closed activation gate; whether the selectivity filter adopts a conductive conformation or not after activation is unknown.

2.2.3.2 Ion Binding Hypothesis

Valiyaveetil and coworkers proposed another hypothesis to explain C-type inactivation based on the observation on several semi-synthesized KcsA channels in which amide-to-ester substitution in the protein backbone at certain sites of the selectivity filter was introduced.[98] In this hypothesis, the inactivation is linked to ion occupancy at the specific sites in the selectivity filter (Fig. 2.6)

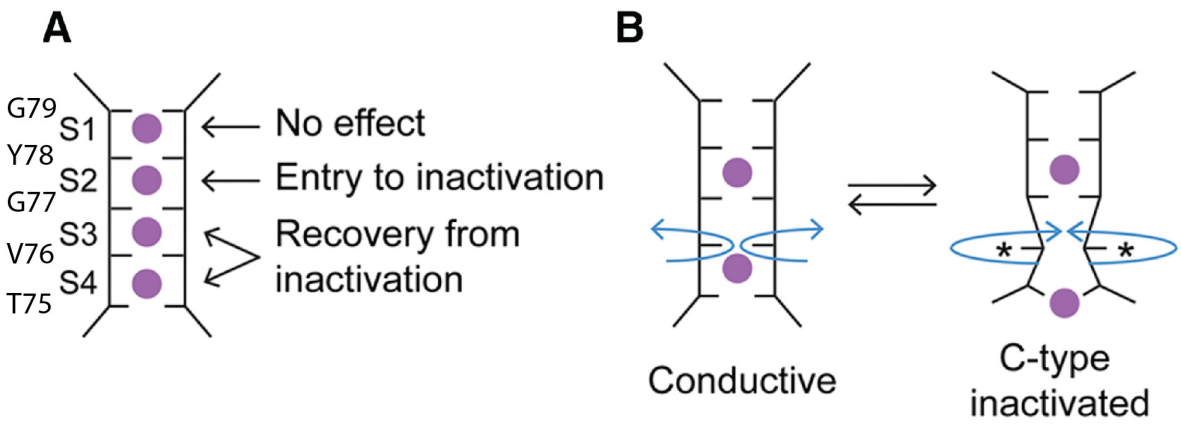

Figure 2.6. The scheme proposed by Valiyaveetil et al to explain the inaction process. (A) Various sites at the selectivity filter have been shown important to inactivation or recovery from inactivation. (B) In the working hypothesis they proposed, the ion binding at the S2 site leads to the deformation at the S3 site, blocking the ion flow and causing inactivation. The figure is taken from reference 99.[99]

When the substitution sites are S2 (i.e. Y78) S3 (i.e. G77), they discovered two events: first, these substitutions slow the inactivation process; second, crystal structures of these two semi-synthesized KcsA show little ion occupancy at the S2 site.[98] Similar phenomena have been observed for Rb^+ permeating through WT-KcsA channel: Rb^+ slows down the inactivation rate and minimal ion density is in the S2 site in the crystal structure.[100] However, when the substitution site is S1 (i.e. G79), the channel still inactivates and in the crystal structure, ion occupancy at S1 is considerably reduced, but ion occupancies at S2-S4 are similar to that in WT. They further introduced perturbations to ion binding at the S3 and S4 sites by applying amide-to-ester substitution at V76 and T75G mutation respectively.[99] These perturbations do not affect the inactivation rate, but strongly prolong the recovery process. Based on this evidence, the authors proposed that the inactivation is caused by local structural distortions at V76 position, which happens when S2 is bound with an ion; this distortion increases the barrier for ions to conduct. Meanwhile, the amide-to-ester substitution will not prevent the selectivity filter entering the collapsed conformation. The reduction of inactivation by amide-to-ester substitution, on the other hand, disproves the hypothesis that inactivation is caused by the constricted selectivity filter.

The application of semisynthesized protein to perturb ion binding at a specific location greatly expands our understanding of the importance role of ion binding on inactivation. It highlights the

importance of ion occupancy in the channel rather than peptide conformation per se. One of the big concerns for these studies is that the introduction of amide-to-ester substitution also causes distortion on the hydrogen-bonding network behind the selectivity filter, which involves the buried water and backbone amide. Valiyaveeti *et al* reasoned that it is not important, as those substitutions do not cause any appreciable structural change in the selectivity filter or the surrounding residues and the critical E71–D80 interaction is maintained. Also the S2 and S3 ester substitutions disrupt different hydrogen bonds, but have similar effects on ion occupancy and inactivation.

However, another MD simulation conducted by Li et al shows that amide-to-ester substituted proteins do transmit from the conductive conformation to the collapsed conformation.[97] The G77ester, due to the lack of amide to form hydrogen bonding with the buried water, destabilizes the stability of the constricted conformation. This would also prevent the inactivation. The reduction of ion occupancy could be simply caused by ester substitution, as shown in other sites, and it is irrelevant to inactivation. The absence of Rb^+ at the S2 site can be explained by the finding that S2 site is the most selective site for K^+ in the selectivity filter.[101] The reduction of inactivation is hypothesized to be caused by the long residence of ions in the selectivity filter, preventing the structure from becoming constricted, which is termed as " the foot at the door". Meanwhile, a recent Isothermal Titration Calorimetry (ITC) measurement shows that Rb^+ binds to KcsA at pH 4 with a higher affinity than K^+ ions, indicating that Rb^+ could stabilize the conductive conformation at the activated condition.[95]

2.3.3.3 Ion dilation hypothesis

The ion dilation hypothesis was proposed by Toshinori Hoshi and Clay Armstrong in the study of voltage-activated potassium channels.[35] (Fig. 2.7) In the hypothesis, C-type inactivation is caused by expansion of the outermost site of the selectivity filter from the perfect oxygen cage structure, reducing its selectivity for binding K^+. Partially hydrated sodium ions could likely bind to the site with high affinities, and prevent K^+ ions from entering the selectivity filter and conducting. With bound K^+ diffusing out of the selectivity filter, the selectivity filter would further dilate from the top to the bottom, allowing permeation of partially dehydrated Na^+. This explains the increasing conductivity for Na^+ in the C-type inactivation state.[31] One strong support for this hypothesis is the antagonistic effect of high $[K^+]$ on C-type inactivation, which is also used to support the activation coupled inactivation hypothesis as discussed above. It is a

challenging task to pinpoint the effects of K^+ on the stabilization of the conductive conformation of the selectivity filter or the prevention of channel dilation, or both, which make it difficult to distinguish the two hypotheses.

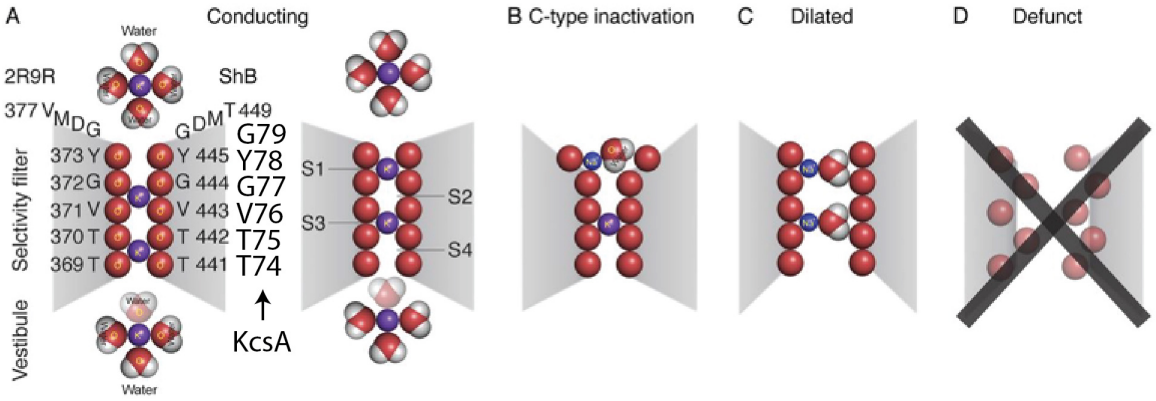

Figure 2.7. The ion dilation hypothesis proposed by Armstrong et al to explain the inaction process in the Shaker channel. The C-type inactivation starts with a local deformation at the mouth (extracellular side) of the selectivity filter, which blocks the ion flow. After the potassium ions are depleted from the selectivity filter, the channel dilates and allows partially dehydrated sodium ion to flow through the channel. The channel eventually enters a defunct state, in which the selectivity filter is in a collapsed conformation. The figure is taken from reference 35.[35]

Mutation of residue T449 (Y82 in KcsA) in Shaker channels, located at the outer mouth, has shown a significant effect on inactivation. The interaction between T449 and selectivity filter residue Y445 (Y78 in KcsA) and pore helix residue W434 (W67 in KcsA) in Shaker is assumed to be critical for channel dilation. When mutations cause more space for Y445 to rotate and predispose its carbonyl to recede from the pore axis, they lead to channel dilation and increase C-type inactivation. Such mutations are W434F, *T449 (A, C, K, E, S)*.[35] Mutation on KcsA at equivalent site (Y82A) also shows enhanced inactivation.[102] In contract, when mutations contain bulky side chain and restrict the motion of Y445, the inactivation is abolished. Such mutations are T449 (Y V I).[35] However, there is little direct support to such a hypothesis; the mutations could induce global structural changes in the selectivity filter. For example, recently a high-resolution Y82A KcsA crystal structure shows a constricted conformation at the selectivity filter, similar to the collapsed conformation (i.e. 1K4C) acquired in the presence of low [K^+].[102] Interestingly, contrary to

the dilation hypothesis on inactivation, Heer et al show that certain extent of channel dilation is actually necessary for the channel to efficiently conduct [K^+].[103]

It is known that the outer mouth site is critical in the C-type inactivation.(Figure 2.2) Yellen et al introduced a mutation to a cysteine residue at the T449 site in Shaker channel, showing that Cd^{2+} binding significantly enhanced the inactivation process in a way that Cd^{2+} stabilizes the inactivation conformation since its affinity is tighter in a four-order magnitude in the inactivated state than in the deactivated state.[104] They further introduced cysteine mutation at other outer mouth sites and measured state-dependent changes in accessibility to chemical modification; the modification rates were significantly enhanced in the inactivation state, indicating that conformational change at the outer mouth happens in the C-type inactivation, rendering those residues accessible to modification reagents.[105] Similar results of Cd^{2+} binding experiments were achieved at the KcsA channel by introducing cysteine mutation at equivalent site (Y82C) by Perozo et al.[106] By introducing cysteine mutations at various sites, such as a signal site, double mutations at adjacent and diagonal sites in the tetramer in KcsA and Shaker channel, they demonstrated Cd^{2+} affects inactivation mainly by cross-linking cysteine in the adjacent sites, implying that the outer mouth loops were constricted to allow Cd^{2+} to bind during inactivation. EPR measurements on radical distances at Y82 sites confirmed that the diagonal distance is shorten from 12 Å to 8 Å after inactivation. These results suggest a closer distance between monomers, instead of dilation. However, comparison of crystal structures between the conductive conformation (1K4C) and the collapsed conformations (1K4C or 3F5W) does not show such a dramatic conformation changes in the outer vestibule. This discrepancy is assumed to be caused by the difference in the dynamics behaviors of the outer vestibule. [107]

By now, we have introduced three hypotheses. The major disputed point that distinguishes these hypotheses is the conformation of the selectivity filter during the C-type inactivation. In the first hypothesis, the collapsed structure, seen in the crystal structure, is regarded as the inactivation structure; while in the other two hypotheses, conformational change at different local sites in the selectivity filter is suggested and the collapsed state is treated as a ‘deeply inactivated state’ or ‘defunct’ state.[35,48] For the functional perspective, the requirement on the conformation of the selectivity filter for K^+ conduction indicates that the conformational change in all three hypotheses could prevent K^+ from conducting.

Because many factors such as K^+ and various mutations can cause coupled changes in the structure and energetics, it is extremely difficult to isolate one variable to test these hypotheses and distinguish one hypothesis from the other.

From the kinetics perspective, the conformation changes in the last two hypotheses contain two processes: first is a small distortion on the selectivity filter, and then is the overall structural collapse. By now, no crystal structure has been discovered corresponding to the initial step, which indicates that the structure might be not thermodynamically stable. Current traces in patch-clamp experiments indicate that C-type inactivation is a seconds-timescale single-exponential decay process for KcsA and many other potassium channels. The recovery from inactivation is even slower, also in a seconds-timescale. From energetics point view, in the later two hypothesis, the inactivation kinetics should be significantly faster than that in the activation-coupled inactivation hypothesis since the energetic barrier for the global structural change hypothesized in the first hypothesis should be greatly larger than that for the local structural change in the later two hypothesis. The fact that inactivation is a seconds-timescale process seems to favor the first hypothesis as the main inactivation process, while the local structural change, as suggested in the later two hypothesis, might exist as an initial process in inactivation with a faster dynamics. This would fit to the features displayed in the current traces in single channel recording experiments, where the channels are in a flicker mode with current constantly on and off before entering a long non-conducting state.[81] However more rigorous measurements on the protein dynamics are needed to further validate such a hypothesis.

2.3.4 Importance of lipid on potassium channel and inactivation

The importance of lipid on membrane protein in term of stability, structure and functions has been discovered in numerous studies.[108–110] The mechanisms of such effects have been generally viewed from two aspects. In the first aspects, lipid affects membrane protein function through a general physical effect; this includes effects on membrane fluidity, curvature and lateral pressure, hydrophobic matching between lipid and protein etc. In the second aspect, lipid can specifically or nonspecifically bind to proteins (i.e. anaular and non-anaular sites) to stabilize certain conformations or induce protein oligomerization and affect functions. Tremendous studies and reviews have focused on these effects on various

proteins.[108,111–114] Potassium channels are one of the proteins that are extensively studied in term of protein-lipid interaction. In the voltage gated potassium channel, interactions between the phospholipids and voltage sensing residues such as arginine are crucial for the channel activation.[41,115] Molecules such as cholesterol have been shown to influence the channel's functions. [116–118]

In KcsA channel, anionic lipids have been found co-crystalized with the protein and also identified in SSNMR experiments to bind at grooves between transmembrane helices, i.e. monomer-monomer interface.[51,119] Residue R64 and R89 have been identified as the main residues to interact with the negative charge lipid head. There interactions have been shown critical not only to stablize the tetramer feature of the channel but also possibly affect the channel inactivation and open probability.[120] AG Lee et al shows that by increasing the anionic lipid (such as PS, PA) content of the membrane, the channel open probability is greatly improved.[121] They hypothesize that the anionic lipids that are bound to the protein helps stabilize the conductive conformation of the selectivity filter and inhibit the inactivation process. Similar effects can be achieved by introducing cardiolipin, which is more negatively chareged, into the lipid bilayer. [122]

By contrast, studies by Molia et al indicate that anionic lipid bound at annular site could cause a conformational change at the back of the selectivity filter, facilitating the W67-E71-D80 hydrogen-bond network, which is known to cause the channel prone to inactivate.[123] Their reasoning is that when anionic lipids are bound, they interact with the R89 and R64, which leaves W67 D80 to form hydrogen bond with E71; in contract, when there is no lipid bound, the proteins tend to dock each other to from a cluster and R89, R64 would, instead, form salt bridges with D80 W67 residues, which weakens the W67-E71-D80 hydrogen-bond network and inhibit channel inactivation. By mutating the arginine residues to alanine, it increased the portion of protein in a cluster form and also the channel open probabilities as shown in the single channel recording experiments.[124] Such a controversy in the literature may come from the experimental setup and conditions and data analysis in different studies, which, clearly, requires much effort to be cleared out.

In a recent elegant experiment, Iwamoto et al prepared the lipid bilayer in an asymmetric fashion so that they could distinguish the effects of lipids in inner and outer membrane on the channels function.[125] They did the most of experiments on the E71A mutants, which has a high open probability;

this provides great experimental convenience for current recording and data analysis. By comparing the channel open probabilities in various situations such as putting negative or positive charged lipid in the inner or outer membrane, they concluded that negative charges lipid in the inner membrane can interact nonspecifically with the positive charges in the N-terminal helix (residues 1-25) after the channel is activated and stabilized the activated pH-gate conformation, which increases the channel open probability in the inactivationless E71A channel. They did not discover any influence of lipid in the outer membrane on channel function, which seems contradictory to the studies we discussed above. However, since the W68-E71-D80 hydrogen-bond network is impaired in E71A and the non-anular lipid seems affect channel through this network, it is probably reasonable to not observe an effect of lipids in outer membrane on channel function. We propose a hypothesis here that in WT channel, the stabilization effect on the open pH-gate conformation by negatively charged lipids could allosterically destabilize the selectivity filter and thus enhance the inactivation in WT and prolong the recovery of the channel from the inactivated state. Such a hypothesis is validated by the limited experiments they did on the WT, indicating that adding negatively charged lipid in the inner membrane actually slightly decreased the channel open probability for WT.

Fewer studies of the influence on the channel in the physical effect are documented or investigated since they are generally more difficult to study and quantify. Rusinova et al showed that the phospholipid acyl chain length could perturb KcsA function primarily by changes in bilayer thickness rather than changes in the local lipid composition around channels.[126] We hypothesize that the allosteric coupling strength could also be modulated by the physical properties of the membrane; thus the inactivation process is affected.

2.3.5 Is KcsA a good model for potassium channel Inactivation study?

A large portion of the research on potassium channels has been done on KcsA due to the availability of crystal structures in various conditions as well as the ease of sample preparation and functional characterization. KcsA has proven to be a good model to study the permeation problem and share a general scheme on how the channel is activated; however, is KcsA also a good model for studying inactivation in potassium channels? The answer to this question is quite complicated.

From the functional perspective, many potassium channels show diversity in the inactivation dynamics. For example, hERG channels show a faster inactivation process compared to that in Shaker or KcsA.[82] Some of the potassium channels do not inactivate as much as KcsA channels. One example is the calcium-gated MthK channel, which shows little inactivation in the lipid bilayer.[41] Therefore, we expect diversity in the mechanisms of inactivation in various potassium channels. Such diversity is probably rooted in the protein sequence. As shown in the sequence alignments (Figure 2.1), many critical residues for inactivation on KcsA are not very conserved in other channels, especially for the critical E71 residue. Furthermore, due to the presence of the voltage sensor in voltage-gated channels, which is coupled to the selectivity filter in the C-type inactivation process, the voltage dependent feature of C-type in these channels is likely to be different from that in KcsA, even though KcsA does show a voltage dependent inactivation behavior, which is mainly attributed to the voltage modulated strength of the E71-D80 hydrogen bonding interaction.[85]

However, evidence from various studies shows that the molecular machinery identified in KcsA provides valuable information for other potassium channels on inactivation. Even though many of the critical residues in inactivation in KcsA are not conserved, mutations introduced at the according positions at other channels could alter the channel behavior. For example, Kv1.2 in Shaker K^+ channel family shows little C-type inactivation after the N-type inactivation is removed, and it has a valine in the position equivalent to the E71 in KcsA. Mutation of E71 to valine in KcsA significantly reduces the inactivation, which is assumed to break the E71-D80-W67 interaction for inactivation. By introducing V370E mutation in Kv1.2, which can interact with D379 (D80 in KcsA), the C-type inactivation behavior was greatly enhanced in the mutant channel.[70] Similarly, in the Shaker channel, by mutating the I470 (F103 in KcsA) to residues with smaller side chains such as alanine and cysteine, the C-type inactivation is greatly reduced, which mirrors the effect of mutating F103 to smaller side chain residues in KcsA.[53] Other examples can be found in the positions such as E51, D80, and Y82 etc.[35,102,127] We hypothesize that even though residues for C-type inactivation in the potassium channel have been constantly evolving and modulated to cope with the evolutionary pressure, the very basic machineries are still shared in many of the potassium channel, which makes KcsA a valuable model for studying inactivation for other potassium channels.

2.3 References

1. Zimmerberg, J. & Kozlov, M. M. How proteins produce cellular membrane curvature. *Nat. Rev. Mol. Cell Biol.* **7,** 9–19 (2006).
2. Lombard, J. Once upon a time the cell membranes: 175 years of cell boundary research. *Biol. Direct* **9,** 32 (2014).
3. McDermott, A. Structure and dynamics of membrane proteins by magic angle spinning solid-state NMR. *Annu. Rev. Biophys.* **38,** 385–403 (2009).
4. Daley, D. O. *et al.* Global Topology Analysis of the Escherichia coli Inner Membrane Proteome. *Science (80-.).* **308,** 1321–1323 (2005).
5. Wallin, E. & Heijne, G. Von. Genome-wide analysis of integral membrane proteins from eubacterial, archaean, and eukaryotic organisms. *Protein Sci.* **7,** 1029–1038 (2008).
6. Früh, V., IJzerman, A. P. & Siegal, G. How to Catch a Membrane Protein in Action: A Review of Functional Membrane Protein Immobilization Strategies and Their Applications. *Chem. Rev.* **111,** 640–656 (2011).
7. MacGurn, J. A., Hsu, P.-C. & Emr, S. D. Ubiquitin and Membrane Protein Turnover: From Cradle to Grave. *Annu. Rev. Biochem.* **81,** 231–259 (2012).
8. Tautermann, C. S. GPCR structures in drug design, emerging opportunities with new structures. *Bioorg. Med. Chem. Lett.* **24,** 4073–4079 (2014).
9. Lappano, R. & Maggiolini, M. G protein-coupled receptors: novel targets for drug discovery in cancer. *Nat. Rev. Drug Discov.* **10,** 47–60 (2011).
10. Palsdottir, H. & Hunte, C. Lipids in membrane protein structures. *Biochim. Biophys. Acta* **1666,** 2–18 (2004).
11. Hong, M. & Su, Y. Structure and dynamics of cationic membrane peptides and proteins: insights from solid-state NMR. *Protein Sci.* **20,** 641–55 (2011).
12. Cournia, Z. *et al.* Membrane Protein Structure, Function, and Dynamics: a Perspective from Experiments and Theory. *J. Membr. Biol.* **248,** 611–40 (2015).
13. Hong, M., Zhang, Y. & Hu, F. Membrane Protein Structure and Dynamics from NMR Spectroscopy. *Annu. Rev. Phys. Chem.* **63,** 1–24 (2012).

14. http://blanco.biomol.uci.edu/mpstruc/.

15. Chipot, C. *et al.* Perturbations of Native Membrane Protein Structure in Alkyl Phosphocholine Detergents: A Critical Assessment of NMR and Biophysical Studies. doi:10.1021/acs.chemrev.7b00570

16. Frotscher, E. *et al.* A fluorinated detergent for membrane-protein applications. *Angew. Chem. Int. Ed. Engl.* **54,** 5069–73 (2015).

17. Gayen, S., Li, Q. & Kang, C. Solution NMR Study of the Transmembrane Domain of Single-Span Membrane Proteins: Opportunities and Strategies. *Curr. Protein Pept. Sci.* **13,** 585–600 (2012).

18. Hu, F., Luo, W. & Hong, M. Mechanisms of proton conduction and gating in influenza M2 proton channels from solid-state NMR. *Science* **330,** 505–8 (2010).

19. Valiyaveetil, F. I., MacKinnon, R. & Muir, T. W. Semisynthesis and Folding of the Potassium Channel KcsA. *J. Am. Chem. Soc.* **124,** 9113–9120 (2002).

20. Gouaux, E. Single potassium ion seeks open channel for transmembrane travels: tales from the KcsA structure. *Structure* **6,** 1221–1226 (1998).

21. Holden, M. A., Jayasinghe, L., Daltrop, O., Mason, A. & Bayley, H. Direct transfer of membrane proteins from bacteria to planar bilayers for rapid screening by single-channel recording. *Nat. Chem. Biol.* **2,** 314–8 (2006).

22. Fernández, C., Hilty, C., Wider, G. & Wüthrich, K. Lipid-protein interactions in DHPC micelles containing the integral membrane protein OmpX investigated by NMR spectroscopy. *Proc. Natl. Acad. Sci. U. S. A.* **99,** 13533–7 (2002).

23. Kuehlbrandt, W. Cryo-EM Enters a New Era. *Elife* **3,** e01963 (2014).

24. Liao, M., Cao, E., Julius, D. & Cheng, Y. Structure of the TRPV1 Ion Channel Determined by Electron Cryo-Microscopy. *Nature* **504,** 107 (2013).

25. Wong, W. *et al.* Cryo-EM structure of the Plasmodium falciparum 80S ribosome bound to the anti-protozoan drug emetine. *Elife* **3,** e01963 (2014).

26. McDermott, A. E. Structural and dynamic studies of proteins by solid-state NMR spectroscopy: rapid movement forward. *Curr. Opin. Struct. Biol.* **14,** 554–561 (2004).

27. Hong, M. & Schmidt-Rohr, K. Magic-Angle-Spinning NMR Techniques for Measuring Long-Range

Distances in Biological Macromolecules. *Acc. Chem. Res.* **46,** 2154 (2013).

28. May, L. T., Leach, K., Sexton, P. M. & Christopoulos, A. Allosteric modulation of G protein-coupled receptors. *Annu. Rev. Pharmacol. Toxicol.* **47,** 1–51 (2007).
29. Tsai, C.-J., Del Sol, A. & Nussinov, R. Protein allostery, signal transmission and dynamics: a classification scheme of allosteric mechanisms. *Mol. Biosyst.* **5,** 207–16 (2009).
30. Yellen, G. The voltage-gated potassium channels and their relatives. *Nature* **419,** 35–42 (2002).
31. McCoy, J. G. & Nimigean, C. M. Structural correlates of selectivity and inactivation in potassium channels. *Biochim. Biophys. Acta* **1818,** 272–85 (2012).
32. LeMasurier, M., Heginbotham, L. & Miller, C. KcsA: it's a potassium channel. *J. Gen. Physiol.* **118,** 303–14 (2001).
33. Jentsch, T. J. Neuronal KCNQ potassium channels: physiology and role in disease. *Nat. Rev. Neurosci.* **1,** 21–30 (2000).
34. HODGKIN, A. L. & HUXLEY, A. F. A quantitative description of membrane current and its application to conduction and excitation in nerve. *J. Physiol.* **117,** 500–44 (1952).
35. Hoshi, T. & Armstrong, C. M. C-type inactivation of voltage-gated K+ channels: pore constriction or dilation? *J. Gen. Physiol.* **141,** 151–60 (2013).
36. Shieh, C.-C., Coghlan, M., Sullivan, J. P. & Gopalakrishnan, M. Potassium Channels: Molecular Defects, Diseases, and Therapeutic Opportunities. *Pharmacol. Rev.* **52,** 557–594 (2000).
37. Parekh, P. K. *et al.* Antimanic Efficacy of a Novel Kv3 Potassium Channel Modulator. *Neuropsychopharmacology* **43,** 435–444 (2018).
38. Heurteaux, C. *et al.* Deletion of the background potassium channel TREK-1 results in a depression-resistant phenotype. *Nat. Neurosci.* **9,** 1134–1141 (2006).
39. Tateishi-Karimata, H., Kawauchi, K. & Sugimoto, N. Destabilization of DNA G-Quadruplexes by Chemical Environment Changes during Tumor Progression Facilitates Transcription. *J. Am. Chem. Soc.* **140,** 642–651 (2018).
40. Hoshi, T., Zagotta, W. & Aldrich, R. Biophysical and molecular mechanisms of Shaker potassium channel inactivation. *Science (80-.).* **250,** (1990).
41. Thomson, A. S. & Rothberg, B. S. Voltage-dependent inactivation gating at the selectivity filter of

the MthK K+ channel. *J. Gen. Physiol.* **136,** 569–79 (2010).

42. Chakrapani, S., Cordero-Morales, J. F. & Perozo, E. A quantitative description of KcsA gating II: single-channel currents. *J Gen Physiol.* **130,** 479–496 (2007).

43. Bhate, M. P. & McDermott, A. E. Protonation state of E71 in KcsA and its role for channel collapse and inactivation. *Proc Natl Acad Sci U S A* **109,** 15265–15270 (2012).

44. MacKinnon, R. Potassium channels. **555 SRC-,** 62–65 (2003).

45. LeMasurier, M., Heginbotham, L. & Miller, C. KcsA: it's a potassium channel. *J Gen Physiol* **118,** 303–314 (2001).

46. Gao, L., Mi, X., Paajanen, V., Wang, K. & Fan, Z. Activation-coupled inactivation in the bacterial potassium channel KcsA. *Proc Natl Acad Sci U S A* **102,** 17630–17635 (2005).

47. Hoshi, T. & Armstrong, C. M. C-type inactivation of voltage-gated K+ channels: pore constriction or dilation? J. Gen. Physiol.**,** 151–160 (2013).

48. Devaraneni, P. K. *et al.* Semisynthetic K+ channels show that the constricted conformation of the selectivity filter is not the C-type inactivated state. *Proc. Natl. Acad. Sci. U. S. A.* **110,** 15698–703 (2013).

49. Pan, A. C., Cuello, L. G., Perozo, E. & Roux, B. Thermodynamic coupling between activation and inactivation gating in potassium channels revealed by free energy molecular dynamics simulations. *J. Gen. Physiol.* **138,** 571–80 (2011).

50. Yifrach, O. & MacKinnon, R. Energetics of Pore Opening in a Voltage-Gated K+ Channel. *Cell* **111,** 231 (2002).

51. Zhou, Y., Morais-Cabral, J. H., Kaufman, A. & MacKinnon, R. Chemistry of ion coordination and hydration revealed by a K+ channel-Fab complex at 2.0 A resolution. *Nature* **414,** 43–8 (2001).

52. MacKinnon, R. Potassium channels. *FEBS Lett.* **555,** 62–65 (2003).

53. Cuello, L. G. *et al.* Structural basis for the coupling between activation and inactivation gates in K(+) channels. *Nature* **466,** 272–5 (2010).

54. Doyle, D. A. The Structure of the Potassium Channel: Molecular Basis of K+ Conduction and Selectivity. *Science (80-.).* **280,** 69–77 (1998).

55. Morais-Cabral, J. H., Zhou, Y. & MacKinnon, R. Energetic optimization of ion conduction rate by

the K+ selectivity filter. *Nature* **414,** 37–42 (2001).

56. Noskov, S. Y. & Roux, B. Importance of hydration and dynamics on the selectivity of the KcsA and NaK channels. *J. Gen. Physiol.* **129,** 135–43 (2007).

57. Åqvist, J., Luzhkov, V., Aqvist, J. & Luzhkov, V. Ion permeation mechanism of the potassium channel. *Nature* **404,** 881–4 (2000).

58. Berneche, S. & Roux, B. The ionization state and the conformation of Glu-71 in the KcsA K+ channel. *Biophys. J.* **82,** 772–780 (2002).

59. Sansom, M. S. P. *et al.* Potassium channels: structures, models, simulations. *Biochim. Biophys. Acta - Biomembr.* **1565,** 294–307 (2002).

60. Bezanilla, F., Perozo, E., Papazian, D. & Stefani, E. Molecular basis of gating charge immobilization in Shaker potassium channels. *Science (80-.).* **254,** 679–683 (1991).

61. Ye, S., Li, Y., Chen, L. & Jiang, Y. Crystal structures of a ligand-free MthK gating ring: insights into the ligand gating mechanism of K+ channels. *Cell* **126,** 1161–73 (2006).

62. Gao, L., Mi, X., Paajanen, V., Wang, K. & Fan, Z. Activation-coupled inactivation in the bacterial potassium channel KcsA. *Proc. Natl. Acad. Sci. U. S. A.* **102,** 17630–5 (2005).

63. Shimizu, H. *et al.* Global twisting motion of single molecular KcsA potassium channel upon gating. *Cell* **132,** 67–78 (2008).

64. Liu, Y. S., Sompornpisut, P. & Perozo, E. Structure of the KcsA channel intracellular gate in the open state. *Nat. Struct. Biol.* **8,** 883–7 (2001).

65. Sand, R., Sharmin, N., Morgan, C. & Gallin, W. J. Fine-tuning of voltage sensitivity of the Kv1.2 potassium channel by interhelix loop dynamics. *J. Biol. Chem.* **288,** 9686–95 (2013).

66. Jensen, M. O. *et al.* Mechanism of Voltage Gating in Potassium Channels. *Science (80-.).* **336,** 229–233 (2012).

67. Thompson, A. N., Posson, D. J., Parsa, P. V & Nimigean, C. M. Molecular mechanism of pH sensing in KcsA potassium channels. *Proc. Natl. Acad. Sci. U. S. A.* **105,** 6900–5 (2008).

68. Imai, S., Osawa, M., Takeuchi, K. & Shimada, I. Structural basis underlying the dual gate properties of KcsA. *Proc. Natl. Acad. Sci. U. S. A.* **107,** 6216–21 (2010).

69. Chakrapani, S., Cordero-Morales, J. F. & Perozo, E. A quantitative description of KcsA gating I:

macroscopic currents. *J. Gen. Physiol.* **130,** 465–78 (2007).

70. Cuello, L. G., Jogini, V., Cortes, D. M. & Perozo, E. Structural mechanism of C-type inactivation in K(+) channels. *Nature* **466,** 203–8 (2010).

71. Kurata, H. T. & Fedida, D. A structural interpretation of voltage-gated potassium channel inactivation. *Prog. Biophys. Mol. Biol.* **92,** 185–208 (2006).

72. Hoshi, T., Zagotta, W. N. & Aldrich, R. W. Two types of inactivation in Shaker K+ channels: Effects of alterations in the carboxy-terminal region. *Neuron* **7,** 547–556 (1991).

73. Molina, M. L. *et al.* N-type inactivation of the potassium channel KcsA by the Shaker B "ball" peptide: mapping the inactivating peptide-binding epitope. *J. Biol. Chem.* **283,** 18076–85 (2008).

74. Choi, K. L., Aldrich, R. W. & Yellen, G. Tetraethylammonium blockade distinguishes two inactivation mechanisms in voltage-activated K+ channels. *Proc. Natl. Acad. Sci. U. S. A.* **88,** 5092–5 (1991).

75. Rasmusson, R. L. *et al.* Inactivation of Voltage-Gated Cardiac K+ Channels. *Circ. Res.* **82,** 739–750 (1998).

76. Burgess, D. E. *et al.* High-risk long QT syndrome mutations in the Kv7.1 (KCNQ1) pore disrupt the molecular basis for rapid K(+) permeation. *Biochemistry* **51,** 9076–85 (2012).

77. Maffeo, C., Bhattacharya, S., Yoo, J., Wells, D. & Aksimentiev, A. Modeling and simulation of ion channels. *Chem. Rev.* **112,** 6250–84 (2012).

78. Kim, D. M. *et al.* Conformational heterogeneity in closed and open states of the KcsA potassium channel in lipid bicelles. *J. Gen. Physiol.* **148,** 119–32 (2016).

79. Piasta, K. N., Theobald, D. L. & Miller, C. Potassium-selective block of barium permeation through single KcsA channels. *J. Gen. Physiol.* **138,** 421–36 (2011).

80. Varga, K., Tian, L. & McDermott, A. E. Solid-state NMR study and assignments of the KcsA potassium ion channel of S. lividans. *Biochim. Biophys. Acta* **1774,** 1604–13 (2007).

81. Chakrapani, S., Cordero-Morales, J. F. & Perozo, E. A quantitative description of KcsA gating II: single-channel currents. *J. Gen. Physiol.* **130,** 479–96 (2007).

82. Wang, W. & MacKinnon, R. Cryo-EM Structure of the Open Human Ether-à-go-go-Related K+

Channel hERG. *Cell* **169,** 422–430.e10 (2017).

83. Ader, C. *et al.* Coupling of activation and inactivation gate in a K+-channel: potassium and ligand sensitivity. *EMBO J.* **28,** 2825–34 (2009).

84. Pan, A. C., Cuello, L. G., Perozo, E. & Roux, B. Thermodynamic coupling between activation and inactivation gating in potassium channels revealed by free energy molecular dynamics simulations. *J. Gen. Physiol.* **138,** 571–80 (2011).

85. Cordero-Morales, J. F. *et al.* Molecular determinants of gating at the potassium-channel selectivity filter. *Nat. Struct. Mol. Biol.* **13,** 311–8 (2006).

86. Tilegenova, C., Cortes, D. M. & Cuello, L. G. Hysteresis of KcsA potassium channel's activation-deactivation gating is caused by structural changes at the channel's selectivity filter. *Proc. Natl. Acad. Sci. U. S. A.* **114,** 3234–3239 (2017).

87. Bhate, M. P., Wylie, B. J., Tian, L. & McDermott, A. E. Conformational dynamics in the selectivity filter of KcsA in response to potassium ion concentration. *J. Mol. Biol.* **401,** 155–66 (2010).

88. Kiss, L., LoTurco, J. & Korn, S. J. Contribution of the Selectivity Filter to Inactivation in Potassium Channels. *Biophys. J.* **76,** 253–263 (1999).

89. Cordero-Morales, J. F. *et al.* Molecular driving forces determining potassium channel slow inactivation. *Nat. Struct. Mol. Biol.* **14,** 1062–9 (2007).

90. Swenson, R. P. & Armstrong, C. M. K+ channels close more slowly in the presence of external K+ and Rb+. *Nature* **291,** 427–429 (1981).

91. Ostmeyer, J., Chakrapani, S., Pan, A. C., Perozo, E. & Roux, B. Recovery from slow inactivation in K+ channels is controlled by water molecules. *Nature* **501,** 121–4 (2013).

92. Xu, Y., Bhate, M. P. & McDermott, A. E. Transmembrane allosteric energetics characterization for strong coupling between proton and potassium ion binding in the KcsA channel. *Proc. Natl. Acad. Sci. U. S. A.* **114,** 8788–8793 (2017).

93. Bhate, M. P. & McDermott, A. E. Protonation state of E71 in KcsA and its role for channel collapse and inactivation. *Proc. Natl. Acad. Sci. U. S. A.* **109,** 15265–70 (2012).

94. Nussinov, R., Ma, B. & Tsai, C. J. Multiple Conformational Selection and Induced Fit Events Take Place in Allosteric Propagation. *Biophys. Chem.* **186,** 22 (2014).

95. Liu, S. *et al.* Ion-binding properties of a K+ channel selectivity filter in different conformations. *Proc. Natl. Acad. Sci. U. S. A.* **112,** 15096–100 (2015).

96. Wylie, B. J., Bhate, M. P. & McDermott, A. E. Transmembrane allosteric coupling of the gates in a potassium channel. *Proc. Natl. Acad. Sci. U. S. A.* **111,** 185–90 (2014).

97. Li, J. *et al.* Chemical substitutions in the selectivity filter of potassium channels do not rule out constricted-like conformations for C-type inactivation. *Proc. Natl. Acad. Sci. U. S. A.* **114,** 11145–11150 (2017).

98. Matulef, K., Komarov, A. G., Costantino, C. A. & Valiyaveetil, F. I. Using protein backbone mutagenesis to dissect the link between ion occupancy and C-type inactivation in K+ channels. *Proc. Natl. Acad. Sci. U. S. A.* **110,** 17886–91 (2013).

99. Matulef, K., Annen, A. W., Nix, J. C. & Valiyaveetil, F. I. Individual Ion Binding Sites in the K(+) Channel Play Distinct Roles in C-type Inactivation and in Recovery from Inactivation. *Structure* **24,** 750–761 (2016).

100. Lockless, S. W., Zhou, M. & MacKinnon, R. Structural and thermodynamic properties of selective ion binding in a K+ channel. *PLoS Biol.* **5,** e121 (2007).

101. Roux, B. Ion conduction and selectivity in K(+) channels. *Annu. Rev. Biophys. Biomol. Struct.* **34,** 153–71 (2005).

102. Cuello, L. G., Cortes, D. M. & Perozo, E. The gating cycle of a K+ channel at atomic resolution. *Elife* **6,** e28032 (2017).

103. Heer, F. T., Posson, D. J., Wojtas-Niziurski, W., Nimigean, C. M. & Bernèche, S. Mechanism of activation at the selectivity filter of the KcsA K+ channel. *Elife* **6,** e25844 (2017).

104. Yellen, G., Sodickson, D., Chen, T. Y. & Jurman, M. E. An engineered cysteine in the external mouth of a K+ channel allows inactivation to be modulated by metal binding. *Biophys. J.* **66,** 1068–75 (1994).

105. Liu, Y., Jurman, M. E. & Yellen, G. Dynamic rearrangement of the outer mouth of a K+ channel during gating. *Neuron* **16,** 859–67 (1996).

106. Raghuraman, H. *et al.* Mechanism of Cd2+ coordination during slow inactivation in potassium channels. *Structure* **20,** 1332–42 (2012).

107. Raghuraman, H., Islam, S. M., Mukherjee, S., Roux, B. & Perozo, E. Dynamics transitions at the outer vestibule of the KcsA potassium channel during gating. *Proc. Natl. Acad. Sci. U. S. A.* **111,** 1831–6 (2014).

108. Lee, A. G. Lipid-protein interactions. *Biochem. Soc. Trans.* **39,** 761–6 (2011).

109. Williamson, I. M., Alvis, S. J., East, J. M. & Lee, A. G. The potassium channel KcsA and its interaction with the lipid bilayer. *Cell. Mol. Life Sci.* **60,** 1581–90 (2003).

110. Laganowsky, A. *et al.* Membrane proteins bind lipids selectively to modulate their structure and function. *Nature* **510,** 172–175 (2014).

111. Ketchem, R. R., Hu, W. & Cross, T. a. High-resolution conformation of gramicidin A in a lipid bilayer by solid-state NMR. *Science* **261,** 1457–60 (1993).

112. Brohawn, S. G., del Mármol, J. & MacKinnon, R. Crystal structure of the human K2P TRAAK, a lipid- and mechano-sensitive K+ ion channel. *Science* **335,** 436–41 (2012).

113. van Dalen, A., Hegger, S., Killian, J. A. & de Kruijff, B. Influence of lipids on membrane assembly and stability of the potassium channel KcsA. *FEBS Lett.* **525,** 33–38 (2002).

114. Sharma, M. *et al.* Influenza A Proton Channel from a Structure in a Lipid Bilayer. 509–512 (2010).

115. Zheng, H., Liu, W., Anderson, L. Y. & Jiang, Q.-X. Lipid-dependent gating of a voltage-gated potassium channel. *Nat. Commun.* **2,** 250 (2011).

116. Delgado-Ramírez, M., Sánchez-Armass, S., Meza, U. & Rodríguez-Menchaca, A. A. Regulation of Kv7.2/Kv7.3 channels by cholesterol: Relevance of an optimum plasma membrane cholesterol content. *Biochim. Biophys. Acta - Biomembr.* **1860,** 1242–1251 (2018).

117. Lingwood, D. & Simons, K. Lipid rafts as a membrane-organizing principle. *Science* **327,** 46–50 (2010).

118. Cornelius, F., Habeck, M., Kanai, R., Toyoshima, C. & Karlish, S. J. D. General and specific lipid-protein interactions in Na,K-ATPase. *Biochim. Biophys. Acta* **1848,** 1729–43 (2015).

119. Weingarth, M. *et al.* Structural Determinants of Specific Lipid Binding to Potassium Channels. doi:10.1021/ja3119114

120. Raja, M. The potassium channel KcsA: A model protein in studying membrane protein oligomerization and stability of oligomeric assembly? *Arch. Biochem. Biophys.* **510,** 1–10 (2011).

121. Marius, P. *et al.* Binding of anionic lipids to at least three nonannular sites on the potassium channel KcsA is required for channel opening. *Biophys. J.* **94,** 1689–98 (2008).

122. van der Cruijsen, E. A. W., Prokofyev, A. V., Pongs, O. & Baldus, M. Probing Conformational Changes during the Gating Cycle of a Potassium Channel in Lipid Bilayers. *Biophys. J.* **112,** 99–108 (2017).

123. Poveda, J. A., Marcela Giudici, A., Lourdes Renart, M., Morales, A. & González-Ros, J. M. Towards understanding the molecular basis of ion channel modulation by lipids: Mechanistic models and current paradigms. *Biochim. Biophys. Acta - Biomembr.* **1859,** 1507–1516 (2017).

124. Molina, M. L. *et al.* Competing Lipid-Protein and Protein-Protein Interactions Determine Clustering and Gating Patterns in the Potassium Channel from Streptomyces lividans (KcsA). *J. Biol. Chem.* **290,** 25745–55 (2015).

125. Iwamoto, M. & Oiki, S. Amphipathic antenna of an inward rectifier K + channel responds to changes in the inner membrane leaflet. doi:10.1073/pnas.1217323110

126. Rusinova, R., Kim, D. M., Nimigean, C. M. & Andersen, O. S. Regulation of Ion Channel Function by the Host Lipid Bilayer Examined by a Stopped-Flow Spectrofluorometric Assay. *Biophys. J.* **106,** 1070–1078 (2014).

127. van der Cruijsen, E. A. W. *et al.* Importance of lipid-pore loop interface for potassium channel structure and function. *Proc. Natl. Acad. Sci. U. S. A.* **110,** 13008–13 (2013).

Chapter III: Characterization and Quantification of Allosteric Coupling in C-type Inactivation in KcsA

Portions of this chapter have been adapted from: Xu, Y., Bhate, M. P. & McDermott, A. E. Transmembrane allosteric energetics characterization for strong coupling between proton and potassium ion binding in the KcsA channel. *Proc. Natl. Acad. Sci. U. S. A.* **114,** 8788–8793 (2017).

3.1 Abstract

The slow spontaneous inactivation of potassium channels exhibits classic signatures of transmembrane allostery. A variety of data support a model in which the loss of K^+ ions from the selectivity filter, along with a conformational change at the selectivity filter, is a major factor in promoting inactivation. This process is allosterically coupled to protonation of key channel activation residues, over 30 Å from the K^+ ion binding site. Here we show that proton binding at the intracellular pH sensor perturbs the potassium affinity at the extracellular selectivity filter by over 3 orders of magnitude for the full length wild-type KcsA, a pH-gated bacterial channel, in membrane bilayers. These results provide quantitative site-specific measurements of allostery in a bilayer environment, and highlight the power of describing ion channel gating through the lens of allosteric coupling.

3.2. Introduction

3.2.1 Protein allostery

Allostery refers to changes at one site of a protein due to perturbations at a remote site and includes structural and dynamic alterations.[1] Frequently the change is elicited by binding of a ligand, and is manifested in terms of a consequent change in the affinity of another ligand binding to a different region of the protein. Allostery is a ubiquitous and efficient mechanism for communication in biology. In examples as diverse as enzyme regulation[2], transmembrane cell signalling[3], and gene expression regulation[4], the binding of one ligand to a protein changes the affinity of other ligands binding at separate binding sites and controls “downstream” events.

Many elegant thermodynamic models have been developed to describe allostery, beginning with the work by Monod, Wyman and Changeux on oxygen binding to the symmetric hemoglobin tetramer[5], and have even be generalized to include non-symmetric systems. Models like induced-fit (ligand binding induces a new conformation),[6] population-shift (ligands modulate populations of different states)[7] and entropy-driven models (ligand binding induces dynamical changes with minimal structural change)[8,9] have been applied to explain various allosteric events based on their energetic features and to provide a quantitative description of the coupling energetics.

3.2.2 Inactivation in KcsA: Electrophysiology Characterization

Both patch-clamp and single channel recording electrophysiology measurements have been applied to characterize the inactivation phenomena in KcsA.[10,11] In both of these experiments, low pH is used to activate the channel and the currents are recording under certain voltages to drive the potassium ion in unitary direction. In Figure 3.1, we show the results of current traces acquired for both the macroscopic and single-channel experiments. Figure 3.1A shows the patch-clamp experiment, in which the sample starts out in a pH 8.0 buffer, which has no current. After the pH jumps to 3, the current rises quickly on a millisecond timescale, indicating the channel is conducting potassium ion through the membrane. Soon after the current reaches the apex, it decreases spontaneously on a second timescale until it arrives at a plateau with minimal current, which indicates the channels are inactivated and not conducting. Figure 3.1B shows data for the single channel experiment in which KcsA is incorporated into a lipid bilayer at the interface of two buffers, one at pH 3 and one at pH 8. Due to the dead time for preparing the sample and measuring the current, the kinetics of the activation and inactivation is not visible and the channel is in the steady state. As seen in the single channel trace, the channel opens in a low open probability, which indicates the channel is in the inactivated state. The open probability in the single channel recording can be calculated from the current trace and is an important parameter to characterize the inactivation phenomena.

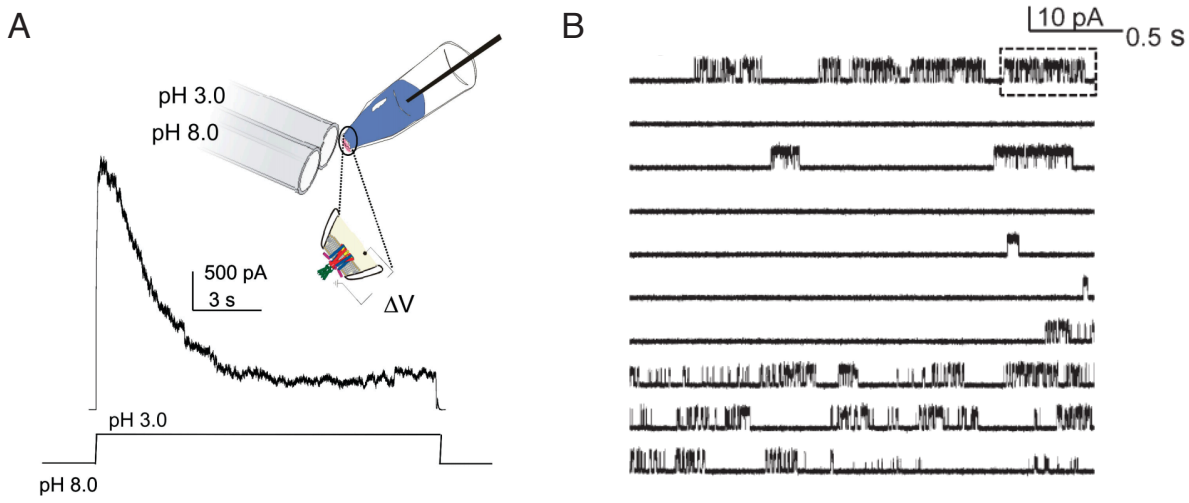

Figure 3.1 Macroscopic and microscopic current trace of the inactivation in KcsA. (A) Patch clamp experimental result shows the current trace during the inactivation. (B) Several single channel recording current traces are shown, in which the channels open in a low probability.

3.2.3 Allostery hypothesis and the kinetics analysis in KcsA

In the Chapter II, we have introduced the activation-coupled inactivation hypothesis. In KcsA, since the channel is activated by the pH, we study the coupling between the pH gate (i.e. the sites where proton binds) and the selectivity filter (i.e. the sites where potassium binds).

A kinetic hypothesis for channel activation and C-type inactivation is shown in Figure 3.2 (a). The Deactivated resting state has permeant ions loaded in the filter but has its transmembrane helices in a compact closed state, occluding flow at the intracellular gate. Protons are known to bind to the pH sensor in the Deactivated state,[12] causing the helical bundle to open[13] and a concomitant surge in current through the channel. This transiently populated conductive form is called the Activated state. Thereafter, a spontaneous structural change inactivates the channel, and the current gradually drops to reach a plateau with very low channel open probability. The formation of the 'Inactivated state' is reversible and in slow equilibrium with other states, as demonstrated by the bursts of open conducting form shown in Figure 3.1B.[14] Inactivation is distinct from deactivation, which is the reverse of activation and is achieved

by removing the activating stimulus, namely pH. Inactivation occurs in the *presence* of the activating stimulus via spontaneous transitions. In contrast to activation and deactivation, mutations that perturb inactivation in KcsA (and in Shaker channels)[15,16] are clustered in region near the selectivity filter, distinct from the activation domain and presumably sensitive to K^+ ion binding.[17,18]

The kinetics of inactivation are dependent on permeant ions; higher concentrations of K^+, or of other permeant ions like Rb^+, can significantly slow the rate of inactivation[11,19] whereas there is little dependence on the activating stimulus (pH for KcsA as it activates at low pH, e.g. pH 3-4.).[10,11] The formation of the Inactivated state is assumed to be an allosteric response to activation[20] because of its spontaneous kinetics following activation. Analogous regulatory mechanisms are known to be important in a range of biological contexts such as regulating the frequency and duration of firing in excitable cells[21] associated with QT syndrome in cardiac tissue, and other pathologies.[22,23]

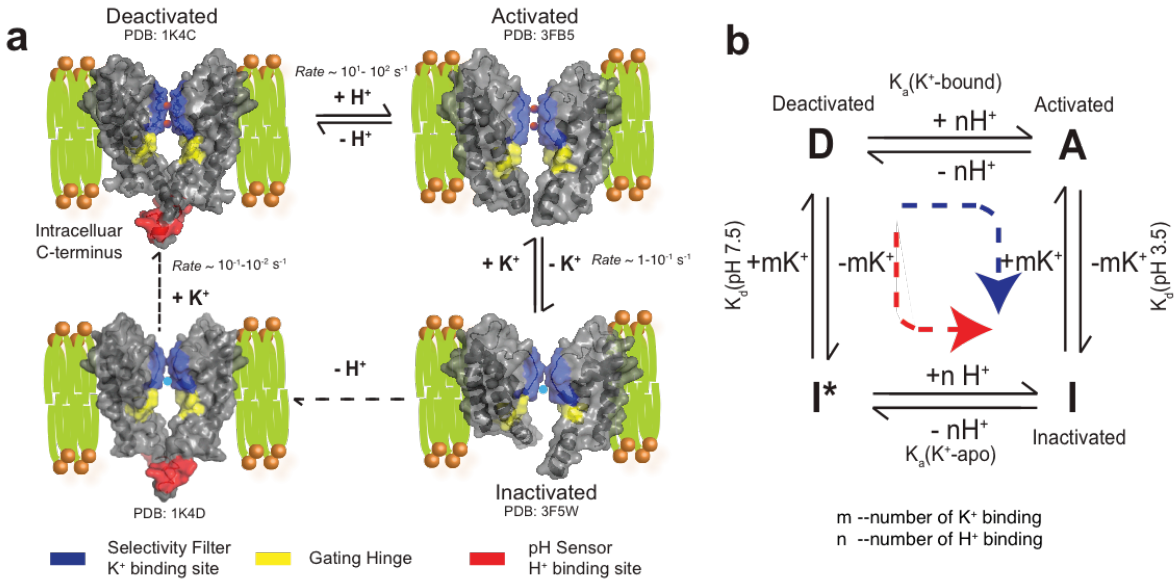

Figure 3.2. **(a)** Structural transitions in KcsA during channel function. In each structure, the K^+ binding selectivity filter (including conserved residues T74, T75, V76, G77, Y78, G79) is highlighted in blue, the pH sensor (E118, E120, H25, mutated in 3FB5 and 3F5W) where protons bind during activation is highlighted in red and the hinge of the inner helix, a site of significant conformational dynamics during activation and allosteric coupling, is highlighted in yellow. The resting state, designated as Deactivated (PDB: 1K4C) has K^+ ions bound in the selectivity filter and is conductive, but has a closed intracellular gate, with a deprotonated pH sensor and the TM2 bundle crossed and occluded. This stable species is

observed in numerous X-rays structures of KcsA. Following a drop in pH, the Activated state, the only conductive state in functional assays, is populated transiently. In this state both the selectivity filter and the intracellular gate are conductive (PDB: 3FB5). The Activated state slowly and spontaneously decays to an Inactivated state (PDB: 3F5W). Our working hypothesis for inactivation is that the Inactivated state differs from the Activated state by loss of the K^+ ions in the selectivity filter and associated conformational and hydration changes. Electrophysiology studies show that protein can recover from the Inactivated state to the Deactivated state at high pH, here represented by the dashed lines through a putative state Inactivated* or I* that is "closed at both gates" meaning both deprotonated at the pH sensor and K^+ deplete or possibly by way of the Activated state. **(b)** A thermodynamic cycle for H^+ and K^+ ion binding in the coupling network of KcsA. The blue dashed and angled arrow represents the activation followed by C-type inactivation as observed in pH jump electrophysiology experiments; the red dashed and angled arrow represents our observations of the result of lowering $[K^+]$ at constant neutral or slightly elevated pH.[35] The allosteric coupling factor defines the strength of the allosteric coupling and is calculated as: $\alpha=K_{apparent}(3.5)/K_{apparent}(7.5)$ or $\alpha'=K_a(K^+\text{-bound})/\ K_a(K^+\text{-apo})$.

3.2.4 Protein conformation in the Inactivated state

The protein conformation in the Inactivated state is the key debating point to understand the mechanism of the inactivation. The Inactivated state is believed to have a distinct structure from the Deactivated or Activated state.[10,11] Kinetic signatures and mutation profiles suggest that inactivation involves ion release in the selectivity filter, due to a large allosteric change in affinity as indicated in the thermodynamic cycle, shown in Figure 3.2 (b); we pursue this hypothesis for the nature of inactivation in this work. Cast in this way, the inactivation process is a classic allosteric effect of one binding event on the affinity for a second ligand in a distant pocket. A number of studies have already suggested that the Inactivated state is similar to a low-K^+ state.[24–27] The putative loss of K^+ ions and associated structural change at the selectivity filter would logically lead to cessation of ion flow: in the "knock-on" mechanism[28] steady-state K^+ binding and facile flow are essential for conduction. In support of this hypothesis, structures of the selectivity filter at low and at high ambient $[K^+]$ show that there is a protein conformational change associated with K^+ binding.[29] This hypothesis is also supported by a series of crystal structures of constitutively open mutants of KcsA,[30] recent simulations,[16,19] properties of mutants near the base of the selectivity filter,[16,19] and by NMR experiments showing that the otherwise tightly bound ion is in fact released when the channel is activated by a pH drop.[25,31,32] Moreover, we showed that

the acid coupled to K^+ ion binding is not the proximal E71, but rather the distal E118 and associated residues in the pH sensor,[31,33] consistent with other studies cited above.

Here we conduct SSNMR experiment to probe the potassium affinity changes at varying pHs. These site-specific binding measurements, carried out in an authentic bilayer environment, are an important step towards gaining a comprehensive understanding of the molecular network that mediates this allosteric coupling and will be a vital "benchmark" for further investigations of coupling. The NMR shifts provide rich structural information for the underlying states. To our knowledge, this is the first quantitative and site-specific analysis of allosteric coupling in a membrane system by NMR.

3.3. Results

3.3.1 KcsA biochemistry and sequence analysis

KcsA is a 64kDa homo tetramer protein. Each of the monomer has 160 amino acids, the sequence of which is shown in Figure 3.3 (A). Seen from the amino acids distribution (Figure 3.3B), most of the amino acids are hydrophobic, such as Leu, Arg, Val, Gly. This is common for membrane protein since a large port of the protein is embedded into the hydrophobic lipid bilayer environment. In KcsA, residues from around 20 to 120 compose the trans membrane part. One particularly important part is the selectivity filter; it has a strongly conserved signature sequence (75-TVGYG-79).

A

```
          10         20         30         40         50
MPPMLSGLLA RLVKLLLGRH GSALHWRAAG AATVLLVIVL LAGSYLAVLA
          60         70         80         90        100
ERGAPGAQLI TYPRALWWSV ETATTVGYGD LYPVTLWGRL VAVVVMVAGI
         110        120        130        140        150
TSFGLVTAAL ATWFVGREQE RRGHFVRHSE KAAEEAYTRT TRALHERFDR
         160
LERMLDDNLV
```

B

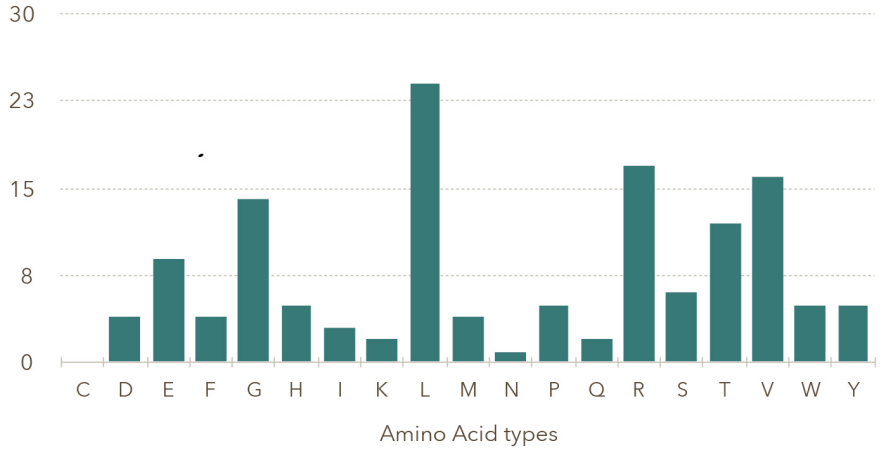

Figure 3.3 The amino acid sequence of KcsA. KcsA is a 64 KDa protein with each monomer containing 160 residues (A). The statistical distribution of amino acids is shown in (B); the residues Gly, Leu, Arg and Val are the most abound residues, which is common in membrane proteins.

3.3.2 Conductive and Collapsed Conformation of the Selectivity Filter in Crystal Structures

There are many crystal structures of KcsA prepared in various conditions and various constructs.[30,34,35] Most of the crystals are made without the first 20 amino acids in the N-terminal and the last 35 amino acids at the C-terminal. They are prepared in a detergent environment and crystalized with the Fab antibody. Roderick Mackinnon et al first solved two crystal structures, which were prepared in high [K+](i.e. 200mM) and low [K^+] (i.e. 3mM) concentrations at neutral pH.[29] These crystal structures are shown in Figure 3.4. One distinguish feature between these two structures is at the selectivity filter. In the 1K4C structure, which is acquired in high [K^+], the selectivity filter displays a conductive conformation, forming a conducting tube by the arrangement of the backbone carbonyl groups for those residues to complex with potassium ion. Based on ion diffraction, potassium ions are discovered to equally occupy at the S1-S4 sites in the selectivity filter; they are hypothesized to be arrange in K^+ -water-K^+-water or water-K^+-water-K^+ when potassium ions are conducted through the channel. In the 1K4D structure, which is

acquired at low [K^+], the selectivity filter is collapsed and constricted by rotating the V76 carbonyl group off the center axis, and dilating the bottom and up sides of the selectivity filter. Ion diffraction can be only seen in the S1 or S4 site. In the conformation, it is supposed that it will not conduct potassium ion. Many other crystal structures were solved later, but their structures, especially at the selectivity filter, are well overlaid with one of these two structures.[30]

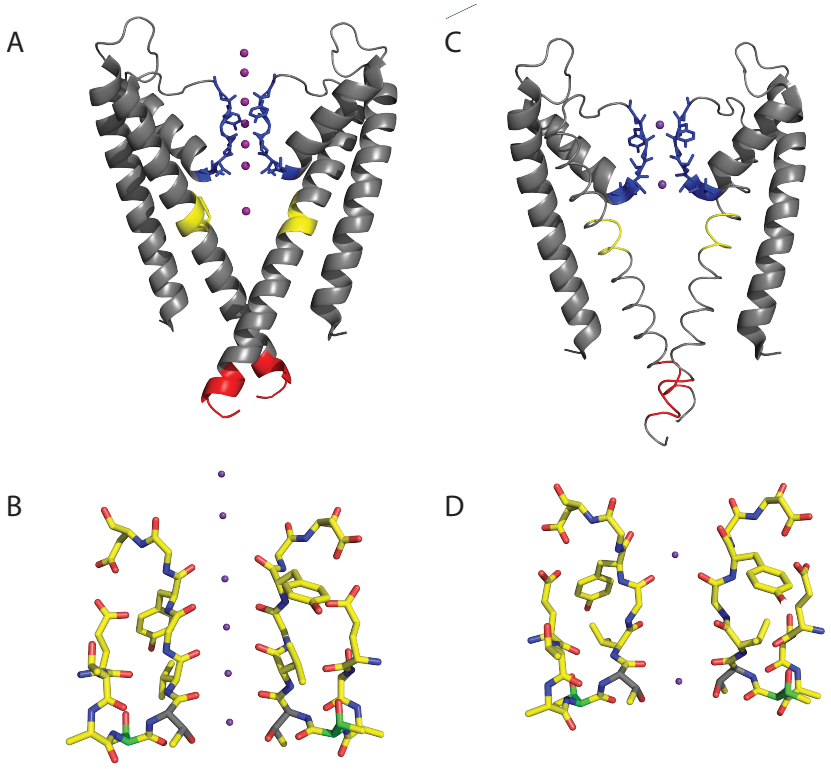

Figure 3.4 Critical structures of the conductive (potassium bound) and collapsed (potassium unbound) states of the selectivity filter in KcsA. The structure in the panel A is the crystal structure acquired with 200mM [K^+] and at neutral pH. (1K4C) The conductive conformation of the selectivity filter is expanded in B. The structure in the panel C is the crystal structure acquired with 3mM [K^+] and at neutral pH (1K4D). The collapsed conformation of the selectivity filter is expanded in D. In A and C, the blue color-coded is the selectivity filter; the yellow color-coded is the hinge region; the red color-coded is the pH gate.

3.3.3 NMR Assignment in KcsA

In NMR study of KcsA, protein assignment is the first step in order to observe the conformational change at various sites. As we see from the crystal structure, most of the residues are in the alpha-helix conformation, which indicates low dispersion in chemical shift distribution and congested spectra. It puts a great challenge for the protein assignments. With the ability to conduct 3D and 4D correlation experiments, many unique assignments have been made by previous group members Manasi Bhate, Benjamin Wilye et al. [31,36,37]Assignments for a large portion of the protein have been made for KcsA prepared at neutral pH and high [K+] (corresponding to the resting state) and a small portion for KcaA prepared at neutral pH and low [K+] in previous work.[31] Currently, some assignments are also made for samples prepared in the low pH condition with low and high [K+]. These assignments are made by both comparing to previous assignments at neutral pH and confirming assignments using various mixing time DARR ^{13}C-^{13}C, NCACX and NCOCX spectra. (Appendix 2, chemical shift table)

In the Figure 3.5, the assignment plot for the neutral pH and high [K+] condition shows the assigned residues. The selectivity filter is in a loop conformation, which makes the chemical shifts of those residues distinctive from that in the transmembrane part. They are easy to assign and their individual assignments can be identified in 2D ^{13}C-^{13}C or ^{15}N-^{13}C correlation spectra. For the first 20 amino acidic in the N-terminal and the residues in the C-terminal, they are thought to be highly dynamic and heterogeneous. Thus the NMR signals from them are weak and they are hardly detected and assigned.

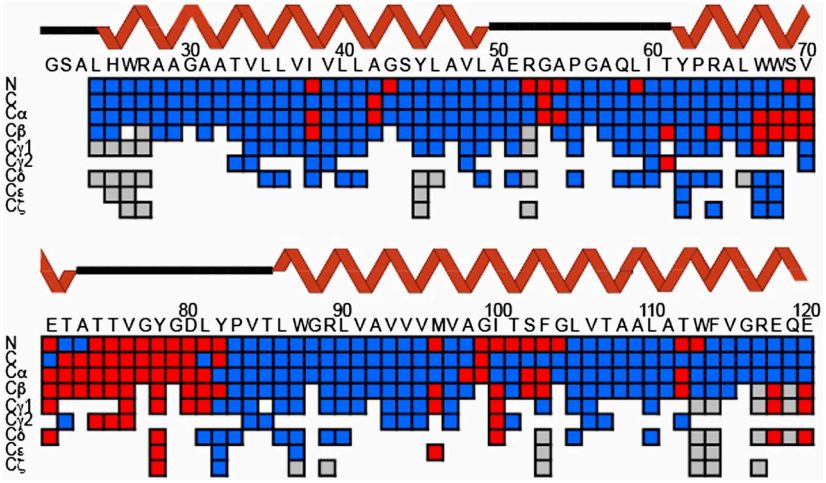

Figure 3.5. Assignment plot for KcsA shows the completeness and K^+ dependent chemical shift change at neutral pH. The figure is taken from reference 31. The backbone assignments from L24 to E120 are complete and side chain assignments are mainly done at high [K^+] concentration. The Red color indicates a chemical shift change (greater than 0.3 ppm); the gray color indicates that the sites are not assigned.

3.3.4 SSNMR Shifts Probe KcsA Structures in Its Apo and Ion Bound States

NMR chemical shift measurements provide highly specific "fingerprints" for the structures of proteins, probing conformation and binding. We used chemical shifts to probe KcsA, with particular focus on the selectivity filter. We contrasted spectra at near neutral (pH 7.5) vs. low (3.5) pH, at a broad range of [K^+], to achieve the four limiting states in Fig. 3.2b, in functionally relevant lipid and buffer conditions. Consistent with the fact that these channels function at low pH, the spectra for acidic samples display narrow linewidths, comparable to those observed at neutral pH and the vast majority of resolved sites show chemical shifts that are indistinguishable from those at neutral pH indicating that KcsA is folded at pH 3.5.

3.3.4.1 *Similar selectivity filter structural transitions are observed at neutral and acidic pH.*

Previously, we characterized K^+ dependent changes in the selectivity filter at neutral pH[37] that correspond to the high K^+ (conductive) and low K^+ (collapsed) states described by crystallography.[38] Several NMR reporters were identified including T74 (CA, CB, CG), T75 (CA, CB, CG) and V76 (CB, CG1, CG2). Here, we observe a similar transition between high and low K^+ states at low pH, each of which shows highly similar structures to its corresponding counterpart at neutral pH (Fig. 3.6). This means that the large

difference in pH does not perturb the structure of selectivity filter directly, and that its capability to bind ions is intact, and moreover the NMR markers for K^+ binding are valid also at low pH.

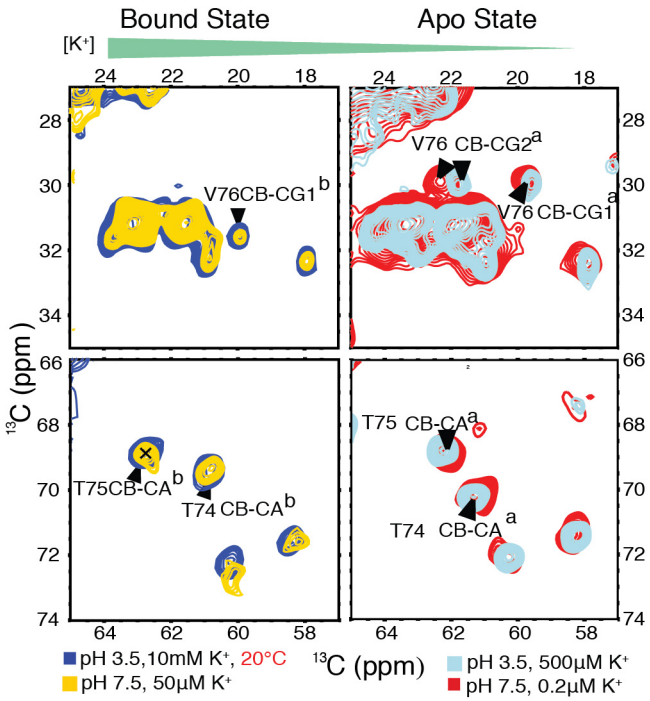

Figure 3.6. Similar changes in chemical shift implying similar structural transitions were seen for the selectivity filter of KcsA. Similar chemical shifts are seen in the selectivity filter for K^+-bound state, regardless of pH; similar chemical shifts are seen in the selectivity filter for K^+-apo state, regardless of pH Marker peaks V76 (CB-CG1/CG2), T75 (CB-CA), T74 (CB-CA) obtained from ^{13}C-^{13}C 2D correlation spectra are shown for a variety of [K^+] and pH values. The left panel contrasts KcsA at pH 7.5, (the Deactivated State, in yellow), to that at pH 3.5 (Activated state, in blue) while both experiments are at "high" ambient [K^+] (bound states). The right panel contrasts the channel at pH 7.5 (Inactivated* State, in red), to pH 3.5 (Inactivated state, in Cyan); both experiments are at "low" ambient [K^+] (apo states). There are significant chemical shift changes between high [K^+] (yellow and blue) and low [K^+](red and grey) conditions, due to ion-release and associated structural changes in the selectivity filter. Excellent agreement in the overlay of this region of the spectra comparing neutral vs. acidic pH illustrates that the structure transition at the selectivity filter at neutral and acidic pH are very similar and the selectivity filter is clearly intact throughout this pH range i.e. the structure of selectivity filter is K^+ dependent, and pH does not directly perturb it. Superscripts refer to the K^+ **a**po and **b**ound states respectively.

3.3.4.2 *pH sensor residues E118 and E120 are protonated at pH 3.5 across a broad range of K^+ concentrations.*

The pH sensor binds protons[12,32] and causes channel activation. Previous studies show that the effective pKa value for activation is 5 or 5.5.[12] Accordingly the E118 and E120 CG-CD NMR cross peaks show diagnostic chemical shift changes associated with significant protonation at pH 3.5;[25,31] at neutral pH, the peaks are characteristic of a deprotonated anionic state (Fig. 3.7). Wylie and coworkers, however, demonstrated that when the ambient [K^+] is significantly lowered, the allosteric coupling between the selectivity filter and the activation gate cause a coupled pronation process[31], providing proof for the strength of this coupling.

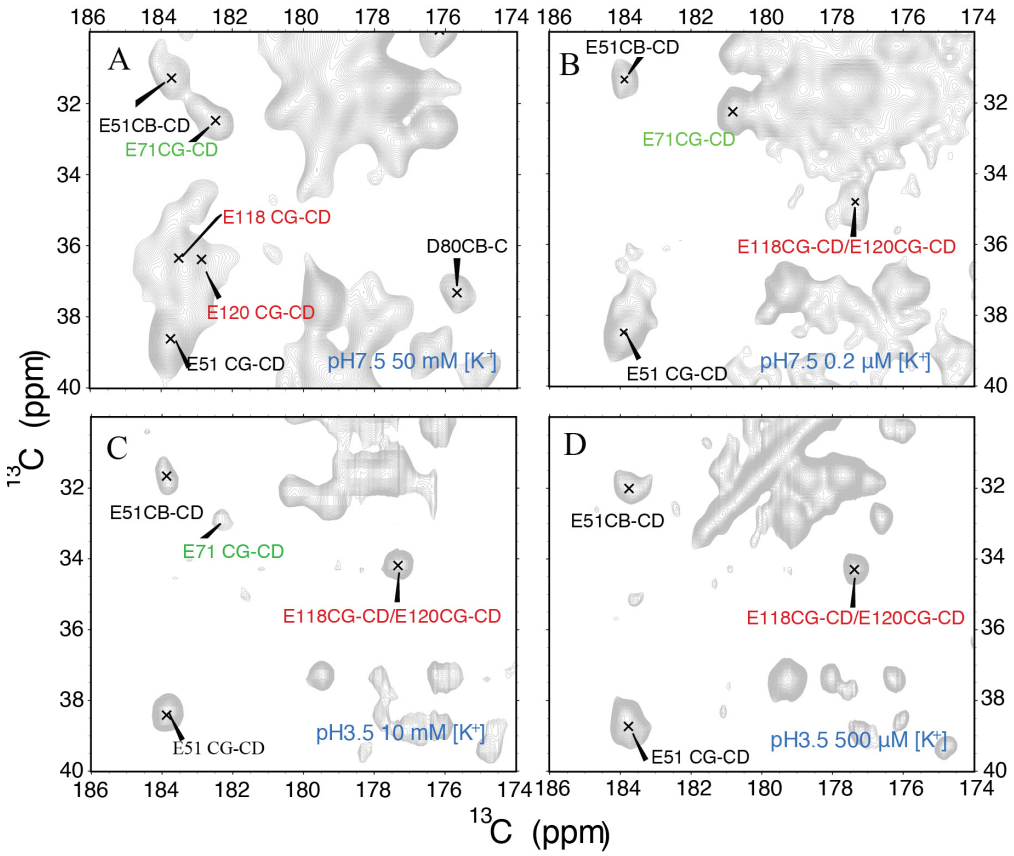

Figure 3.7 NMR spectra of the glutamic acid residues in the intracellular pH sensor. NMR spectra of the glutamic acid residues in the intracellular pH sensor controlling the activation gate of KcsA show that the pH gate residues Glu118 and Glu120 are protonated at pH 3.5 across a broad range of [K^+], while at pH 7.5, the behavior is more complex, and at high [K^+], the pH sensor residues are deprotonated as

expected, but at low [K^+], due to coupling between K^+ ion release and H^+ binding, the sensor residues are protonated based on the NMR spectra. Panels A-D show spectra for samples at (respectively) pH 7.5 and 50mM [K^+], pH 7.5 and 0.2uM [K^+], pH 3.5 and 10mM [K^+] and pH 3.5 and 500uM [K^+]. The signals associated with Glu118 and Glu120's CG-CD correlation show comparable chemical shifts in panel (B, C, D), indicating that they are protonated, whereas in (A) they show clear indication of deprotonation. We conclude that the local environment of these residues are similar at acidic pH across a range of [K^+], and also at neutral pH if the [K^+] is very low.[35]

3.3.5. Potassium Ion Affinity at Acidic pH: Quantifying the Strength of Allosteric Coupling

To confirm strong allosteric coupling of the two binding events, and the participation of specific residues in the allosteric process, we developed a SSNMR approach to analysis of binding strength and applied it to this system. Although the low K^+ and high K^+ *structures* (and NMR shifts) of the selectivity filter show little sensitivity to pH, we demonstrate here that the *energetics* of the transition, as characterized by the affinity of the selectivity filter for K^+ ions, are dramatically dependent on pH. Such a pH dependence was suggested by previous studies but has not been studied systematically or quantified in a membrane environment.[26,39] Our four-state thermodynamic formulation allows the magnitude of the allosteric coupling to be quantitatively recast as the difference in the equilibrium K^+ binding affinity at high vs. low pH. We are able to measure the K^+ affinity in a site-specific manner and in a native bilayer environment using solid-state NMR. Since the K^+ binding event is coupled with structural changes, the apparent potassium affinity ($K_{apprent}$) is measured. This titration study is rich with structural information because it is based on NMR shifts.

We measured $K_{apparent}$, contrasting acidic pH (3.5) vs. neutral pH (7.5) by quantifying the relative populations of K^+ bound vs. apo states using the "marker" cross-peaks identified above, including T74 (CB-CA), T75 (CB-CA, CA-CG), and V76 (CA-CG1, CG2) (Fig. 3.8). These residues were selected due to their robust signal and good resolution with respect to other signals in 2D spectra. Fitting the titration data (using a fixed Hill coefficient of 1) yielded a $K_{apparent}$ of 14 ± 1 mM at pH 3.5 at 0 ºC; in contrast, the $K_{apparent}$ at neutral pH is 4 ± 1 μM, under otherwise comparable conditions (Fig. 3.9). The temperature control for these measurements is improved relative to prior measurements[37] due to the use of an "E-Free" probe with reduced sample heating.[40] We calculated the allosteric coupling factor alpha, defined as the ratio of the potassium affinities contrasting open vs. closed activation gate (i.e. at low vs. neutral pH);

there is a remarkable shift of the $K_{apparent}$ by more than three orders of magnitude (α =3,500) over the pH range where the channel converts from the Deactivated to the Inactivated state (7.5 to 3.5).

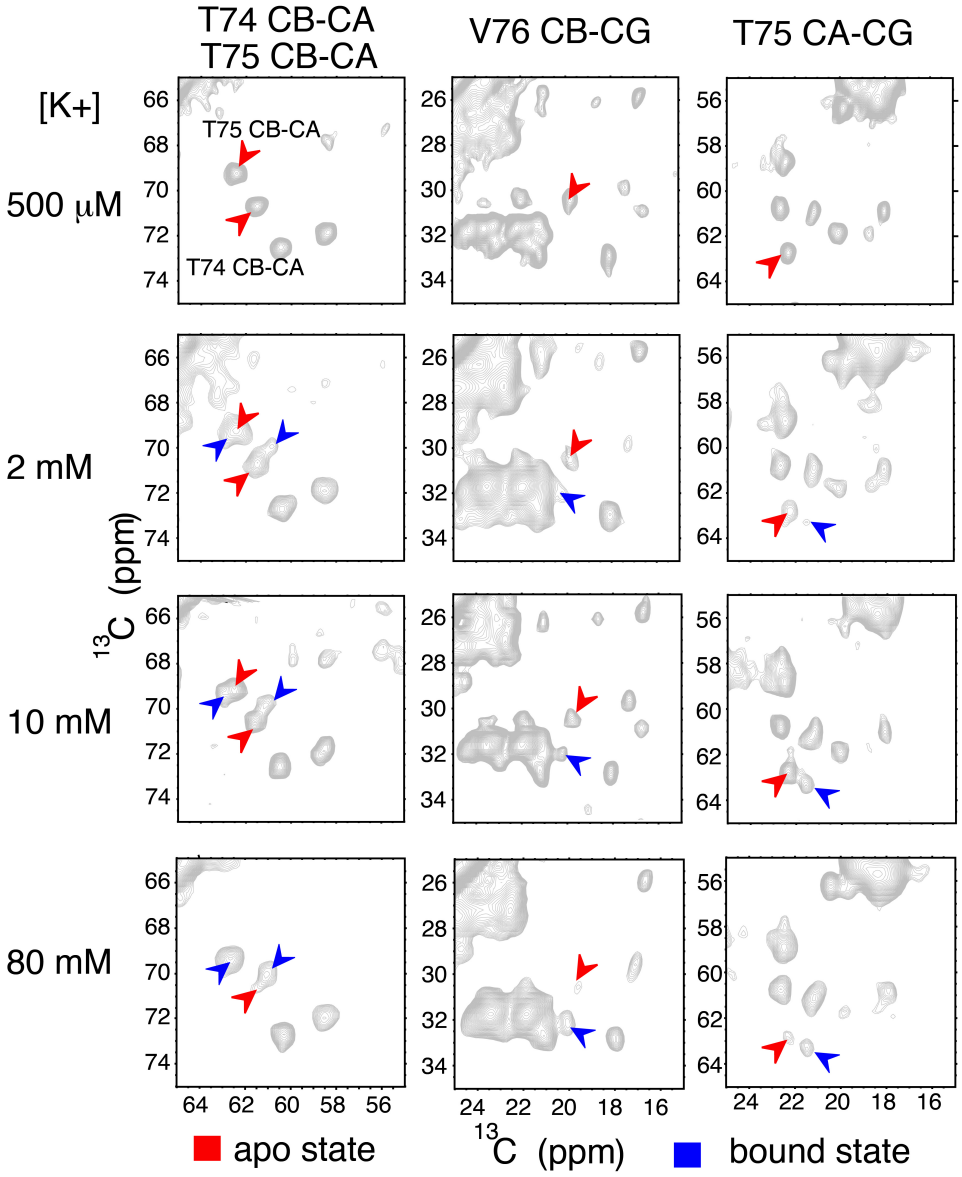

Figure 3.8 Marker peaks in NMR spectra showing the structural transition at the selectivity filter at acidic pH 3.5 as the environmental [K^+] changes from 500 mM to 80 mM. The volumes of cross peaks indicated by arrows are used to calculate the bound state population ratio and $K_{apparent}$ calculations in Figure 3.8.

The thermodynamic cycle (Fig. 3.2b) also dictates that if the ambient pH affects the equilibrium K^+ affinity, then the ambient K^+ level must also alter the apparent pKa of the coupled pH sensor. Prior work

showed that pH gate residues E118 and E120 bind protons as the [K^+] is lowered to about 0.2 μM at pH 7.5. This indicates a large pKa shift in the pH sensor as a function of K^+,[31] and confirmed the identity of the pH sensor as the coupled general base (while in contrast, the proximal E71 remains protonated in all [K^+][26]). The K^+ dependent pKa shift in E118 and E120 has not been fully quantified, but it is clear that the pKa is altered by at least 3 pH units comparing low and high potassium conditions, since at low [K^+] the pKa must be 8.0 or higher and at high [K^+] the pKa value is known to be approximately 4-5 and is consistent with our experimental results.[11,32]

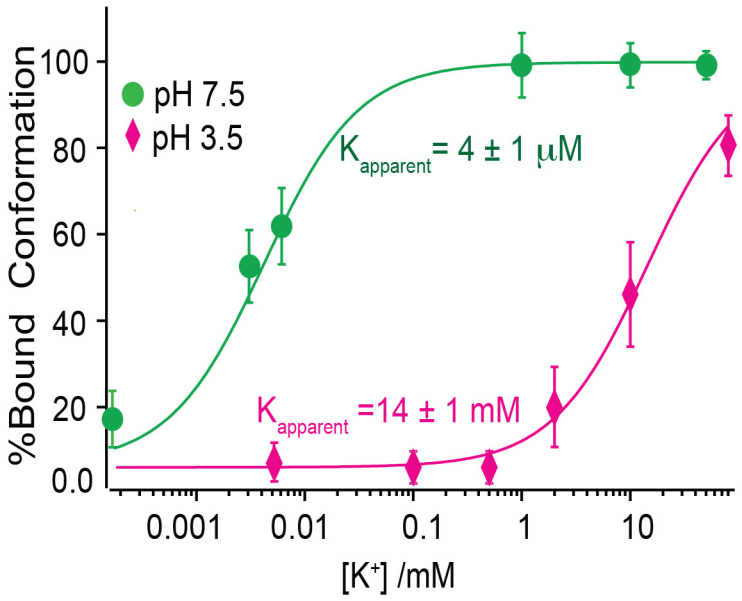

Figure 3.9 Differences in K+ binding at neutral vs. acidic pH values for WT -KcsA. A significant change in potassium ion affinity (α =3,500) is observed comparing channels with an open activation gate measured at pH 3.5 (magenta) vs. a closed gate measured at pH 7.5 (green). The K_d values calculated by fitting the data to a non-cooperative binding equation (Hill coefficient n=1) are 4±1 μM for pH 7.5 and 14±1 mM at pH 3.5.

The free energy of allosteric coupling between K^+ and H^+ binding was estimated from the pH dependence of the K^+ $K_{apparent}$ values: $\Delta\Delta G = -RT\ln [K_{apparent}(pH7.5)/K_{apparent}(pH3.5)] = -19 \pm 2$ kJ mol^{-1}. A tentative value estimated from the pKa shift with [K^+] would similarly be $\Delta\Delta G = -2.303RT\Delta pKa = -16$ kJ mol^{-1}. (Appendix 3) We regard these energies as estimates; they were calculated using a simplified

binding model that treats both K^+ and H^+ binding as single-ligand, non-cooperative events. The stoichiometry and cooperativity of the binding events is certainly more complex and the details remain debated. [41–43]

Due to the relatively large pH range utilized, the phenomenological shift in binding affinity can include a number of effects. We argue that a large portion of it is allosteric coupling. Guoy-Chapman analysis suggests that the differences with respect to previous micelle measurements are too large to be explained by K^+ ions concentrating at a negatively charged lipid interface (an approximately 10-fold effect).[33] Non-specific effects of pH on the lipid bilayer and protein structure and thermodynamics could certainly also contribute to the altered affinity, although our data show that KcsA remains folded throughout this range. Finally, a large and specific effect of site-specific mutation involving the non-ionizable F103 (next chapter) and a control experiment on H25R&E118A mutant (discussed below) provides strong support that the altered affinity is dominated by contacts in the protein that result in non-additive energies of binding.[16,19]

3.3.6 Kinetics of ion release are slow across all conditions studied

Inactivation has a clear kinetic signature, and is a remarkably slow process (on the seconds timescale).[11] The origin of the kinetic barrier is debated; molecular dynamics simulations suggest that changes in solvation associated with the conformational change in the filter present a kinetic bottleneck.[14] We observe clear evidence for slow conformational exchange between the K^+ bound and depleted states at both acidic and neutral pH. At both conditions, intermediate K^+ concentrations result in sharply resolved NMR lines corresponding to two states of the filter and indicating slow exchange (100 ms or slower, which is well below estimates of k_{off} based on the affinities measured here).[37] The relative populations are significantly affected by temperature changes *in situ* (Table 3.1), supporting the assumption that the system is in slow dynamic equilibrium during the NMR experiments. The slow kinetics observed here are in contrast to those observed by solution NMR in detergent micelles at higher temperatures and at pH 6.0,[44] but are consistent with the slow inactivation kinetics observed in electrophysiology.[10,11]

Table 3.1. Summary of K^+ affinities at various pH conditions and temperatures for WT-KcsA and F103A mutant. The affinities for were computed by simulating data using Hill equation (see Method).

Construct	pH	Temperature	K^+ $K_{apparent}$ (mM)	RTln($K_{apparent}$) (KJ/mol)
WT	3.5	273K	14 +/-1	-9.7+/- 0.2
WT	3.5	293K	1.0 +/- 0.2	-16.8+/-0.5
WT	7.5	258K	0.003+/- 0.001	-27.3+/-0.7
WT	7.5	270K	0.004+/-0.001	-27.9+/-0.6
WT	7.5	283K	0.005+/-0.002	-28.7+/-0.9

3.3.7 Potassium Affinity on Mutant H25R&E118A - A Control Experiment

The titration results on WT-KcsA provide a unique insight on C-type inactivation. However, even though a very acid pH is needed to activate the channel and used for the titration study, many concerns have been raised on it. One concern is that the low pH protonates the lipids head groups, competing with potassium ions to lower the local [K^+]. It can bias the measured large affinity difference. On the other hand, the very acid pH can accelerate the degradation of lipid bilayer by hydrolysis. The lipid bilayer in this study is composed of DOPE and DOPS, whose pKas are 1.7/11.25 and 2.5/5.5/11.55, respectively. (Fig. 3.10) Authentic and integral lipid bilayers have been shown of great importance for membrane protein integrity and function. In order to address these concerns, we planned experiments in which H25R&E118A mutant is used to proxy the pH-gate opened channel. Based on previous electrophysiology experimental results, the pH gate of H25R/E118A mutant stays open up until to pH 9.0.[41] In such way, we can measure the potassium affinity of a channel with open pH-gate conformation at neutral pH (i.e. pH 7.5).

The spectrum for the H25R&E118A is shown in Fig. 3.11. The spectrum of the mutant can be well overlaid with the WT-KcsA spectra, indicating that the mutant is well folded. We then conducted the titration experiments on the mutant and the results are shown in Fig. 3.12. The apparent K^+ affinity is around 80mM, which is 20,000 folds higher than the affinity for WT-KcsA sample at the same pH. This result confirms our hypothesis that the huge potassium affinity difference is caused by the specific coupling effect to the pH gate, instead of other environmental effects, such as the acidic pH we applied in the study.

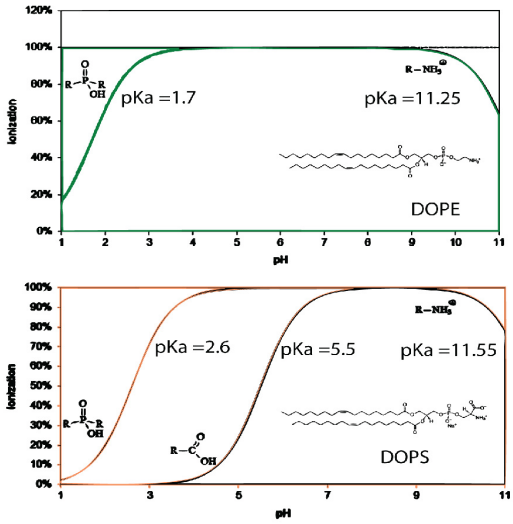

Figure 3.10. The pKa values for the lipids DOPE and DOPS, which are used in this study.

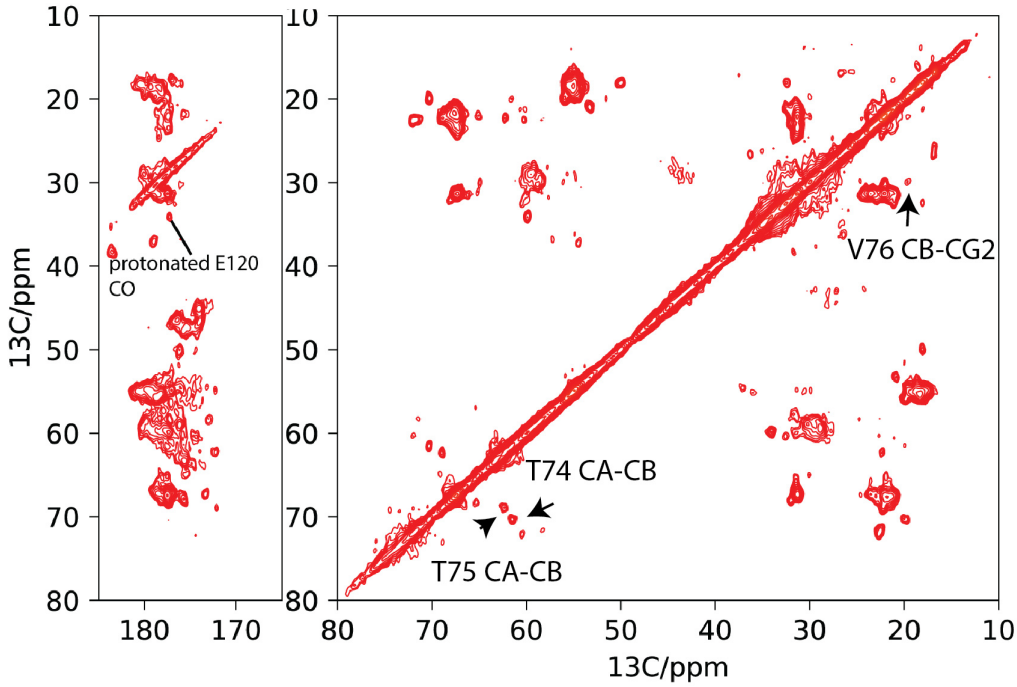

Figure 3.11 ^{13}C-^{13}C DARR spectrum is shown for the H25R&E118A mutant sample at pH 7.5 and at 50 μM [K^+]. The spectrum can highly overlay with that of WT-KcsA, indicating that the structure is well folded. From the marker peaks labeled in the spectrum, the selectivity filter at such a conditions is still in the collapsed/K^+-unbound conformation, contracting to that in WT-KcsA where the selectivity filter is in the conductive/ K^+-bound conformation.

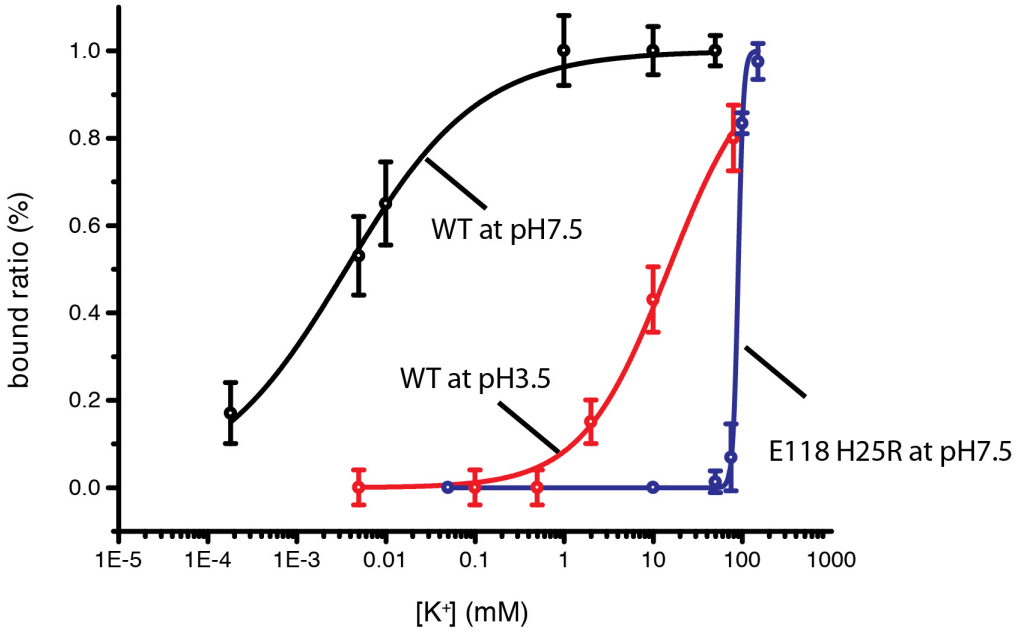

Figure 3.12. The titration curve of the H25R & E118A mutant at neutral pH is compared to that of WT-KcsA at both neutral and acidic pH. The potassium affinity of this mutant is around 80mM at pH7.5, significantly shifted from 4uM at neutral pH and 14mM at acid pH for WT-KcsA. This confirms the observed allosteric coupling effect between the pH gate and the selectivity filter at the WT-KcsA.

However, surprisingly, the measured affinity is even looser than the affinity measured for WT-KcsA at pH3.5 (i.e. 14mM). This shift to lose affinity leads us to hypothesize that the inactivated structure is stabilized by a larger extent of opening at the pH gate in the mutant than that in the WT-KcsA-KcsA at pH3.5. We reason that for the WT-KcsA, after the pH sensor residues such as H25, E118, E120 are protonated, they can switch roles from protonated acceptors to proton donors in the hydrogen-bonding network, which prevent the pH gate opening extensively. While the mutant is mutated to be open, the mutation to residue to alanine might totally break the hydrogen-bonding network, not only keeping the pH gate open but also losing the ability to prevent extensive opening. Various extents of opening at the pH gate were observed in a series of crystal structure of KcsA with C-terminal truncated and the pH gate mutated open; the largest opening, measured at T112 sites is about 32 Å.[30] However, the opening of the pH gate for WT-KcsA at the same position is estimated to be 17-20 Å based on the chemical shift analysis .[31] Furthermore, the larger opening at the pH gate is also linked to a more collapsed structure at

the selectivity filter and less ion binding.[30] However, more experimental and computational evidence are required to validate such a hypothesis.

Another interesting observation from the titration curve for the H25R&E118A mutant is that the transition from the bound to the unbound state is very steep comparing to those for sample at pH7.5 and pH 3.5. We interpret this as an increasing in the cooperativity during the potassium ion binding at the selectivity filter. However, the system is complicated in term of proton binding and potassium binding and the coupling between them, which prevent us from drawing a clean conclusion on this observation.

It is worthy noting that similar experiments on E118A&H25R mutant were carried out in previous Isothermal titration calorimetry (ITC) study on a sample, which was prepared in the detergent environment. The results show that the affinity for K+ at pH is 0.13mM, close to the affinity for WT-KcsA in their measurement.[45] This is inconsistent with our results, indicating that there is little coupling between the pH gate and the selectivity filter. We attribute this inconsistency mostly to the usage of detergent in their experiment. Or as suggested by the author, ITC is not sensitive to structural transition from the conductive state to the inactivated state. This experiment adds another example that the lipid bilayer is crucial for pursing the correct thermodynamic or kinetics information from a membrane protein system.

3.3.8 Hill Coefficient and Cooperativity: Number of Proton and Potassium Binding

KcsA, as a tetramer protein, shows tremendous complexity in term of allostery and cooperativity. In term of the proton binding, each monomer has several proton binding residues, such as E118, E120, H25, etc.[12] How many protons are essential to be bound to open the pH gate? Does the channel show cooperativitity in the proton binding process, i.e. does proton binding to one monomer accelerates proton binding to other monomers? These same mysteries exist in the potassium-binding site: how many potassium ions are needed to transit the collapsed conformation to the conductive conformation and whether there is any cooperativity in term of potassium binding? The energetics gets more complicated as these two binding events are coupled. Therefore, these questions are extremely hard to study and the stoichiometry is still under heated debates.

In the voltage-gated channel, altering the number of the voltage sensing arginine residues change the channel sensitivity to the voltage as the slope of Conductance-Voltage is flattened.[46] In a recent study on KcsA by Posson et al,[41] mutations on various sites at the pH gate also show that they changed the steepness of the pH –channel open probability curves or shifted the pKa. Based on these mutations data, they concluded that the H25 is the major proton-binding site and E118 is the secondary proton-binding site. Even though the study is very elegant, the data per se are complicated; hence they require some assumptions to be interpreted. The whole study was based on the inactivationless E71A mutant, which almost abolish the coupling between the pH gate and the selectivity filter.

Here we aim to build a thermodynamic model for the WT-KcsA, including constraints from our affinity results and previous electrophysiological study. Through building such a semi-quantitative thermodynamics model, we hope it will be helpful to distinguish some models and provide information on stoichiometry.

We first build our general thermodynamic model as shown in the following scheme:

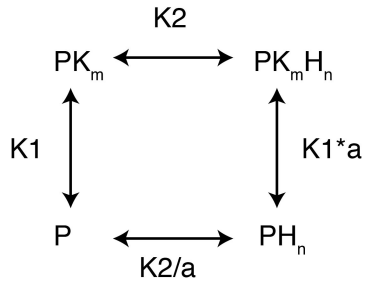

Figure 3.13 A thermodynamic framework used for the stoichiometry modeling.

In this thermodynamic cycle, n and m are the numbers of protons and potassium ions binding, respectively. The 'a' is an allosteric coupling coefficient; in a case where there is no allosteric coupling between the two ligand binding, a equals 1. P represents the protein; H, K represents the proton and potassium ions, respectively. K1 and K2 are the equilibrium constants for the transitions between P (I* state in the Figure 3.2b) and PK_m (D state in the Figure 3.2b) and PK_m and PK_mH_n (A state in the Figure 3.2b), respectively.

Based on the simple general frame, we can derive the following equations:

$K1=[PK_m]/([P]*[K^+]^m)$ $\quad K1=1/K_{d1}{}^m$ (3.1)

$K2=[PK_mH_n]/([PK_m]*[H^+]^n)$ $K2=1/K_{d2}{}^n$ (3.2)

$K2/a=[PH_n]/([P]*[H^+]^n)$ $K1/a=1/K_{d22}{}^n$ (3.3)

$K1*a= [PK_mH_n]/([PH_n]*[K^+]^m)$ $K1*a=1/K_{d12}{}^m$ (3.4)

The K_{d1}, $K_{d2,}$ $K_{d22,}$ K_{d12} are the apparent affinities for each of the binding reactions, which is the ligand concentration at which the populations of bound and unbound spices are equal. We can rewrite the above equations as fellows:

$[PK_m] =K1*[P]*[K^+]^m$ (3.5)

$[PH_n]=K2/a*([P]*[H^+]^n)$ (3.6)

$[PK_mH_n]= K1K2 *[P]*[K^+]^m[H^+]^n$ (3.7)

Then we can calculate the percentage of the four components:

$P\% = [P]/([P]+ [PK_m] + [PH_n]+ [PK_mH_n])$ (3.8)

$=1/(1+ K1*[K^+]^m + K2/a*[H^+]^n + K1K2*[K^+]^m[H^+]^n)$

$=1/(1+ K1*[K^+]^m + K2/a*(10^{-pH})^n + K1K2*[K^+]^m(10^{-pH})^n)$

$= K_{d1}{}^m K_{d2}{}^n/(K_{d1}{}^m K_{d2}{}^n+ K_{d2}{}^n *[K^+]^m + K_{d1}{}^m /a*(10^{-pH})^n + [K^+]^m(10^{-pH})^n)$

$PK_m \% = [PK_m]/([P]+ [PK_m] + [PH_n]+ [PK_mH_n])$ (3.9)

$= K1*[K^+]^m /(1+ K1*[K^+]^m + K2/a*[H^+]^n + K1K2*[K^+]^m[H^+]^n)$

$= K1*[K^+]^m /(1+ K1*[K^+]^m + K2/a*(10^{-pH})^n + K1K2*[K^+]^m(10^{-pH})^n)$

$= [K^+]^m K_{d2}{}^n/(K_{d1}{}^m K_{d2}{}^n+ K_{d2}{}^n *[K^+]^m + K_{d1}{}^m /a*(10^{-pH})^n + [K^+]^m(10^{-pH})^n$

$PH_n \% = [PH_n]/([P]+ [PK_m] + [PH_n]+ [PK_mH_n])$ (3.10)

$= K2/a*[H^+]^n /(1+ K1*[K^+]^m + K2/a*[H^+]^n + K1K2*[K^+]^m[H^+]^n)$

$= K2/a*(10^{-pH})^n /(1+ K1*[K^+]^m + K2/a*(10^{-pH})^n + K1K2*[K^+]^m(10^{-pH})^n)$

$= K_{d1}{}^m /a*(10^{-pH})^n /(K_{d1}{}^m K_{d2}{}^n+ K_{d2}{}^n *[K^+]^m + K_{d1}{}^m /a*(10^{-pH})^n + [K^+]^m(10^{- pH})^n)$

$$PK_mH_n\ \% = [PK_mH_n]/([P]+[PK_m]+[PH_n]+[PK_mH_n]) \quad (3.11)$$

$$= K1K2*[K^+]^m[H^+]^n /(1+ K1*[K^+]^m + K2/a*[H^+]^n + K1K2*[K^+]^m[H^+]^n)$$

$$= K1K2*[K^+]^m(10^{-pH})^n /(1+ K1*[K^+]^m + K2/a*(10^{-pH})^n + K1K2*[K^+]^m(10^{-pH})^n)$$

$$= [K^+]^m(10^{-pH})^n /(K_{d1}{}^m K_{d2}{}^n + K_{d2}{}^n *[K^+]^m + K_{d1}{}^m /a*(10^{-pH})^n + [K^+]^m(10^{-pH})^n)$$

According to the electrophysiological data on E71A mutant, where the proton binding is isolated from the potassium binding, the fitted hill coefficient is around 4.4, indicating high cooperativity between monomers in the proton binding.[41] In our experiment on the H25R&E118A potassium titration data, where the potassium binding is isolated from the proton binding, based the steep slope of the titration curve, we conclude that the potassium ion binding is also highly cooperative. Therefore, we assume only the four major species in the thermodynamic cycle are dominated; by limiting states with partial ligand binding, it greatly simplify our analysis of the system.

In SSNMR study, in the potassium affinity measurement, we are able to measure the apparent affinity, and based on above assumption, it is the potassium concentration when the following equation is met:

$$Po\ (PK_m) + Po\ (PK_mH_n) - [Po(P) + Po\ (PH_n)] = 0 \quad (3.12)$$

which leads to the following equation:

$$[K^+]^m = K_{d1}{}^m K_{d2}{}^n + (1/a)K_{d1}{}^m *(10^{-pH})^n /(K_{d2}{}^n + (10^{-pH})^n) \quad (3.13)$$

$$m*pKd = -\log(K_{d1}{}^m K_{d2}{}^n + (1/a)K_{d1}{}^m *(10^{-pH})^n) + \log(K_{d2}{}^n + (10^{-pH})^n) \quad (3.14)$$

When we use the equation $(1/a)\ K_{d1}{}^m = K_{d12}{}^m$, we acquire the following equation, in which it indicates that the measurable pKd (i.e. $-\log_{10}K_d$ value) is pH dependent:

$$pKd = -(1/m)\log(K_{d1}{}^m K_{d2}{}^n + K_{d12}{}^m *(10^{-pH})^n) + \log(K_{d2}{}^n + (10^{-pH})^n) \quad (3.15)$$

Based on the previous experimental ssNMR affinity data and electrophysiology pKa data, we are able to have an estimate of values of $K_{d1,}\ K_{d2,}\ K_{d12,}$ which are the apparent potassium affinity when the pH gate is closed, the apparent proton affinity when the K^+ is bound and the selectivity filter is in the

conductive form and the apparent potassium affinity when the pH gate is open. We applied the constraints from following data: 1. The apparent potassium affinity measured in SSNMR for WT-KcsA at pH 3.5, which is 14mM; at pH 3.5, based on our spectra in the titration, the pH gate stays protonated; therefore, the apparent K_d for the transition between PH_n and PK_mH_n (i.e. K_{d12}) is 14mM; 2. The apparent potassium affinity measured in SSNMR for F103A at pH 7.5, which is 2 uM; (See Chapter V) we did not use the affinity we acquired from WT-KcsA at pH7.5, as we found that at such a pH, the coupled transition happens between the pH gate and the selectivity filter. The coupling at F103A is significantly reduced, therefore, the apparent affinity K_{d1} between transition P and PK_m can be estimated with less systematic error. 3. The pKa value measured in electrophysiological experiments for the WT-KcsA channel activation, which is 4.3;[47] it is an estimate of the apparent affinity K_{d2}.

After we input these constraints, the parameters n, m, which are the stoichiometries for proton and potassium binding were modeled. We proposed several possible stoichiometries, based on previous experimental knowledge. In order to determine the stoichiometry, we applied two extra experimental data that we acquired by SSNMR as criteria. The two experimental data are the potassium affinity at pH 7.5 (4 uM) and at pH 5.0 (20 uM). The pKa and pH plots for various stoichiometries are shown in Fig.3.14 and the experiment data used as criteria are also plotted as dots. As we can see, the slope increases as the numbers of proton ions binding increases; on the contrary, the slope decreases as the number of potassium ions binding increases. The two best fits for the experimental data is that m:n =2:8, m:n =1:4.

Based on crystal structures, it is hypothesized that two potassium ions bound at the selectivity filter are needed to stabilize the conductive conformation of the selectivity filter. As we mentioned above, Posson et al identified that E118 and H25 are the two proton binding sites.[41] With all this information, we consider =2:8 as a better model for the proton and potassium ion binding. Then we will be able to plot the populations of the four dominated species in all pH and $[K^+]$ regions, which is a great tool for sample preparation and analysis. (Figure 3.15) However, we have limited experimental data for the n and m fitting. We expect that more experimental data, such more potassium affinities at other pH, can provide more validation to our conclusion.

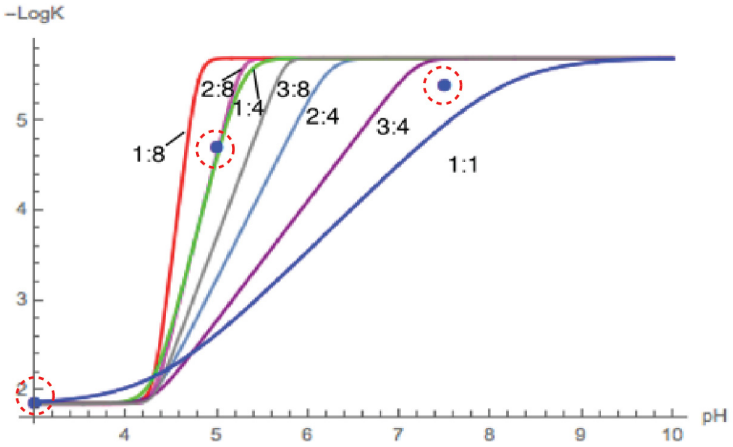

Figure 3.14 Stoichiometry modeling for the number of proton and potassium ions binding. The equation 3.15 is plotted with various m n values, which respects the number of proton ions and number of potassium ions respectively. The various ratios are indicated in the plots. Experimental constraints from WT-KcsA titration data are respected as dots (highlighted with dash circle) in the plot. As we can see, when m:n =2:8 or 1:4, the experimental data are fitted best.

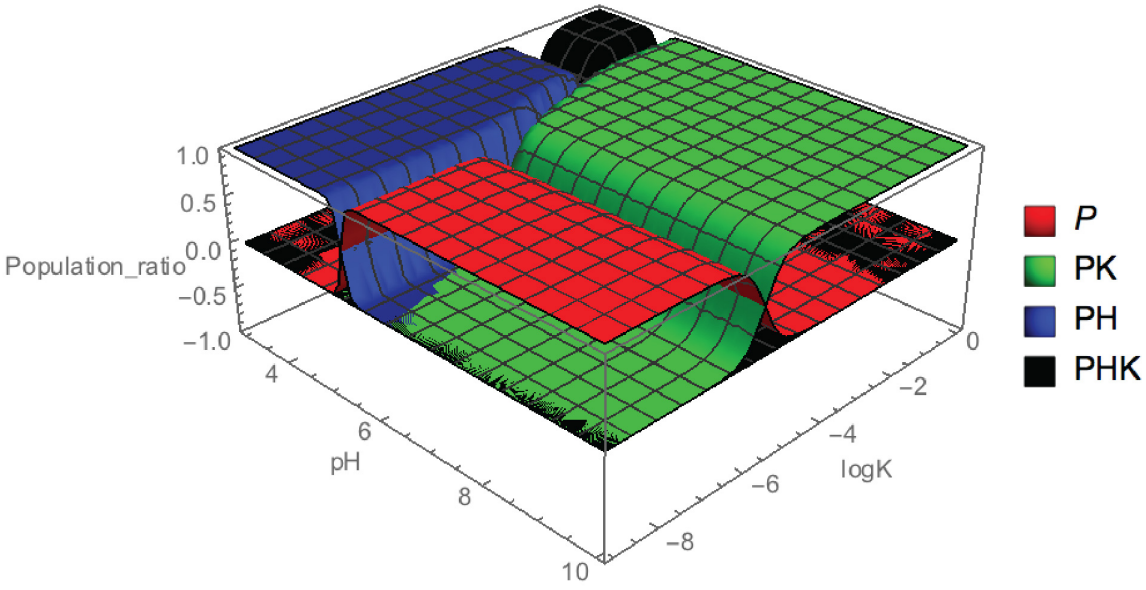

Figure 3.15. The populations of various states in the thermodynamic landscape are simulated. In this simulation, the assumption that m:n=2:8 is taken. The simulations also incorporates experimentally determined equilibrium constants. The simulation was done in the software Mathematica. (The code is in Appendix 4)

3. 3 Discussion and Conclusion

We offer insights into the slow allosteric transition underlying C-type inactivation, a vital gating mechanism in potassium channels that partly controls mean open time. This titration study, carried out in an authentic lipid environment, allowed us to prepare and stabilize functionally critical states, presumably closely related to the intermediates of electrophysiology experiments. Detailed information from SSNMR such as chemical shifts, therefore helps to form a more direct connection between structure and function.

We quantitatively probed the allosteric coupling strength for wild type channel in membranes using these pH-dependent ion titrations. We observe a difference of three-orders-of-magnitude in K^+ affinity over the typically used pH range, which indicates substantial transmembrane coupling. Quantification of the potassium affinities of KcsA under various conditions has been the subject for several previous studies, using different methods. Functional methods suggest that the affinity of the selectivity filter for K^+ at pH 7.5 (deactivated channel) is approximately 29 μM,[48] and inactivation at pH 3.5 is associated with ion loss with an affinity around 0.9 mM.[25] A different picture emerged in isothermal titration calorimetry experiments in detergents, which showed the potassium affinity to be 0.41 mM at pH 7.5.[42] The group of Shimada reported elegant solution NMR experiments with detergent-stabilized KcsA showing that the potassium affinity changes from 6 mM to 50 mM between pH 3.2 and pH 6.7 at 45 °C;[32] the pH dependence of potassium affinity in these studies is much weaker than estimates based on functional studies. Our experiments show a pH dependence that is much larger than these previously reported, and are more compatible with the available functional data and with the hypothesis that ion loss is the essential step of inactivation. Namely, we demonstrate a potassium affinity of 4 μM at pH 7.5, and 14 mM at pH 3.5.

We presume the difference between the solution NMR or thermo-calorimetric affinity measurements for KcsA and these SSNMR studies is due to our use of membrane bilayers, and conclude that dramatically stronger allosteric coupling occurs in the bilayer. The importance of the membrane environment for membrane protein integrity and function has been reported in numerous studies.[49–52]case of Yeast pyruvate kinase, in which pH modulates protonation state of various ionizable residues to ultimately allosterically affect the reactivation rates.[53]

Through this study we also stabilized the Activated state of a wild-type functional KcsA at low pH and high [K^+], with both the activation gate open (protonated pH sensor) and inactivation gate open (K^+ bound in the selectivity filter). The Activated state is normally an evanescent or metastable intermediate in functional studies of KcsA, and has been difficult to stabilize for structural characterization, requiring use of multiple mutations and other alterations in the system. Stabilizing this species can enable structural and dynamics studies by NMR in native bilayers.

3.4 Materials and Methods

NMR Sample Preparation ^{13}C-^{15}N uniformly enriched WT-KcsA and the mutant H25R&E118A-KcsA were prepared by overexpression in *Escherichia coli* JM83 cells in M9 minimum media using a tetracycline regulated expression vector pask90, as described previously.[24,54] Both constructs have an N-terminal hexa-histidine tag. The H25R&E118A mutant was a gift from Nimigean Lab at Weil Cornell Medical School. H25R&E118A stays a tetramer as indicated by SDS gels. KcsA was reconstituted into liposomes by reducing the detergent concentration through dialysis; the liposomes contain 9:1 ratio of 1,2-dioleoyl-*sn*-glycero-3-phosphoethanolamine (DOPE), 1,2-dioleoyl-*sn*-glycero-3-phospho-L-serine (DOPS) by mass, and 1:1 ratio of protein:lipid by mass. To prepare samples at acidic pH values, proteoliposomes were first dialyzed at room temperature against a 50 mM Tris, 50 mM KCl buffer at pH 7.5 with the desired potassium concentrations and then further dialyzed at 4°C against 10 mM sodium citrate buffer at pH 3.5 with the appropriate potassium concentration. NaCl was added, to achieve a consistent total concentration ([K^+] + [Na^+]) of 50 mM to keep the ionic strength constant in the titration series (except the sample with 80 mM [K^+]). After dialysis, liposomes were centrifuged using a Sorvall benchtop centrifuge at 4,125 rpm (3,697×g, 4°C) for 40 min. The pH values of the supernatants after centrifugation were verified to be within 0.1 unit of the desired pH value. The proteoliposomes were then subject to three freeze-thaw cycles to remove excess water. Finally, samples were packed into 3.2 mm Bruker rotors for NMR measurement.

NMR Data Collection and Processing NMR spectra were collected on a Bruker Avance 750 MHz (17.6 T) spectrometer, or a Bruker Avance III 600 MHz (14.1 T) spectrometer with a 3.2-mm E-free probe, at

MAS spinning frequencies of 12 kHz or 14 kHz. The Dipolar Assistant Recoupling Resonance (DARR) pulse sequence63 was used for 13C-13C correlation experiments with a 15 ms mixing period. Sample temperature was calibrated based on an external reference using methanol chemical shift64 to correct for heating during MAS spinning and RF-pulsing. All spectra were measured at 0 ± 2°C if the temperature is not otherwise specifically indicated. Carbon chemical shifts were referenced externally to the downfield adamantane line at 40.48 ppm. All spectra were measured at 0 ± 2°C if the temperature is not otherwise specifically indicated. All spectra were processed in NMRpipe55 with -30 Hz Lorentzian and 90 Hz Gaussian apodization; Sparky56 was used for spectral visualization and integration of cross peaks. The populations of the bound states for each residue were quantified by integrating the bound and apo cross-peaks of T74 (CB-CA), T75 (CB-CA, CA-CG) and V76 (CB-CG, CG2) on a 13C-13C 2D correlation (Fig. S2). The normalized population ratios of protein were calculated by averaging the population ratios of reporter residues T74, T75 and V76. The normalized bound state percentage was defined as Integral(bound)/[Integral(bound)+Integral(apo)]*100% for each residue. Normalized populations were fit to the binding expression below with Hill coefficient, n, equal to 1 (non-cooperative), where θ is the normalized population: $\theta = \frac{[K+]^n}{[K+]^n + Kd}$. The reported errors are dominated by the fitting error (Kd), which is roughly on the same scale of errors from peak integration and averaging.

3.5 References

1. Cui, Q. & Karplus, M. Allostery and cooperativity revisited. *Protein Sci.* **17,** 1295–307 (2008).
2. Dokholyan, N. V. Controlling Allosteric Networks in Proteins. *Chem. Rev.* **116,** 6463–6487 (2016).
3. Changeux, J.-P. & Edelstein, S. J. Allosteric mechanisms of signal transduction. *Science* **308,** 1424–8 (2005).
4. Maniatis, T. & Reed, R. An extensive network of coupling among gene expression machines. *Nature* **416,** 499–506 (2002).
5. MONOD, J., WYMAN, J. & CHANGEUX, J. P. ON THE NATURE OF ALLOSTERIC TRANSITIONS: A PLAUSIBLE MODEL. *J. Mol. Biol.* **12,** 88–118 (1965).
6. Koshland, D. E., Némethy, G. & Filmer, D. Comparison of Experimental Binding Data and Theoretical Models in Proteins Containing Subunits *. *Biochemistry* **5,** 365–385 (1966).
7. Hilser, V. J., Wrabl, J. O. & Motlagh, H. N. Structural and Energetic Basis of Allostery. *Ann. Rev. Biophys.* **41,** (2012).
8. Popovych, N. Dynamically driven protein allostery. *Nat. Struct. Mol. Biol.* **13,** (2006).
9. Ferreon, A. C. M., Ferreon, J. C., Wright, P. E. & Deniz, A. A. Modulation of allostery by protein intrinsic disorder. *Nature* **498,** 390–4 (2013).
10. Chakrapani, S., Cordero-Morales, J. F. & Perozo, E. A quantitative description of KcsA gating II: single-channel currents. *J. Gen. Physiol.* **130,** 479–96 (2007).
11. Chakrapani, S., Cordero-Morales, J. F. & Perozo, E. A quantitative description of KcsA gating I: macroscopic currents. *J. Gen. Physiol.* **130,** 465–78 (2007).
12. Thompson, A. N., Posson, D. J., Parsa, P. V & Nimigean, C. M. Molecular mechanism of pH sensing in KcsA potassium channels. *Proc. Natl. Acad. Sci. U. S. A.* **105,** 6900–5 (2008).
13. Liu, Y. S., Sompornpisut, P. & Perozo, E. Structure of the KcsA channel intracellular gate in the open state. *Nat. Struct. Biol.* **8,** 883–7 (2001).
14. Ostmeyer, J., Chakrapani, S., Pan, A. C., Perozo, E. & Roux, B. Recovery from slow inactivation in K+ channels is controlled by water molecules. *Nature* **501,** 121–4 (2013).
15. Cordero-Morales, J. F. *et al.* Molecular driving forces determining potassium channel slow inactivation. *Nat. Struct. Mol. Biol.* **14,** 1062–9 (2007).

16. Pan, A. C., Cuello, L. G., Perozo, E. & Roux, B. Thermodynamic coupling between activation and inactivation gating in potassium channels revealed by free energy molecular dynamics simulations. *J. Gen. Physiol.* **138,** 571–80 (2011).

17. Cheng, W. W. L., McCoy, J. G., Thompson, A. N., Nichols, C. G. & Nimigean, C. M. Mechanism for selectivity-inactivation coupling in KcsA potassium channels. *Proc. Natl. Acad. Sci. U. S. A.* **108,** 5272–7 (2011).

18. Cordero-Morales, J. F. *et al.* Molecular determinants of gating at the potassium-channel selectivity filter. *Nat. Struct. Mol. Biol.* **13,** 311–8 (2006).

19. Cuello, L. G. *et al.* Structural basis for the coupling between activation and inactivation gates in K(+) channels. *Nature* **466,** 272–5 (2010).

20. Gao, L., Mi, X., Paajanen, V., Wang, K. & Fan, Z. Activation-coupled inactivation in the bacterial potassium channel KcsA. *Proc. Natl. Acad. Sci. U. S. A.* **102,** 17630–5 (2005).

21. Rasmusson, R. L. *et al.* Inactivation of Voltage-Gated Cardiac K+ Channels. *Circ. Res.* **82,** 739–750 (1998).

22. Sanguinetti, M. C. & Tristani-Firouzi, M. hERG potassium channels and cardiac arrhythmia. *Nature* **440,** 463–9 (2006).

23. Jentsch, T. J. Neuronal KCNQ potassium channels: physiology and role in disease. *Nat. Rev. Neurosci.* **1,** 21–30 (2000).

24. Bhate, M. P. *et al.* Preparation of uniformly isotope labeled KcsA for solid state NMR: expression, purification, reconstitution into liposomes and functional assay. *Protein Expr. Purif.* **91,** 119–24 (2013).

25. Ader, C. *et al.* Coupling of activation and inactivation gate in a K+-channel: potassium and ligand sensitivity. *EMBO J.* **28,** 2825–34 (2009).

26. Bhate, M. P. & McDermott, A. E. Protonation state of E71 in KcsA and its role for channel collapse and inactivation. *Proc. Natl. Acad. Sci. U. S. A.* **109,** 15265–70 (2012).

27. Xu, Y., Bhate, M. P. & McDermott, A. E. Transmembrane allosteric energetics characterization for strong coupling between proton and potassium ion binding in the KcsA channel. *Proc. Natl. Acad. Sci. U. S. A.* **114,** 8788–8793 (2017).

28. Köpfer, D. A. *et al.* Ion permeation in K^+ channels occurs by direct Coulomb knock-on. *Science* **346,** 352–5 (2014).

29. Zhou, Y., Morais-Cabral, J. H., Kaufman, A. & MacKinnon, R. Chemistry of ion coordination and hydration revealed by a K+ channel-Fab complex at 2.0 A resolution. *Nature* **414,** 43–8 (2001).

30. Cuello, L. G., Jogini, V., Cortes, D. M. & Perozo, E. Structural mechanism of C-type inactivation in K(+) channels. *Nature* **466,** 203–8 (2010).

31. Wylie, B. J., Bhate, M. P. & McDermott, A. E. Transmembrane allosteric coupling of the gates in a potassium channel. *Proc. Natl. Acad. Sci. U. S. A.* **111,** 185–90 (2014).

32. Imai, S., Osawa, M., Takeuchi, K. & Shimada, I. Structural basis underlying the dual gate properties of KcsA. *Proc. Natl. Acad. Sci. U. S. A.* **107,** 6216–21 (2010).

33. Bhate, M. P. Mechanistic studies of ion binding and inactivation in the potassium channel KcsA by solid state NMR. (2012).

34. Valiyaveetil, F. I., Sekedat, M., Mackinnon, R. & Muir, T. W. Glycine as a D-amino acid surrogate in the K(+)-selectivity filter. *Proc. Natl. Acad. Sci. U. S. A.* **101,** 17045–9 (2004).

35. Jiang, Y. *et al.* Crystal structure and mechanism of a calcium-gated potassium channel. *Nature* **417,** 515–22 (2002).

36. Varga, K., Tian, L. & McDermott, A. E. Solid-state NMR study and assignments of the KcsA potassium ion channel of S. lividans. *Biochim. Biophys. Acta* **1774,** 1604–13 (2007).

37. Bhate, M. P., Wylie, B. J., Tian, L. & McDermott, A. E. Conformational dynamics in the selectivity filter of KcsA in response to potassium ion concentration. *J. Mol. Biol.* **401,** 155–66 (2010).

38. Jiang, Y. *et al.* The open pore conformation of potassium channels. *Nature* **417,** 523–6 (2002).

39. Ader, C. *et al.* A structural link between inactivation and block of a K+ channel. *Nat. Struct. Mol. Biol.* **15,** 605–12 (2008).

40. Gor'kov, P. L. *et al.* Using low-E resonators to reduce RF heating in biological samples for static solid-state NMR up to 900 MHz. *J. Magn. Reson.* **185,** 77–93 (2007).

41. Posson, D. J., Thompson, A. N., McCoy, J. G. & Nimigean, C. M. Molecular interactions involved in proton-dependent gating in KcsA potassium channels. *J. Gen. Physiol.* **142,** 613–24 (2013).

42. Lockless, S. W., Zhou, M. & MacKinnon, R. Structural and thermodynamic properties of selective

ion binding in a K+ channel. *PLoS Biol.* **5,** e121 (2007).

43. Lewandowski, J. R., Halse, M. E., Blackledge, M. & Emsley, L. Direct observation of hierarchical protein dynamics. *Science (80-.).* **348,** 578–581 (2015).

44. Chill, J. H., Louis, J. M., Baber, J. L. & Bax, A. Measurement of 15N relaxation in the detergent-solubilized tetrameric KcsA potassium channel. *J. Biomol. NMR* **36,** 123–36 (2006).

45. Liu, S. *et al.* Ion-binding properties of a K+ channel selectivity filter in different conformations. *Proc. Natl. Acad. Sci. U. S. A.* **112,** 15096–100 (2015).

46. Hulse, R. E., Li, Q. & Perozo, E. Up a Hydrophobic Creek with a Short Paddle. *Cell* **142,** 515–516 (2010).

47. Cuello, L. G. *et al. Design and characterization of a constitutively open KcsA*. *FEBS Letters* **584,** (2010).

48. Piasta, K. N., Theobald, D. L. & Miller, C. Potassium-selective block of barium permeation through single KcsA channels. *J. Gen. Physiol.* **138,** 421–36 (2011).

49. Francis I. Valiyaveetil, ‡ *et al.* Lipids in the Structure, Folding, and Function of the KcsA K + Channel †. *Biochemistry* **41,** 10771–10777 (2002).

50. Martens, C. *et al.* Lipids modulate the conformational dynamics of a secondary multidrug transporter. *Nat. Struct. Mol. Biol.* **23,** 744–751 (2016).

51. Song, Y., Mittendorf, K. F., Lu, Z. & Sanders, C. R. Impact of Bilayer Lipid Composition on the Structure and Topology of the Transmembrane Amyloid Precursor C99 Protein. *J. Am. Chem. Soc.* **136,** 4093–4096 (2014).

52. Sébastien F. Poget, Sean M. Cahill, and & Girvin*, M. E. Isotropic Bicelles Stabilize the Functional Form of a Small Multidrug-Resistance Pump for NMR Structural Studies. (2007). doi:10.1021/JA0679836

53. Susan-Resiga, D. & Nowak, T. The proton transfer step catalyzed by yeast pyruvate kinase. *J. Biol. Chem.* **278,** 12660–71 (2003).

54. Heginbotham, L., Kolmakova-Partensky, L. & Miller, C. Functional Reconstitution of a Prokaryotic K+ Channel. *J. Gen. Physiol.* **111,** 741–749 (1998).

55. Delaglio, F. *et al.* NMRPipe: A multidimensional spectral processing system based on UNIX pipes.

J. Biomol. NMR **6,** (1995).

56. Hediger, S., Meier, B. H. & Ernst, R. R. Cross polarization under fast magic angle sample spinning using amplitude-modulated spin-lock sequences. *Chem. Phys. Lett.* **213,** 627–635 (1993).

Chapter IV: Allosteric Coupling Pathway- Role of Residue F103

Portions of this chapter have been adapted from: Xu, Y., Bhate, M. P. & McDermott, A. E. Transmembrane allosteric energetics characterization for strong coupling between proton and potassium ion binding in the KcsA channel. *Proc. Natl. Acad. Sci. U. S. A.* **114,** 8788–8793 (2017).

4.1 Abstract

In the previous chapter, we show that the pH gate and the selectivity gate are strongly coupled. It is noteworthy that the intracellular pH gate (activation gate) and the extracellular selectivity filter (inactivation gate) are quite remote (> 30Å), so elucidating the molecular pathway for communication between the coupled domains is of great interest. The residue F103 has been shown to be critical for the coupling. In the chapter, we aim to test the participation of F103 in the allosteric coupling by NMR thermodynamic measurements via mutational analysis. Our results show that mutation of F103 to alanine significantly reduces the allosteric coupling strength and increases potassium affinity at acidic pH. These results are consistent with the observation that F103A significantly reduces inactivation in electrophysiology.

4.2 Introduction

4.2.1 Introduction to protein allosteric pathway

In the previous chapters, we provided a general introduction to allosteric coupling, which is ubiquitously discovered in biological systems to facilitate various functions.[1–3] In chapter II, we mentioned briefly the many thermodynamic models developed to provide a theoretical framework for quantitatively analyzing the system.[4] In studies of allosteric coupling systems, much effort has been spent understanding which thermodynamic model best fits a particular system. These studies are particularly important since fully understanding the allostery is essential to predicting protein response to external perturbations. Another important type of study is that which pinpoints the molecular mechanism that supports such allosteric machinery.[5,6] It has been suggested that these two aspects are closely related.[7] Here we provide a more detailed introduction to the allosteric thermodynamics models and the associated molecular machinery, which is normally named the allosteric pathway.[5]

The understanding of allosteric systems has been greatly advanced with the development of techniques to probe the structures and dynamics of minor species. Two general mechanisms were initially proposed to explain the coupling effect: one is the induced fit model, in which the binding of ligands at one site induces a new conformation that changes the affinity at another site for a same or different type of ligand. In another model, the binding event only shifts the populations of a set of conformations to favor one of the conformations[8]. In contrast to induced fit model, there is no new conformation generated, but only populations get changed; since different conformation have different

functional activities, function can get tuned accordingly. Recent studies reveal a new type of allosteric coupling model, named dynamic allosteric coupling, in which no conformation changes are required for functional activities, but the ligand binding changes the dynamic properties of the protein, thus triggering the coupling.[9] Examples of dynamic allosteric coupling have already been found in several systems.[10–12] All of these thermodynamic models can be extended to a more general description of the protein as a conformational ensemble with population weighted by its free energy; the external perturbation will change the population distribution to favor some biological events. [13]

One of the main challenges is to figure out the molecular pathway that is responsible for the propagation of the signal from perturbation site to the distal active site. In the thermodynamic description of allostery, of course, direct contacts between residues are not necessary for ligand binding to influence the energetics of the various conformations[4]. The energetic contribution can be due to entropy, enthalpy, or a combination of both which influences the conformational ensemble after ligand binding. In some cases in dynamic allosteric coupling, it is not always possible to figure out a pathway because the coupling is actually driven entropically, and none of the residues is specifically important for the allosteric coupling.[14]

However, there are many cases- especially those described in terms of the induced fit model of allostery- in which a molecular pathway can be elucidated, and changes in the conformations or dyanmics of specific amino acids are found to be responsible for the allostery, perhaps through altered steric contacts. One important example is of course the salt bridges in hemoglobin whose structure is altered upon binding of oxygen, which definitively contributes to the allostery in that system. [15]

Different methods have been developed to probe allosteric coupling pathway, such as sequence analysis[16], which relies on the philosophy of coevolution theory of important residues; random mutation methods, which combined with functional assays that provide direct evidence.[17] NMR has also been applied by covariance analysis on the chemical shift changes and successfully applied to the case of Abelson tyrosine kinase. [18] In Chapter V we introduce another approach for NMR detection of allostery participants.

In this chapter, we will focus on a single residue in the allosteric pathway and demonstrate its influence upon the thermodynamic cycle constructed in Chapter III.

4.2.2 Allosteric coupling pathways in KcsA

In the Chapter III, we have confirmed that the pH gate in KcsA is tightly allosterically coupled to the selectivity filter, propose that this contributes to the phenomenon of C-type inactivation, and describe the thermodynamic relationship between the states involved in inactivation. It is also of great interest to elucidate the molecular pathway for communication between the coupled domains, since the selectivity filter and the pH gate are respectively located at the extra-membrane and intra-membrane surfaces. The identification of such residues can significantly strengthen the mechanistic picture of the allosteric coupling.

F103 has been previously suggested as a possibly important allosteric residue.[19] F103 is located at the hinge region of the protein, distal to both the selectivity filter and the pH gate. Prior evidence from crystallography and molecular simulations suggested that steric interactions between T74 at the base of the selectivity filter, F103 in the TM2 "hinge" (second transmembrane helix hinge), and I100 from a neighboring monomer are involved in the allosteric coupling.[19–21] Experimental support for this role consisted of changes in inactivation upon mutation of F103A. Here we provide a direct experimental test of the quantitative contribution of F103A to allosteric coupling. The quantitative contribution of F103 to the allosteric coupling was probed by using a mutant, F103A. We speculated that if the F103A mutant "loosens" this network, the energetic coupling between the pH gate and the selectivity filter will become much weaker, rendering K^+ affinity at the selectivity filter relatively insensitive to environmental pH, and in particular we predicted that it would not release K^+ at low pH.

4.3 Results

4.3.1. F103A Stays as Tetramer in the Liposome

F103A-KcsA was expressed in JM83 E Coli system with a good yield. From the electrophoresis experiment, it showed that the F103A mutant is not as stable as the WT-KcsA, since there is a noticeable increase in the intensity of monomer band.(Figure 4.1a) However, a more gentle measurement by FPLC indicated that the majority of protein sample is in the tetramer state even in detergent.(Figure 4.1b) As it was known that the lipid environment could stabilize the tetramer feature of KcsA, thus we hypothesized that the F103A mutant stays as tetramer in liposomes. This hypothesis was confirmed by our SSNMR

measurement of the mutant, which shows an overall homologous structure to the WT channel. (Figure 4.2)

a

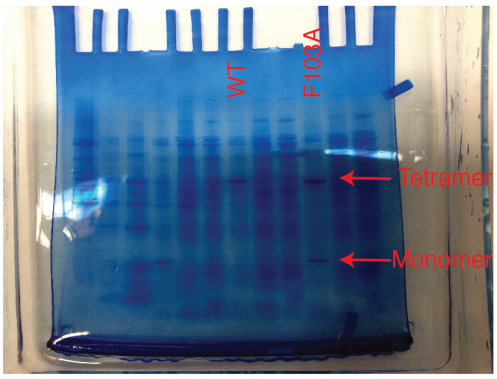

b

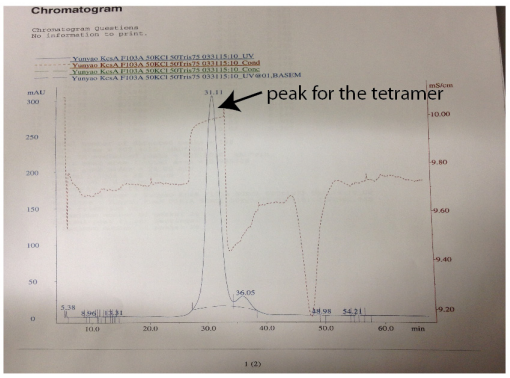

Figure 4.1 F103A is not stable as WT-KcsA, but stays as a tetramer. (a) From the SDS-page, we can see that there is signicant increase on the band for momomer in the F103A. (b) From the chomotography result, the peak where the F103A comes out matches the position calibrated as peaks for a tetramer using a WT-KcsA.

4.3.2. Electrophysiology Study Confirmed that F103A is Less Inactivated.

Perozo et al studied the single channel recording and macroscopic behaviors of the F103A mutant and shows that the inactivation in F103A is significantly reduced and the open probability in the single channel recording experiment is much higher than WT.[20] More interestingly, they found that F103A could rescue the enhanced inactivation behavior of an E71H mutant in the double mutant. In order to confirm the functions of our mutant samples, we carried out similar single channel recording experiments on the F103A mutant. As shown in Figure 4.3, the open probability of F103A is much higher than the one of WT-KcsA, which confirms that the mutant we made is functional and behaved as indicated in the literature. [20]

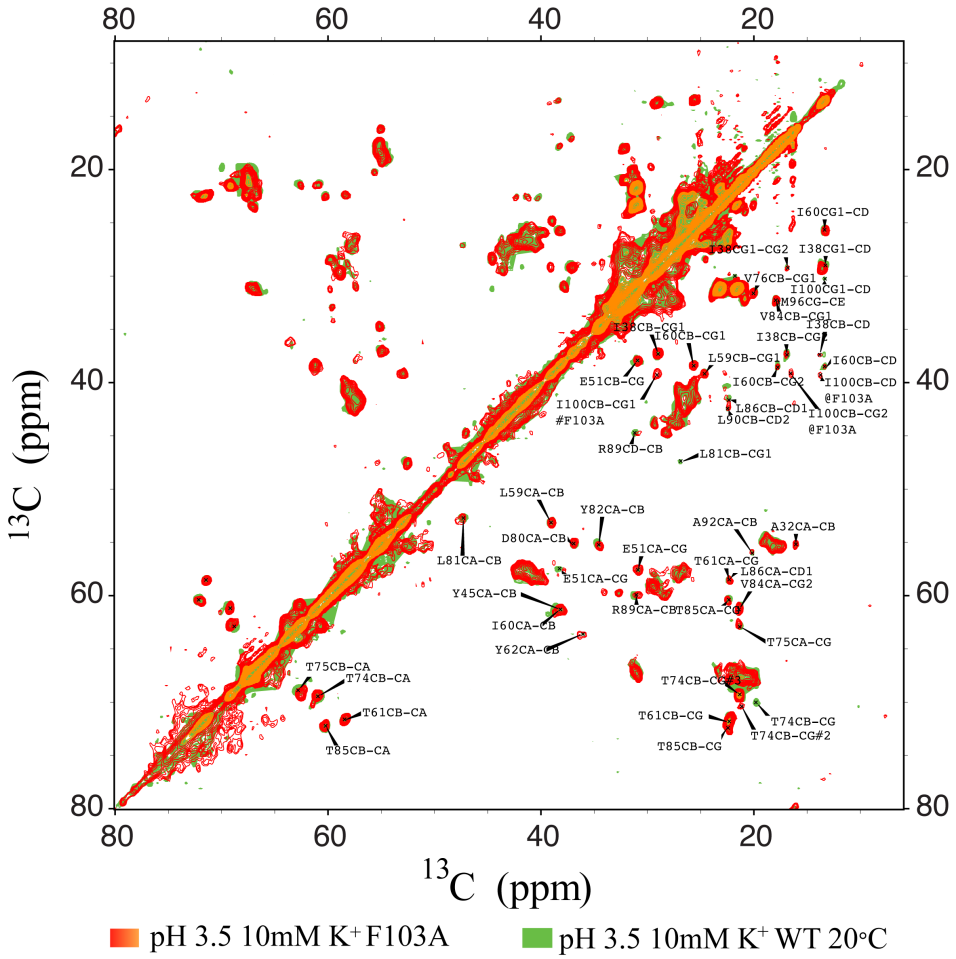

Figure 4.2. Comparison of 2D homonuclear ^{13}C spectra of wild-type KcsA vs. F103A shows that the chemical shift changes displayed in F103A are specific to the hinge residues. As illustrated by this overlay, the great majority of peaks in the wild-type channel are identical to the peaks in F103A. Specific exceptional changes have been seen in I100 and T74.

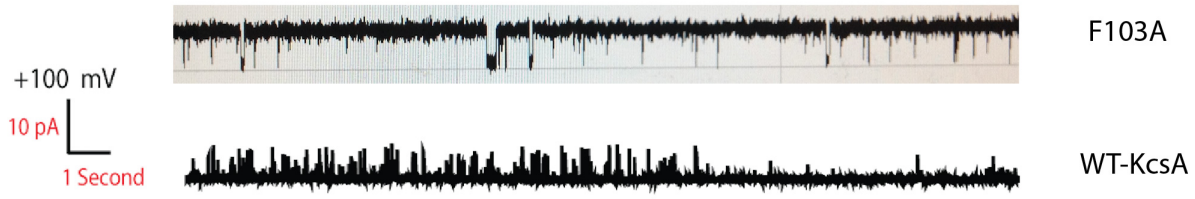

Figure 4.3. Representative traces for F103A mutant and WT-KcsA indicate that F103A is inactivationless. Single channel recording measurement were conducted on F103A mutant and WT-KcsA. In F103A, the

channel is mostly conducting with occasional closing; while in the WT-KcsA, the channel is mostly closed with occasional conducting.

4.3.3. Allosteric Coupling Strength is Reduced in F103A.

In Chapter III, we measured the allosteric coupling strength in the WT sample . This enables us to study the effect of mutations on the allosteric coupling. Therefore, we measured the potassium affinities of F103A at both pH 7.5 and 3.5 to investigate how much the allosteric coupling strength is changed by the single mutation.

As we mentioned above, the F103A mutant displayed high quality NMR spectra, which are highly overlaid with those of the WT samples. Many marker peaks for conformational changes identified in the WT samples are still useful in the F103A mutant. However, the energetics of the transition between the bound and unbound conformation are greatly changed. As seen in Figure 4.3, while WT-KcsA shows almost equal populations of the K^+-bound and K^+-unbound conformations at pH 3.5 10mM K^+, in the F103A mutant the selectivity filter stays mostly K^+-bound, indicating that the mutant has a tighter affinity for potassium ions at low pH. This implies that the activation gate, where protons bind, has been partially decoupled from the selectivity filter, which therefore retains a high potassium affinity even at lowered pH.

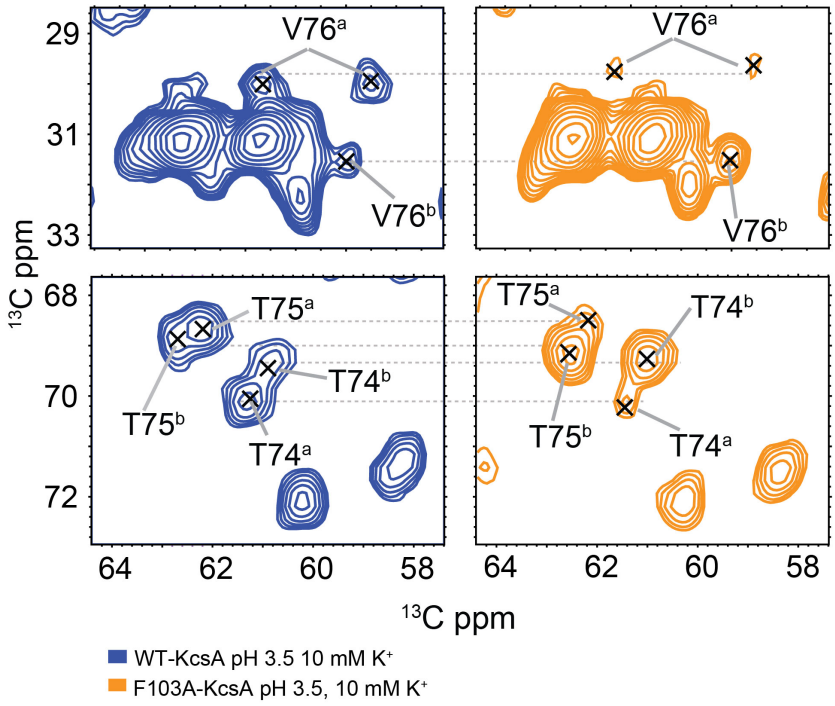

Figure 4.4. Spectra of WT-KcsA (blue) are compared with those of the F103A mutant (orange), exhibiting marker peaks in the selectivity filter. Superscripts refer to the K^+ **a**po and **b**ound states respectively. The chemical shift values for WT and F103A are nearly identical in both the bound and apo states, which simplifies our analysis (no reassignment needed) and indicates that F103A minimally perturbs the structure (see Supplementary Fig.4 for the full overlay). In contrast, the relative populations of the states change significantly between F103A (pH3.5 10mM K^+, 9% apo) and wild type (pH3.5 10mM K^+, 57% apo).

Quantitative analysis of full titration experiments on F103A at both pH 7.5 and pH 3.5 showed that, the mutant channel F103A indeed exhibits much weaker allosteric coupling. As seen in Figure 5.5, the K^+ affinity of the F103A ($K_{apparent}$ = 2 ± 1 μM) is comparable to that of WT-KcsA at a neutral pH, while at acidic pH, the affinity is much tighter ($K_{apparent}$ = 0.32 ± 0.10mM), which indicates a significantly reduced allosteric coupling strength (Fig. 4.5) (α=160; contrasted with 3,500 for WT-KcsA under the same conditions) (see Chapter III for the definition of α). These results are interesting in light of electrophysiology studies on mutant E71H-F103A, where the mutant channel shows significant conductance despite the presence of the strongly inactivating mutation E71H.[19] We note that these data provide strong additional support for the hypothesis that ion loss is a key step of the inactivation process:

F103A is expected to be virtually inactivation-less from prior studies, whereas our new NMR results on F103A indicate it does not release K^+ ions upon activation.

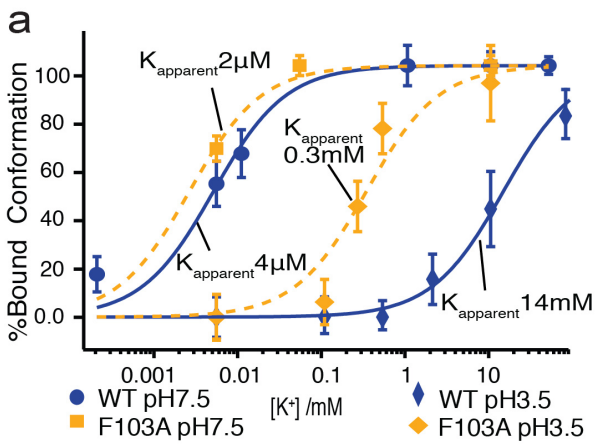

b

	WT	F103A
pH3.5 affinity	14 mM	0.3 mM
pH7.5 affinity	4 μM	2 μM
Allosteric factor α	3,500	150

Figure 4.5. F103 is a critical residue in the allosteric pathway. (a) The potassium ion titration curves of mutant F103A are compared at neutral and acidic pH, with those for the wild-type channel to contrast the affinity and coupling changes. (b) The allosteric coupling strength is significantly weaker for mutant F103A as compared to WT-KcsA.

4.3.4. Chemical shift changes indicate local structure contact with F103

Even though NMR chemical shifts of F103A show high overlay with those in WT-KcsA in both the bound and unbound conformations, (Fig. 4.2), we did observe perturbations for specific residues, such as I100, which is proximal to F103. As mentioned above, I100 is also suspected to be important in the coupling network.[21,2] We speculate that the dramatic chemical shift perturbation is caused by the change in environment of I100. In F103A mutant, the strong interaction between I100 and F103 during channel activation is absent (Figs. 4.6 c-h). The side chain CG of T74 is also sensitive to the mutation F103A: in WT-KcsA, CG shows a large chemical shift change in the transition from bound to apo state; in contrast, in F103A, the CG chemical shift does not change even though the backbone shows the same structural transition (Figs. 4.6c-h). These observations are consistent with the hypothesis that steric contacts occur between the aromatic ring of F103 and the T74 sidechain during inactivation.

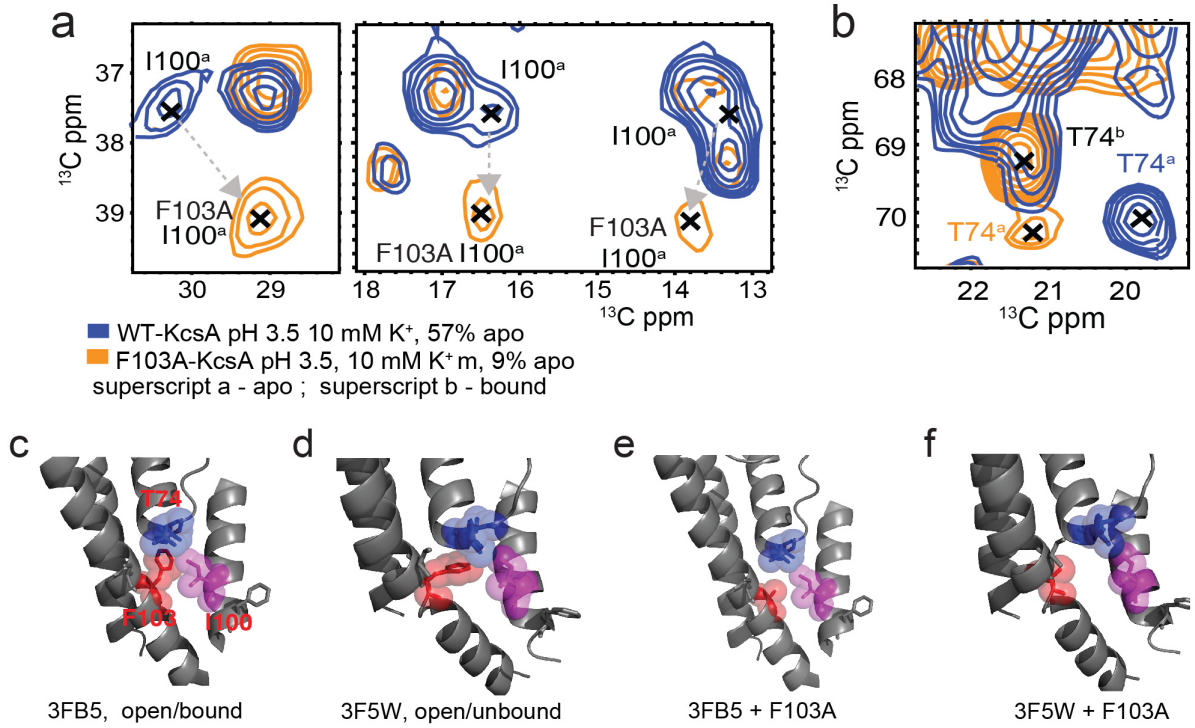

Figure 4.6. Specific chemical shift perturbations are observed for the F103A mutant. (a) Specific chemical shift perturbations are observed for the F103A mutant, as compared with the WT-KcsA, underscoring the important interactions between F103 and I100 and with T74. Peaks in spectrum are I100 (CB-CG1, CB-CG1 CB-CD), respectively. In WT-KcsA, I100 shows a perturbation in the peaks associated with the bound, putatively Activated state: the peaks are missing or broadened due to dynamics or heterogeneity. Similarly, the bound state peaks for I100 in F103A mutant, where allostery has been reduced, are also missing; but the apo state peaks shows significant chemical shift change, especially at CB. (b) Similarly T74 sidechain correlations show changes in the apo state (putative Inactivated state) between the wild type and the F103A mutant. (c-f) Crystal structure analysis reveals that the steric contact between T74, I100 and A103 is reduced in the F103A mutant compared to WT-KcsA. Steric contact between F103 (red) and I100 (magenta) occurs between monomers in the tetrameric structure. Contact between F103 (red) and T74/T75 (blue) particularly in the apo state can be seen for the WT sample in both the bound state (c, PDB 3FB5) and in the apo state (d, PDB 3F5W). Our data is consistent with a model in which the clash is largest for the Activated state. This steric clash is relieved when the bulky F103 sidechain is mutated to alanine (e, f, made with Pymol).

4.3.5. Temperature Effect on K^+ Affinity Change: Dissecting Coupling Energetics.

One great advantage of NMR study of biological system is the ease of applying a wide range of temperatures to the system so that the thermodynamics of processes can be further dissected. Here, we measured ion affinities at various temperatures for neutral WT-KcsA, pH 3.5 WT-KcsA, and the F103A in order to dissect the energetics of inactivation into enthalpic and entropic contributions. The results are shown in the Table 5.1.

Table 5.1. Summary of K^+ affinities at various pH conditions and temperatures for WT-KcsA and F103A mutant. The affinities for were computed by simulating data using Hill equation.

Construct	pH	Temperature	K^+ $K_{apparent}$ (mM)
WT	3.5	273K	14 +/-1
WT	3.5	293K	1.0 +/- 0.2
WT	7.5	258K	0.003+/- 0.001
WT	7.5	270K	0.004+/-0.001
WT	7.5	283K	0.005+/-0.002
F103A	7.5	273K	0.002+/-0.001
F103A	7.5	290K	0.0006+/-0.0005
F103A	3.5	273K	0.035+/-0.015

To calculate the enthalpy (ΔH) and entropy (ΔS) of the transitions, we use the Van't Hoff equation (Equation 5.1). This is based on the assumption that the heat capacity C_p is small, which means that ΔH is essentially temperature insensitive and the ΔS is also treated as constant.

$$-\ln K_d = -\frac{\Delta H}{RT} + \frac{\Delta S}{R} \tag{5.1}$$

Taking the date from the table 5.1, a plot of $\ln(K_d)$ against inverse temperature (1/T) is shown in Figure 5.7. The slope of the plot yields $\Delta H/R$; the intercept yields $-\Delta S/R$. The results of these calculations at neutral and acidic pH are shown below in Figure 5.8C. $\Delta H_{neutral}$= -12 ±3 KJ.mol^{-1}; $\Delta S_{neutral}$= 0.06 ±0.01 KJ.K^{-1}.mol^{-1}; ΔH_{acidic}= 88±5 KJ.mol^{-1}; ΔS_{acidic}= 0.36±0.02 KJ.K^{-1}.mol^{-1}. The $\Delta H_{neutral, F103A}$= 47 ±8 KJ.mol^{-1}; $\Delta S_{neutral, F103A}$= 0.28 ±0.02 KJ.K^{-1}.mol^{-}.

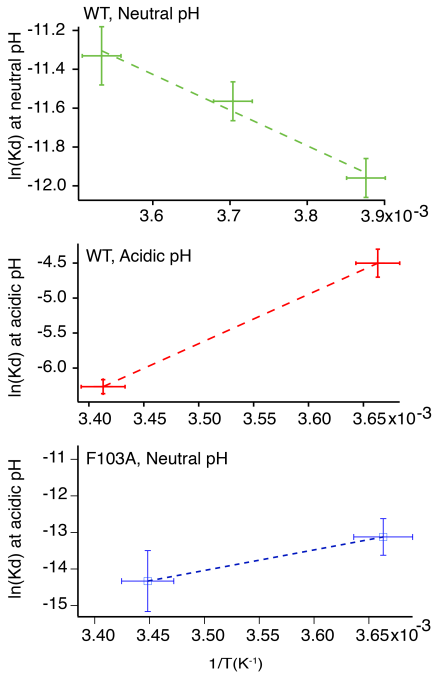

Figure 4.7. The temperature effect on the transition from apo to bound state at both neutral and acidic pH. For the neutral pH, the temperature is increased form 258K to 283K, and for acidic pH sample, the temperature is increased from 273K to 293k. The affinities estimated in Table S1 are used for the plots. Based on the slope and interception of the fitting, we estimated the enthalpy $\Delta H_{neutral}$= -12 ±3 KJ.mol^{-1} and entropy $\Delta S_{neutral}$=0.06 ±0.01 KJ.K^{-1}.mol^{-1} at the neutral pH transition process; and the enthalpy ΔH_{acidic}= 88±5 KJ.mol^{-1} and entropy ΔS_{acidic}= 0.36±0.02 KJ.K^{-1}.mol^{-1}. (See Supplementary Data processing). For the F103A mutant at neutral pH, the measurement was done on the pH 7.5 F103A sample; the result shows: $\Delta H_{neutral, F103A}$= 47 ±8 KJ.mol^{-1}; $\Delta S_{neutral, F103A}$= 0.28 ±0.02 KJ.K^{-1}.mol^{-1}.

These results can be used to once again estimate the strength of the allosteric coupling. Previously we estimated the allosteric coupling from comparing the K_{eq} at the two pHs. We can also estimate the allosteric coupling strength from the enthalpy and entropy at the two pHs by assuming that $\Delta\Delta G=\Delta\Delta H-T\Delta\Delta S$. Using this equation, the allosteric coupling strength at 273K is -18.1 ± 16 KJ.mol^{-}and at T= 293K, $\Delta\Delta G=\Delta\Delta H-T\Delta\Delta S$ = -11.1 ± 17 KJ.mol^{-1}. These results show consistency to the calculated allosteric coupling strength through comparison of the K_D (-19 ± 2 KJ.mol^{-1})^4. It also implies the coupling energy decreases as temperature increases.

At neutral pH, the system is highly coupled because the pH gate can adopt a variety of conformations based on the ambient potassium, as demonstrated by chemical shift measurements by Wylie and coworkers. Either lowering the pH or mutating F103A essentially isolates the potassium binding

transition; at acidic pH, because the pH gate is forced open, and for F103A because the coupling is weakened. We see that ion binding at the selectivity filter and the associated structural changes have an unfavorable enthalpy (Figure 58a, red pointer), as seen in the positive ΔH value for both WT-KcsA at pH 3.5 and F103A mutant where it is assumed that the pH gate is kept isolated (Fig. 5.8c). However, when potassium binding is *coupled* to the pH gate opening the net reaction is enthalpically driven, as seen by the negative ΔH value in the WT-KcsA at neutral pH. (Fig. 5.8c).

Dissecting the various contributions to ΔH quantitatively is not possible. Here we offer a number of speculative contributions to the observed enthalpy and entropy changes based on former knowledge of KcsA. First we consider the observed positive enthalpy of potassium binding, breaking it down into isolated events. We can assume that the isolated K^+ binding event at the selectivity filter has a negative enthalpy due to the binding energetics. This is accompanied by a global structural change at the selectivity filters whose energetics are unknown. However, a third event occurring along with K^+ binding is the release of bound waters at the back of the selectivity filter, based on computational modeling and X-ray crystallography.[22,23] Hydrogen bonds between waters and residues Y78 and D80 would be broken,[24,25] presumably at a huge enthalpic cost ($\Delta H_{app} > 0$).(Fig.5.8b). Thus, we observe based on the $\Delta H_{3.5}$ that the overall binding transition is not enthalpy-favorable but is driven mainly by entropy (Fig. 5.8c). The entropy change comes from two parts; the first part is associated with freeing bound water molecules ($\Delta S_{app}>0$).[22,23] The second part is associated with ~~the~~ increasing dynamics at residues at the out month and the selectivity filter ($\Delta S_{app} > 0$). [26]

However, as mentioned previously, when it occurs in a coupled reaction (Fig. 5.8a, blue pointers), there is an additional contribution from the pH gate, which turns the whole process into enthalpy-favorable. The coupled process of deprotonation and channel closing at neutral pH might be expected to gain free energy by reforming the hydrogen bond network at the activation gate and/or by releasing potential steric clashes in the hinge areas ($\Delta H_{app}<0$); but it might involve an entropy cost because the C-terminal helix may become restrained ($\Delta S_{app}<0$).[27–29] In this sense, our measured data show a consistent picture with former knowledge gained from various studies.

a

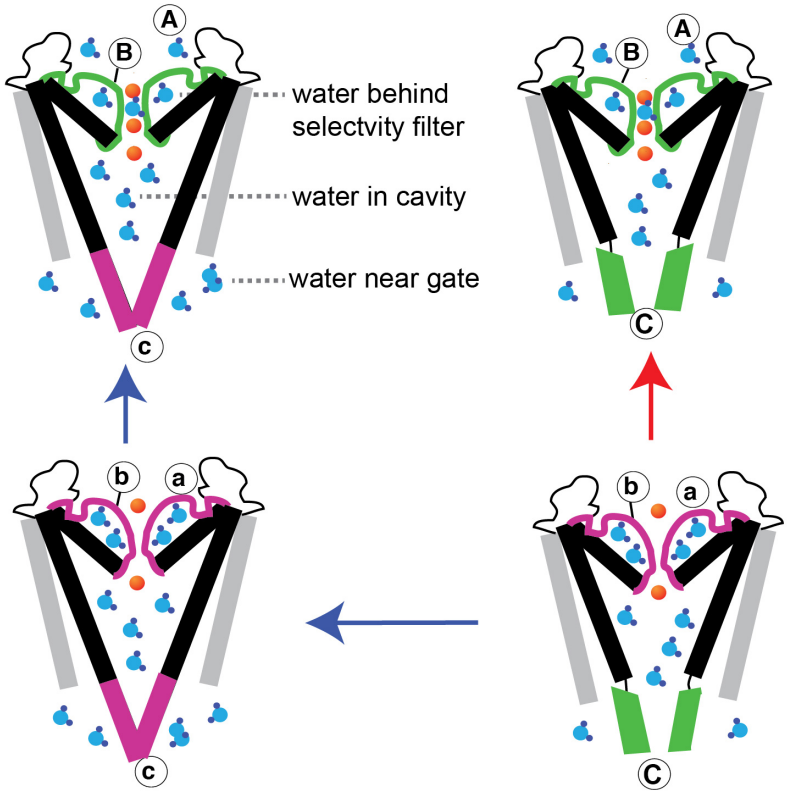

b

Transition	Labels	Processes	ΔH	ΔS
K+ binding at the selec-tivty filter	a → A	Bound water at the back of the selectivity filter is released; hydro-gen bond network between H_2O and residues breaks	+	+
	b → B	K^+ binding, global structural change at the selectivity filter, outer vestible and the hinge; higher flexibilty at the outer vestible.	?	+
Closing of the pH gate	C → c	The hydrogen bond networking at pH gate reforms and closing the pH gate releases a steric clash; the C-terminal helix gets restrained.	-	-

c

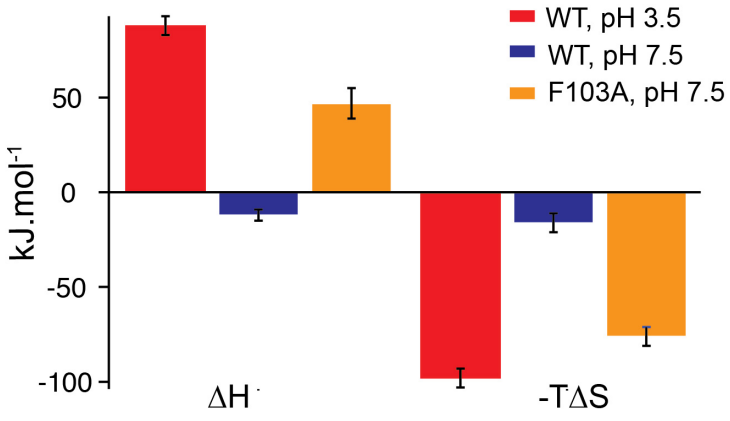

Figure 4.8. Thermodynamic analysis of structural transitions at neutral and acidic pH. (a,b) Schematic graph shows various contributions to the ΔH and ΔS in different transitions. We assume an isolated transition at selectivity filter at acidic pH (red pointer); a coupled transition between selectivity filter and pH gate at neutral pH (Blue pointers). The (a to A, b to B) show shared transitions at selectivity filter. The (C to c) process shows an extra coupled transition at neutral pH. For simplicity of analysis, we assume the same ΔH and ΔS values for transitions at selectivity filter at neutral ($\Delta H^1_{pH7.5}$, $\Delta S^1_{pH7.5}$) and acidic pH(($\Delta H_{pH3.5}$, $\Delta S_{pH3.5}$). (c) shows the distinctive values of ΔH and $-T^*\Delta S$ (T assumed as 273K) at neutral (blue) and acidic (red) pH for wild-type, which is consistent to the analysis in (b) and indicates different structural transitions at neutral and acidic pH. The thermodynamic values for F103A mutant at neutral pH (yellow), are closer to those for WT at acidic pH due to weaker allosteric coupling in F103A, in which the transition is localized to the selectivity filter (a to A, b to B), similar to in wild-type at acidic pH.

While the above analysis overlooked the contribution from the lipids, the similarity of the F103A energetics to the low pH energetics indicates that our analysis is likely still valid. As mentioned above, we consider both F103A and the low pH condition to be "uncoupled" with respect to potassium binding. Based on our results and others,[20] replacement of bulky F103 for alanine greatly disrupts the coupling between the pH gate and the selectivity. Therefore, the structural transition at the selectivity filter in F103A at neutral pH is presumably close to that for WT-KcsA at pH3.5 (Fig. 5.8a, red pointer), even though their conformations at the pH gate are different. The measured ΔS_{app} and ΔH_{app} for the F103A at pH 7.5 are closer to those of WT-KcsA at pH 3.5 rather than at pH 7.5 (Figure 5.8c), indicating that the contribution from the lipids is not significant and our analysis above are probably valid.

4.5. Methods

Sample preparation ^{13}C-^{15}N uniformly enriched mutant F103A-KcsA were prepared by overexpression in *Escherichia coli* JM83 cells in M9 minimum media using a tetracycline regulated expression vector pask90, as described previously.[30,31] The KcsA-F103A mutant was prepared using a QuikChange Lighting Site-Directed Mutagenesis kit (Agilent Technologies) and verified by gene sequencing (Genewiz). F103A-KcsA is less stable as a tetramer compared to WT-KcsA-KcsA, as indicated by SDS gels, but stay as tetramer revealed by size-exclusion chromatography. The reconstitution protocol and

dialysis protocol for preparing samples for specific potassium ion concentration and pH are the same as indicated in the last chapter.

Electrophysiology F103A and WT KcsA purified protein was reconstituted into liposomes (3:1 POPE/POPG) at a concentration of 1 μg per mg of lipid, and stored at −80°C, as described previously.[32] The protocol is attached in the Appendix 5. Liposomes, thawed on the day of use and sonicated briefly, were applied to artificial lipid bilayers made of 3:1 POPE:POPG dissolved in decane at a concentration of 10mg/ml. The lipid bilayers are formed over a 100 μm diameter hole in a transparency partition separating 2 aqueous chambers in a horizontal lipid bilayer setup, as described.[32] The *trans* recording chamber contained a buffer solution with 10 mM succinate, pH 4.0, 100 mM KCl, and the *cis* chamber (where liposomes are applied) contained a buffer solution with 10 mM HEPES, pH 7.0, 100 mM KCl. Current traces were recorded under voltage-clamp at +100 mV with an Axopatch 200B amplifier (Molecular devices), sampled at 20 kHz.

NMR measurements The NMR measurement is the same as we did in the chapter II, which is not further discussed here. For the various temperature experiments, we waited around 20mins for the sample temperature to reach equilibrium with the set VT temperature. The real sample temperatures were adjusted by methanol proton NMR calibration.[33]

4.6 Reference:

1. May, L. T., Leach, K., Sexton, P. M. & Christopoulos, A. Allosteric Modulation of G Protein–Coupled Receptors. *Annu. Rev. Pharmacol. Toxicol.* **47,** 1–51 (2007).
2. Peters, C. J., Fedida, D. & Accili, E. A. Allosteric coupling of the inner activation gate to the outer pore of a potassium channel. *Sci. Rep.* **3,** 3025 (2013).
3. Borthakur, S. *et al.* Mapping of the CD23 Binding Site on Immunoglobulin E (IgE) and Allosteric Control of the IgE-fc EpsilonRI Interaction. *J. Biol. Chem.* **287,** 31457 (2012).
4. Xu, Y., Bhate, M. P. & McDermott, A. E. Transmembrane allosteric energetics characterization for strong coupling between proton and potassium ion binding in the KcsA channel. *Proc. Natl. Acad. Sci. U. S. A.* **114,** 8788–8793 (2017).
5. Elber, R. Simulations of allosteric transitions. *Curr. Opin. Struct. Biol.* **21,** 167–72 (2011).
6. Boulton, S. & Melacini, G. Advances in NMR Methods To Map Allosteric Sites: From Models to Translation. *Chem. Rev.* **116,** 6267–6304 (2016).
7. Changeux, J.-P. 50 Years of Allosteric Interactions: The Twists and Turns of the Models. *Nat. Rev. Mol. Cell Biol.* **14,** 819 (2013).
8. Csermely, P., Palotai, R. & Nussinov, R. Induced Fit, Conformational Selection and Independent Dynamic Segments: An Extended View of Binding Events. *Trends Biochem. Sci.* **35,** 539 (2010).
9. Itoh, K. & Sasai, M. Entropic mechanism of large fluctuation in allosteric transition. *Proc. Natl. Acad. Sci. U. S. A.* **107,** 7775–80 (2010).
10. Tsai, C.-J. C.-J., del Sol, A. & Nussinov, R. Allostery: absence of a change in shape does not imply that allostery is not at play. *J. Mol. Biol.* **378,** 1–11 (2008).
11. Weinkam, P., Chen, Y. C., Pons, J. & Sali, A. Impact of mutations on the allosteric conformational equilibrium. *J. Mol. Biol.* **425,** 647–61 (2013).
12. Ma, J. & Karplus, M. The Allosteric Mechanism of the Chaperonin GroEL: a Dynamic Analysis. *Proc. Natl. Acad. Sci. U. S. A.* **95,** 8502 (1998).
13. Wrabl, J. O. *et al.* The role of protein conformational fluctuations in allostery, function, and evolution. *Biophys. Chem.* **159,** 129–41 (2011).
14. Popovych, N., Sun, S., Ebright, R. H. & Kalodimos, C. G. Dynamically driven protein allostery. *Nat.*

Struct. Mol. Biol. **13,** 831–8 (2006).

15. Szabo, A. & Karplus, M. A Mathematical Model for Structure-Function Relations in Hemoglobin. *J. Mol. Biol.* **72,** 163 (1972).
16. Süel, G. M., Lockless, S. W., Wall, M. A., Ranganathan, R. & S|[uuml]|el, G. M. Evolutionarily conserved networks of residues mediate allosteric communication in proteins. *Nat. Struct. Biol.* **10,** 59–69 (2003).
17. Horovitz, A. Double-mutant cycles: a powerful tool for analyzing protein structure and function. *Fold. Des.* **1,** R121–R126 (1996).
18. Skora, L., Mestan, J., Fabbro, D., Jahnke, W. & Grzesiek, S. NMR reveals the allosteric opening and closing of Abelson tyrosine kinase by ATP-site and myristoyl pocket inhibitors. *Proc. Natl. Acad. Sci. U. S. A.* **110,** E4437 (2013).
19. Cuello, L. G., Jogini, V., Cortes, D. M. & Perozo, E. Structural mechanism of C-type inactivation in K(+) channels. *Nature* **466,** 203–8 (2010).
20. Cuello, L. G. *et al.* Structural basis for the coupling between activation and inactivation gates in K(+) channels. *Nature* **466,** 272–5 (2010).
21. Pan, A. C., Cuello, L. G., Perozo, E. & Roux, B. Thermodynamic coupling between activation and inactivation gating in potassium channels revealed by free energy molecular dynamics simulations. *J. Gen. Physiol.* **138,** 571–80 (2011).
22. Ostmeyer, J., Chakrapani, S., Pan, A. C., Perozo, E. & Roux, B. Recovery from slow inactivation in K+ channels is controlled by water molecules. *Nature* **501,** 121–4 (2013).
23. Weingarth, M. *et al.* Quantitative Analysis of the Water Occupancy around the Selectivity Filter of a K(+) Channel in Different Gating Modes. *J. Am. Chem. Soc.* **136,** 2000–7 (2014).
24. Cordero-Morales, J. F. *et al.* Molecular determinants of gating at the potassium-channel selectivity filter. *Nat. Struct. Mol. Biol.* **13,** 311–8 (2006).
25. Cordero-Morales, J. F. *et al.* Molecular driving forces determining potassium channel slow inactivation. *Nat. Struct. Mol. Biol.* **14,** 1062–9 (2007).
26. Raghuraman, H., Islam, S. M., Mukherjee, S., Roux, B. & Perozo, E. Dynamics transitions at the outer vestibule of the KcsA potassium channel during gating. *Proc. Natl. Acad. Sci. U. S. A.* **111,**

1831–6 (2014).

27. Wylie, B. J., Bhate, M. P. & McDermott, A. E. Transmembrane allosteric coupling of the gates in a potassium channel. *Proc. Natl. Acad. Sci. U. S. A.* **111,** 185–90 (2014).

28. Thompson, A. N., Posson, D. J., Parsa, P. V & Nimigean, C. M. Molecular mechanism of pH sensing in KcsA potassium channels. *Proc. Natl. Acad. Sci. U. S. A.* **105,** 6900–5 (2008).

29. Uysal, S. *et al.* Mechanism of activation gating in the full-length KcsA K+ channel. *Proc. Natl. Acad. Sci. U. S. A.* **108,** 11896–9 (2011).

30. Bhate, M. P. *et al.* Preparation of uniformly isotope labeled KcsA for solid state NMR: expression, purification, reconstitution into liposomes and functional assay. *Protein Expr. Purif.* **91,** 119–24 (2013).

31. Heginbotham, L., Kolmakova-Partensky, L. & Miller, C. Functional Reconstitution of a Prokaryotic K+ Channel. *J. Gen. Physiol.* **111,** 741–749 (1998).

32. Posson, D. J., Thompson, A. N., McCoy, J. G. & Nimigean, C. M. Molecular interactions involved in proton-dependent gating in KcsA potassium channels. *J. Gen. Physiol.* **142,** 613–24 (2013).

33. Raiford, D. S., Fisk, C. L. & Becker, E. D. Calibration of methanol and ethylene glycol nuclear magnetic resonance thermometers. *Anal. Chem.* **51,** 2050–2051 (1979).

Chapter V: Coupled Clusters of Allostery Participants: Identification by Chemical Shift

Portions of this chapter have been adapted from: Xu, Y., Zhang, D., Rogwaski, R., Nimigean, C. M., McDermott, A. E. Coupled Clusters of Allostery Participants: Identification by Chemical Shift. Submitted.

5.1 Abstract

Allosteric coupling underlies most cell signaling processes, and allosteric interactions represent an exciting avenue for development of new diagnostics and therapeutics. Nevertheless, a general method for identifying allosteric mechanisms has been elusive, and it remains difficult to predict the involvement of specific residues due to the complexity of long-range phenomena. Here we introduce a new NMR method to identify residues involved in allosteric coupling between two ligands binding sites in a protein: Chemical shift detection of Allostery Participants (CAP). Functional networks responding to each ligand are defined through correlated NMR perturbations. In addition, allostery participants, residues that play a role in the coupling between the binding sites, are identified. Such residues show responses to both binding events, although one or both events is distal, and therefore exhibit multiple functional states with distinct chemical shifts. We use the NMR shift responses to identify sites that depend on both binding events and are thus viewed as candidates for transmitting information between functional units. This strategy was applied to the prototypical ion channel, KcsA, analyzing proton and potassium binding networks and residues critical for their mutual coupling. The vital role of one such identified amino acid was validated through site-specific mutagenesis, electrophysiology functional studies, and with NMR-detected thermodynamic analysis of allosteric coupling. This strategy for identifying allostery participants is likely to have applications for many other systems.

5.2 Introduction

Allostery refers to changes in a protein due to perturbations at a remote site, including structural or dynamic alterations.[1] Frequently the change is elicited by binding of a ligand, and is manifest in terms of a consequent change in the affinity of another ligand binding to a different region of the protein. Allostery is a ubiquitous and efficient mechanism for communication in biology. In examples as diverse as enzyme regulation[2], transmembrane cell signalling[3], and gene expression regulation[4], the binding of one ligand to a protein changes the affinity of other ligands binding at separate binding sites, and controls "downstream" events.

Many experimental studies have focused on elucidating the molecular mechanism by which the perturbation is propagated within or between the functional units[5,6], for example by identifying changes in the close contacts between specific residues that are responsible for allostery. It has been emphasized that there may not be a single set of conformational changes that is crucial for the coupling network; rather, ligand binding may cause numerous changes in the protein's conformational and dynamic ensemble which result in changes in thermodynamics and affinity at distant sites.[7,8] Nevertheless, in most allosteric systems there are key residues whose participation is important to the underlying mechanism; in some cases these sites have particular medical relevance.[9] Identifying these key residues, which can be quite distant from either of the binding sites, is of great interest for a mechanistic understanding of allostery, protein engineering and drug design. In combination with experimental strategies, computational methods such as molecular dynamics simulations to identify the correlation motions of residues can further clarify the atomistic mechanism by which these residues participate in allostery[6,10,11].

A number of methods show promise for identifying the key residues involved in allostery. For example, sequence analysis can identify evolutionary residues pairs as allostery candidates.[12] Another approach makes use of graph theory to calculate the optimal residue connections for the allosteric network.[13] A new algorithm called contact networks through alternate conformation transitions (CONTACT) used experimental X-ray data to identify contact networks of conformationally heterogenous residues in dihydrofolate reductase and proline isomerase cyclophilin A.[14] Double-mutation cycle methods aim to identify the cooperative residue pairs.[15,16] These experiments provide powerful insights, but (even

despite the ease of mutagenesis nowadays) these approaches can be challenging and time intensive. Overall, both theoretical and experimental identification of pathway residues remains challenging.

NMR has proven to be a particularly powerful tool for the analysis of allostery. The study of protein dynamics via NMR provides a unique tool to characterize entropy driven allostery, dissecting the contribution of dynamics to the coupling energy.[7,17–25] NMR titration studies can quantitatively measure the energetics of the allosteric transition.[26–28] Moreover, analysis of chemical shift perturbations in various states of the protein provides a global snapshot of the various residues affected by a given perturbation, presumably reporting on the allosteric nature of the transition. However, chemical shifts are sensitive to a variety of effects, so methods are needed to dissect those resides whose chemical shift perturbation is specifically due to allosteric coupling. Melacini et al advanced previous chemical shift analysis by introducing CHEmical Shift Covariance Analysis (CHESCA), which combines Singular Value Decomposition (SVD) and hierarchical analysis to identify allosterically coupled residues.[29] CHESCA specifically highlights long-range effects of ligand binding that are similar for a large number of ligands. Residues were clustered based on the covariance of chemical shift changes, invoking the assumption that residues belonging to the same functional unit show correlated behavior in terms of NMR shifts.

We demonstrate here a method based on NMR shifts to identify players in allostery for systems with two ligand-binding events, which we call Chemical shift detection of Allostery Participants (CAP). We hypothesize that if a residue contributes to allostery, the local environment is strongly dependent on both binding events, and therefore its NMR resonance frequency will depend on the combination of ligands present, exhibiting three or four distinct local environments as the two ligands are varied in an appropriate range (when the kinetics of the system are in slow exchange). Established NMR methods can be used to identify residues directly involved in binding of a ligand and those that are coupled to the binding of a specific binding even if they are quite distant[30–32]. Many prior NMR studies of allostery explore the complex set of long-range effects from single ligand binding sites.[7,33,34] A residue might serve as a simple reporter, showing two possible environments, depending on occupation of one of the binding sites but being independent of occupation of the other. We consider here a system where two separate ligand-binding events can be observed, and could be allosterically coupled. In this case, residues can be divided into four groups (see Figure 5.1a): Sites that respond to binding of the first ligand, which form a network

including sites distant from the actual ligand binding site (I); analogously, sites that respond to the binding of the second ligand (II); sites that are not sensitive to either ligand binding event (III); and sites that are responsive to the combination of occupation of the two ligand binding sites (IV). The latter are considered to be energetically coupled to both binding events and are strong candidates for playing key roles in mediating the allosteric coupling between the two sites, making them critical to function. We name them 'Allostery Participants'. In a strongly allosteric protein, a handful of residues are expected to show "multistate" behavior (three or more possible chemical shifts) depending on the combination of binding of ligands.

We demonstrate these methods on the ion channel KcsA reconstituted in liposomes. KcsA is a 64kD tetrameric pH-gated bacterial potassium channel (Figure 5.1c,d). KcsA channels, once activated by very low pH, exhibit inactivation, a process where ion channel activity decreases even if the activation stimulus (in this case exposure to low pH) persists.[35–42] Inactivation in KcsA has properties similar to the C-type inactivation described in Shaker channels[35,43]. Inactivation is common in many potassium channels and it has consequences for channel open times and for refractory periods in action potentials,[44] including channels control of heartbeat.[45–47]

Many functional and structural studies indicated that the allosteric coupling between the proton binding sites (termed the activation gate or pH sensor) and the potassium binding sites underlies inactivation[35,38,39,41,42].(Figure 5.1c) We recently characterized this allosteric system by solid state nuclear magnetic resonance (SSNMR) and found that protonation of the intracellular pH-sensor (which opens the intracellular activation gate) allosterically reduces the K^+ affinity by more than three orders of magnitude at the selectivity filter, which we hypothesized to be the basis for inactivation.[26] Previous NMR studies have shown that the pKas of the proton binding residues are also dependent on the conformations of the selectivity filter.[38,39] Crystal structures of KcsA channel constructs with open intracellular gates also show a correlation between the extent of opening at the pH gate and both ion occupancy and structural changes at the selective filter.[48,49] NMR data further indicate that the inactivation-induced release of K+ ions from the KcsA selectivity filter is in slow exchange on the NMR timescale,[50] namely the conformation changes associated with binding or release of K^+ and H^+ have rate constants slower than the difference in NMR resonance frequencies (slower than a few milliseconds).

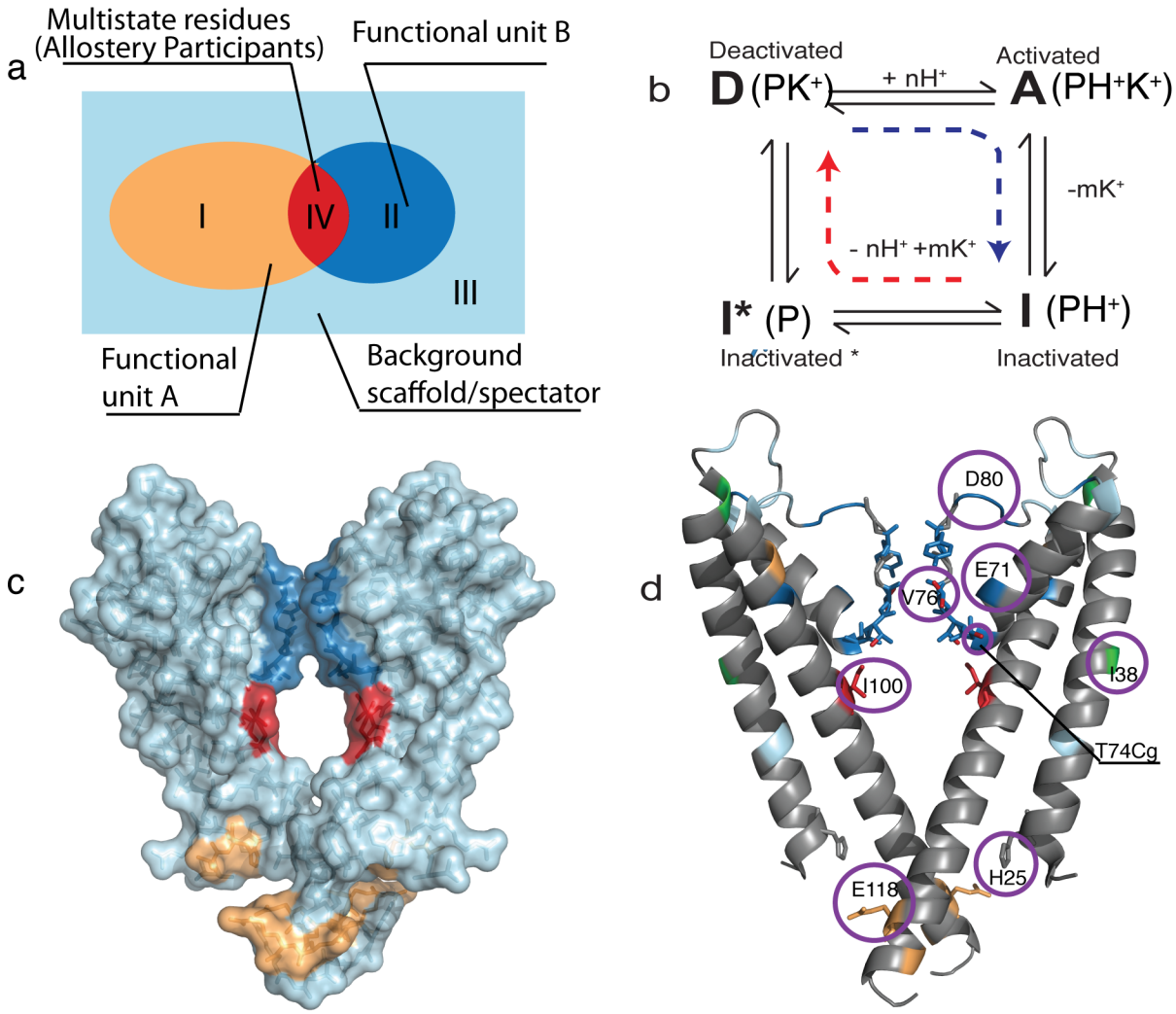

Figure 5.1. The rationale of applying CAP analysis to KcsA. (a) In an allosteric protein with two ligand binding sites, we categorize the residues into the following groups: networks of residues sensitive to binding each ligand (Group I for ligand A and Group II for ligand B), spectator residues that are not sensitive to either ligand binding (Group III) and residues that are sensitive to both ligands, and can report the combination of ligands bound (Group IV). CAP analysis is designed to experimentally cluster the NMR preorders for a protein into these four groups. (b) A typical four-states allosteric coupling system with two ligand binding are illustrated in the case of KcsA. P represents the apo protein, and H^+ and K^+ are the ligands. Electrophysiological terminologies are indicated for the four conditions. The blue dash line indicates the inactivation process, which has a rate in a range of 10^{-1}-1 s^{-1}; the red dash line indicates the recovery process, which has a rate in a range of 10^{-1}-10^{-2} s^{-1}. The activation is a transition from D to A, which has a rate in a range of 10^{1}-10^{2} s^{-1}. [48](c) Crystal structure (PDB: 1K4C) of the model system, the KcsA potassium channel is displayed, which, based on previous studies, we classified into potassium

binding sites (marine), proton binding sites (orange), KcsA scaffold (light blue), and "allostery participants", where responses are based on the combination of ligands binding (red). (d) With CAP analysis, we can assign individual residues or sites into groups. The results of CAP analysis are highlighted in the crystal structure of KcsA. Residues belonging to different groups are color-coded: Spectator (light blue); Two State pH Markers (orange); Two State K+ Binding Markers (marine); Residues that are apparently sensitive to other aspects of the environment (green); Allosteric Participants (Red). Residues mentioned in the paper are also highlighted.

NMR markers of binding of potassium ions and protons in KcsA were identified in our recent studies.[26] The proton and potassium binding units are remote (> 30Å) and the residues involved in the process of transmitting the information between units were not well characterized in our recent studies. KcsA is thus an ideal model to illustrate the CAP method for studying allostery in systems of two coupled remote binding sites. Here, we apply CAP to KcsA in liposome preparations,[51] and identified residues that are likely to play a role in allosteric coupling. We subsequently studied the effect of mutations in these residues on function using complementary biophysical methods. Future applications to allosteric transmembrane proteins in native-like environments, such as GPCRs or membrane transporters, are expected to be also powerful.

5.3 Results

5.3.1 Identifying Residues That Serve as Markers

To cluster the residues of KcsA into four groups, we obtained spectra of our protein in four limiting conditions with respect to ligand binding, using saturating conditions of ligand (the four conditions shown in Figure 1b). Specifically, for KcsA the apo state prepared with 0.1μM K^+ at pH 7.5 (referred to as a Deeply Inactivated state, I*), the K^+-bound state with 50 mM K^+ at pH 7.5 (referred to as the resting or Deactivated state, D), the H^+-bound state with 0.5 mM K^+ at pH 3.5 (the Inactivated state, I), and the doubly ligated K^+ and H^+ bound state with 100 mM K^+ at pH 3.5 (the Activated state, A). The conditions for preparing these samples were selected based on our previously measured affinity (K_d) values for K^+ at pH 7.5 and pH 3.5. The chemical shift assignments for these samples were made based on Dipolar Assistant Rotation Resonance (DARR)[52] Carbon-Carbon homonuclear experiment with various mixing times and hetronuclear Nitrogen-Carbon Double Cross polarization (SPECIFIC-CP) experiments[38] (see Methods).

The KcsA residues that respond to a single ligand are expected to exhibit two alternative chemical shift values in slow exchange, whose intensities track the presence or binding of their corresponding ligands. Comparing chemical shifts among this set of spectra in the four sample conditions shows that many sites in the protein exhibit two chemical shifts whose intensities depend on a single ligand. Many of these residues are found in the selectivity filter, which is the potassium binding site, or the pH gate, and were used in prior work to study K^+ affinity (Figure 5.2). It is notable that residues quite distant from the potassium and proton binding site sometimes exhibit two state behavior (Appendix 2, Figure 5.1d). Some of the remote reporters that respond to potassium ion binding are located for example behind the selectivity filter, such as E71 and D80; some are located in the outer month of the N terminal site such as Y81, I60; other residue such as I38 is located in transmembrane helix, embedding into the lipid bilayer. Interestingly, these residues did not show a clear physical contact network, but are spread out all over the protein. It is worth noting that atoms within the same residue can have different chemical shift response to torsion or steric interactions, so they do not always reflect the same trends (Appendix 2).[53] We discuss details of the assignment to the two networks more below. Numerous other sites in KcsA were observed to have chemical shifts that were invariant with respect to ligand concentrations, confirming that the basic fold of the protein is not affected by K^+ or pH over a broad range (Appendix 2).

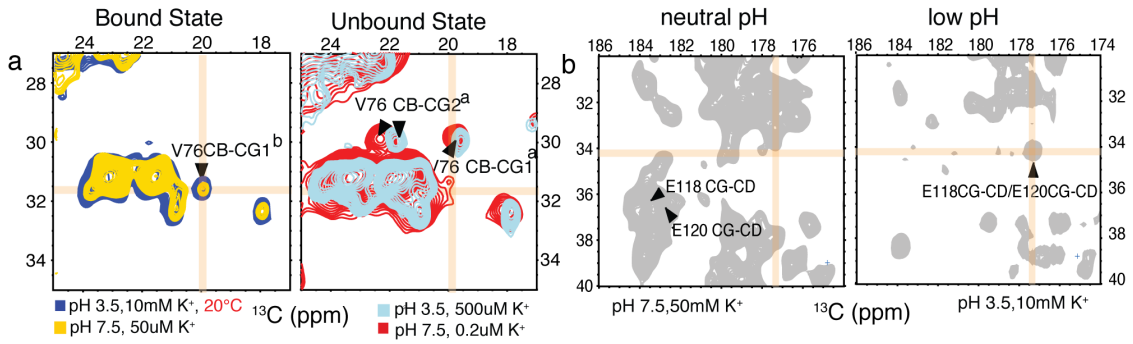

Figure 5.2. Representative residues assignments for proton and potassium ion binding. In the panel a, we showed the peaks for V76 CB-CG1, which are potassium ion binding makers. They display chemical shift perturbation in response to ambient [K^+] change. In the panel b, we showed peaks for E118/E120 CGG-CD, which are proton ion binding makers. They display chemical shift perturbation in response to the pH change.

Here we explore the observation that a handful of residues exhibit multiple (more than two) chemical shifts, whose intensities reflect the combinations of ligand occupancies (Figure 5.3a). Some of these involve the residue's sidechain, while the backbone atoms exhibit two-state behavior. Examples include T74 and T75, in which the CG sidechain displays three different chemical shifts (Figure 5.3b), but the CA and CB only display two chemical shifts each (Figure 5.3a). We reason that the sidechain atoms have more flexibility, or are in more direct contact with other residues in the networks of both binding pockets.

Multistate behavior can manifest as a change in chemical shift, as illustrated by T74 and T75, or can manifest as a change in dynamics, illustrated by the behavior of residue I100 (Figure 5.3b).[38] Allostery has been shown to involve changes in the dynamic behavior of various states, along with structural changes for many systems.[7,22,54] NMR is very sensitive to protein dynamics on timescales from picosecond to seconds.[55,56] For I100, we observed two sets of chemical shifts for the CB-CG2 correlation in the Apo, Deactivated and Inactivated states; in the Activated state (protonated/K^+ binding state), the peak corresponding to I100 is missing, suggesting a greatly reduced transverse relaxation time or inefficient magnetization transfer due to short rotating frame relaxation or interference with dipolar evolution. Another possibility is that the peaks can be significantly broadened and weakened due to structural inhomogeneity of I100. In either case, it is reasonable to assume that the structure or dynamics of I100 in the Activated state is distinctive from the other states. These residues- namely T74 and T75, as well as I100, are likely involved in the allosteric coupling between the two binding sites in that the combination of the binding of the two ligands is important rather than one ligand or the other. Importantly, the role of I100 in mediating the coupling has already been proposed and examined by various methods,[57] and is thought to act via contacts to F103. The sidechains of T74 and T75 are similarly located between the proton and potassium ion binding sites, which further supports their potential roles for connecting the two networks (Figure 5.3c).

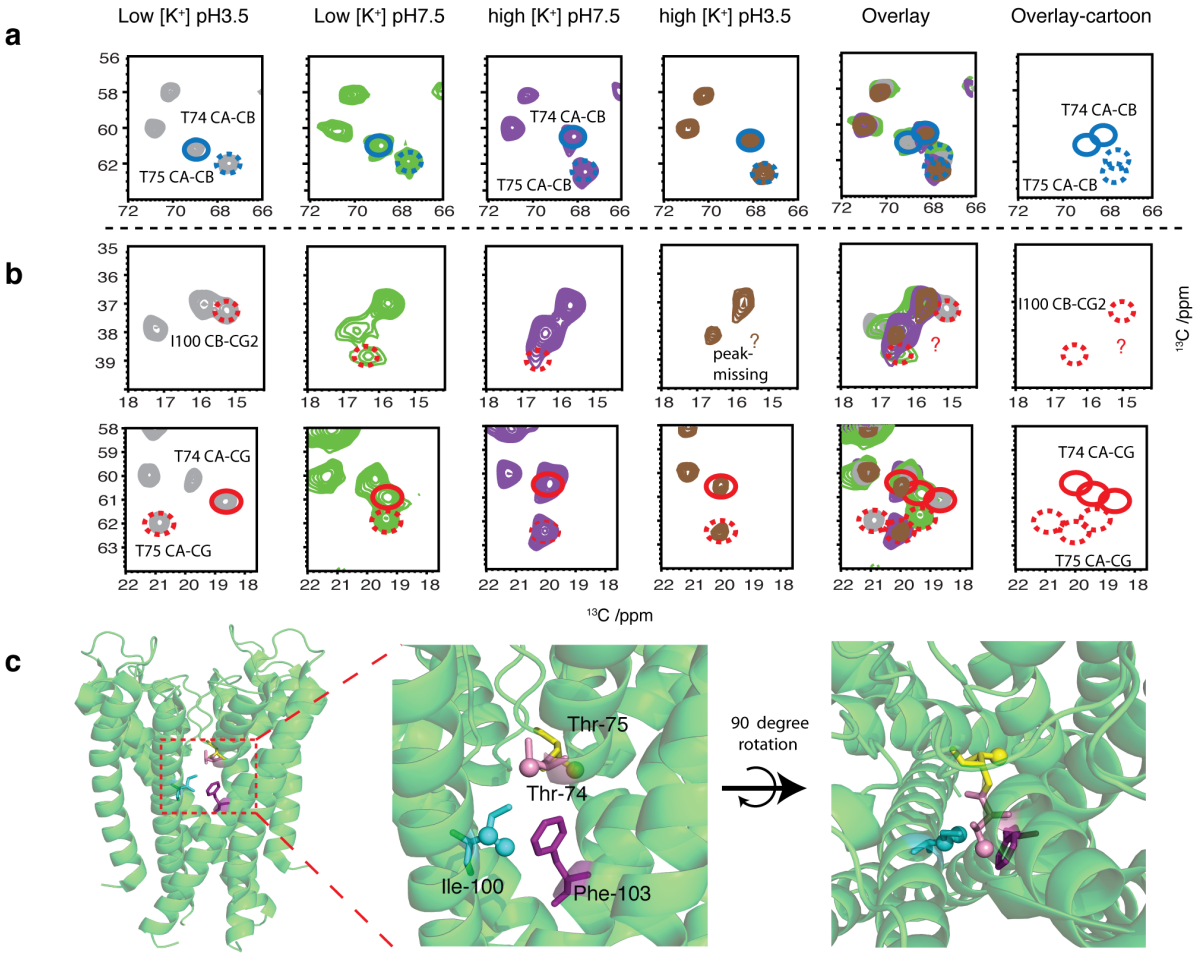

Figure 5.3. NMR markers are shown for various states or ligand concentrations. (a) Two typical "two-state" NMR markers for K+ binding are illustrated, namely T74 (blue circle) and T75 (blue dash circle) backbone CA CB correlations. (b) Two cases of multi-state "allostery participants" are shown. In the first row, marker I100 CB-CG2 in various conditions is shown and labeled by a red dashed line circle. In low pH and high [K^+], the peak for I100 is not detected. We surmise that this may be due to dynamics or heterogeneous conformations. In any event, the appearance of the peak depends on the combination of ligands present, and not specific on one or the other. In the second row, two multiple-state markers are shown, the sidechain CG of T74 (red circle) and T75 (red dash circle), displaying three distinctive chemical shifts for the four spectra of KcsA in various conditions. (b) The Allosteric Participants T74, T75, I100, F103 are highlighted in a crystal structure (PDB: 1K4C), indicating the plausible locations connecting two binding sites in KcsA.

5.3.2 Identifying Networks by Chemical Shift Correlation

We hypothesize that residues in same functional units will experience correlated population changes as ligands are titrated. Given the strong allosteric coupling, in some regimes the binding of one

ligand will induce binding or release of the other, leading to an apparent correlation of the two networks. In other words, for some experimental conditions a straightforward titration of one variable (K^+ for example) can lead to changes in binding in the other (H^+) binding site. Thus reporters from both networks will appear although only one ligand has been added to the sample. For example, E118 and E120 change chemical shifts between the high and low potassium spectra at neutral pH;[38,39] however, they are known to be the proton binding markers.[58] Such a correlation will occur only in a restricted concentration regime. To separate the two events, and distinguish residues that belong to one reporter network from those in the other network, we made use of our prior titration data to select a variety of conditions where the binding of the ligands can be separately controlled by concentrations. For example, in KcsA, one K^+ titration was done at pH3.5, where the pH sensor remains protonated throughout the K^+ titration, allowing us to uniquely identify K^+ binding markers. Titrations did at pH 5 or 7.5 reflect simultaneous changes in both pockets, preventing us from unambiguously distinguishing the network of K^+ markers from H^+ markers. We have limited data at pH 9 where the pH sensor is expected to be deprotonated throughout the K^+ titration.

Titrations were detected using Carbon-Carbon 2D spectra of KcsA, in which the populations for various states can be monitored at a large number of sites by integrating the corresponding peaks since the exchange process is slow (consistent with the millisecond to second time scale of the inactivation and recovery process as measured by electrophysiology[48,59] and the exchange rate estimated by NMR as <500 /s[28]). The assignments of the residues were verified by other 2D or 3D homo- or hetero- nuclear correlation. Various residues show different magnitudes of chemical shift change in term of ppm (0.5 - 2ppm) that are useful in this analysis and are enumerated in Appendix 2.

As demonstrated by previous NMR studies,[29,60] correlation analysis is a useful tool to evaluate the relationship between two residues. Here we monitored the population shifts of individual sites as we titrated ligands through the system and then evaluated the *Pearson* correlation efficient for residue pairs (as discussed further in the Methods section):

$$Conv(X,Y) = \frac{E(XY) - E(X)E(Y)}{\sqrt{E(X^2) - (E(X))^2}\sqrt{E(Y^2) - (E(Y))^2}} \quad (5.1)$$

, where X, Y represents an array of population percentage of bound state (peaks dominate in high [K+] condition) in a series of titration points of the two residues for correlation analysis. From the coefficients, we conducted the covariance matrix of population changes in response to the ligands (Figure 5.4a-d).

Our results show that numerous residues are highly correlated: at pH 7.5, we observed a global network, which includes residues in the potassium binding sites such at V76, T75, T74 and flanking residues like I60, E71, D80, L81, Y82 and proton binding residues E118/120. (Figure 5.4a, 5.4b) As mentioned above, near these conditions a coupled binding event occurs. By contrast, the decoupled transition at pH 3.5 involves only potassium binding. Many residues exhibit correlated shifts and serve as potassium-binding markers, including residues in the binding site and quite distal residues. (Figure 5.4c) The proton-binding residues E118 remain protonated throughout the titration at pH 3.5 as is indicated by the NMR spectra. (Figure 5.4c, 5.4d) By comparison with the globally coupled network identified at pH7.5, we identified the residues belonging to the proton binding functionality.

We also identified I38 and E51 as residues that show chemical shift changes but the population changes do not show a strong covariance with other two state marker sites in response to [K^+] change. (Figure 5.4a, 5.4c) The chemical shift change is more likely to be caused by other environmental factors, which have not been clarified here.

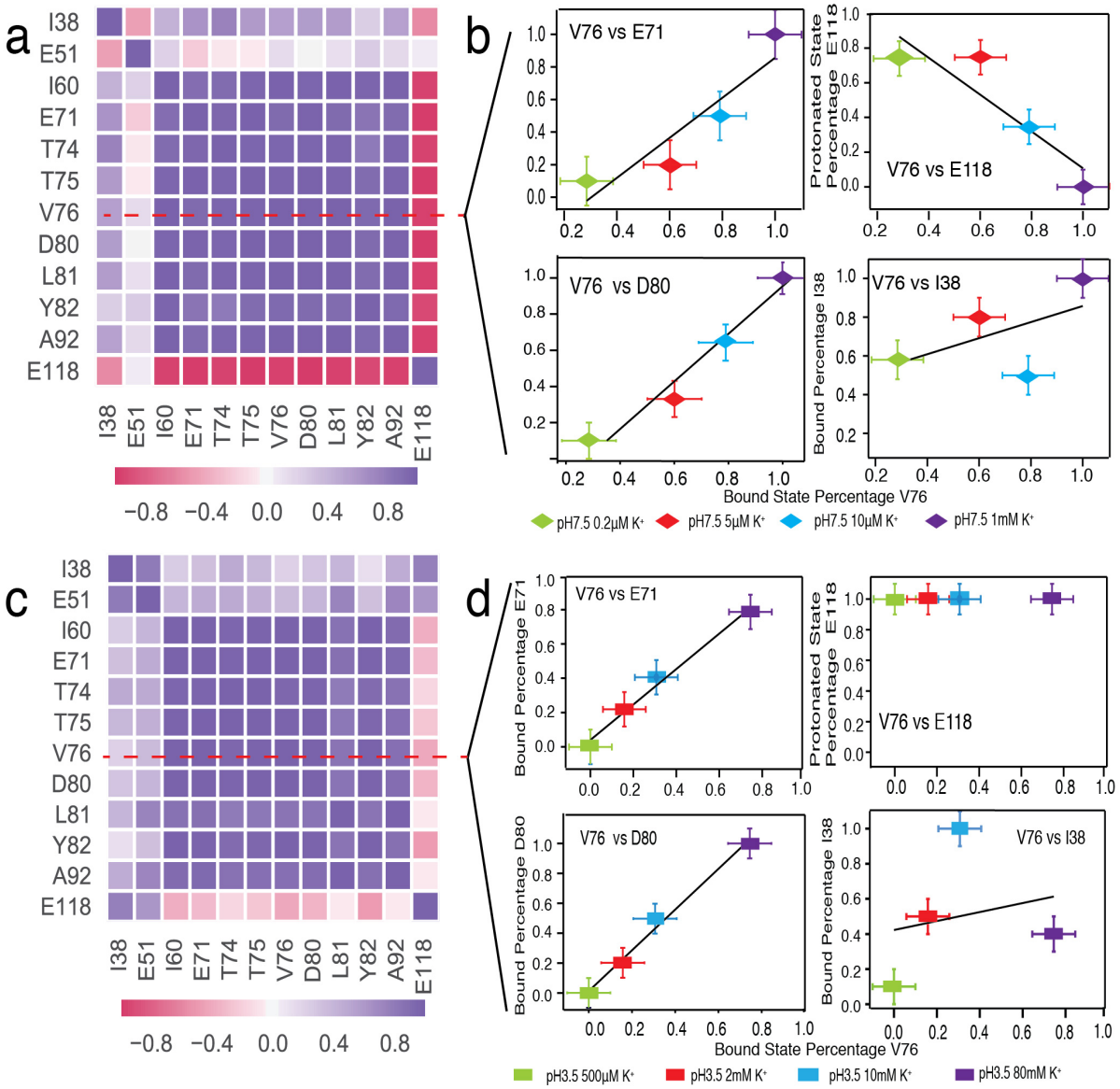

Figure 5.4. Chemical shift correlation analysis reveals that residues in KcsA are clustered into networks for K^+ and proton binding. The covariance of population change of the two state residues (as [K+] is changed) is illustrated in correlation analysis results displayed as a heat map for pH 7.5 (a) and pH 3.5 (c). As an illustration of the correlation, a cross section at V76 is expanded to show chemical shift correlation analysis for V76 vs. other residues at both neutral (diamond, b) and acidic pH (rectangle, d). A network of potassium binding sites is revealed at pH 3.5 (a condition where potassium binding is decoupled from proton binding in the titration). The network is dispersed throughout the protein and includes I60, E71, T74, T75, V76, D80, L81, Y82, and A92. The correlation network at pH7.5 also includes E118 because at this pH potassium binding is coupled to proton binding in the titration. E118 shows a negative correlation at neutral pH, due to allosteric coupling, indicating that E118 is a protonation marker for the activation gate. For I38 and E51, we observe very low or no correlation to other residues

such as V76 at both pHs, indicating that the observed chemical shift changes for these residues are likely to be unrelated to these ligands. (For additional correlation plots see Appendix 6)

5.3.3 Functional Tests of Putative Allostery Participants Identified by CAP

We next identified the "allostery participants" sites where the chemical shift serves as a marker for the combination of binding states. Such sites exhibit more than two chemical shifts for four distinct combinations of "gates" or binding states. We propose that they are potentially involved in energetic coupling between the two binding sites. We sought corroborative evidences for the role of putative residues identified through their NMR shift behaviors. We examine the functional behavior of site-specific mutations involving the putative coupling participants, and compared with wild type. I100 and F103 have previously been suggested as possibly important allosteric coupling residues (Figure 5.1c).[35,57] Mutagenesis, molecular simulation and our recent NMR study have provided strong evidence for the participation of F103 and I100.[26,35]

T74 is another possible important allostry participant in allosteric coupling, as suggested by this CAP analysis (Figure 5.3a); it has been previously suspected to interact with F103, I100 during inactivation,[49,57] but without direct evidence. Its involvement is also difficult to detect simply by comparing crystal structures of various states (Figure 5.5). The observation of "multistate behavior" of the NMR peaks for T74 CG sidechain, and its sensitivity to the combination of binding states, led us to propose that the sidechain of T74 is important for propagating allostery. To test this hypothesis, we mutated T74 to a serine, to remove the CG methyl group of the threonine and characterized the allosteric coupling by NMR, namely the potassium affinity changes as a function of pH. The mutant shows great titrimetric stability and displays high quality spectroscopic data, indicating that the mutant is well folded. (Figure 5.6) As shown in Figure 5.7a, the affinity for K^+ in T74S KcsA decreased only 4 fold upon switching from pH 5 to pH 3.5 (red), while for WT KcsA the K^+ affinity decreased 250 folds for the same pH change (purple). Thus the T74S mutation dramatically reduced the pH sensitivity of the K^+ affinity, indicating that the allosteric coupling network is significantly reduced. This result suggests that channel opening is less coupled to inactivation at the selectivity filter.

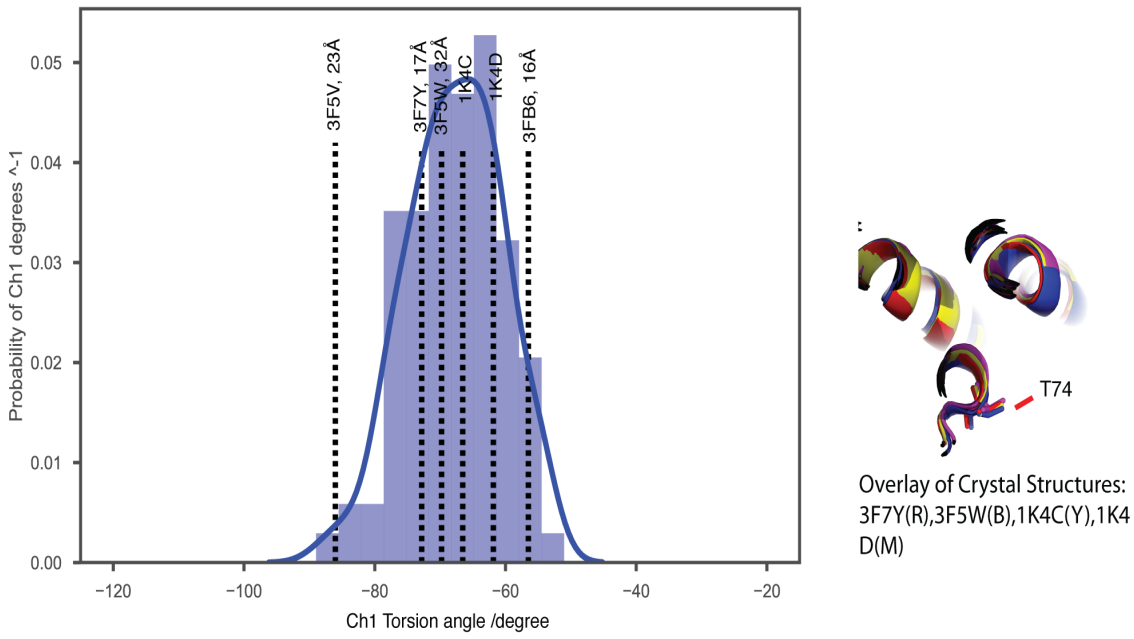

Figure 5.5. We calculated the Ch1 torsion angle of T74 side chain distribution in a molecular dynamics simulation. The details of the simulation can be found in the reference. The distribution is shown in bar plot and fitted with the blue curve. We also calculated the Ch1 torsion angle of T74 side chain for the crystal structures in various states. In 1K4C and 1K4D, the pH gate is closed. In the other structures represented here, the pH gate is open to various degrees, and the inter-subunit Cα–Cα distances at position T112 (the residue near the bundle crossing) are shown together with the PDB codes (when the pH gate is closed, the distance is 12 Å). These structures are hypothesized to represent inactivated states. No correlation was found between the Ch1 torsion angles and the functional states. In the crystal structure overlay, minimal differences between the T74 side chain conformations can be seen. Therefore, the importance of the T74 sidechain is difficult to glean from crystal structures. This could be caused by the limited resolutions of some of the structures.

To investigate the impact of the T74S mutation on channel activity, we further analyzed this mutant using single channel recordings in lipid bilayers. As shown in Figure 5.7b-c, T74S shows long opening and high open probability. In contrast, WT shows brief openings and a low open probability of 1.4+/-1.0% (Figure 5.7b, d). The low open probability of WT-KcsA is consistent with previous electrophysiological data and is a manifestation of activation-coupled inactivation.[48,61] These results

confirm that removing the methyl group of T74 in the T74S mutant leads to partially breaking this communication pathway, and to an essentially inactivation-less channel variant. It is remarkable that such a simple chemical change could lead to a large effect in thermodynamics and function.

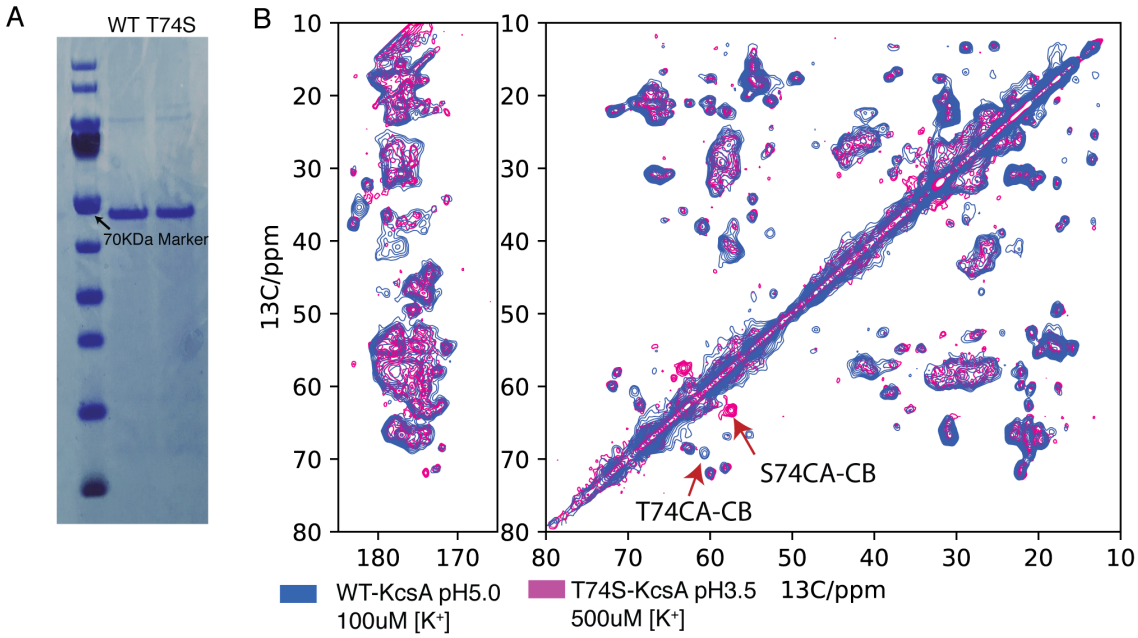

Figure 5.6. T74S and WT-KcsA bands on SDS page gel show that T74S and WT-KcsA are both stable tetramers in a denaturing gel. KcsA is a 64kDa protein (as the tetramer) and the bands appear near the level of the 70KDa marker. (b) Overlay of CC2D DARR spectra for T74S and WT shows that T74S is well folded. The majority of the peaks in the T74S spectra do not show perturbation. The missing peak at chemical shift (61.15, 69.78) confirms its assignment as T74 residues.

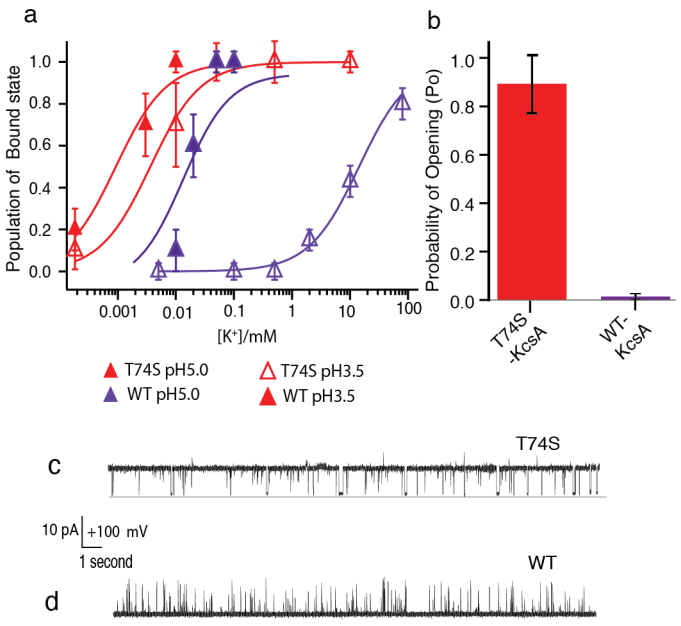

Figure 5.7. Mutation of T74 to serine indicates that the sidechain is a crucial player for propagating allosteric interaction and C-type inactivation. (a) This NMR titration study shows that the pH effect on the K^+ affinity (i.e. coupling strength) of the T74S mutant is much weaker than that of WT. A prior titration study on WT shows that the affinity of K^+ is around 250-fold weaker at pH 3.5 than that at pH 5.0. (i.e. 16μM vs. 4mM, the purple symbols in the plot, taken from reference 26). The titration study on T74S in this study shows that the affinity for K^+ is only 4-fold weaker at pH 3.5 than that at pH 5.0. (i.e. 1μM vs. 4μM, the red symbols) The extremely high affinities for K^+ at both pH values leads us to suspect that T74S is not only a coupling mutant but also an affinity mutant similar to E71A.[36](b) The opening probability of T74S and WT-KcsA are 0.89+/-0.12 and 0.014+/-0.010, respectively. The values are mean+/- SD from 9 and 3 experiments for T74S and WT-KcsA, respectively. (c,d) Representative single channel traces for the T74S mutant and WT-KcsA at +100 mV. The much higher open probability of T74S than WT is interpreted to mean that the loss of a methyl group has led to failure of inactivation.

5.4 Discussion and Conclusion

We introduced a method, CAP, for analyzing an allosteric protein with two coupled ligand binding sites. NMR chemical shift analysis was used to cluster the protein into distinct networks of reporters (Figure 5.1a) and specifically highlight allostery participants who depend on the combinations of binding events at the two binding sites. We used ligand concentrations as a perturbation, based on our prior knowledge of the system, to fine tune our analysis of the clusters.

We paid specific attention to the residues showing multistate behavior in their chemical shifts, reasoning that these residues could be important allosteric participants. A number of the putative partners in allosteric coupling that resulted from the studies could then be confirmed by functional analysis, giving strong support for the power of this kind of analysis. For example the electrophysiology and NMR characterization of T74S mutation in KcsA demonstrated the crucial role of T74 sidechain in allosteric coupling, as predicted from the CAP analysis. The critical role of I100 in allosteric coupling has been confirmed by previous electrophysiology and molecular dynamic simulations,[57] providing another example of correct prediction from this CAP analysis.

Using statistical analysis in CAP distinguishes likely function-related chemical shift perturbations from non-specific effects, as illustrated in the case of I38 and E51 in KcsA. It further clusters the residual sites into groups according to function. For example, E71 in KcsA is located behind the selective filter and it was proposed to be critical for C-type inactivation. It was hypothesized that E71 becomes protonated at low pH, breaks the E71-D80 hydrogen-bonding network, which causes inactivation. Instead, here we show that E71 is only a potassium binding marker, which is consistent with previous results showing that this residue remains protonated throughout the entire pH range.[62]

We propose that CAP type analysis may have broader utility for studying allostery in other systems, where the detailed experiments can be modified based on systems. We provide an experimental workflow for carrying out CAP (Figure 5.8). The time scale of protein activities has a fundamental influence on the NMR spectra and the details of utility of this approach. In KcsA, the conversion between states is slow in comparison to difference in chemical shift; therefore we can observe individual peaks for each conformation and calculate their populations. For cases where the motion is in fast exchange, and a single averaged peaks is observed, a modified analysis may be required, and development of experiments and analysis techniques such as relaxation dispersion experiments may allow extraction of information on populations and chemical shift changes. Efficient assignment of proteins in various conditions, such as strategic isotope labeling and advanced spectrometers and methodologies will be important for future applications.

a. Measure fingerprint spectra such as HN HSQC for solution NMR, CC DARR or CN DCP for SSNMR in four sample conditions.

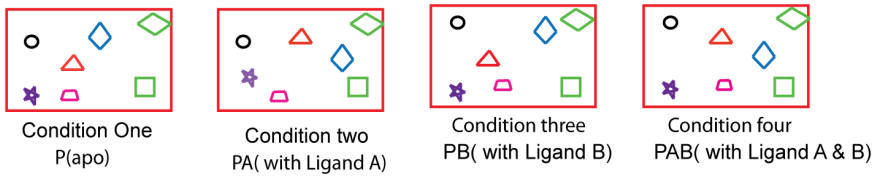

b. Group the residues based on their chemical shift behaviors, i. e. no change; two sets of chemical shifts; more than two sets of chemical shifts.

two-states residues	
multistates residues	
spectator	

c. Take two sets of titration experiments to further distinguish sub-networks for ligands binding in two states makers

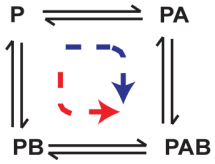

choice ONE: a coupled transition (dash) + one horizental or vertical transition

choice TWO: one horizental transition (titrating Ligand A) + one vertical transition (titrating Ligand B)

d. Measure peak populations and calculate Pearson correlation and construct covariance matrix. (examples are shown for correlations in different scenarios)

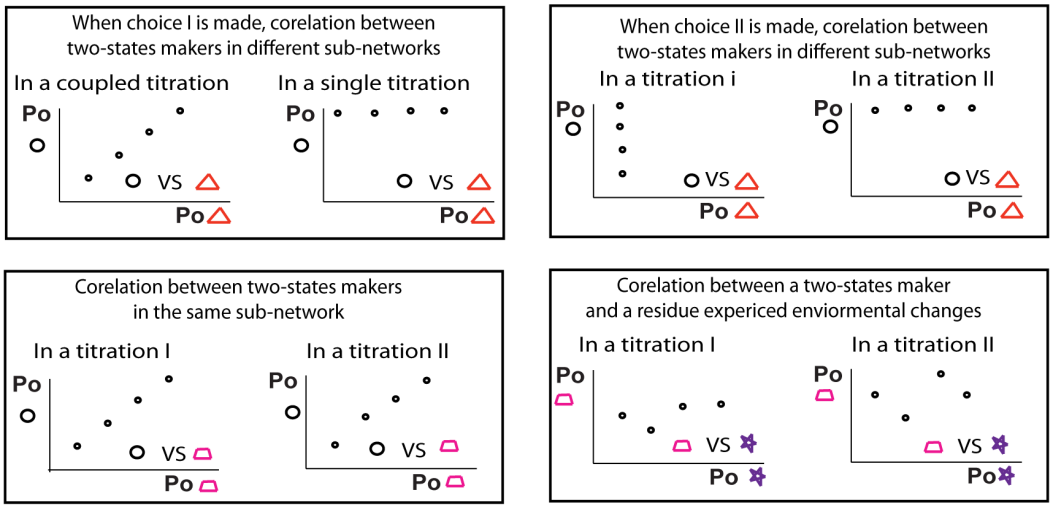

e. Assign sites or residues into sub-networks based on functions.(Functional studies to further validate the results.)

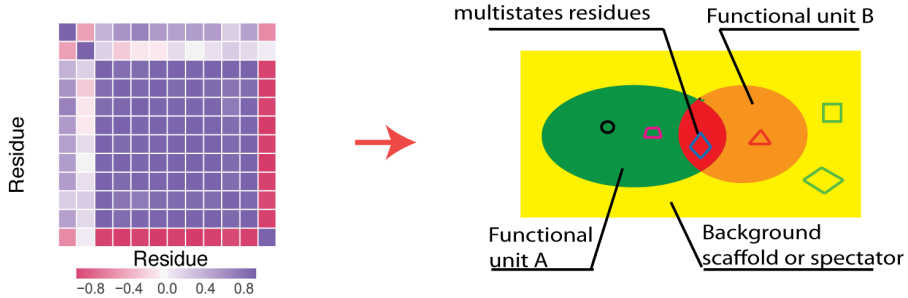

Figure 5.8. The procedure of carrying out CAP analysis is shown. The various shapes (i.e. circle, triangle etc) represent chemical shift peaks for different residues or sites. Particularly, in step c, when the titration studies are carried out to distinguish different networks for ligand binding, we proposed two choices as shown. In the KcsA analysis, the second choice was chosen. In different choices, the correlation plots are different, which are shown in the first and second examples in step d. The purple star represents a two-state marker where chemical shifts are caused by other environmental factors. Its correlation to another two-state markers is displayed in the forth example in d. This procedure provides an overall guidance for how to implement CAP analysis, however modifications can be made based on the studied systems.

CAP can be compared to a number of other methods for analyzing allosteric couplings. For example, using a method mentioned above, CHESCA, residues can be clustered into groups for ligand binding and allostery based on their chemical shift change (essentially population change) in response to a library of agonist and antagonist.[23,63] A somewhat similar analysis was obtained for a barrel enzyme by introducing Ala-to-Gly mutations at various sites and clustering the results based on responses to the mutations.[64] In another study of an allosteric system, mutations were specifically introduced at the catalytic site, which causing chemical shift change at the hidden allosteric sites due to the reciprocal interactions between an allosteric site and its coupled orthosteric site.[65] We add to these prior analyses the emphasis on correlated or joint responses to two different binding sites, and the multiple environments that result, which connect NMR analysis to one of the essential energetic and functional features of allostery. We expect that multiple NMR lines from allostry participants will likely be observed in many other systems. One recent example has been observed in GTPase atlastin: residue F151 displays multiple conformation states in the crystal structures collected in various states and is reasoned to be the connecting residue between the active and the nucleotide binding sites.[66] Such a “multiple-states” behavior takes advantage of the inherent plasticity of proteins in their response to multiple external stressors. Clearly not every allosteric participant will be detected in an analysis like CAP, but we propose that this analysis could produce a useful set of hypotheses for functional testing.

Although allostery in KcsA has been studied in the past, this method has added to the description of the coupling. An activation-coupled inactivation explanation for the functional behavior of KcsA has recently gained significant support from numerous biophysical studies Here CAP analysis allowed us to cluster residues into groups, to obtain a better understanding of molecular underpinnings of the coupling

(Figure 5.1d). Remarkably, we observed a high overlap between the residues identified as energetically or structurally connected to both binding events, and those residues whose mutants show functional changes in allosteric coupling strength, demonstrating the power of CAP analysis as a tool for detecting allosteric participants.

5.5 Materials and Methods:

Protein sample preparation: KcsA protein expression and purification protocols, and reconstitution into bilayers (DOPE:DOPS=9:1) for NMR are as described in previous references.[33] To adjust pH and [K^+], the proteoliposomes were first dialyzed against pH 7.5 buffer with appropriate [K^+] (2-3 changes), then further dialyzed at 4°C against 10 mM sodium citrate buffer at pH 3.5 with the appropriate [K^+] until the pH reached equilibrium, typically 5 hours. The pH of the supernatant was confirmed to be within 0.1 unit of the desired value. For all dialysis buffers, the total ion concentration ([K^+] +[Na^+]) was maintained at 50mM, except the 80 mM [K+] sample at pH3.5. The samples were centrifuged to form hydrated pellets and packed in 3.2 mm Bruker rotors for NMR experiments after 3 rounds of free-thaw cycles to remove extra buffer solution.

The plasmid for the T74S mutant was made using gene synthesis and its sequence was verified by Genewiz. On Coomassie-stained SDS gels, the mutant shows a similar band with WT-KcsA around 70 kDa (Figures 5.6), which indicates the mutant maintains the characteristic tetrameric structure.

NMR experiments Approximately 10mg ^{13}C-^{15}N KcsA samples were used for each NMR experiment. NMR spectra were collected on a Bruker 750MHz or 600MHz spectrometer and spinning rates of 12kHz or 14kHz were applied to avoid sidebands overlap with regions of interest. For protein assignment, Dipolar Assistant Recoupling Resonance (DARR) with various mixing times (15ms, 50ms, 100ms, and 200ms) and NCOCX, NCACX, DREAM[67] were applied. Typical 90 pulse lengths are ~2.5 μs for proton, ~5 μs for carbon and ~8 μs for nitrogen. We used 95-100 kHz decoupling using TPPM[68] in proton channel during acquisition. For titration curves, DARR (15ms mixing time) was used, with a calibrated sample temperature at 0 ± 2°C. Carbon chemical shifts were referenced externally to the downfield Adamantane line at 40.48 ppm and nitrogen chemical shift are referenced accordingly by calculation. The spectra were

processed in NMRpipe with -30 Hz Lorentzian and 90 Hz Gaussian apodization; Sparky[69] was used for spectral visualization and integration of cross peaks.

Electrophysiology T74S and WT KcsA purified protein was reconstituted into liposomes (3:1 POPE/POPG) at a concentration of 1 μg per mg of lipid, and stored at −80°C, as described previously.[34] Liposomes, thawed on the day of use and sonicated briefly, were applied to artificial lipid bilayers made of 3:1 POPE: POPG dissolved in decane at a concentration of 10mg/ml. The lipid bilayers are formed over a 100 μm diameter hole in a transparency partition separating 2 aqueous chambers in a horizontal lipid bilayer setup, as described[34]. The *trans* recording chamber contained a buffer solution with 10 mM succinate, pH 4.0, 100 mM KCl, and the *cis* chamber (where liposomes are applied) contained a buffer solution with 10 mM HEPES, pH 7.0, 100 mM KCl. Current traces were recorded under voltage-clamp at +100 mV with an Axopatch 200B amplifier (Molecular devices), sampled at 20 kHz. The data were further filtered offline at 2 kHz processed and analyzed using Clampex and Clampfit v10 (Molecular Devices). Single-channel current amplitudes were measured by hand from recordings lasting longer than 15 seconds, and open probabilities (NPo) were determined from 9 traces for T74S mutant and 3 traces for WT-KcsA with the Single-Channel Search module from Clampfit. Single-channel open probabilities (Po) for T74S mutant were then determined by dividing the NPo to the total number of channels. For WT-KcsA, due to the low opening probability, the total number of channels is difficult to determine; therefore, only the NPo is reported in the manuscript.

Data processing The normalized population ratios were used for potassium affinity measurement and correlation analysis. The K_d values were measured in Igor Pro (WaveMetrics) by fitting to the titration curve using the following equation: $\theta = \frac{[K^+]^n}{[K^+]^n + K_d}$, $\theta\ is\ the$ normalized bound state population ratio and the Hill coefficient n is fixed to be 1. *Pearson* correlations analysis was calculated in Mathematica (Wolfram) using the following formula: $Conv(X,Y) = \frac{E(XY)-E(X)E(Y)}{\sqrt{E(X^2)-(E(X))^2}\sqrt{E(Y^2)-(E(Y))^2}}$, X, Y is the bound state population percentages for two different residues or protonation percentage for E118 /E120 residue; E in the equation represents the expectation value. The values are used to plot the heat map covariance plot in

Figure 2. The linear fitting is done in Igor Pro (WaveMetrics). The error reported in the paper mainly comes from the fitting as well as the population integration and averaging between several marker peaks. The crystal structures presented in the paper were prepared with Pymol (Schrodinger).

5.6 References:

1. Cui, Q. & Karplus, M. Allostery and cooperativity revisited. *Protein Sci.* **17,** 1295–307 (2008).
2. Dokholyan, N. V. Controlling Allosteric Networks in Proteins. *Chem. Rev.* **116,** 6463–6487 (2016).
3. Changeux, J.-P. & Edelstein, S. J. Allosteric mechanisms of signal transduction. *Science* **308,** 1424–8 (2005).
4. Maniatis, T. & Reed, R. An extensive network of coupling among gene expression machines. *Nature* **416,** 499–506 (2002).
5. Sadovsky, E. & Yifrach, O. Principles underlying energetic coupling along an allosteric communication trajectory of a voltage-activated K+ channel. *Proc. Natl. Acad. Sci. U. S. A.* **104,** 19813–8 (2007).
6. Feher, V. A., Durrant, J. D., Van Wart, A. T. & Amaro, R. E. Computational approaches to mapping allosteric pathways. *Curr. Opin. Struct. Biol.* **25,** 98–103 (2014).
7. Petit, C. M., Zhang, J., Sapienza, P. J., Fuentes, E. J. & Lee, A. L. Hidden dynamic allostery in a PDZ domain. *Proc. Natl. Acad. Sci. U. S. A.* **106,** 18249–54 (2009).
8. Popovych, N., Sun, S., Ebright, R. H. & Kalodimos, C. G. Dynamically driven protein allostery. doi:10.1038/nsmb1132
9. Nussinov, R. & Tsai, C.-J. J. Allostery in Disease and in Drug Discovery. *Cell* **153,** 293 (2013).
10. Vesper, M. D. *et al.* Collective Dynamics Underlying Allosteric Transitions in Hemoglobin. *PLoS Comput. Biol.* **9,** e1003232 (2013).
11. Rodgers, T. L. *et al.* Modulation of global low-frequency motions underlies allosteric regulation: demonstration in CRP/FNR family transcription factors. *PLoS Biol.* **11,** e1001651 (2013).
12. Lockless, S. W. & Ranganathan, R. Evolutionarily conserved pathways of energetic connectivity in protein families. *Science* **286,** 295–9 (1999).
13. Vendruscolo, M., Dokholyan, N., Paci, E. & Karplus, M. Small-world View of the Amino Acids That Play a Key Role in Protein Folding. *Phys. Rev. E Stat. Phys., Plasmas, Fluids, Relat. Interdiscip. Top.* **65,** 61910 (2002).
14. van den Bedem, H., Bhabha, G., Yang, K., Wright, P. E. & Fraser, J. S. Automated identification of functional dynamic contact networks from X-ray crystallography. *Nat. Methods* **10,** 896 (2013).

15. Schreiber, G. & Fersht, A. R. Energetics of Protein-protein Interactions: Analysis of the Barnase-barstar Interface by Single Mutations and Double Mutant Cycles. *J. Mol. Biol.* **248,** 478 (1995).

16. Gleitsman, K. R., Shanata, J. A. P., Frazier, S. J., Lester, H. A. & Dougherty, D. A. Long-range coupling in an allosteric receptor revealed by mutant cycle analysis. *Biophys. J.* **96,** 3168–78 (2009).

17. Sugase, K., Dyson, H. J. & Wright, P. E. Mechanism of coupled folding and binding of an intrinsically disordered protein. *Nature* **447,** 1021–1025 (2007).

18. Lisi, G. P. & Loria, J. P. Solution NMR Spectroscopy for the Study of Enzyme Allostery. *Chem. Rev.* **116,** 6323–6369 (2016).

19. Baldwin, A. J. & Kay, L. E. NMR spectroscopy brings invisible protein states into focus. *Nat. Chem. Biol.* **5,** 808–14 (2009).

20. Velyvis, A., Yang, Y. R., Schachman, H. K. & Kay, L. E. A solution NMR study showing that active site ligands and nucleotides directly perturb the allosteric equilibrium in aspartate transcarbamoylase. *Proc. Natl. Acad. Sci. U. S. A.* **104,** 8815 (2007).

21. Zhuravleva, A. & Gierasch, L. M. Substrate-binding Domain Conformational Dynamics Mediate Hsp70 Allostery. *Proc. Natl. Acad. Sci. U. S. A.* **112,** E2865 (2015).

22. Boulton, S. & Melacini, G. Advances in NMR Methods To Map Allosteric Sites: From Models to Translation. *Chem. Rev.* **116,** 6267–6304 (2016).

23. Akimoto, M. *et al.* Signaling Through Dynamic Linkers as Revealed by PKA. *Proc. Natl. Acad. Sci. U. S. A.* **110,** 14231 (2013).

24. Swain, J. F. *et al.* Hsp70 chaperone ligands control domain association via an allosteric mechanism mediated by the interdomain linker. *Mol. Cell* **26,** 27–39 (2007).

25. Tzeng, S.-R. & Kalodimos, C. G. Protein activity regulation by conformational entropy. *Nature* **488,** 236–40 (2012).

26. Xu, Y., Bhate, M. P. & McDermott, A. E. Transmembrane allosteric energetics characterization for strong coupling between proton and potassium ion binding in the KcsA channel. *Proc. Natl. Acad. Sci. U. S. A.* **114,** 8788–8793 (2017).

27. Dissecting Dynamic Allosteric Pathways Using Chemically Related Small-Molecule Activators.

Structure **24,** 1155–1166 (2016).

28. Bhate, M. P., Wylie, B. J., Tian, L. & McDermott, A. E. Conformational dynamics in the selectivity filter of KcsA in response to potassium ion concentration. *J. Mol. Biol.* **401,** 155–66 (2010).
29. Selvaratnam, R., Chowdhury, S., VanSchouwen, B. & Melacini, G. Mapping allostery through the covariance analysis of NMR chemical shifts. *Proc. Natl. Acad. Sci. U. S. A.* **108,** 6133–8 (2011).
30. Williamson, M. P. Using chemical shift perturbation to characterise ligand binding. *Prog. Nucl. Magn. Reson. Spectrosc.* **73,** 1 (2013).
31. Hajduk, P. J., Meadows, R. P. & Fesik, S. W. Discovering High-Affinity Ligands for Proteins. *Science (80-.).* **278,** (1997).
32. Mayer, M. & Meyer, B. Characterization of Ligand Binding by Saturation Transfer Difference NMR Spectroscopy. *Angew. Chemie Int. Ed.* **38,** 1784–1788 (1999).
33. Whittier, S. K., Hengge, A. C. & Loria, J. P. Conformational Motions Regulate Phosphoryl Transfer in Related Protein Tyrosine Phosphatases. *Science (80-.).* **341,** (2013).
34. Liu, J. J., Horst, R., Katritch, V., Stevens, R. C. & Wüthrich, K. Biased signaling pathways in β2-adrenergic receptor characterized by 19F-NMR. *Science* **335,** 1106–10 (2012).
35. Cuello, L. G., Jogini, V., Cortes, D. M. & Perozo, E. Structural mechanism of C-type inactivation in K(+) channels. *Nature* **466,** 203–8 (2010).
36. Cordero-Morales, J. F. *et al.* Molecular driving forces determining potassium channel slow inactivation. *Nat. Struct. Mol. Biol.* **14,** 1062–9 (2007).
37. Devaraneni, P. K. *et al.* Semisynthetic K+ channels show that the constricted conformation of the selectivity filter is not the C-type inactivated state. *Proc. Natl. Acad. Sci. U. S. A.* **110,** 15698–703 (2013).
38. Wylie, B. J., Bhate, M. P. & McDermott, A. E. Transmembrane allosteric coupling of the gates in a potassium channel. *Proc. Natl. Acad. Sci. U. S. A.* **111,** 185–90 (2014).
39. Ader, C. *et al.* Coupling of activation and inactivation gate in a K+-channel: potassium and ligand sensitivity. *EMBO J.* **28,** 2825–34 (2009).
40. Hoshi, T. & Armstrong, C. M. C-type inactivation of voltage-gated K+ channels: pore constriction or dilation? *J. Gen. Physiol.* **141,** 151–60 (2013).

41. Li, J. *et al.* Chemical substitutions in the selectivity filter of potassium channels do not rule out constricted-like conformations for C-type inactivation. *Proc. Natl. Acad. Sci. U. S. A.* **114,** 11145–11150 (2017).

42. Imai, S., Osawa, M., Takeuchi, K. & Shimada, I. Structural basis underlying the dual gate properties of KcsA. *Proc. Natl. Acad. Sci. U. S. A.* **107,** 6216–21 (2010).

43. Choe, S. Potassium channel structures. *Nat. Rev. Neurosci.* **3,** 115–21 (2002).

44. Curran, M. E. *et al.* A molecular basis for cardiac arrhythmia: HERG mutations cause long QT syndrome. *Cell* **80,** 795–803 (1995).

45. Shieh, C.-C., Coghlan, M., Sullivan, J. P. & Gopalakrishnan, M. Potassium Channels: Molecular Defects, Diseases, and Therapeutic Opportunities. *Pharmacol. Rev.* **52,** 557–594 (2000).

46. MacKinnon, R. Potassium channels. *FEBS Lett.* **555,** 62–65 (2003).

47. McCoy, J. G. & Nimigean, C. M. Structural correlates of selectivity and inactivation in potassium channels. *Biochim. Biophys. Acta* **1818,** 272–85 (2012).

48. Chakrapani, S., Cordero-Morales, J. F. & Perozo, E. A quantitative description of KcsA gating I: macroscopic currents. *J. Gen. Physiol.* **130,** 465–78 (2007).

49. Cuello, L. G. *et al.* Structural basis for the coupling between activation and inactivation gates in K(+) channels. *Nature* **466,** 272–5 (2010).

50. Arthur G. Palmer III, ‡, John Williams, †,§ and & Ann McDermott*, †. Nuclear Magnetic Resonance Studies of Biopolymer Dynamics. (1996). doi:10.1021/JP9606117

51. LeMasurier, M., Heginbotham, L. & Miller, C. KcsA: it's a potassium channel. *J. Gen. Physiol.* **118,** 303–14 (2001).

52. Takegoshi, K., Nakamura, S. & Terao, T. 13C–1H dipolar-assisted rotational resonance in magic-angle spinning NMR. *Chem. Phys. Lett.* **344,** 631–637 (2001).

53. Case, D. A. The use of chemical shifts and their anisotropies in biomolecular structure determination. *Curr. Opin. Struct. Biol.* **8,** 624–630 (1998).

54. Manley, G. & Loria, J. P. NMR insights into protein allostery. *Arch. Biochem. Biophys.* **519,** 223–31 (2012).

55. McDermott, A. E. Structural and dynamic studies of proteins by solid-state NMR spectroscopy:

rapid movement forward. *Curr. Opin. Struct. Biol.* **14,** 554–561 (2004).

56. Akke, M., Brueschweiler, R. & Palmer, A. G. NMR order parameters and free energy: an analytical approach and its application to cooperative calcium(2+) binding by calbindin D9k. *J. Am. Chem. Soc.* **115,** 9832–9833 (1993).

57. Pan, A. C., Cuello, L. G., Perozo, E. & Roux, B. Thermodynamic coupling between activation and inactivation gating in potassium channels revealed by free energy molecular dynamics simulations. *J. Gen. Physiol.* **138,** 571–80 (2011).

58. Posson, D. J., Thompson, A. N., McCoy, J. G. & Nimigean, C. M. Molecular interactions involved in proton-dependent gating in KcsA potassium channels. *J. Gen. Physiol.* **142,** 613–24 (2013).

59. Chakrapani, S., Cordero-Morales, J. F. & Perozo, E. A quantitative description of KcsA gating II: single-channel currents. *J. Gen. Physiol.* **130,** 479–96 (2007).

60. Masterson, L. R., Mascioni, A., Traaseth, N. J., Taylor, S. S. & Veglia, G. Allosteric Cooperativity in Protein Kinase A. *Proc. Natl. Acad. Sci. U. S. A.* **105,** 506 (2008).

61. Gao, L., Mi, X., Paajanen, V., Wang, K. & Fan, Z. Activation-coupled inactivation in the bacterial potassium channel KcsA. *Proc. Natl. Acad. Sci. U. S. A.* **102,** 17630–5 (2005).

62. Bhate, M. P. & McDermott, A. E. Protonation state of E71 in KcsA and its role for channel collapse and inactivation. *Proc. Natl. Acad. Sci. U. S. A.* **109,** 15265–70 (2012).

63. Selvaratnam, R., Chowdhury, S., VanSchouwen, B. & Melacini, G. Mapping Allostery through the Covariance Analysis of NMR Chemical Shifts. *Proc. Natl. Acad. Sci. U. S. A.* **108,** 6133 (2011).

64. Axe, J. M. *et al.* Amino Acid Networks in a $(\beta/\alpha)_8$ Barrel Enzyme Change during Catalytic Turnover. *J. Am. Chem. Soc.* **136,** 6818–6821 (2014).

65. Cui, D. S., Beaumont, V., Ginther, P. S., Lipchock, J. M. & Loria, J. P. Leveraging Reciprocity to Identify and Characterize Unknown Allosteric Sites in Protein Tyrosine Phosphatases. *J. Mol. Biol.* **429,** 2360–2372 (2017).

66. O'Donnell, J. P., Byrnes, L. J., Cooley, R. B. & Sondermann, H. A hereditary spastic paraplegia–associated atlastin variant exhibits defective allosteric coupling in the catalytic core. *J. Biol. Chem.* **293,** 687–700 (2018).

67. Verel, R., Ernst, M. & Meier, B. H. Adiabatic dipolar recoupling in solid-state NMR: the DREAM

scheme. *J. Magn. Reson.* **150,** 81–99 (2001).

68. Bennett, A. E., Rienstra, C. M., Auger, M., Lakshmi, K. V. & Griffin, R. G. Heteronuclear decoupling in rotating solids. *J. Chem. Phys.* **103,** 6951–6958 (1995).

69. Goddard TD, Kneller DG, SPARKY 3 (University of California, San Francisco).

Chapter VI

Multinuclear SSNMR Characterization of Inorganic Superatoms

6.1 Abstract

$Co_6Se_8(PEt_3)_6$ “superatom” clusters show promise as single molecule magnets.[1,2] The magnetic properties can be tuned by means of choice of ligand, oxidation state and temperature, and show distinct behavior compared to either single atoms or bulk materials. Moreover, the “superatom” can serve as a building block to synthesize novel hierarchical solids with distinctive properties.[3,4]. Details of the molecular structure, dynamics and especially electron spin state and distribution of these superatoms remain of interest. We characterized three examples of these clusters using Solid State Nuclear Magnetic Resonance (SSNMR), which provides a unique and sensitive probe of electronic environment. Here we use chemical shifts of the ^{59}Co nuclei in the neutral and oxidized clusters and ^{31}P atoms in the associated ligands to probe oxidation state and magnetic susceptibility.

6.2. Introduction

6.2.1 Introduction to superatoms

Metal clusters have attracted tremendous attention in recent years due to their special size, electronic, magnetic and thermodynamic properties, which are distinct from those found in either atoms or the bulk materials.[5–8] Many efforts have been made to combine different clusters as superatoms to build molecular cluster compounds, which display new and interesting properties and can be potentially applied for building electronics, energy storage devices, and other novel materials.[6,7] The use of clusters as superatoms is inspired by the concept that the clusters can behave as individual atoms and thus mimic the chemistry typically exhibited by single elements.[9] One of the main advantages over conventional bulk materials is the tunabliity of the chemical and physical properties of these building blocks, which allows for fine tuning the properties of new materials.[9,10]

Recently Roy and others have successfully synthesized a series of molecular cluster compounds. These cluster compounds are the structural analogues of traditional binary ionic compounds, such as NaCl, CsCl. In these materials, metal chalcogenide clusters, composed of an inorganic core and a passivating ligand shell, assemble with other clusters, such as $Fe_8O_4pz_{12}Cl_4$ (pz = pyrazolate, $C_3H_3N_2^-$) and fullerenes to form cluster compounds through charge transfer or designed molecular recognition.[7] Importantly, unlike traditional atomic solids, where the atoms (or ions) are spherical and chemically immutable, superatoms can be flexibly modified with different ligands to tune the crystal packing within the molecular cluster compound. [9,11]

These superatoms and their cluster compounds have been identified with many intriguing properties. For example, they studied the electrical resistivity of various cluster compounds, such as $[Cr_6Te_8\ (PEt_3)_6][C_{60}]_2$, $[Co_6Se_8(PEt_3)_6][C_{60}]_2$ as a function of temperature.[3] The electric conductivity properties can be tuned by inserting redoxactive molecules into the lattices to change the carrier density.[12] Single molecule junction measurement on the Co_6Se_8 superatom showed that the conductivity of the cluster is dependent on the charge state of the cluster, which can be controlled by the external voltage, making it a potential material for preparing transistors.[13] They also discovered that the cluster compounds potentially have unique thermal transport behavior due to the complex vibrational landscape

caused by the diverse inter- and intra- superatom interaction.[14] The atomically precise hierarchical structure of inorganic molecular clusters, which could potentially tune the interaction between the large magnetic moments possessed by the superatoms, produces long-range cooperative magnetic properties.[7,15] As shown in the case of $[Ni_9Te_6(PEt_3)_8]$-$[C_{60}]$, superconducting quantum interference device (SQUID) magnetometry showed the magnetic motifs of the Ni_9Te_6 cores spontaneously couple and stabilize a ferromagnetic ground state at a temperature around 4K.[16,17]

Even though great success has been achieved from a material-synthesis perspectives, there is need for more tools to fully characterize of these superatoms and probe the structure, dynamics, and functions. Single crystal X-ray diffraction (SCXRD) has been the routine technique to provide structural information on those superatoms and the cluster compounds. Even though information on atomic electron environment can be estimated from the measured bond length and angle, the information is generally averaged due to sample rotation and is limited by the resolution of the crystals. The details of the structural, dynamic (in terms of ligand mobility), and electronic makeup of the superatoms is crucial for characterizing and predicting the behavior of these superatoms and molecular cluster compounds. Specifically, the surface ligands have been shown to be of great importance to the stability of the clusters, and also an integral part for electronic properties.[16] The ligands are also the key to "tuning" the clusters; the study of ligands is critical to the success to build new and functional cluster compounds.[7,9,15,16] The relationship between ligand properties and functional properties of the cluster compounds is poorly understood. Therefore, it is necessary to develop methods to characterize these properties.

6.2.2 NMR study on materials

NMR, especially Solid State Nuclear Magnetic Resonance (SSNMR), has proven to be an excellent tool for probing site-specific information, providing structural and dynamic information in various systems including organic/inorganic materials, colloidal nanoparticles and metal-organic frameworks.[18–22] The isotropic chemical shift, chemical shift anisotropy and qaudroplar coupling constants are very sensitive to the local electronic environment. The dipolar coupling and the J-Coupling can be used to generate constraints for structural determination. The relaxation rate can provide local information on magnetic properties such as paramagnetism vs. diamagnetism as well as the local dynamics. Here we

focused our study on a series of $Co_6Se_8(PEt_3)_6$ clusters and mixtures with C_{60} to demonstrate application of SSNMR study to superatoms and their cluster compounds, with the assistance from software to simulate NMR spectra and theoretical calculations.

6.3 Results and Discussions

6.3.1 NMR characterization of $Co_6Se_8(PEt_3)_6$

$Co_6Se_8(PEt_3)_6$ "superatom" clusters (Figure 6.1a) were characterized using SSNMR. The cluster core was characterized by ^{59}Co and ^{77}Se NMR and the surficial ligands were studied by mainly ^{31}P as well as ^{13}C and ^{1}H NMR. We have recorded ^{31}P NMR of the neutral, +1 and +2 $Co_6Se_8(PEt_3)_6$ "superatom" clusters as well as ^{59}Co NMR of the neutral cluster and used chemical shifts and relaxation properties to probe oxidation state and magnetic susceptibility. These data in aggregate lead us to conclude that the neutral cluster is diamagnetic, while both the +1 and +2 clusters are paramagnetic.

6.3.3.1 The neutral cluster is diamagnetic

The ^{31}P CPMAS SSNMR spectrum of the ligands in the neutral cluster (figure 6.1b) is split into 8 J-coupled peaks due to the coupling of ^{31}P to the ^{59}Co nucleus (a quadrupolar nucleus with spin S=7/2).[23] Two different multiplets, with distinct chemical shifts and J-coupling values are detected (coupling values of 640Hz and 702Hz). The interpretation that the splittings are due to coupling to ^{59}Co was confirmed by performing decoupling of ^{59}Co during detection. In this experiment, the splittings were absent and two broad peaks were observed in the Co decoupled ^{31}P spectrum (shown in the inset of figure1b). This experiment confirms our interpretation of the multiplet structure as arising from coupling to ^{59}Co.

^{59}Co WURST-QCPMG experiments[24] of the neutral cluster revealed a broad ^{59}Co spectrum (ca. 10^4 ppm), with a number of unique spectra features (Fig. 6.1c). The spectral shape manifests features of a quadrupolar tensor coupled to a CSA tensor. The relatively narrow lines of this spectrum, the presence of resolved J-splittings in the ^{31}P spectrum, and the fact that the temperature dependence of the shift is quite small (see Figure 6.3b) all suggest that this species is diamagnetic. We are in the process of simulating these spectra to obtain useful constraints on the structure and electronic structure.

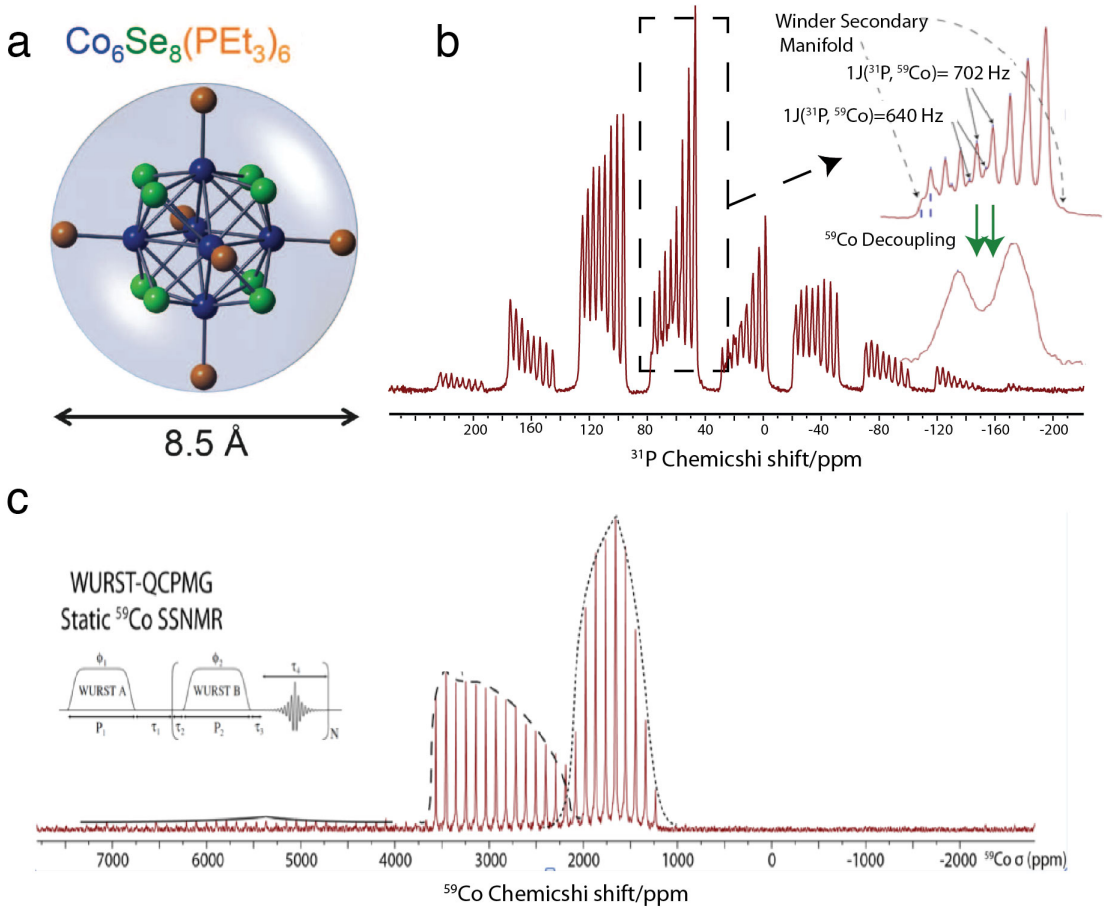

Figure 6.1. SSNMR characterization of the neutral superatom. (a) Structure of the superatom cluster. (b) ^{1}H-^{31}P CP spectrum of ^{31}P in the phosphiene ligands of the neutral superatom cluster. The spectrum was taken at room temperature at 8 kHz MAS spinning. (c) WURST-QCPMG spectrum of ^{59}Co nucleus of the neutral superatom cluster. The spectrum was taken at a static condition with 80 kHz proton decoupling.

6.3.3.2 The +1 and +2 clusters are paramagnetic

We next investigated the +1 charged cluster prepared by stoichiometric oxidation. This species is hypothesized to share a common structure with the neutral species. The ^{31}P NMR spectrum of +1 charged cluster displays an upfield chemical shift at approximately -400 ppm compared to the neutral cluster. (Figure 6.2) These large shifts, the broad linewidths, and short T_1 values (<0.3 s) all suggest that the +1 cluster is paramagnetic. The T_1 time is the required time for a nucleus to recover to its equilibrium state for the next excitation; in the paramagnetic sample, due to the paramagnetic effect on nuclear spin

relaxation, the T_1 time is significantly shorter compared to diamagnetic samples (usually in seconds or minutes).

We further investigated the +2 charge cluster, which is also prepared by stoichiometric oxidation and also hypothesized to share a common structure motif with the neutral species. The ^{31}P of the +2 cluster shows even more shifted chemical shifts. These large shifts, the broad linewidths, and short and temperature dependent T1 values (<0.3 s) all suggest that the +2 cluster is also paramagnetic.

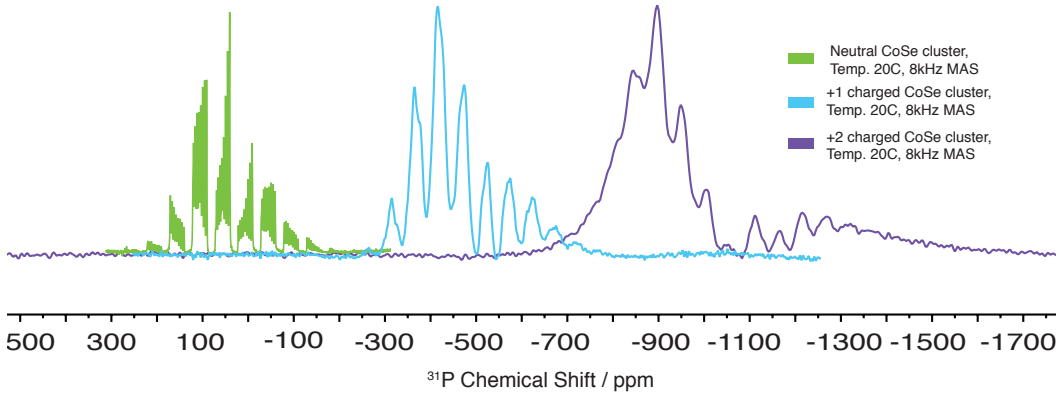

Figure 6.2. ^{31}P spectra of $Co_6Se_8(PEt_3)_6$ clusters with various net charges. The spectra of the +2 (violet, right) and +1 (blue, middle) charged clusters were taken using direct excitation MAS NMR, without proton decoupling. The spectrum of the neutral cluster (green, left) was taken using ^{1}H to ^{31}P cross polarization excitation and proton decoupling during detection. All spectra were taken using magic angle spinning at a frequency of 8 kHz, on a 400 MHz instrument.

6.3.2 Spin state determination by SQUID and temperature dependent NMR study

SQUID susceptibility measurements also indicated that the oxidized (but not the neutral) samples are paramagnetic. The susceptibilities suggest spin states of S=0, S=1/2 and (tentatively) S=1 for the neutral, +1 and +2 clusters, respectively. (Figure 6.3a)

In order to further investigate the spin states in these clusters, we studied the temperature dependence of the chemical shifts of the ^{31}P NMR lines (Figure 6.4 and Figure 6.5); linear trends are observed as a function of inverse temperature consistent with the statement that the +1 and +2 clusters are paramagnetic and the neutral cluster is diamagnetic. (Figure 6.3b) The detailed temperature dependences suggest agreement with susceptibilities obtained from SQUID suggesting spin states of

S=0, S=1/2 and (tentatively) S=1 for the neutral, +1 and +2 clusters, respectively. (Appendix 7 for spin state calculation) These apparent spin states are not consistent with a charge and spin trapped model for the Co ions, and suggest significant delocalization on the cluster.

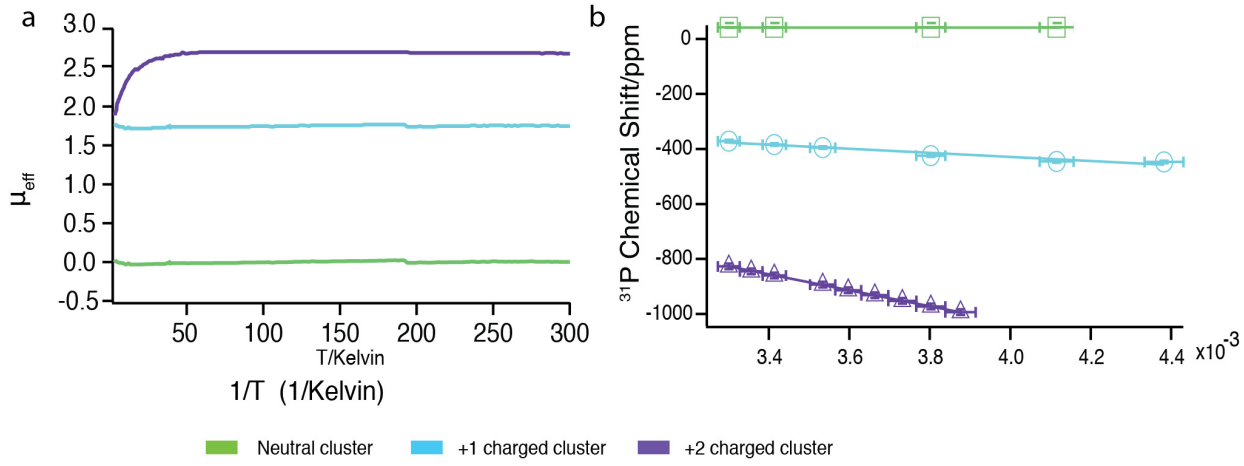

Figure 6.3. Magnetic properties probed by SQUID and temperature-dependent SSNMR studies. (a) Through SQUID measurements, we calculated that there is zero, one and two unparied electrons in the neutral, +1 and +2 clusters, respectively. (b) Comparison of the temperature dependences of the ^{31}P chemical shifts for $Co_6Se_8(PEt_3)_6$ neutral (green, top) +1 charged (blue, middle) and +2 charged (violet, bottom) clusters. The peak of the maximum intensity in the ^{31}P spectra were chosen to calculate the chemical shift change at various temperatures for all the three clusters. By contrast the neutral cluster shows shifts that are nearly temperature independent.

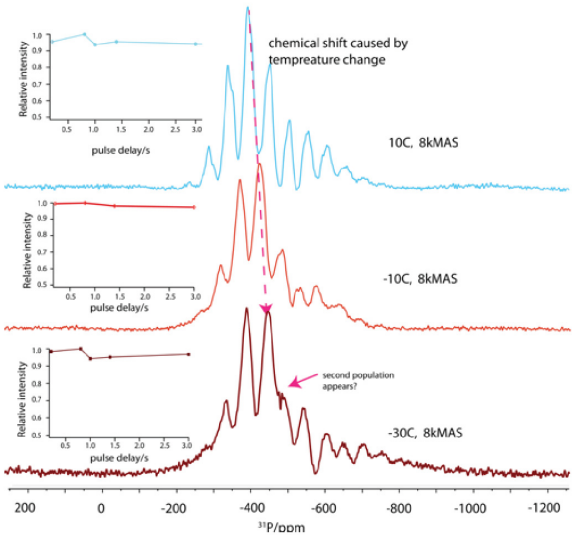

Figure 6.4. Temperature –dependent chemical shift of the +1 charged cluster. The inset plots show that when the recycle delay is lengthened, the signal intensity does not change, implying a T_1 value for ^{31}P in the cluster that is less than 0.3 s.

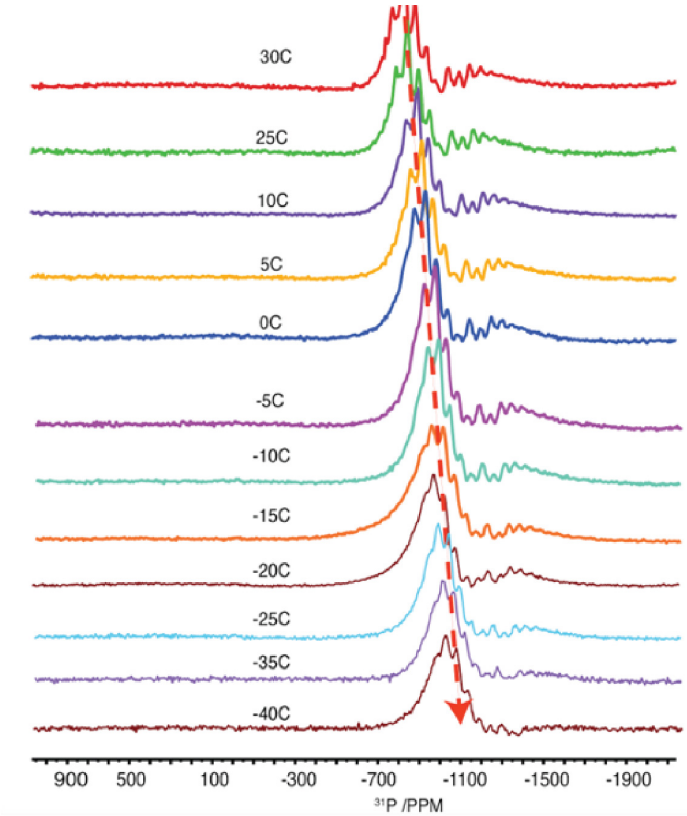

Figure 6.5. Temperature –dependent chemical shift of the +2 charged cluster.

6.3.3 NMR characterization of a combined-cluster mixture

After we characterized the single Co_6Se_8 at various charge states, we aimed to study the cluster in complex with the C_{60} cluster, which forms a superatomic ionic compound. It is hypothesized that there is an electron transferring between the Co_6Se_8 and the C_{60} cluster in this superatomic ionic compound, which is analogous to ionic compound NaCl.

Our first question towards this compound is what is the oxidation state of the Co_6Se_8 in the compound. It is assumed to +1 charged as an electron is transferred to the C_{60} cluster. Based on our previous results that ^{31}P chemical shift of the phosphorus atom directly linked to the Co atoms is a good indicator for cluster oxidization state, we carried out ^{31}P direct excitation MAS experiments on the complex. The ^{31}P spectrum for the complex is shown below in comparison to the previous results on the single Co_6Se_8 at the neutral, +1 and +2 charged states. (Figure 6) It is obvious that the ^{31}P chemical shift is most similar to the +1 charged cluster, which in consistent with the hypothesis that one electron is transferred from the Co_6Se_8 cluster to the C60 cluster.

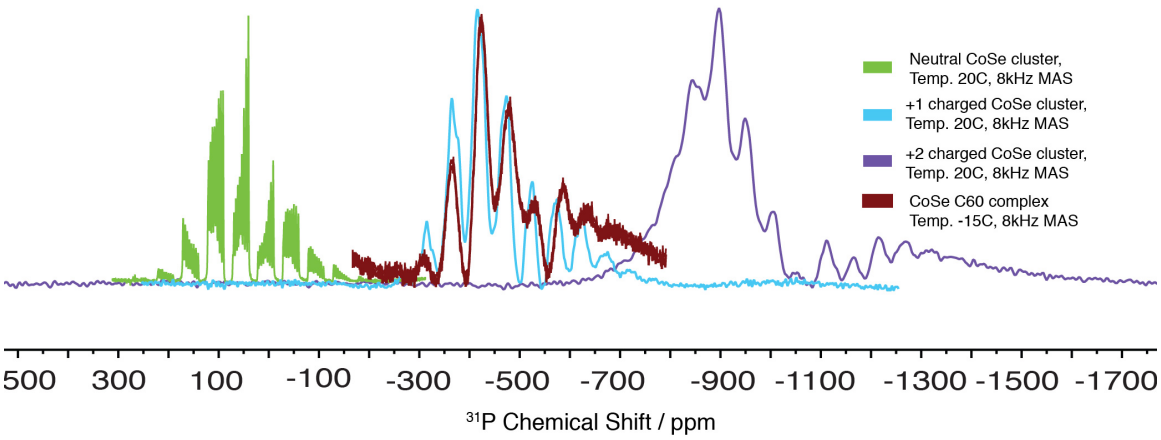

Figure 6.6. SSNMR detects the of Co_6Se_8 superatom in the cluster compound. Comparison of ^{31}P spectra of the Co_6Se_8-C60 complex to that of single clusters at various charged states indicates that the Co_6Se_8 in the complex is in the +1 charged state.

As we showed in above, the single +1 charged cluster Co_6Se_8 cluster is paramagnetic; the ^{31}P chemical shift shows temperature-dependent shift. We did the same characterization on the complex. The result T_1 measurement on the ^{31}P nucleus indicated that the Co_6Se_8 is paramagnetic in the cluster

compound, which is consistent with the broad linewidth we observed for the ^{31}P spectrum.(Figure 6.7) We further characterized the temperature dependent shift for the ^{31}P chemical shift to quantitatively probe the magnetic properties of the cluster compound, which is shown in Figure 6.8. Importantly, the ^{31}P do show temperature-dependent shift and the shift is quantified as shown in Figure 6.9. The slope of the chemical shift change is similar but flatter than that of the +1 charged cluster, indicating that there is less electron spin in the compound cluster. This result is in contract to the chemical shift change (Figure 6.6), where ^{31}P chemical shift in the compound cluster shows similar but more deshielded shift, indicating that there is more electron density in the compound cluster. We hypothesize that such an inconsistency between the electron density and spin density is related to the existence of C_{60}.

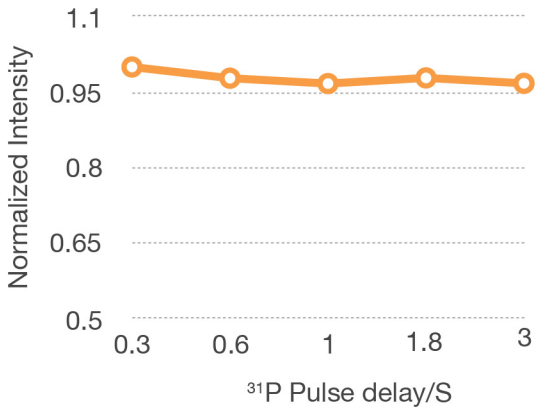

Figure 6.7. In ^{31}P pulse delay experiment, the signal intensity reaches to maximum at the 0.3 second, indicating the T_1 value for the ^{31}P nuclei is shorter than 0.3 second. This confirms that the Co_6Se_8 in the Co_6Se_8-C_{60} cluster compound is paramagnetic. The spectra were taken using magic angle spinning at a frequency of 8 kHz, on a 400 MHz instrument.

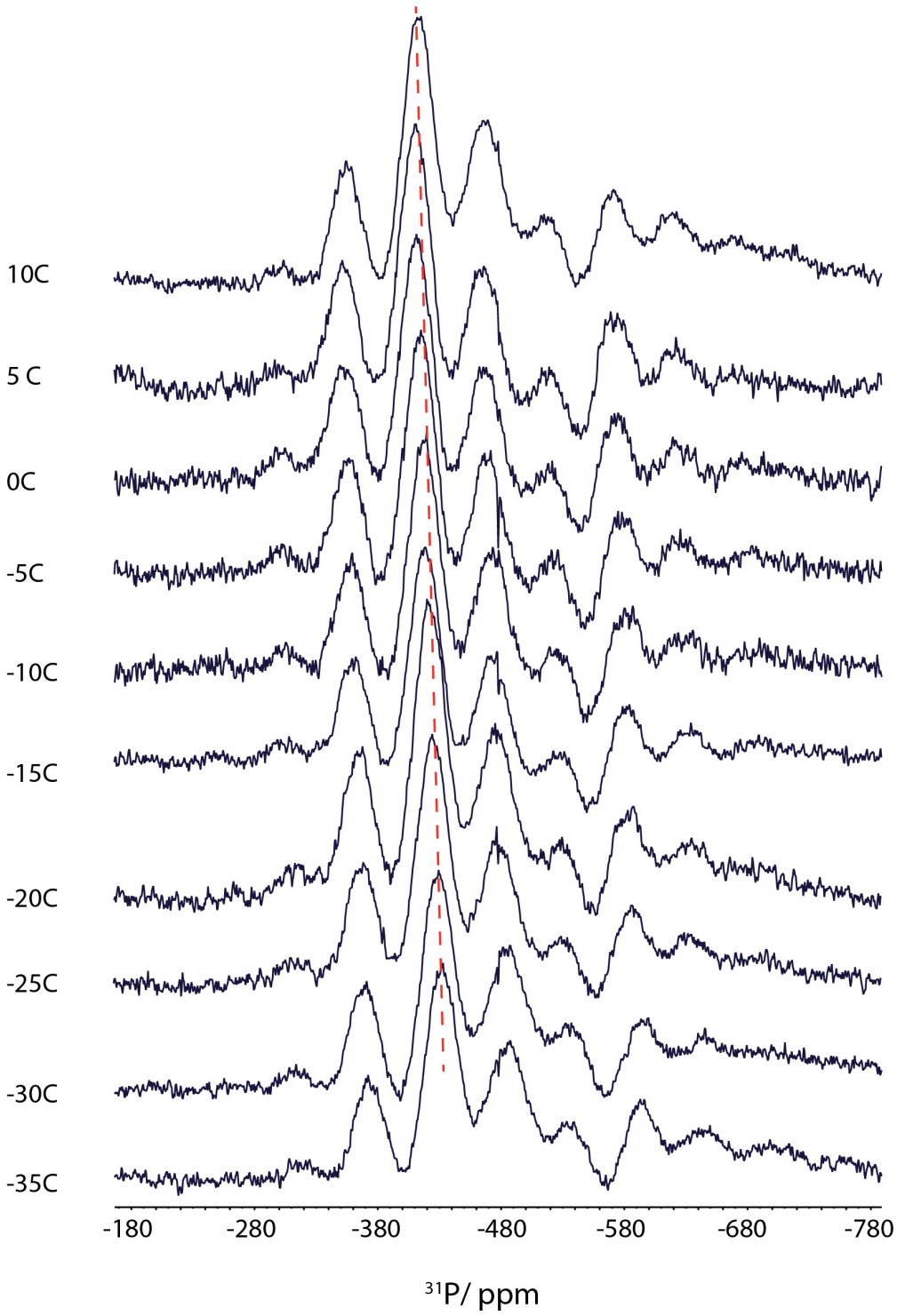

Figure 6.8. ^{31}P spectra of the Co_6Se_8-C_{60} cluster compound show temperature-dependent shift. All the spectra were taken using magic angle spinning at a frequency of 8 kHz, on a 400 MHz instrument. A more quantitative analysis is shown in Figure 6.9.

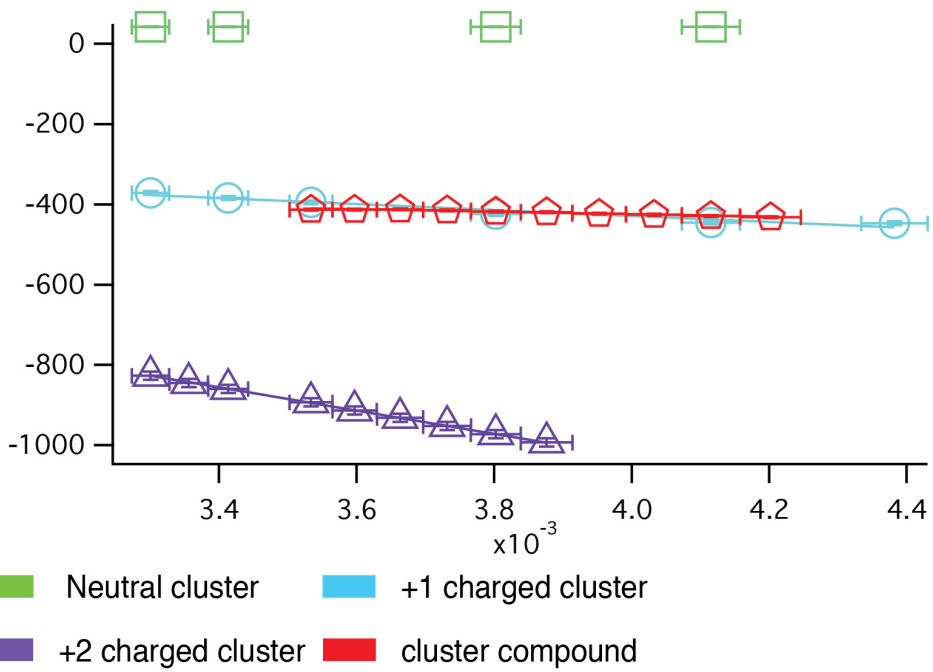

Figure 6.9 Comparison of the temperature dependences of the ^{31}P chemical shifts for $Co_6Se_8(PEt_3)_6$ C_{60} culster compound(red) to that of neutral (green) +1 charged (blue) and +2 charged (violet) clusters.

C_{60}, as the electron acceptor, is assumed to be in the -1 charged state and also paramagnetic. We conducted the direct excitation experiment on ^{13}C with proton decoupling to probe the C_{60}. (Figure 6.10) There peaks are observed in the spectrum; two of them are dominant and the other peak is minor and assigned the ethyl ligand. Based on literatures, the chemical shift near 150 ppm is assigned the carbon on the neutral C_{60} and peak width is around 17Hz. The peak around 180ppm is tentatively also assigned to C_{60}, which shows chemical shift change due to the electron transferring from the Co_6Se_8 cluster.[25] Integration of these two peaks indicate that the population ratio between the neutral and reduced form is close to 2:1.

The narrow lineshape in the ^{13}C spectra leads us to suspect that the C_{60} is not paramagnetic. We estimated the T_1 value by the pulse-delay measurement and the results show that the ^{13}C nuclei in C60 at both sites have a quite long T_1 (> 3s).(Figure 6.11) Previous T_1 measurement results on the C_{60} polycrystalline indicate that the T_1 value is close to 40s at around room temperature.[26] Due to the lack of data points, the estimated T_1 value cannot be compared with confidence. Therefore, we further studied

temperature dependence of the ^{13}C chemical shift. (Figure 6.12); the results show that the chemical shifts do not display temperature dependence. It is known that C_{60} tumbles extremely fast in the complex due to its isotropic feature. We hypothesized that the NMR behavior of the C_{60}, i.e. the T_1 and apparent T_2, may be complicated by the fast dynamics and the presence of an free electron or electron spin is not determined. Interestingly, we do not observe chemical shift change for the ^{13}C in the ethyl ligand, which connects to the ^{31}P atom.

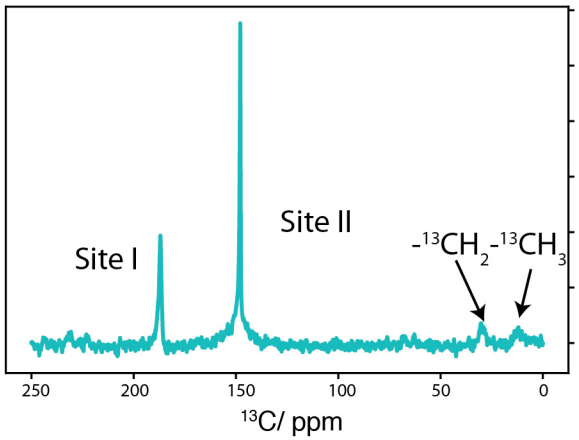

Figure 6.10. ^{13}C spectrum for the C_{60} in the Co_6Se_8-C_{60} complex is displayed. There are two major peaks. The peak at around 150ppm is assigned to C_{60}, based on previous literature. The linewidth for this peak is 17Hz, indicating that the coherence time is long due to the fast tumbling of the C_{60} cluster. The peak around 180ppm is tentatively also assigned to C_{60}, which shows chemical shift change due to the electron transferring from the Co_6Se_8 cluster.

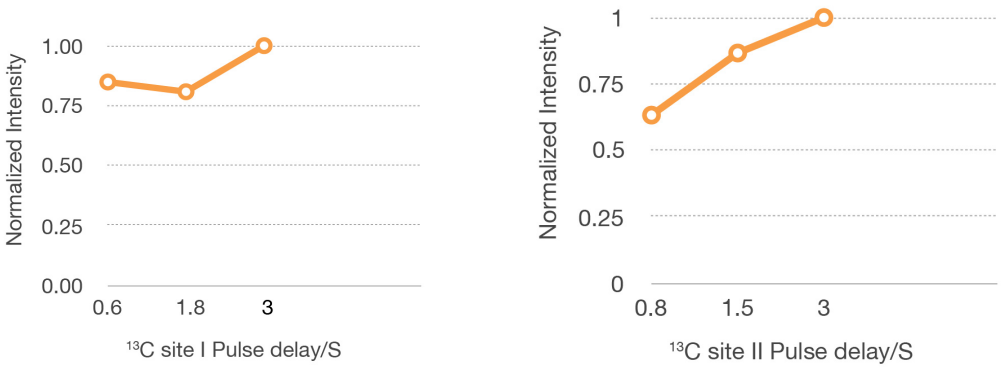

Figure 6.11. ^{13}C pulse delay experiment results are shown for the site I and site II peaks in the ^{13}C spectrum. Based on the signal intensity, the ^{13}C at site I has a relatively short T_1, but ^{13}C at both sites have a T_1 value over 3 second.

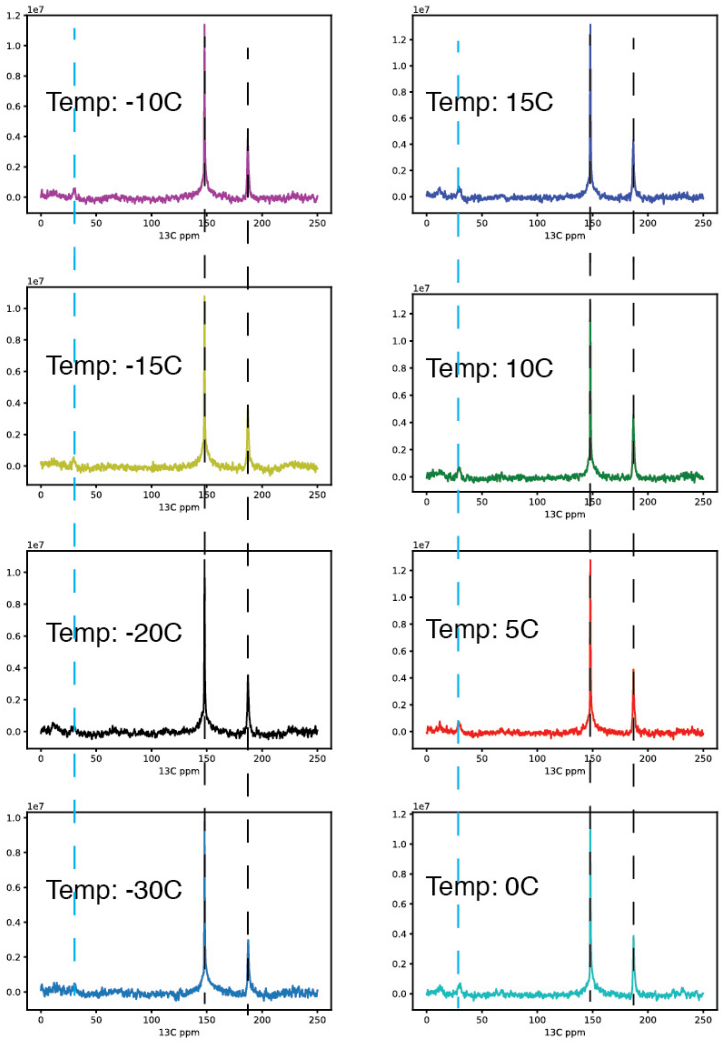

Figure 6.12. ^{13}C peaks of the carbon in the C_{60} and in the ligand of the Co_6Se_8 cluster do not show a temperature dependent shift.

6.4 Experiments

SSNMR measurement

NMR experiments were performed on a Varian Infinityplus NMR console with an Oxford 9.4 T narrow bore magnet using HXY APEX probe. The resonance frequency (v0) for ^{31}P is 160.64 MHz; ^{77}Se is 75.65 MHz ; ^{59}Co is 94.09 MHz ; ^{13}C is 99.78 MHz; ^{1}H is 396.776 MHz. The typical central transition selective 90 pulse widths of ca. 2.4 μs for carbon, 5.0 us for phosphorus, 3.0 us for proton were employed along with pulse delays typically 3.0 s. Continuous wave ^{1}H decoupling was applied for most MAS and static experiments. For the acquisition of broad static ^{59}Co NMR spectra the WURST-QCPMG pulse sequences were employed. 4.0 mm outer diameter ZrO2 air-tight rotors were used. The chemical shift is externally referenced to the downfield carbon chemical shifts adamantane line at 40.48 ppm. Other nuclei are referenced to carbon based on the gyromagnetic ratio.

6.5 References:

1. Komeda, T. *et al.* Observation and electric current control of a local spin in a single-molecule magnet. *Nat. Commun.* **2,** 217 (2011).
2. Rusponi, S. *et al.* The remarkable difference between surface and step atoms in the magnetic anisotropy of two-dimensional nanostructures. *Nat. Mater.* **2,** 546–551 (2003).
3. Roy, X. *et al.* Nanoscale Atoms in Solid-State Chemistry. *Science (80-.).* **341,** (2013).
4. Turkiewicz, A. *et al.* Assembling Hierarchical Cluster Solids with Atomic Precision. doi:10.1021/ja508698w
5. Mitzinger, S., Broeckaert, L., Massa, W., Weigend, F. & Dehnen, S. Understanding of multimetallic cluster growth. *Nat. Commun.* **7,** 10480 (2016).
6. Oro, L. A., Braunstein, P. (Pierre), Raithby, P. R. (Paul R. . & Wiley InterScience (Online service). *Metal clusters in chemistry*. (Wiley-VCH, 1999).
7. Pinkard, A., Champsaur, A. M. & Roy, X. Molecular Clusters: Nanoscale Building Blocks for Solid-State Materials. doi:10.1021/acs.accounts.8b00016
8. Luo, Z., Castleman, A. W. & Khanna, S. N. Reactivity of Metal Clusters. doi:10.1021/acs.chemrev.6b00230
9. Schacht, J. & Gaston, N. Cluster assemblies as superatomic solids: a first principles study of bonding & electronic structure. *Phys. Chem. Chem. Phys. Phys. Chem. Chem. Phys* **20,** 6167–6175 (2018).
10. Luo, Z. *et al.* What determines if a ligand activates or passivates a superatom cluster? *Chem. Sci.* **7,** 3067–3074 (2016).
11. Turkiewicz, A. *et al.* Assembling Hierarchical Cluster Solids with Atomic Precision. *J. Am. Chem. Soc.* **136,** 15873–15876 (2014).
12. O'Brien, E. S. *et al.* Single-crystal-to-single-crystal intercalation of a low-bandgap superatomic crystal. *Nat. Chem.* **9,** 1170–1174 (2017).
13. Lovat, G. *et al.* Room-temperature current blockade in atomically defined single-cluster junctions. *Nat. Nanotechnol.* **12,** 1050–1054 (2017).
14. Ong, W.-L. *et al.* Orientational order controls crystalline and amorphous thermal transport in

superatomic crystals. *Nat. Mater.* **16,** 83–88 (2017).

15. Reber, A. C., Chauhan, V. & Khanna, S. N. Symmetry and magnetism in Ni_9Te_6 clusters ligated by CO or phosphine ligands. *J. Chem. Phys.* **146,** 24302 (2017).
16. Chauhan, V., Sahoo, S. & Khanna, S. N. Ni 9 Te 6 (PEt 3) 8 C 60 Is a Superatomic Superalkali Superparamagnetic Cluster Assembled Material (S 3 -CAM). doi:10.1021/jacs.5b10986
17. Lee, C.-H. *et al.* Ferromagnetic Ordering in Superatomic Solids. *J. Am. Chem. Soc.* **136,** 16926–16931 (2014).
18. Lucier, B. E. G., Chen, S. & Huang, Y. Characterization of Metal–Organic Frameworks: Unlocking the Potential of Solid-State NMR. *Acc. Chem. Res.* **51,** 319–330 (2018).
19. Summers, M. F. 113Cd NMR spectroscopy of coordination compounds and proteins. *Coord. Chem. Rev.* **86,** 43–134 (1988).
20. Pecher, O., Carretero-González, J., Griffith, K. J. & Grey, C. P. Materials' Methods: NMR in Battery Research. *Chem. Mater.* **29,** 213 (2017).
21. Smith, M. E. & Strange, J. H. NMR techniques in materials physics: a review. *Meas. Sci. Technol.* **7,** 449–475 (1996).
22. Templin, M., Wiesner, U. & Spiess, H. W. Multinuclear solid-state-NMR studies of hybrid organic-inorganic materials. *Adv. Mater.* **9,** 814 (1997).
23. Schurko, R. W., Wasylishen, R. E. & Nelson, J. H. Effect of Cobalt-59 Self-Decoupling on the Solid-State 31 P CP/MAS NMR Spectra of Cobaloximes. (1996).
24. O'Dell, L. A. & Schurko, R. W. QCPMG using adiabatic pulses for faster acquisition of ultra-wideline NMR spectra. *Chem. Phys. Lett.* **464,** 97–102 (2008).
25. Tycko, R. *et al.* 3C NMR Spectroscopy of KC60: Phase Separation, Molecular Dynamics, and Metallic Properties. (2018).
26. JOHNSON, R. D., YANNONI, C. S., DORN, H. C., SALEM, J. R. & BETHUNE, D. S. C60 Rotation in the Solid State: Dynamics of a Faceted Spherical Top. *Science (80-.).* **255,** 1235–1238 (1992).

Future direction

In the thesis, we did systemic measurements on the thermodynamics of the KcsA protein to illustrate the important role of allosteric coupling in regulating the channel's functions. There data provides useful energetic information to understand the conversion between various states.

However, it is difficult to fully understand the whole mechanistic picture without incorporation of dynamic study of the protein. One example is that in the activation-coupled inactivation hypothesis, we prove that the opening of the pH gate is coupled to the selectivity filter; but the question like how the pH gate is coupled to the selectivity filter is largely untouched and still puzzling, especially considering that the timescales of these two coupled conformational changes happen in different timescales. One hypothesis I come up to explain this difference is that the fast motions of the pH gate can gradually cumulate and eventually convert the higher energetic barrier during the conformational change at the selectivity filter. It can be analogous to a system with two coupling cogwheels with very different radius, in which the fast rotation of the wheel with a small radius only cause a slow rotation of the wheel with a large radius. Another similar hypothesis but in a less mechanic view is that opening the pH gate allows certain probability of the structural transition from one conformation to the other conformation. Measurement on the residual dynamics at various states will be of great importance to explore this question. One particular interesting aspect is to find residual dynamics distribution over the allosteric coupling pathway to see if a transition exists from fast to slow dynamics. Specific attention is needed on the allosteric participants we have identified. This may help us get a better understanding of the functional behavior of T74S mutant: the small methyl side chain dramatically changes the inactivation behavior. To fully explore this problem, I expect that other biophysical methods such as molecular dynamic simulation can offer great assistance.

In this thesis, we measured the potassium affinity in term of the structural conformation change at the selectivity filter. However, during the permeation process, when the selectivity filter is kept in a conductive form, what are the affinities of potassium ion in each site in the selectivity filter? This question is directly related to debate on the selectivity and the fast permeation rate in recent years. Based on previous knock-on mechanism, the affinity needs be high. However, recent results from Crina lab cast doubt on it, indicating that a slight loose affinity can accelerate the permeation rate. We have not acquired any chemical shift evidence responding to solely ion binding instead of conformation change; hence we are not able to measure the affinity directly. In the water–K^+-water-K^+ hypothesis, the lack of chemical

shift change responding to the K^+ ion binding may be due to the likewise environment when a water is bound. Or the fast dynamics of ion permeation simply average out the chemical shift difference. However, we might be able to acquire the ion dynamics by directly observing the ions. ^{39}K NMR is not sensitive due to the low receptivity of ^{39}K. Since Tl^+ is a good proxy for K^+, it is probably worthwhile doing ^{205}Tl NMR.

One question left in this thesis is that T74S and T74A both show a high potassium affinity in NMR study; however, the electrophysiology result shows that their open probabilities are quite different. Even though we do not know if the lower open probability in T74A mutant is caused by inactivation, it is interesting to find out why the high affinity at the selectivity filter do not lead to high open probability. The hydroxyl group in T or S has been shown to form hydrogen bonding with the back bond of the helix residue. How this stability effort or other unknown effects lead to the low open probability is likely to provide some unexplored information on the channel.

In the future study, it is of great importance to apply the knowledge we learned from KcsA to other channels, such as potassium channel in other family, or sodium and calcium channels. The ability of NMR to provide atomic resolution information makes it probably a great tool to identify the similarity and difference of different channels. We will certainly encounter many challenges, such as the low protein yield, the lower S/N and higher level of peak overlap due to the higher molecular weight. However, development on NMR instruments such as DNP and fast spinning probe may provide us an opportunity to extend more difficult systems.

APPENDICES

1.SIMPSON CSA and dipolar interaction simulation files

1. CSA_Static spectrum simulation

```
spinsys {
  channels 13C
  nuclei 13C
  shift 1 180.6p -90p 0.64 0 0 0
}

par {
  variable index  6
  crystal_file    repulsion16000
  proton_frequency 400e6
  method          direct
  gamma_angles    1
  spin_rate       0
  start_operator  I1x
  detect_operator I1p
  np              2048
  sw              1e5
  verbose         1101
  variable tsw    1e6/sw
}

proc pulseq {} {
  global par

  delay $par(tsw)
  store 1
  reset
  acq $par(np) 1
}


proc main {} {
  global par
  set f [fsimpson]
  faddlb $f 500 0
  fsave $f $par(name),$par(index).fid
  fzerofill $f 4096
  fft $f
  fsave $f $par(name),$par(index).spe
}
```

2. CSA MAS spectrum simulation

```
spinsys {
  channels 13C
  nuclei 13C
  shift 1 180.6p -90p 0.64 0 0 0
}

par {
  spin_rate       10000
  variable index   4
  np              2048
  proton_frequency 400e6
  start_operator   I1x
  detect_operator  I1p
  method          direct
  crystal_file     rep2000
  gamma_angles     8
  sw              20000
  variable tsw     1e6/sw
  verbose         1101
}

proc pulseq {} {
  global par

  acq
  for {set i 1} {$i < $par(np)} {incr i} {
    delay $par(tsw)
    acq
  }
}

proc main {} {
  global par

  set f [fsimpson]
  faddlb $f 30 0
  fsave $f $par(name),$par(index).fid
  fzerofill $f 8192
  fft $f
  fsave $f $par(name),$par(index).spe
}
```

3. Dipolar interaction static spectrum simulation

```
spinsys {
  channels 13C 1H
  nuclei   13C 1H
  shift 1 50p 0p 0 0 0 0
  shift 2 7.0p 0p 0 0 0 0
  dipole  1 2 -20000 0 0 0
}

par {
  variable index  6
  crystal_file    repulsion16000
  proton_frequency 400e6
  method          direct
  gamma_angles    1
  spin_rate       0
  start_operator  I1x
  detect_operator I1p
  np              2048
  sw              1e5
  verbose         1101
  variable tsw    1e6/sw
}

proc pulseq {} {
  global par
  delay $par(tsw)
  store 1
  reset
  acq $par(np) 1
}


proc main {} {
  global par
  set f [fsimpson]
  faddlb $f 500 0
  fsave $f $par(name),$par(index).fid
  fzerofill $f 4096
  fft $f
  fsave $f $par(name),$par(index).spe
}
```

4. Dipolar interaction MAS spectrum simulation

```
spinsys {
  channels 13C 1H
  nuclei   13C 1H
  shift 1 50p 0p 0 0 0 0
  shift 2 7.0p 0p 0 0 0 0
  dipole  1 2 -20000 0 0 0
}

par {
  spin_rate       20000
  variable index   6

  np              2048
  proton_frequency 400e6
  start_operator   I1x
  detect_operator  I1p
  method          direct
  crystal_file     rep2000
  gamma_angles     8
  sw              100000
  variable tsw     1e6/sw
  verbose          1101
}

proc pulseq {} {
  global par

  acq
  for {set i 1} {$i < $par(np)} {incr i} {
    delay $par(tsw)
    acq
  }
}

proc main {} {
  global par

  set f [fsimpson]
  faddlb $f 30 0
  fsave $f $par(name),$par(index).fid
  fzerofill $f 8192
  fft $f
  fsave $f $par(name),$par(index).spe
}
```

2. Chemical shift for KcsA in various states

Chemical shifts of selected marker peaks and reference peaks at various [K^+] and pH. L-H-L-K represents low pH/ low [K^+]; H-H-L-K represents High pH/ Low [K^+]; L-H-H-K represents Low pH/ High [K^+]; H-H-H-K represents High pH/High [K^+].

Residue	Conditions	CA	CB	CG/CG1	CG2	CD	CO
A32 TM1, Helix	L-H-L-K						
	H-H-L-K	55.53	16.37	-	-	-	
	L-H-H-K	55.49	16.45	-	-	-	
	H-H-H-K	55.48	16.43	-	-	-	177.8
I38 TM1, Helix	L-H-L-K	66.68	37.71	29.76	17.47	14.44	-
	H-H-L-K	66.68	37.69	29.68	17.4	14.23	
	L-H-H-K	66.32	37.55	29.38	17.31	13.78	
	H-H-H-K	66.44	37.81	29.49	17.26	13.94	
E51 Helix-loop	L-H-L-K	57.85	31.82	38.6	-	183.7	
	H-H-L-K	57.97	31.33	38.49	-	183.9	
	L-H-H-K	57.85	31.82	38.6	-	183.7	
	H-H-H-K	57.84	31.29	38.76		183.8	176.5
A54 outer loop	L-H-L-K	50.35	18.22	-	-	-	176.4
	H-H-L-K	50.48	18.26	-	-	-	-
	L-H-H-K	50.22	18.07	-	-	-	
	H-H-H-K	50.31	18.34	-	-	-	-
A57 outer loop	L-H-L-K	53.58	21.06	-	-	-	
	H-H-L-K	-	-	-	-	-	-
	L-H-H-K	53.26	21.38	-	-	-	
	H-H-H-K	53.37	21.39	-	-	-	-
L59 outer loop	L-H-L-K	53.33	39.3	25.15	-	-	
	H-H-L-K	53.42	39.35	25.16	-	-	174.6
	L-H-H-K	53.26	39.28	25.07	-	-	
	H-H-H-K	53.33	39.47	25.14	-	-	174.9
I60 outer	L-H-L-K	61.82	38.6	25.97	18.83	13.74	
	H-H-L-K	61.59	38.64	26.04	18.49	13.82	-
	L-H-H-K	61.81	38.76	26.05	18.23	13.83	-
	H-H-H-K	61.7	38.74	26.06	17.99	13.8	-

loop							
T61 Outer loop	L-H-L-K	58.63	71.67	22.59	-	-	173.3
	H-H-L-K	58.75	71.73	22.54	-	-	173.3
	L-H-H-K	58.81	72.03	22.63	-	-	173.5
	H-H-H-K	58.89	71.95	22.85	-	-	173.3

Y62 Outer loop E71 Pore helix	**L-H-L-K**	**63.95**	**36.36**	**-**	**-**	**-**	
	H-H-L-K	64.11	36.65	-	-	-	173.6
	L-H-H-K	63.98	36.56	-	-	-	-
	H-H-H-K	63.97	36.47	-	-	129.6	-
	L-H-L-K	-	-	32.14	-	180.7	-
	H-H-L-K	-	-	32.23	-	180.8	-
	L-H-H-K	-	-	32.61	-	182.5	-
	H-H-H-K	58.29	-	32.48	-	182.5	-

Residue	Conditions	CA	CB	CG/CG1	CG2	CD	CO
T74 Selectivity filter	L-H-L-K	61.78	70.63	20.25	-		177.4
	H-H-L-K	61.64	70.48	20.8	-	-	176.9
	L-H-H-K	61.23	69.74	21.5	-	-	176.4
	H-H-H-K	61.15	69.78	21.51	-	-	176.4
T75 Selectivity filter	L-H-L-K	62.67	69.12	22.45	-	-	172.4
	H-H-L-K	62.57	69.23	21.02	-	-	172.3
	L-H-H-K	63.23	69.33	21.55	-	-	172.6
	H-H-H-K	63.16	69.36	21.67	-	-	172.5
V76 Selectivity filter	L-H-L-K	65.38	30.34	22.15	20.04		
	H-H-L-K	65.25	30.24	22.72	20.13		-
	L-H-H-K	66.14	31.89	-	20.36		-
	H-H-H-K	66.26	31.89	-	20.31		
Y78 Selectivity filter	L-H-L-K	61.96	38.66	-	-	-	
	H-H-L-K	61.77	38.82	-	-	-	-
	L-H-H-K	61.81	38.56	-	-	-	-
	H-H-H-K	61.66	38.48	130.5	-	117.4	178.1
D80 Outer loop	L-H-L-K	54.79	37.32	-	-	176.3	179.3
	H-H-L-K	55.19	37.12	-	-	176.1	179.3
	L-H-H-K	55.57	37.37	-	-	175.6	179.5
	H-H-H-K	55.64	37.39	-	-	175.7	179.4
L81 outer loop	L-H-L-K	53.6	48.44	27.27	27.18	-	-
	H-H-L-K	53.56	48.44	27.22	-	-	-
	L-H-H-K	52.96	47.74	-	27.13	-	-
	H-H-H-K	53.12	47.71	27.51	27.46	-	175.7

Y82 Outer loop	L-H-L-K	55.47	36.24	-	-	-	172.5
	H-H-L-K	55.47	36.41	-	-		172.4
	L-H-H-K	55.64	34.93	-	-	-	172.1
	H-H-H-K	55.54	34.88	118.3		127.4	172.0
V84 Outer loop	L-H-L-K	60.82	32.77	18.23	21.36	-	
	H-H-L-K	60.85	32.63	18.4	21.34	-	-
	L-H-H-K	60.86	32.62	18.28	21.26	-	-
	H-H-H-K	60.65	32.58	18.28	21.36	-	176.4
T85 Loop-helix TM2	L-H-L-K	60.69	72.41	22.8	-	-	174.7
	H-H-L-K	60.79	72.4	22.85		-	174.5
	L-H-H-K	60.69	72.69	22.67	-	-	174.8
	H-H-H-K	60.69	72.51	22.84	-	-	174.6
R89 TM2 helix	L-H-L-K	60.21	31.57	28.51	-	45.17	
	H-H-L-K	-	-	-	-	-	
	L-H-H-K	60.25	31.48	28.63	-	45.05	-
	H-H-H-K	59.42	29.84			44.24	
A92 TM2 helix	L-H-L-K	56.25	20.07	-	-	-	
	H-H-L-K	56.2	20.24	-	-	-	-
	L-H-H-K	56.04	20.69	-	-	-	-
	H-H-H-K	56.08	20.63	-	-	-	-

Residue	Condition	CA	CB	CG/CG1	CG2	CD	CO
Ile100 TM2 helix	L-H-L-K	66.25	37.94	30.86	16.81	13.96	181
	H-H-L-K	65.96	39.63	-	17.97	13.94	
	L-H-H-K	-	-	30.58	16.72	-	-
	H-H-H-K	66.13	39.42	-	18.16	-	-
E118/120 pH sensor	L-H-L-K	-	-	34.2	177.4	-	
	H-H-L-K	-	-	34.5	177.4	-	-
	L-H-H-K*	-	-	34.09/ 36.1	177.6 /183	-	-
	H-H-H-K	59.61	29.81	36.11	183.1	-	-

*Two chemical shift values indicate that two conformations appear in the same sample.

3. Allosteric coupling and related thermodynamic parameters

We calculated the free energy for conformational transitions at neutral and acidic pH based on the equation 1, which relates the measured affinity (K_d), to the free energy (ΔG) of the transition.

$$1/K_d = K_{eq} = \exp(-\frac{\Delta G}{RT}) \qquad \text{Eq. 1}$$

The strength of the allosteric coupling is related to the difference in the relative free energy of the transition at neutral vs. acidic pH, as described in equation 2.

$\Delta\Delta G = \Delta G_{neutral} - \Delta G_{acidic} = RT\ln(K_d(\text{neutral})) - RT\ln(K_d(\text{acidic}))$ Eq. 2

Based on our measurements of K^+ affinities of 4±1 mM for pH 7.5 and 14±1 mM at pH 3.5, and making the simplifying assumption that the Hill coefficient is 1 for both K^+ and H^+, the $\Delta\Delta G$ representing the allosteric coupling is -19±2 kJ.mol^{-1}, at a temperature T=273K, (R is the universal gas constant). This value represents a lower bound on the allosteric coupling strength, because we assume that the binding involves a single K^+ and a single H^+. The stoichiometry of the binding reaction is debated and difficult to measure. An equation of allosteric coupling energy for n K^+ binding will be:

$\Delta\Delta G = \Delta G_{neutral} - \Delta G_{acidic} = nRT\ln(K_d(\text{neutral})) - nRT\ln(K_d(\text{acidic}))$ Eq. 3

4. Population distribution for various states at different pH and [K^+]- mathematics document

(*Dual binding thermodynamics equation*)

(* P+K-->PK Kd1; PK + H--> PKH Kd2; P+ H-->PH Pka Kd2/a; PH+K-->PHK Kd12)

P = Kd1^m * Kd2^n/(Kd1^m* Kd2^n + Kd2^n*(10^logK)^m + Kd12^m*(10)^(-pH*n) + (10^logK)^m*10^(-pH*n)); PK = Kd2^n*(10^logK)^ m/(Kd1^m* Kd2^n + Kd2^n*(10^logK)^m + Kd12^m*(10)^(-pH*n) + (10^logK)^m*10^(-pH*n)); PH = Kd12^ m*(10)^(-pH*n)/(Kd1^m* Kd2^n + Kd2^n*(10^logK)^m + Kd12^m*(10)^(-pH*n) + (10^logK)^m*10^(-pH*n)); PHK = (10^logK)^ m*10^(-pH*n)/(Kd1^m* Kd2^n + Kd2^n*(10^logK)^m + Kd12^m*(10)^(-pH*n) + (10^logK)^m*10^(-pH*n)); Kd1 = 4*10^(-6); Kd12 = 14*10^(-3);

m = 2; n = 8;

P; PH; PK; PHK; P

P

Kd2^8/(62500000000 (49 2^(-4 - 8 pH) 5^(-6 - 8 pH) + 10^(2 logK - 8 pH) + Kd2^8/62500000000 + 10^(2 logK) Kd2^8))

PH

(49 2^(-4 - 8 pH) 5^(-6 - 8 pH))/(49 2^(-4 - 8 pH) 5^(-6 - 8 pH) + 10^(2 logK - 8 pH) + Kd2^8/62500000000 + 10^(2 logK) Kd2^8)

PK

(10^(2 logK) Kd2^8)/(49 2^(-4 - 8 pH) 5^(-6 - 8 pH) + 10^(2 logK - 8 pH) + Kd2^8/62500000000 + 10^(2 logK) Kd2^8)

PHK

10^(2 logK - 8 pH)/(49 2^(-4 - 8 pH) 5^(-6 - 8 pH) + 10^(2 logK - 8 pH) + Kd2^8/62500000000 + 10^(2 logK) Kd2^8)

Manipulate[Plot3D[{Kd2^8/(62500000000 (49 2^(-4 - 8 pH) 5^(-6 - 8 pH) + 10^(2 logK - 8 pH) + Kd2^8/62500000000 + 10^(2 logK) Kd2^8)), (10^(2 logK) Kd2^8)/(49 2^(-4 - 8 pH) 5^(-6 - 8 pH) + 10^(2 logK - 8 pH) + Kd2^8/ 62500000000 + 10^(2 logK) Kd2^8), (49 2^(-4 - 8 pH) 5^(-6 - 8 pH))/(49 2^(-4 - 8 pH) 5^(-6 - 8 pH) + 10^(2 logK - 8 pH) + Kd2^8/ 62500000000 + 10^(2 logK) Kd2^8), 10^(2

logK - 8 pH)/(49 2^(-4 - 8 pH) 5^(-6 - 8 pH) + 10^(2 logK - 8 pH) + Kd2^8/ 62500000000 + 10^(2 logK) Kd2^8)}, {pH, 3, 10}, {logK, -9, 0}, PlotRange -> 01.0, PlotStyle -> {Red, Green, Blue, Black}, PlotLegends -> {P, PK, PH, PHK}, AxesLabel -> {pH, logK, Population_ratio}], {Kd2, 10^(-7), 10^(-3)}]

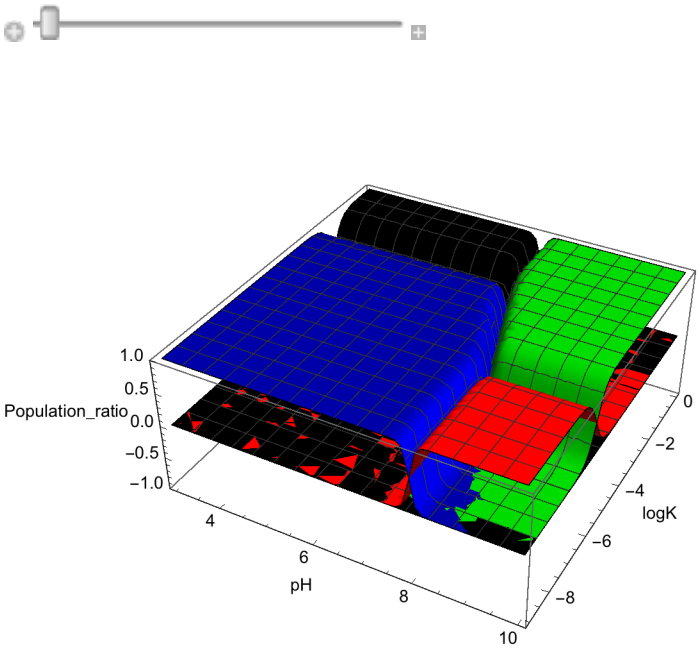

5. Protein reconstitution for single channel recording experiemnts

1. Prepare lipids: POPE/POPG 3:1 (for KcsA lipid bilayers) or E.Coli lipids for fluxes or any other desired lipids or lipid combinations. Thaw ampules or containers in the hood. After reaching RT, transfer in glass tubes and blow the chloroform away with nitrogen by using a Pasteur pipette instead of the needle gizmo. Rinse with 1 volume of pentane to remove all traces of chloroform (by blowing N again). Add 1 volume of swelling buffer and sonicate. While sonicating, add CHAPS detergent (enough powder to reach 34 mM concentration to solubilize the lipids, and leave there until no more chunks and clear (the solution never looks clear enough). Leave the solubilized lipids at rt for 1-2 hours before adding the protein (Voodoo step).

2. Make the reconstitution buffer (RB) and the sephadex beads (G-50 fine on chromatography shelf)

   Swelling buffer (1 liter):

   - 400 mM KCl …….. ……..29.82 g
   - 10 mM HEPES…….. 2.38 g
   - 5 mM NMG (adjusts pH to 7.6) ……0.976 g

     pH = 7.6

   200 uM cAMP if needed (dilute 1:500 from 100 mM stock)

   Sephadex columns (6-7 columns):

   - 300 ml swelling buffer
   - 20 g sephadex beads

   It can be prepared the night before and left on bench overnight. If the saturated sephadex is in the fridge, allow to reach RT, degas by applying some vacuum to the flask (~ 3 min., care should be taken not to chill the mixture too much).

   After combining the desired protein concentration with the lipid, pour the saturated beads into 20 ml columns with stopper valves, leave the liquid go through, close the valves and then pour a little more swelling buffer on top to prevent drying out and cracking. Add slurry until the volume reaches 20 ml (marked on col).

The columns should be vertical, there should be no air bubbles and the beads should be permanently wet on top.

3. Mix lipids and protein extract in an appropriate ratio for single channels or multiple channels:

    500 ul lipid

    2.5 (5) ug Kcsa for single channels

    Let sit for 20min.

Add mixture on the column right after drying the column top. Add approximately 5 ml swelling buffer (1/3 of the column volume goes through before the protein-lipid complexes reach the bottom of the column) after adding the protein-lipid mix and let it go through, no need to collect. After the above-mentioned 5 ml of wash, collect the eluate in fractions of ~ 500 ul in borosilicate glass tubes. The turbid eluate (1-2 middle tubes) contain the lipid-protein vesicles.

Aliquot the vesicles in small PCR tubes, 60 ul each, and rapidly freeze them in liquid N after which they should be stored in –80.

6. Population correlation plots between various residues with V76

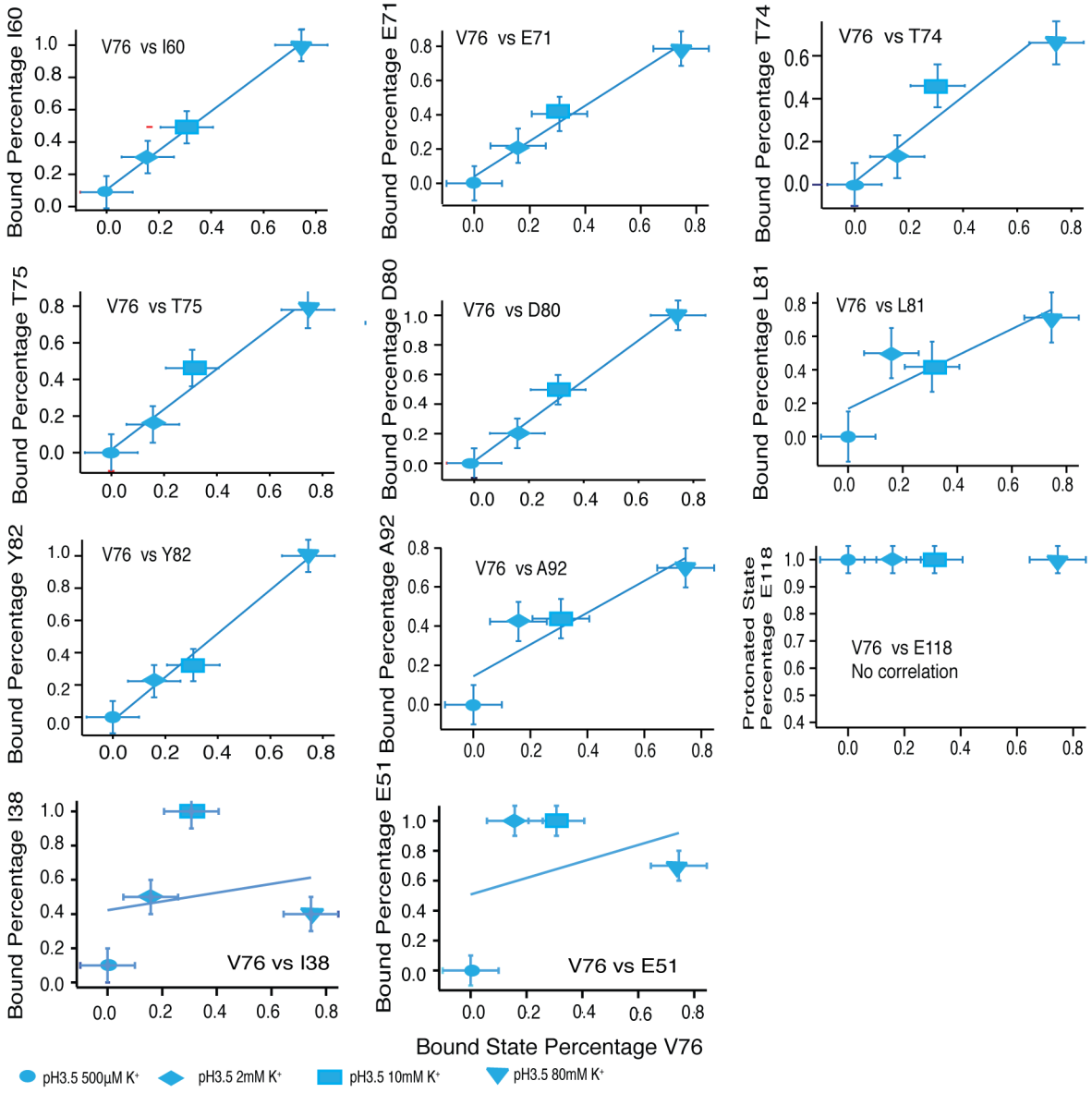

	I60	E71	T74	T75	D80	L81
Corr.	1	0.99	0.95	0.98	0.99	**0.85**
Slop.	0.82	0.73	1.03	1.0	0.91	**0.73**

Y82	A92	E118	I38	E51
0.95	0.85	NA	0.72	0.37
0.79	0.74	NA	0.26	0.52

Pairwise correlation analysis of the fractional population of the K^+ bound state, comparing various residues at the acidic pH. Pearson correlations of bound state populations for different residues were calculated for various pairs, for example, between Val76 and other residues (I60, T74, T75, E71, D80, L81, Y82, A92 etc.), wherein both bound and unbound state cross peaks can be identified. This is an expansion of the covariance matrix at Val76 at acidic pH. (Figure 3) The table shows the correlation coefficients and slopes of the linear fittings.

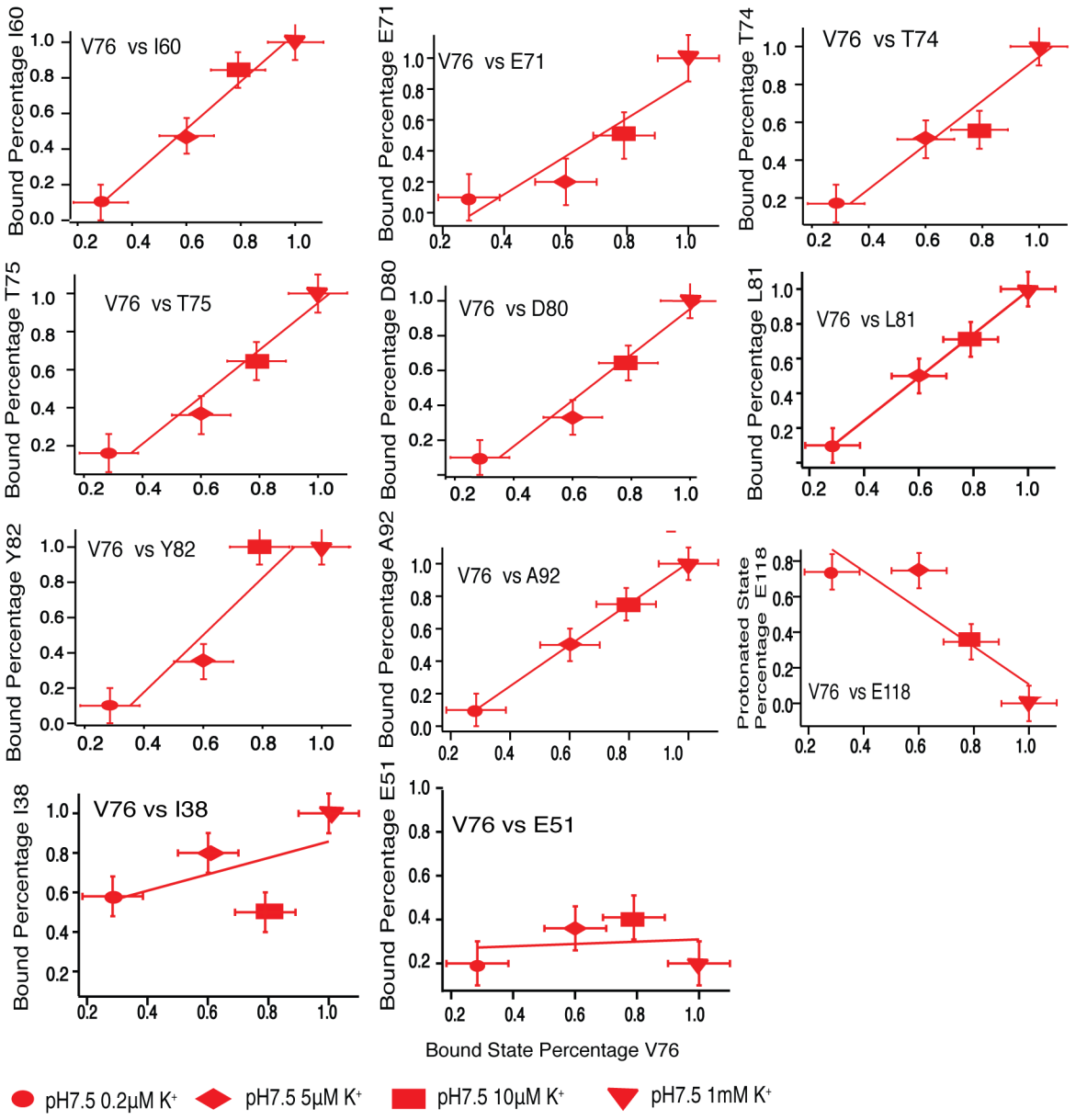

	I60	E71	T74	T75	D80	L81
Corr.	0.99	0.92	0.96	0.97	0.99	1.0
Slop.	0.82	1.23	0.86	0.81	0.76	1.24

Y82	A92	E118	I38	E51
0.95	0.99	-0.89	0.56	0.15
0.62	1.26	-1.06	0.41	0.05

Pairwise correlation analysis of fractional bound state population comparing different residues at neutral pH. Similar *Pearson* correlations of bound state population of different residues were calculated between V76 and other residues (I60, T74, T75, E71, D80, L81, Y82, A92 etc) for neutral pH sample. At this pH, E118 shows a negative correlation with V76.

7. Magnetic moment and spin quantum number calculation

We characterized the temperature dependences of the chemical shift for the neutral +1 and +2 cluster. The NMR shifts in angular units (not Hz) are plotted against the inverse temperature in the high temp limit to obtain slopes, which in this case were k~ 0 for the neutral cluster, k=2 π 7.4*e4 for the +1 cluster, and k= 2π 2.89*e5, for the +2 cluster.(Figure 6.3) Based on Curie's law, the slope, k, can be used to determine the magnetic moment k= (μ /2.828)^2. By using this equation, we assume that the individual carrier of magnetic moment does not interact with one other.

For the +1 cluster, μ=sqrt(0.0743*2*3.14) * 2.828= 1.92

For the +2 cluster, μ= sqrt(0.289*2*3.14) * 2.828= 3.8

In Superconducting Quantum Interference Devices (SQUID) magnetic susceptibility measurements, μ was observed to be 1.8 for the +1 cluster and 2.6 for the +2 at high temperature. The agreement between the NMR characterization and the SQUID determination is excellent for the +1 cluster, and for the +2 cluster there is approximate agreement and more study or discussion of errors is needed.

The spin quantum number of the unpaired electron can be calculated from the total magnitude of the spin magnetic moment through the equation: $\mu_s = g\sqrt{S\,(S+1)}$, in which g is the g-factor and the value is expected to be around 2 (although it has not been measured for these specific species to the best of our knowledge). In this equation, the contribution from orbital angular momentum is omitted.

In the following calculation, g-factor is assumed to be 2. The spin quantum numbers S calculated from SQUID data is 0.53 for +1 cluster and 0.89 for +2 cluster. The spin quantum numbers S calculated form NMR data is 0.58 for the +1 and 1.46 for the +2 cluster. In the +2 cluster, the result suggests that the orbital angular momentum contribution is important, which is expected when the ground term is triply degenerate i.e. a T state.

Based on these results, we conclude that a single unpaired electron exists in the +1 cluster and possibly two net unpaired spins are observed in the +2 cluster.